Coherent acoustic-phonon dynamics in GaAs/AlAs heterostructures

Omar Hernán Ortiz Cabello

▶ To cite this version:

Omar Hernán Ortiz Cabello. Coherent acoustic-phonon dynamics in GaAs/AlAs heterostructures. Acoustics [physics.class-ph]. Université Paris-Saclay, 2021. English. NNT : 2021UPASP021 . tel-03268382

HAL Id: tel-03268382
https://theses.hal.science/tel-03268382v1

Submitted on 23 Jun 2021

Coherent acoustic-phonon dynamics in GaAs/AlAs heterostructures

Dynamique de phonons acoustiques cohérents dans des hétérostructures GaAs/AlAs

Thèse de doctorat de l'Université Paris-Saclay

École doctorale n° 572, Ondes et Matière (EDOM)
Spécialité de doctorat: Physique
Unité de recherche: Université Paris-Saclay, CNRS, Centre de Nanosciences et de Nanotechnologies, 91120, Palaiseau, France
Référent: Faculté des sciences d'Orsay

Thèse présentée et soutenue à Paris-Saclay,
le 31 mars 2021, par

Omar Hernán ORTIZ CABELLO

Composition du jury

Juan Ariel Levenson Directeur de recherche, C2N/CNRS	Président
Andrea Bragas Professeure, Universidad de Buenos Aires	Rapporteur & examinatrice
Sebastian Volz Directeur de recherche, LIMMS - University of Tokyo	Rapporteur & examinateur
Anthony Kent Professeur, University of Nottingham	Examinateur
Samuel Raetz Maître de conférences, LAUM - Le Mans Université	Examinateur

Direction de la thèse

Daniel Lanzillotti-Kimura Chargé de recherche, C2N / CNRS	Directeur de thèse
Pascale Senellart Directrice de recherche, C2N / CNRS	Co-encadrant

Thèse de doctorat

NNT: 2021UPASP021

Synthèse en français

Les phonons sont des quasi-particules relativement peu exploitées à des fins d'application, en comparaison avec les électrons ou les photons. Les hétérostructures faites de GaAs/AlAs comme les super-réseaux ont été établies comme une plateforme qui permet l'ingénierie de la propagation et du confinement des phonons acoustiques dans les nanostructures. Les dispositifs nanophononiques se caractérisent par leur fonctionnement à des fréquences généralement comprises entre quelques gigahertz et les térahertz. Au cours de cette thèse, nous avons développé des techniques expérimentales pour l'étude des structures nanotechnologiques qui contrôlent la propagation de phonons acoustiques cohérents dans la gamme du gigahertz au térahertz. Afin de détecter les phonons à des fréquences si élevées, la spectroscopie optique pompe-sonde peut être utilisée pour effectuer des expériences cohérentes de génération et de détection de phonons qui résolvent dans le temps leurs effets sur l'échantillon à l'étude. Nous développons de nouvelles techniques expérimentales basées sur l'utilisation de fibres monomodes et sur la spectroscopie pompe-sonde qui nous permettent d'identifier la présence de phonons cohérents avec une robustesse et une reproductibilité sans précédent. À l'aide des outils expérimentaux développés, trois résonateurs acoustiques fonctionnant à des fréquences de 18, 200 et 390 GHz ont été étudiés. Ils ont été fabriqués dans les salles blanches du Centre des Nanosciences et Nanotechnologies (C2N). Un accent particulier de ce travail a été mis sur les structures hybrides, fonctionnant à la fois comme résonateurs acoustiques et comme cavités optiques. En outre, nous avons étudié expérimentalement la structure multicouche sous la forme de micropiliers résonants à environ 18 GHz. Nous avons introduit une nouvelle approche pour étudier les structures enmicropiliers mettant en avant l'utilisation de fibres monomodes. En collant un système micropilierà la pointe d'une fibre monomode, nous avons pu coupler la lumière dans son mode de cavité optique créant un nouveau dispositif: un résonateur micropilier intégré à la fibre. Au moyen de la spectroscopie pompe-sonde, nous avons étudié la dynamique des cavités optiques subie par les résonateurs micropiliers ainsi que leurseffets lors de la détection de phonons cohérents dans les structures résonantes. Nous avons étudié la robustesse des mesures effectuées sur le micropilier intégré à la fibre et avons pu mesurer les spectres acoustiques de tels dispositifs avec une stabilité sans précédent au cours de plus de 40 heures. Cette nouvelle technique nous a permis d'obtenir une quantité de données importante à partir de l'étude des micropiliers. En faisant varier les conditions spectrales temporelles des mesures de spectroscopie pompe-sonde, nous avons introduit un modèle qui reproduit la dynamique de la cavité optique subie par les systèmes de micropilierssoumis à une action laser ultra-rapide à différentes puissances de pompe. En plus de la ligne de recherche expérimentale suivie dans cette thèse, une autre ligne de recherche s'est concentrée sur l'investigation théorique des structures multicouches. Un type particulier de dispositif multicouches appelé cavité adiabatique, résultant de la modification progressive des paramètres de conception des structures de super-réseaux, a été étudié à des fins de confinement. De plus,comme résultat secondaire de cette recherche, nous avons développé une méthode pour l'ingénierie de structures adiabatiques multicouches capable de reproduire l'effet des potentiels pour les phonons. Malgré l'absence de masse des phonons, nous avons démontré par des simulations comment il est possible de modifier leur vitesse de groupe dans une structure multicouche agissant ainsi comme des potentiels nanomécaniques. Ces nouveaux dispositifs peuvent contrôler la propagation des ondes acoustiques et, en outre, nous permettre d'étudier et d'imiter des phénomènes de physiques des solides de nature différente.

Mais, que les efforts soient plus ou moins favorisés par la vie,
il faut, quand on approche du grand but, être en droit de se dire :
«J'ai fait ce que j'ai pu»
– Louis Pasteur

Acknowledgements

First and foremost I would like to thank my mother, Nelly Cabello Ormachea. I am the proud son of a single mother who raised me by herself. It is to her to whom I am mostly grateful for motivating my scientific curiosity since I was a child and for educating me in principles that are part of me forever. I thank my wife, Jimena Vargas, who has been part of my journey for more than a decade, bringing joy, amazing conversations and without whom I would not be here now. I want to thank my uncle Rodolfo Luna Cabello, who sadly departed early from this life while I was working in this thesis. His lessons will always be part of me.

Over the course of more than three years of this thesis I have got to know so many wonderful people from whom I have learned a lot. I would like to thank in general the Centre de Nanosciences et de Nanotechnologies that has hosted me during my thesis and that comprises all the amazing technologies and people that push forward the way we understanding of nature. I thank Daniel Lanzillotti Kimura who gave me the opportunity to be part of his team and guided me during the course of this thesis. The rich discussions with him about physics, his openness to new ideas in the laboratory and his driving force for research are the main reasons behind the work accomplished during this thesis. I thank Martin Esmann, postdoc in the team of Daniel, with whom I have shared plenty of time in the laboratory and who has also guided me through the ups and downs of the work both in the laboratory and outside of it. The rich discussion with him about physics and several other topics were one of many reasons that made my time at the C2N a wonderful experience. To both of them I would like to thank not only for the guidance but also for their friendship.

I thank the other members of the phonon team and friends Anne Rodriguez, Priya, Edson Cardozo and Fabrice Lamberti all of them who were always there for me in a kind and helpful way. Sadly I did not have too much time in the laboratory with Edson but I am sure the perspectives of his work are very promising and I am sure he will accomplish a lot during his postdoc in the group. To Priya, I thank for her friendship, her amazing willingness to help and to transmit her knowledge. Her work with quantum dots has great perspectives and I am sure she will accomplish a lot. To Anne, with whom I have shared more time in the laboratory I am very grateful. Not only she became a great friend of mine but also she always pointed interesting questions and since day one, during her master internship, she was willing to put her heart into the experiments. I know she will succeed during her thesis as she already is demonstrating.

I want to thank the GOSS team for all their support and help. In particular I thank Pascale Senellart and Loïc Lanco, whose advice and guidance were indispensable over the course of this thesis. I also thank Juan Loredo for his long standing friendship, for his advice and for always being there to support me over the course of this thesis. Special thanks to professor Francisco De Zela from Peru for being the first to motivate my work in the laboratory and for all his support.

I would like to thank the help provided by the laboratory staff, in particular to the administrative and informatics departments. I thank Alain Pean and Laoges Thao whose help saved my day on more than one occasion. I would also like to thank the groups of Aristide Lemaître and Isabelle Sagnes. Without them, many of the experiments presented in this would not have been possible. In addition, I want to thank Abdelmounaim Harouri whose help and friendship were always appreciated.

I want to thank all jury members: Andrea Bragas, Sebastian Volz, Juan Ariel Levenson, Anthony Kent and Samuel Raetz. It is an honor to have such outstanding jury members and to be able to receive their feedback and perspective on my work.

I thank those friends who have been part of my formation since my early years. To Roberto Rodriguez, Adrian Hartill, Esteban Almuelle, Oscar Rincón, Gonzalo Diaz, Christian Pasquel and Juan Pablo Velasquez. Without the amazing discussions and adventures we have had over the course of several years I would not be the person I am today.

Contents

Chapter 1

Motivation

In physics, the study of mechanical vibrations constitutes the field of acoustics. Its origins date back more than two and a half millennia ago, with Pythagoras performing experiments using taut strings, pipes, glasses filled with water, etc. and studying how we hear the sounds they produce [1, 2]. For the most part of its history, acoustics has been limited to the study of vibrations we can hear, i.e. with frequencies between 20 Hz and 20 kHz. Over the last century, technological developments have allowed us to go beyond these limits to study mechanical vibrations in a wide range of length and temporal scales for multiple applications. Focusing on small length scales and fast phenomena, this thesis addresses the engineering of acoustic waves in the tens to hundreds of gigahertz range.

Figure 1.1 presents the acoustic spectrum together with few examples of how the study and control of mechanical vibrations is applied at different scales [3]. Infrasound, for example, is nowadays used to monitor volcano craters acting as giant resonators at frequencies of fractions of Hertz with wavelengths in the order of hundreds of meters. By monitoring the infrasound in the vicinity of active volcanoes, geologists have been able to identify signals of future eruptions (figure 1.1 (a)) [4, 5]. At the audible range a wide variety of musical instruments have been developed to control sound. As an example, the Cajón is an Afro-Peruvian musical instrument with a simple design consisting of a wooden box (~ 50 cm$\times$30 cm$\times$25 cm) with a circular hole centered on its back side (figure 1.1 (e)) [6]. It is a percussion instrument played by slapping it on its front side, causing the air inside to resonate at frequencies of few hundreds of Hertz as imposed by the boundary conditions the wooden box enforces [7]. The wavelengths corresponding to these resonant frequencies are on the order of meters, with typical values lying between 1 and 2 meters. With wavelengths in the range from centimeters down to hundreds of micrometers, ultrasound required the development of electronic transducers in order to be experimentally studied. In 1880, Jacques and Pierre Curie discovered piezoelectricity, a phenomenon that causes some materials to accumulate surface charge when subject to stress [8]. More than three decades later and driven by the first world war efforts to detect submarines, sensors using ultrasound found their first application [9]. From that moment until now, ultrasound has revolutionized multiple disciplines with remarkable examples like sound navigation ranging (SONAR, see figure 1.1 (b)) [10, 11], non-invasive imaging technologies for medical applications [12, 13] and a vast variety of sensors and actuators based on micro-electromechanical systems (MEMS) [14–16]. At frequencies higher than one hundred megahertz up to tens of gigahertz, mechanical vibrations are known as hypersound. The control of hypersound requires devices ranging from the micrometer to the nanometer scale. Nanoelectromechanical systems (NEMS) like freely suspended nanostructures and inter-digital transducers (IDT) are capable of reaching frequencies up to few gigahertz and have demonstrated potential for several applications given their unique attributes [17–19]. At higher frequencies, the lack of standard electronic transducers leave us mainly with optical tools to study acoustics. Micro- and nanomechanical systems such as superlattices, crystals (figure 1.1 (f)), nanobeams and micropillars (figure 1.1 (g)) have demonstrated capabilities to control vibrations with frequencies ranging from few gigahertz up to several hundreds of gigahertz [20–23]. Mechanical vibrations with

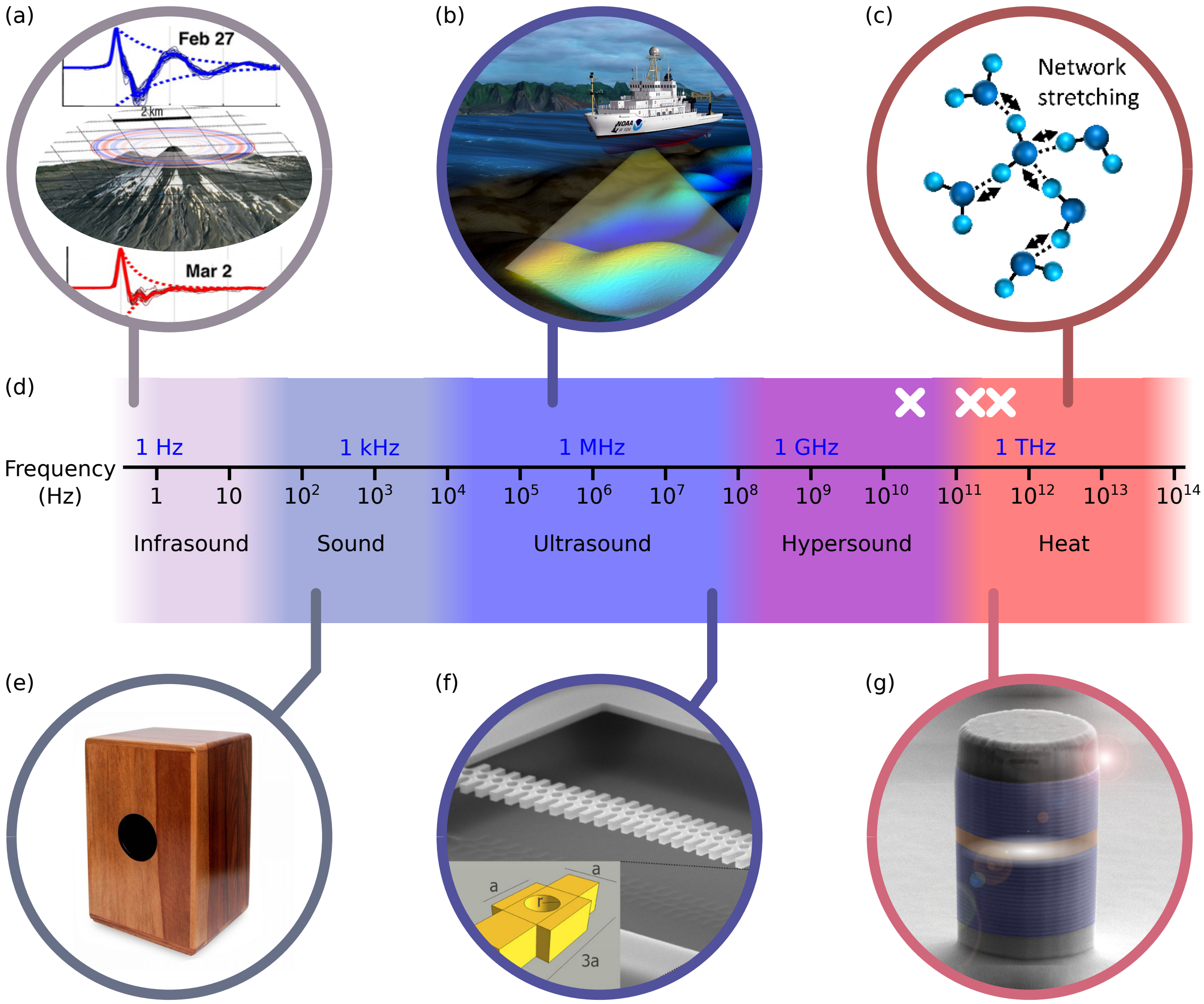

Figure 1.1: Spectrum of mechanical vibrations with insets presenting examples of research and applications at different scales. (a) Signals of volcano eruption. Infrasound waveforms recorder from Villarica volcano prior to its eruption of the 3th of March 2015. Adapted from [4]. (b) SONAR systems operating at hundreds of kilohertz are used to imagine the seafloor. (c) Molecules like water vibrate at frequencies in the order of terahertz. Adapted from [32]. (d) Spectrum of mechanical vibrations. White crosses mark the resonant frequencies of the devices experimentally studied for this manuscript (20, 200 and 390 GHz). (e) Cajón. Afro-peruvian musical instrument with resonant frequencies in the hundred Hertz [7]. (f) Optomechanical crystal structure supporting mechanical modes at 54 MHz. Adapted from [33]. (g) Optophononic micropillar confining acoustic phonons at 300 GHz [21].

frequencies in the order of terahertz and more are associated with heat. The control of heat in micro and nano devices is of great importance for many applications in particular for nanoelectronic devices [24, 25]. Structures fabricated at the nanoscale can be engineered to control heat propagation [26–31]. In the terahertz frequency range, vibronics, focus on the study of molecular vibrations like water for example with intermolecular vibration modes in the range between 1 and 10 THz (figure 1.1 (c)) [34]. From fractions of Hertz up to several terahertz, we have presented few examples of mechanical systems at different scales. In the course of this thesis, we have studied mechanical vibrations in the gigahertz to terahertz range as illustrated by the white crosses in figure 1.1 (d) spectrum marking the resonant frequencies (18, 200 and 390 GHz) of the acoustic systems experimentally investigated for this manuscript.

At extremely high frequencies beyond several gigahertz, mechanical vibrations occur at the scale of the atomic structure constituting the medium that sustains them. In this limit we encounter the field of nanophononics. Phonons are the quanta of vibrations, they are the result of quantizing the displacement of the atomic nuclei forming the medium supporting the vibrations being described [35]. Nanophononics as a field of physics, addresses the study of phonons in solid-state nanostructures. Nanophononic devices are characterized by operating at frequencies commonly in the range of few gigahertz up to terahertz. In typical solid-state materials the corresponding wavelengths associated with such rapid vibrations are at the nanometric scale. In comparison with electronics and photonics, the development of nanophononics is quite recent [22, 23, 36–39]. Nowadays, the technological revolution we are living has nanotechnology at its core, but only photons and electrons have been the particles mostly exploited for application purposes [40]. While the size of electronic and photonic devices kept reducing towards the nanoscale, the role phonons play in their dynamics became more relevant, motivating the development of nanophononics from different communities [37]. Nanoelectronics, for example, addresses the study of electronic systems at the nanoscale. Nanoelectronic devices are designed to control the propagation and, in general, the electron dynamics by engineering the electromagnetic environment in them. An intrinsic part of this environment is the atomic structure of the device itself. As a consequence, there is always a contribution to the electronic dynamics resulting from the interaction between electrons and the overall atomic structure. Typically known as heat, the energy leaked in these processes is commonly understood as wasted and can lead to unwanted behavior affecting the performance of nanoelectronic systems [24, 25]. Through careful design of the phononic dynamics in nanoelectronic devices, heat transport can be engineered in order to reduce its deleterious effects for a given application [26, 28–31]. Beyond their direct link to heat control, phonons themselves can be included in the overall design of hybrid systems which, by exploiting the different characteristics of photons, electrons and phonons, are engineered for applications purposes. Quantum technologies are an example of a field where such a strategy can and is currently being applied for the development of novel devices [41, 42]. Despite being commonly associated to decoherence effects, phonons can be used to carry and process quantum information [43–47]. In addition, it is possible to engineer devices that counteract the detrimental effects phonons typically have when trying to preserve quantum states hosted in solid-state systems [48, 49]. Another perspective on the work with phonons comes from the idea of using nanophononic structures as a simulation platform for complex wave dynamics [50–52]. In contrast with photons, phonons feature slow propagation speeds and coherence lengths in the scale of hundred of micrometers for phonons with wavelengths in the tens of nanometers. Consequently, complex wave dynamics can be studied in quasi-infinite systems while remaining experimentally accessible optically by probing it on time scales well below the mechanical oscillation period. All these examples show the relevance of nanophononics for the development of new technologies. It addresses the study of a quasi-particle relatively unexploited for application purposes, in comparison with electrons and photons. Moreover, their strong interaction in solid-state devices brings a new design aspect for the future of nanotechnology.

State of the art fabrication techniques like molecular beam epitaxy (MBE), electron-beam lithography, optical lithography, inductively coupled plasma etching, etc. allow the engineering of micro- and nano-structures that control the propagation and confinement of acoustic and optical fields. In nanophotonics, structures such as micropillars, nanobeams and photonic crystals have demonstrated many applications, for example, operating as quantum light sources [53–56], for sensing applications [57, 58] and as optical cavities with ultra high quality factors [59]. In an analogous way, phononic devices can be engineered to control the propagation and confinement of acoustic fields. In contrast with visible optical waves, hypersound at the range of tens of gigahertz up to terahertz has wavelengths in solid-state materials that can reach values down to few nanometers (for example phonons in $GaAs$ at 100 GHz have a corresponding wavelength of less than 50 nm). This results in nanophononic structures being more challenging to fabricate given the higher resolution required. In order to fabricate an acoustic analog of what in optics are dielectric mirrors, i.e. distributed Bragg reflectors for phonons, it is not uncommon that layer thicknesses reach values one order of magnitude lower than those required in optics. By modern fabrication techniques and, by using the same design principles as in optics i.e. multiple interference phenomena, analogous devices like acoustic distributed Bragg reflectors and structures confining phonons, i.e. resonators, can be fabricated [22, 23, 38, 39, 60–65]. Multilayer structures like superlattices have played an important role for the development of different fields. In nanoelectronics for example, superlattices were at the core of technological advances like the measurement of the giant magnetoresistance. In nanophononics, superlattices have been used not only to engineer acoustic fields inside a structure, but also to enhance their transduction into optical signals [38, 39, 66–68]. Remarkable realizations using superlattices include optical cavities doubling as acoustic resonators by colocalizing acoustic and optical fields within the same region [69, 70], acoustic structures in the range of hundreds of gigahertz embedded in optical cavities [60, 71, 72] and coherent phonon amplification [22, 23]. While remarkable results have been obtained using superlattices there is always a need for novel and versatile strategies to control phonon dynamics. The first line of research of this thesis comprehends the theoretical study of multilayer structures controlling the propagation and confinement of acoustic phonons. Within this line two objectives were pursued. First, the engineering of acoustic nanoresonators exploiting novel confinement strategies that allows the fabrication of resonators with enhanced robustness. Second, the development of engineering strategies to mimic electronic solid-state phenomena using acoustic phonons.

Nowadays, there exists a demand for novel techniques that facilitate the experimental study of nanophononic devices. The second line of research of this thesis focuses on the experimental study of acoustic resonators by means of ultrafast laser action [73–75]. The resonators are multilayer structures fabricated by MBE technology in the state of the art clean room facilities of the Centre for Nanoscience and Nanotechnology (C2N). Ultrafast lasers are a key tool for the study of physical phenomena occurring at the picosecond timescale. During the mid-1980s, pioneering experiments demonstrated coherent phonons generation in semiconductors and metals by means of ultrafast laser action [74, 75]. This provided a different approach to detect phonons, instead of detecting scattered light by resolving it spectrally, using ultrashort pulses we could resolve in time the phonon induced changes in the reflectivity (or transitivity, depending on the experimental configuration used) of a sample under study. The use of ultrafast laser pulses enable the generation and detection of acoustic phonons [73]. This technique led to the development of picosecond ultrasonics, a research field where phonon dynamics is studied through coherent phonon generation and detection experiments using picosecond pulsed lasers [76]. Also known as time-domain Brillouin scattering [77], this experimental technique is based on an all-optical pump-probe spectroscopy technique where a first pulse, called the pump, generated phonons while a second pulse, called the probe, sense them through a phonon-induced altered reflection (or transmission). In this work, we develop novel experimental techniques based on pump-probe spectroscopy that allow us to study the dynamics of coherent phonons in the range of tens to hundreds of gigahertz. Three goals were set for this purpose. First, the development of a versatile optical setup for coherent phonons generation and detection experiments. We aim at the optimization of conditions for the detection of coherent phonons with high signal to noise ratio. Second, the use of the developed experimental tools for the characterization and study of phonon dynamics in planar structures operating as acoustic resonators. Third, the study of coherent phonon confinement in micropillars operating simultaneously as phononic resonators and optical cavities.

The present manuscript provides a description of the work done for this thesis and it compiles the obtained results. First, the theoretical concepts and tools needed along the full manuscript are introduced. Then, we focus on the simulation of resonators and we explore novel confinement strategies. Finally, we address the development of novel experimental techniques for the study of phononic structures with resonances in the range of tens to hundreds of gigahertz. The manuscript is organized in six chapters that are structured as follows:

- **Chapter 2** serves as an introductory chapter where we provide the fundamental concepts to be used in this thesis. First, we briefly cover the theoretical framework of solid-state physics involving phonons in semiconductors. Second, we present the theoretical description of acoustic and electric fields which is the basis for the simulation tools to be introduced. These concepts are used to implement a transfer matrix method algorithm described in this chapter which, together with a photoelastic model, allows us to predict the outcome of the experimental demonstrations presented in this work. Third, we introduce the experimental techniques used to probe the dynamics of coherent acoustic phonons in nanostructures i.e. coherent phonon generation and detection using a pump-probe technique. Finally, we present a brief introduction on multilayer structures and some of the standard devices that can be fabricated, such as distributed Bragg reflectors, optical cavities and acoustic resonators.

- In **Chapter 3**, we present the work done on the engineering of nanophononic band structures in multilayer devices. We introduce the concept of an acoustic local band structure and how it can be used as a toolbox to control the phonon density of states. In addition, we present results on how exploiting the tools introduced in this chapter, we can engineer structures replicating the effect of mechanical potentials, acting on phonons regardless of their lack of mass and charge.

- **Chapter 4** addresses the experimental study of acoustic confinement in nanostructures and the development of novel experimental techniques for the implementation of time-domain Brillouin scattering experiments. In this chapter we focused on planar multilayer samples operating as one-dimensional resonators i.e. confinement only occurs along the growth axis of the sample. We investigated hybrid devices where both light and sound are confined, significantly enhancing the measured signals extracted in experiments. We present the results obtained experimentally where we probe acoustic phonons in different types of resonators confining mechanical vibrations by band inversion, by the breaking of the periodicity in a superlattice and by traditional confinement strategies such as those of Fabry-Perot cavities.

- **Chapter 5** presents the experimental study of confinement in three dimensional structures. Micropillar structures are used as the subject of study for which novel experimental techniques were developed. We investigated hybrid opto-phononic micropillars and we present results unveiling the optical cavity dynamics undergoing after ultrafast laser action. Motivated by the results using single-mode fibers in free space optical setups, we integrated the hybrid micropillars to a fibered system and performed a fibered version of time-domain Brillouin scattering experiments. The novel technique demonstrated unprecedented stability and reproducibility as we assessed during the course of more than forty hours. Equipped with the new experimental tools we perform a systematic study varying the spectral and power conditions used during the experiments in order to extend our investigation of the optical cavity dynamics in our experiments and to assess their effect in the measured phononic spectra.

- Finally, in **Chapter 6** we summarize the results obtained and present the conclusions of this thesis together with the perspectives resulting from this work.

Chapter 2

Fundamentals of phonon engineering

Phonon engineering involves the design of nanometric structures that control the propagation of phonons. It also requires a careful consideration of how these phonons are going to be experimentally accessible in a given structure. In this chapter, we provide the fundamental concepts needed for the engineering of nanophononic structures in one dimension. Firstly, we briefly introduce the physics behind the emergence of phonon band structures in solid-state materials. Secondly, we describe the simulation techniques used for this manuscript including the implementation of a transfer matrix method (TMM) for the modeling of both acoustic and optical fields in one dimension. Then, the photoelastic model is introduced which, together with the TMM, has been used in this work to simulate the expected signals in experimental realizations. Thirdly, we present the pump-probe technique for coherent phonon generation and detection together with the physical description of how phonons are generated by ultrafast laser pulses [73]. Finally we address multilayer structures. We present the concept of superlattices which constitute a powerful platform for the engineering of phonon propagation. Extending the scope on multilayer structures we introduce common phonon devices such as distributed Bragg reflectors (DBR), Fabry-Perot cavities and resonators.

2.1 Phonon band structure

In this section we introduce the phononic band structure following the theory on semiconductor physics as described in Cardona et al. [78]. To give a complete description of a solid-state material like *GaAs*, we need to consider the general expression for the Hamiltonian describing a perfect crystal structure:

$$\mathscr{H} = \sum_i \frac{p_i^2}{2m_i} + \sum_j \frac{P_j^2}{2M_j} + \frac{1}{2}\sum_{j,j'}^{j\neq j'} \frac{Z_j Z_{j'} e^2}{4\pi\varepsilon_0|\vec{R}_j - \vec{R}_{j'}|} + \frac{1}{2}\sum_{i,i'}^{i\neq i'} \frac{e^2}{4\pi\varepsilon_0|\vec{r}_i - \vec{r}_{i'}|} - \sum_{i,j} \frac{Z_j e^2}{4\pi\varepsilon_0|\vec{r}_i - \vec{R}_j|}, \tag{2.1}$$

where m_i, $\vec{r}_i$ and p_i correspond to the i-th electron mass, position and momentum, respectively. M_i, $\vec{R}_i$, P_i and Z_j are the j-th nucleus mass, position, momentum and atomic number, respectively. Finally, the constant ε_0 is the vacuum permittivity and e is the electron charge.

Each of the addends of the right hand side of equation 2.1 corresponds to a different aspect of the electron-nucleus dynamics. The first two are the kinetic energy associated to each electron and nucleus in that order. The third one accounts for the Coulomb interaction between nuclei. The fourth one is the same but for interactions between electrons only. The fifth and last addend corresponds to the interaction between nuclei and electrons. Taking into consideration the different contributions to the Hamiltonian, we can separate them in three groups. One only for the electronic energy

$$\mathscr{H}_e = \sum_i \frac{p_i^2}{2m_i} + \frac{1}{2}\sum_{i,i'}^{i\neq i'} \frac{e^2}{4\pi\varepsilon_0|\vec{r}_i - \vec{r}_{i'}|} \tag{2.2}$$

one associated to the nuclei

$$\mathscr{H}_Z = \sum_j \frac{P_j^2}{2M_j} + \frac{1}{2}\sum_{j,j'}^{j\neq j'} \frac{Z_j Z_{j'} e^2}{4\pi\varepsilon_0 |\vec{R}_j - \vec{R}_{j'}|} \tag{2.3}$$

and a last one related to the Coulomb interaction between the electrons and nuclei

$$\mathscr{H}_{e-Z} = -\sum_{i,j} \frac{Z_j e^2}{4\pi\varepsilon_0 |\vec{r}_i - \vec{R}_j|} \tag{2.4}$$

Then, equation 2.1 can be rewritten as

$$\mathscr{H} = \mathscr{H}_e + \mathscr{H}_Z + \mathscr{H}_{e-Z} \tag{2.5}$$

Solving this Hamiltonian is not feasible because the number of electrons and nuclei involved in the problem is extremely large (Avogadro's number is on the order of 10^{23}). Consequently, several simplifications need to be done in order to find a useful solution. The first one is not to assume nuclei but ion cores instead. The reason is that electrons in the lowest energy orbitals tend to be much closer to the nucleus than those in outer ones. Then, we can group these low energy electrons with the nucleus and consider them as ion cores, significantly reducing the number of electrons to describe. The second approximation involves the different time scales at which these ions and the rest of electrons evolve. Basically, ion cores are large and slow and electrons are small and fast. The time scale on which ion dynamics evolves is much slower than the one corresponding to the electronic dynamics. As a result we can assume that ions effectively experience time-averaged electronic dynamics. Electrons, in contrast, respond rapidly to ionic motion. This is known as the Born-Oppenheimer approximation. Taking all this into consideration we can rewrite the Hamiltonian as

$$\mathscr{H} = \mathscr{H}_e(\vec{r}_i, \vec{R}_{j0}) + \mathscr{H}_{ion}(\vec{R}_j) + \mathscr{H}_{e-ion}(\vec{r}_i, \delta\vec{R}_j) \tag{2.6}$$

where $\vec{R}_{j0}$ correspond to the ion cores' equilibrium position as experienced by the fast electronic system and $\delta\vec{R}_j$ to the perturbation of the ions from their equilibrium position. Three contributions add up to the full Hamiltonian. The first one accounts for the electronic system considering only the electrons in orbitals that are not completely filled

$$\mathscr{H}_e(\vec{r}_i, \vec{R}_{j0}) = \sum_i \frac{p_i^2}{2m_i} + \frac{1}{2}\sum_{i,i'}^{i\neq i'} \frac{e^2}{4\pi\varepsilon_0 |\vec{r}_i - \vec{r}_{i'}|} - \sum_{i,j} \frac{Z_j e^2}{4\pi\varepsilon_0 |\vec{r}_i - \vec{R}_{j0}|} \tag{2.7}$$

A second one considering the ions, i.e. the nucleus and the core electrons in the low energy orbitals

$$\mathscr{H}_{ion}(\vec{R}_j) = \sum_j \frac{P_j^2}{2M_j} + \frac{1}{2}\sum_{j,j'}^{j\neq j'} \frac{Z_j Z_{j'} e^2}{4\pi\varepsilon_0 |\vec{R}_j - \vec{R}_{j'}|} - \sum_{i,j} \frac{Z_j e^2}{4\pi\varepsilon_0 |\vec{r}_i - \vec{R}_j|} \tag{2.8}$$

Note that we are using the same index i to iterate through the electrons in $\mathscr{H}_{ion}$ and $\mathscr{H}_e$. These cover two different groups of electrons, those which are bound to the core and those which are not. The third and final element takes into account the effect of the perturbations to the crystal structure altering the electronic system. This is expressed by using a Taylor expansion around the equilibrium point as given by

$$\mathscr{H}_{e-ion}(\vec{r}_i, \delta\vec{R}_j) = \sum_j \left(\frac{\partial \mathscr{H}_e}{\partial \vec{R}_j}\right)\Bigg|_{\vec{R}_{j0}} \cdot \delta\vec{R}_j + \dots \tag{2.9}$$

The electronic band structure results from $\mathscr{H}_e$, the first of the three elements adding up to form the full system Hamiltonian presented in equation 2.6. The other two terms $\mathscr{H}_{ion}$ and

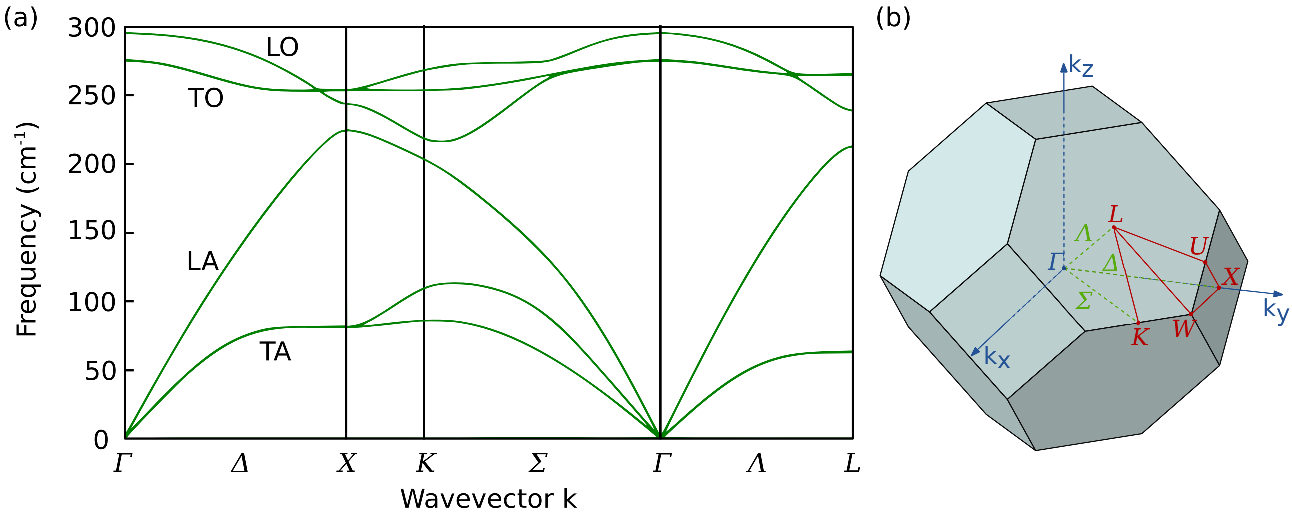

Figure 2.1: (a) Phonon band structure of *GaAs*. Adapted from reference [83]. (b) Plot of the first Brillouin zone of a face-centered cubic lattice.

$\mathscr{H}_{e-ion}$ involve the ion cores in our crystal model and how these core movements perturb the electronic Hamiltonian $\mathscr{H}_e$, respectively. The former, $\mathscr{H}_{ion}$, describes the vibrational dynamics of the crystal structure, and in a similar fashion as its electronic counterpart results in band structures describing the supported phononic modes of the system.

As a result of the fast dynamics of the electrons, the ion dynamics, taking place at a slower time scale, experience an averaged contribution from the electrons. Consequently, we can invoke again the Born-Oppenheimer approximation and remove the dependence on each electron position in equation 2.8. Then, we can rewrite the ion Hamiltonian as

$$\mathscr{H}_{ion}(\vec{R}_j) = \sum_j \frac{P_j^2}{2M_j} + E_e(\vec{R}_1, \vec{R}_2, \dots) \tag{2.10}$$

with $E_e(\vec{R}_1, \vec{R}_2, \dots)$ the energy of the valence electrons affecting the ions at positions $\vec{R}_1, \vec{R}_2, \dots$. Nowadays these energy values can be obtained by computational means and then solve the eigenvalues problem [79]. It can also be directly measured through scattering techniques. Inelastic neutron and x-ray scattering allow to experimentally access the supported vibrational modes of the structure by measuring the energy lost after neutrons or x-ray photons are inelastically scattered by phonons [80–82].

Figure 2.1 (a) presents the phonon band structure of *GaAs* calculated through a density functional perturbation theory technique [83–85]. As in the case of the electronic band structure this band diagram acts as a sort of map displaying the different vibrational modes supported at different directions in the k-space of the Brillouin zone. *GaAs* has a zinc blend structure where the two types of atoms form two face-center cubic lattices interpenetrating each other. The first Brillouin zone for a face-centered cubic lattice is displayed in panel (b). Different points are labeled in both the surface and the interior of the depicted volume. These are used to graphically represent in two dimensions the phononic dispersion presented in panel (a). In the region enclosed between the Γ point and the X point, four dispersion curves are labeled as TA, LA, TO and LO. These correspond to a categorization used to distinguish different kind of vibrations supported by the substructure. The prefix T or L stands for transversal and longitudinal, respectively and it is used to describe how the ion cores vibrate relative to the wavevector direction. Longitudinal phonons correspond to vibrations for which both displacement of the ion cores and wavevector are parallel. Transversal phonons correspond to those where the displacement of the ion cores lies in a perpendicular plane to the wavevector. The suffix A and O stands for acoustic and optical, respectively. This category distinguishes between different vibrational modes associated to the unit cell forming the crystal lattice. In the case of two atoms per cell, we can distinguish between different modes by the sense of the

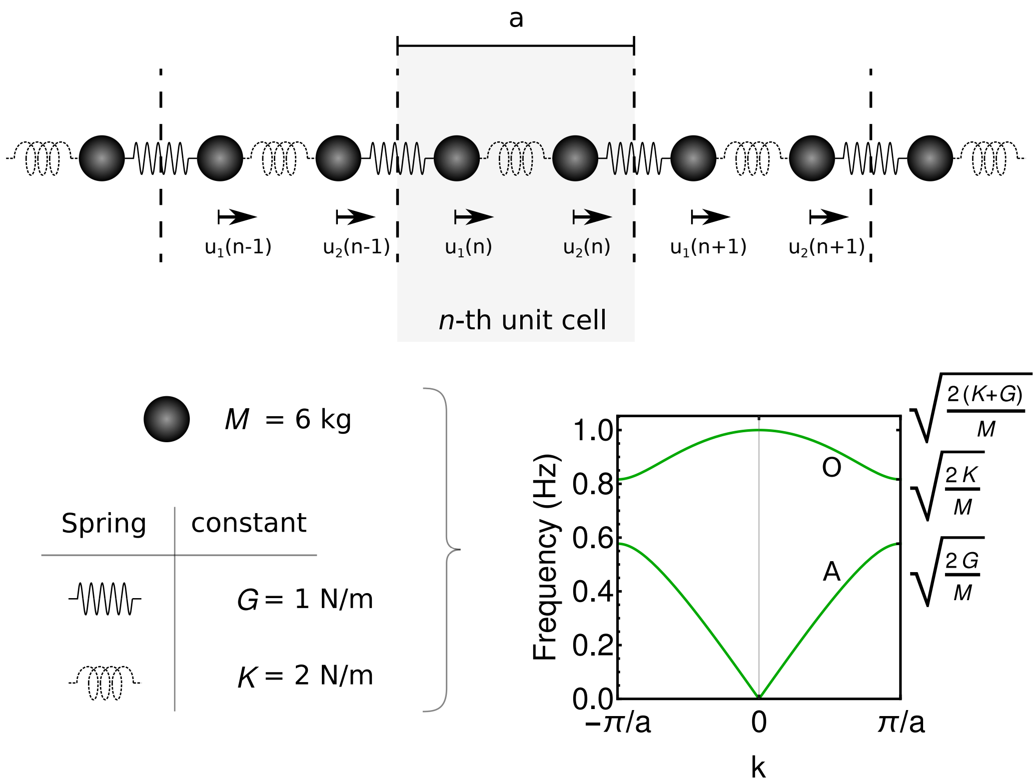

Figure 2.2: Top: One dimensional chain of identical atoms connected by springs with alternating constant K and G. Within each unit cell the atoms are labeled 1 and 2 from left to right. Bottom: For the set of parameters $K = 2\ N/m$, $G = 1\ N/m$ and $M = 6\ kg$, the dispersion relation is plotted. Labeled by O and A the optical and acoustic branches are distinguished.

relative displacement between ion cores within each unit cell (in phase or in counter phase).

Additional information about the materials properties is present in the phononic band structure. In particular, the sound group velocity for different kinds of phonons is illustrated as it is the derivative of the dispersion relation. Table 2.1 contains material properties for $GaAs$ and $AlAs$ used for all computations in this manuscript. For both materials, the sound velocity corresponds to the derivative of the dispersion relation for LA phonons close to the Γ point.

Material	Density (g/cm^3)	Sound velocity (m/s)	Refractive index
GaAs	5.35	4780	3.54
AlAs	3.77	5660	2.96

Table 2.1: *GaAs* and *AlAs* mechanical and optical properties [68, 86, 87].

The nature of acoustic and optical phonons can be exemplified in a much simpler system: a one dimensional chain of identical atoms connected by springs of alternating strength [88]. Figure 2.2 presents this system formed by atoms of mass M connected by springs with spring constants K and G, alternating between them. The chain repeats itself periodically with equal unit cells of length a distance. We can classically describe this periodic system such that for the n-th pair of atoms, Newton's second law is given by

$$\begin{aligned} M\ddot{u}_1(n) &= -K[u_1(n) - u_2(n)] - G[u_1(n) - u_2(n-1)] \\ M\ddot{u}_2(n) &= -K[u_2(n) - u_1(n)] - G[u_2(n) - u_1(n+1)] \end{aligned} \tag{2.11}$$

We can expect the solutions of this system to be expressed in a basis of oscillations. Therefore, to solve this problem we take as an ansatz a function corresponding to a traveling wave with angular frequency ω and wavevector k such as

$$\begin{aligned} u_1(n) &= \varepsilon_1 \exp[i(kna - \omega t)] \\ u_2(n) &= \varepsilon_2 \exp[i(kna - \omega t)] \end{aligned} \tag{2.12}$$

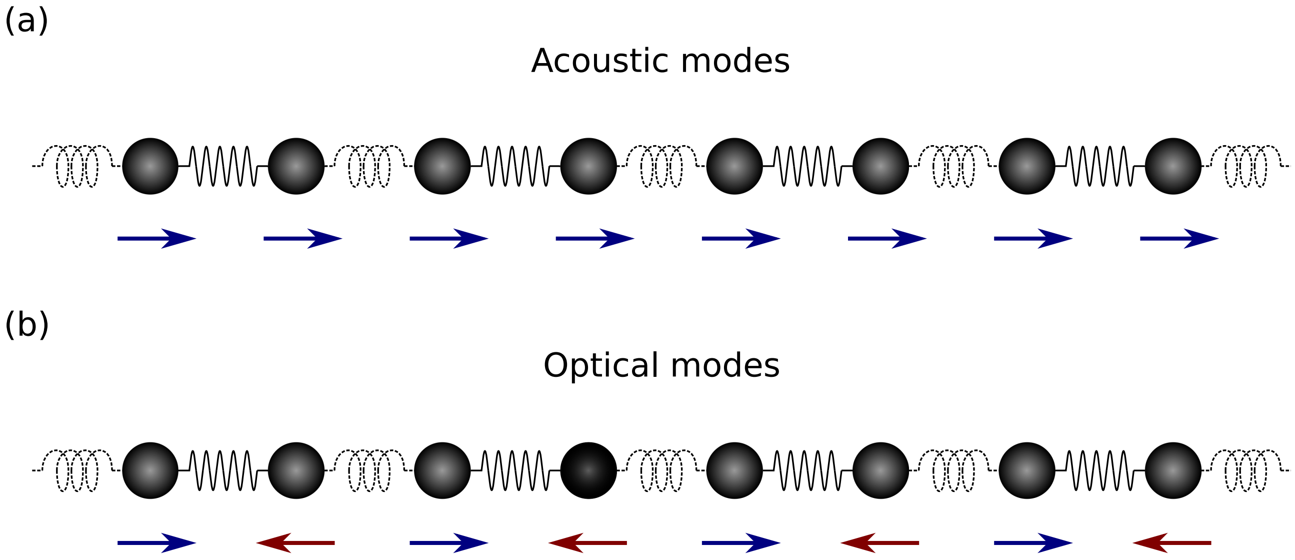

Figure 2.3: Acoustic (a) and optical (b) vibrational modes of the atomic linear chain presented in figure 2.2. The arrows pointing in opposed direction represent the sign of the amplitudes ε_1 and ε_2. For acoustic modes (a) both atoms within the same unit cell move in phase. In contrast, for the optical modes, atoms within the same cell oscillate with π phase shift between each other.

where ε_1 and ε_2 are complex constants to be determined that set both the amplitude and phase of the propagating wave solutions. Inserting equation 2.12 in equation 2.11 we obtain a system of equations whose determinant needs to equal zero to have a solution. From this condition we find that the angular frequency need to satisfy

$$\omega^2 = \frac{K+G}{M} \pm \frac{1}{M}\sqrt{K^2 + G^2 + 2KG\cos(ka)} \tag{2.13}$$

with

$$\frac{\varepsilon_2}{\varepsilon_1} = \mp \frac{K + G\exp(ika)}{|K + G\exp(ika)|} \tag{2.14}$$

Equation 2.13 states two type of solutions (notice the ± symbol) that determine the dispersion curves. In order to exemplify the two solution branches let us consider the particular case where the parameters defining the linear chain of atoms are $K = 2\ N/m$, $G = 1\ N/m$ and $M = 6\ kg$ [1]. Figure 2.2 presents at the bottom the corresponding dispersion plotted in the first Brillouin zone. The bottom branch of solutions presents approximately a linear dispersion relation near the center of the reduced zone ($k = 0$). The derivative of the dispersion relation gives us the group velocity of the propagating waves. A linear dispersion relation is a characteristic of macroscopic sound waves which is why this branch is labeled as acoustic (A in figure 2.2) [88]. The top branch in contrast, has a smaller slope therefore the group velocity of their wave solutions are lower. While out of the scope of this example, in bulk materials atomic lattices this branch couple more easily with light than the acoustic branch and therefore is labeled as optical.

In order to illustrate the differences between the two branches let us consider, in addition to the example parameters given above, the case of long wavelengths, i.e. $k \ll \pi/a$. In this particular case, equation 2.14 reduces to $\varepsilon_2 = \mp\varepsilon_1$. Figure 2.3 presents and schematic illustrating the displacement direction of each atom as given by the sign of the amplitudes ε_1 and ε_2. For the acoustic modes (panel a), we can see how all atoms has oscillate with amplitudes

---

[1] These set of parameters are chosen not to represent the atomic lattice but a classical macroscopic system formed of large masses and weak springs. This is intended to emphasize that the different nature of optical and acoustic vibrations is common to both the classical and the quantum description of periodic systems.

all with the same sign. For the optical modes these directions are inverted between consecutive atoms i.e. there is a π phase shift in the oscillatory solutions between consecutive atoms.

We have briefly introduced the theoretical framework describing the physics of phonons in solid-state materials. We have presented the Hamiltonian describing a perfect crystal and showed how different terms account for different contributions of the system: ion cores, electrons and interactions between them. Finally we have presented the phonon band structure resulting from the ion cores dynamics in the periodic crystal structure. In particular, we have showed examples of these for *GaAs* which, together with *AlAs*, have been the materials used for the simulations and experimental realizations in this manuscript. In this thesis, we have focused on the study of acoustic phonon in *GaAs*/*AlAs* heterostructures. In contrast with optical phonons, acoustic phonons feature a linear dispersion relation over a large range of frequency and they can propagate in solid-state materials over hundreds of micrometers [89]. This characteristics allow us to strongly modify their propagation by engineering multilayer devices. In the following section we present the simulation techniques used to model complex systems like *GaAs*/*AlAs* multilayer structures controlling the propagation of acoustic phonons along them.

2.2 Simulation techniques

The engineering of phononic nanostructures has been done using numerical simulations of structures formed by stacks of layers of different materials. For this purpose, an algorithm was implemented in order to model longitudinal acoustic phonons and electromagnetic plane waves, propagating at normal incidence towards the structure layers. Given the wave nature of both phonons and photons in such a specific context we can model their propagation dynamics using the same algorithm. It models both the displacement and electromagnetic fields propagating through solid-state materials and it is based on a standard approach to treat this kind of problems known as the transfer matrix method [90].

2.2.1 Transfer matrix method

The transfer matrix method (TMM) is a mathematical technique used to model the propagation of acoustic and optical waves through stacks of layers of different materials [67, 91–93]. Here, we describe the implementation of a TMM algorithm to model the propagation at normal incidence of light and of longitudinal acoustic phonons through layers of *GaAs* and *AlAs*. In general, the materials modeled are assumed to be homogeneous, isotropic and to have a linear response under perturbation.

We introduce the TMM by addressing the optical case, modeling an electromagnetic field propagating through a layered structure. Later, we use the same algorithm to model acoustic waves by replacing refractive indices by acoustic impedances.

Let us consider the case of a structure formed by two layers of different materials with thicknesses d_1 and d_2 as depicted in figure 2.4. Defining z as the propagating axis normal to all interfaces, we can describe a plane wave incident from the left side of the structure and propagating through the two layers. Each interface produces a reflection and therefore the field in each layer can be thought of as being composed from multiple fields propagating forward and backwards as depicted by the red arrows in figure 2.4. As an exception, in the semi-infinite half space on the right we can safely assume there is no field propagating backwards for an incident wave coming from the left of the structure, since there is no further interface to the right able to reflect the light back.

Let us define the input electric field $\vec{E'}$ as a plane wave of the form

$$\vec{E'} = \vec{E'}_0(z) \exp[i(\omega t - k_0 z)] \tag{2.15}$$

where ω is the angular frequency and k_0 is the wavevector in the ambient medium. We are considering a linearly polarized field $\vec{E'}_0(z)$ perpendicular to the propagation direction z.

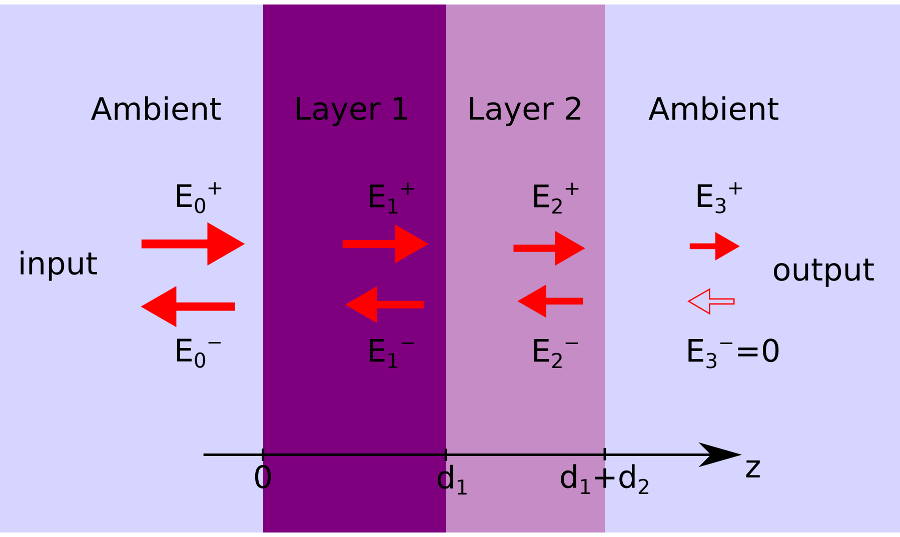

Figure 2.4: Schematic representation of a two layers structure to be modeled using the TMM. Light, propagating from left to right as showed in the figure, inputs the layered system and outputs of the right of the structure. Within each region, a subsystem is considered. Each one of these subsystems is characterized by two electric fields propagating in the two opposed directions which are represented by the red arrows. These arrows correspond to the wave vectors towards positive (+) and negative values (−) of z. The field results from the addition of these two contributions. Since the light only has an input from the left side, there is no field propagating in the system from the right side of the structure (i.e. $E_3^- = 0$).

Since we are assuming linearly polarized light the resulting field after the input wave propagates through the full structure can be expressed in terms of magnitudes. In order to describe the field amplitude along the full structure we can separate it in its two contributions coming from plane waves propagating forward and backward simultaneously. Then, the electric field in each layer is given by

$$E = \begin{cases} E_0^+ \exp(ik_0 z) + E_0^- \exp(-ik_0 z) & z < 0 \\ E_1^+ \exp(ik_1 z) + E_1^- \exp(-ik_1 z) & 0 < z < d_1 \\ E_2^+ \exp(ik_2 z) + E_2^- \exp(-ik_2 z) & d_1 < z < d_1 + d_2 \\ E_3^+ \exp(ik_3 z) + E_3^- \exp(-ik_3 z) & d_1 + d_2 < z \end{cases} \tag{2.16}$$

with the superscript + (−) denoting the complex field amplitude of a wave propagating forward (backward) as represented by the red arrows in figure 2.4 and the subscripts denoting the four different regions. The boundaries conditions between each of these regions impose specific relations between the complex amplitudes adding up to form the total field in each region of the structure. At each interface between materials both electric and magnetic fields parallel to the interfaces must be continuous as dictated by Maxwell's equations. Consider the interface between the ambient at the input (region 0) and the first layer (region 1). The boundary condition can be expressed as the following equations

$$E_0^+ + E_0^- = E_1^+ + E_1^- \tag{2.17}$$
$$H_0^+ + H_0^- = H_1^+ + H_1^- \tag{2.18}$$

valid at the interface between materials, i.e. at $z = 0$ according to figure 2.4. The H stands for the magnetic field amplitude using the same sub- and super-script notation. From Faraday's law, equation 2.18 can be rewritten as

$$n_0 E_0^+ - n_0 E_0^- = n_1 E_1^+ - n_1 E_1^- \tag{2.19}$$

Formulating equations 2.17 and 2.19 as a system of equation using matrices we obtained

$$\begin{pmatrix} 1 & 1 \\ n_0 & -n_0 \end{pmatrix} \begin{pmatrix} E_0^+ \\ E_0^- \end{pmatrix} = \begin{pmatrix} 1 & 1 \\ n_1 & -n_1 \end{pmatrix} \begin{pmatrix} E_1^+ \\ E_1^- \end{pmatrix} \tag{2.20}$$

where we have defined a vectors using the amplitude of the fields propagating in opposite directions. These vectors represent the electric field but do not belong to the three dimensional space where the field exists. The actual field results from the sum of each pair of complex amplitudes forming the vector and points along the direction of the chosen polarization. Here, we have dropped polarization already since we restrict the discussion to the case of normal incidence on isotropic, homogeneous materials. Nevertheless, in this form, we can reformulate equation 2.20 as

$$\begin{pmatrix} E_1^+ \\ E_1^- \end{pmatrix} = M_{0,1}^{int} \begin{pmatrix} E_0^+ \\ E_0^- \end{pmatrix} \tag{2.21}$$

where

$$M_{0,1}^{int} = \frac{1}{2} \begin{pmatrix} 1 + \frac{n_0}{n_1} & 1 - \frac{n_0}{n_1} \\ 1 - \frac{n_0}{n_1} & 1 + \frac{n_0}{n_1} \end{pmatrix} \tag{2.22}$$

is a matrix that transforms the new defined vector modeling an electromagnetic wave passing through an interface between different materials. In a similar fashion, the propagation through a layer of a given medium can be expressed also in a matrix form. For example, the field in layer 1 at a position $z = d_1$ can be expressed in terms of a matrix applied to the field at the origin

$$\begin{pmatrix} E_1^+ \\ E_1^- \end{pmatrix}_{z=d_1} = M_{k_1,d_1}^{prop} \begin{pmatrix} E_1^+ \\ E_1^- \end{pmatrix}_{z=0} \tag{2.23}$$

where

$$M_{k_1,d_1}^{prop} = \begin{pmatrix} \exp(ik_1 d_1) & 0 \\ 0 & \exp(-ik_1 d_1) \end{pmatrix} \tag{2.24}$$

transforms the vector by modeling the propagation of the optical waves in the layered medium.

Equations 2.21 and 2.23 allow us to obtain the electric field at any point of the structure once it is known at one of its positions. Departing from a known vector, one only needs to apply the required matrices modeling the propagation along layers and those corresponding to waves passing through interfaces in order to obtain the vector at a given position, thus the field. In the example case depicted in figure 2.4, we can consider as the known vector the one at the output of the structure, i.e. at region 3. Note that we do not choose the incident vector in region 0, which includes the input field E_0^+ since we do not know (yet) the second element of the vector, the field coming back from the structure i.e. E_0^-. This kind of "backwards" approach to model fields along multiple layers is typical for the TMM where we can assume an output field $E_3^+ = 1$ and later renormalize all fields accordingly to the real known field i.e. the input field E_0^+. Since the system we are modeling consist of light incident from the left, there can only be light propagating forward in the rightmost region. Then, we can set $E_3^- = 0$ and compute the field along the structure in terms of E_3^+ the forward propagating field at the output. The electric field at region 0 is given by

$$\begin{pmatrix} E_0^+ \\ E_0^- \end{pmatrix} = M_{1,0}^{int} \cdot M_{k_1,-d_1}^{prop} \cdot M_{2,1}^{int} \cdot M_{k_2,-d_2}^{prop} \cdot M_{3,2}^{int} \begin{pmatrix} E_3^+ \\ 0 \end{pmatrix}_{z=0} \tag{2.25}$$

Notice that we are departing from the right and propagating the field to the left. This results in the inversion of the subscripts at the interface matrices and the negative sign in the distance of the propagating matrices. Using these results we can directly obtain the complex reflectivity $r = E_0^-/E_0^+$ and transmission $t = E_3^+/E_0^+$ of the modeled structure. The matrix resulting from multiplying all matrices contributing to the wave propagation is know as the transfer matrix.

For all simulations used for this work an algorithm based on the TMM was used. In order to extend the usage of the propagation and interface matrices for the acoustic field we need to create a similar vector. In this case, instead of modeling electric field waves we model an acoustic wave, i.e. a displacement u as a function of position. We can describe the acoustic systems by the wave equation

$$\frac{\partial}{\partial t}\left(\rho(z)\frac{\partial u(z,t)}{\partial t}\right) = \frac{\partial}{\partial z}\left(C(z)\frac{\partial u(z,t)}{\partial z}\right) \tag{2.26}$$

where we are considering materials with a lattice structure with C being the stiffness constant along the (001) direction. This continuous model have been demonstrated suitable to describe longitudinal acoustic phonons propagating along the (001) direction of cubic crystals [94, 95]. For a medium formed by concatenated layers of different materials and within the domains where the material composition is constant, we can rewrite equation 2.26 as

$$\rho_j \frac{\partial^2 u_j(z,t)}{\partial t^2} = C_j \frac{\partial^2 u_j(z,t)}{\partial z^2} \tag{2.27}$$

where j is an index assigned to each layer in the same order as they are concatenated. In addition, we need to consider both displacement and stress normal to the layers interfaces resulting in the boundaries conditions given by

$$\begin{aligned} u_j(z_{int},t) &= u_{j+1}(z_{int},t) && (2.28)\\ C_j\frac{\partial u_j(z_{int},t)}{\partial z} &= C_{j+1}\frac{\partial u_{j+1}(z_{int},t)}{\partial z} && (2.29)\end{aligned}$$

The propagation of both acoustic and optical waves can be modeled by the same propagation matrix after an appropriate redefinition of the wavevector (i.e. in terms of acoustic magnitudes like the speed of sound). The matrix describing an acoustic wave traversing an interface between materials can be obtained in a similar way as for the electromagnetic case, using similar boundary conditions. Given the nature of the acoustic waves we are describing there are two conditions that must be fulfilled. The first one, given by equation 2.28, ensures the displacement continuity at the interface between different layers. This can be expressed for the first interface in terms of displacements as

$$u_0^+ + u_0^- = u_1^+ + u_1^- \tag{2.30}$$

where, as for the electromagnetic case, we have separate the contributions of the acoustic field u by separating those waves propagating forward (super script $+$) and those propagating backward (super script $-$). The second condition, implicit in equation 2.29, is the conservation of momentum. It can be formulated as

$$(u_0^+ - u_0^-)\rho_0 v_0 = (u_1^+ - u_1^-)\rho_1 v_1 \tag{2.31}$$

with ρ_0 and v_0 (ρ_1 and v_1) being the mass density and speed of sound in region 0 (1), respectively. Then, we can reformulate equations 2.30 and 2.31 in a matrix form as

$$\begin{pmatrix} 1 & 1 \\ Z_0 & -Z_0 \end{pmatrix}\begin{pmatrix} u_0^+ \\ u_0^- \end{pmatrix} = \begin{pmatrix} 1 & 1 \\ Z_1 & -Z_1 \end{pmatrix}\begin{pmatrix} u_1^+ \\ u_1^- \end{pmatrix} \tag{2.32}$$

where $Z_0 = \rho_0 v_0$ ($Z_1 = \rho_1 v_1$) is the acoustic impedance in region 0 (1). As we can see from the comparison with equation 2.20, there is a direct analogy in the model used for acoustic and optical waves. The acoustic impedance plays the role of the index of refraction. This result allows us to use the same algorithm developed for the optical domain in order to describe acoustic waves propagating in the studied layered structures.

2.2.2 Photoelastic model

In the context of small deformations of a continuum volume, the deformation of a three dimensional object can be expressed in terms of a second rank tensor known as the strain tensor [68, 78]

$$\eta_{ij} = \frac{1}{2}\left(\frac{\partial u_i}{\partial x_j} + \frac{\partial u_j}{\partial x_i}\right) \tag{2.33}$$

where the vector u_i corresponds to the displacement due to a deformation in the direction x_i, i.e. using a reference frame given by (x_1, x_2, x_3). The alteration of the optical properties in the deformed material can be expressed in terms of the strain tensor. This mechanically induced alteration can be formulated as a variation in the inverse of the dielectric tensor as a result from the strain present in the structure such as

$$\Delta(\varepsilon^{-1})_{ij} = \sum_{kl} p_{ijkl}\eta_{kl} \tag{2.34}$$

where p_{ijkl} is the photoelastic tensor. It is a fourth rank tensor since it relates the strain with the inverse dielectric tensor, both second rank tensors. This tensor depends on the material properties and scales the deformation into a change in the dielectric tensor. This can be reformulated in terms of the index of refraction of the medium. For cubic crystal structures like *AlAs* and *GaAs*, and assuming no birefringence present, we can rewrite equation 2.34 as

$$\Delta\varepsilon_{ij} = -n^4 \sum_{kl} p_{ijkl}\eta_{kl} \tag{2.35}$$

where the scalar n represents the index of refraction in the medium.

Equation 2.35 states the effect of strain onto the optical properties of a medium. As we have stated before, the experimental realization to detect the phonons relies on the inelastic scattering of photons by phonons. While in a quantum formalism this can occur with a given probability for each photon propagating in the structure, it can be described from a classical scope using both the displacement and the electric fields. In this context it is possible to express the Raman scattering cross section σ_{Raman} as a function of acoustic wave angular frequency ω as [68, 91, 94, 96]

$$\sigma_{Raman}(\omega) \propto \int E_i(z)p(z)\frac{\partial u(z)}{\partial z}E_s^*(z)dz \tag{2.36}$$

where E_i and E_s are the input and the scattered electric field, respectively. $p(z) = -n^4 p_{1133}(z)$ is called the photoelastic constant and depends on the material response to strain. It is defined assuming longitudinal acoustic phonons so the deformation of the structure takes place only in one direction, which coincides with the propagation direction z.

Equation 2.36 explicitly states how the probability to scatter photons due to phonons is proportional to a measure of the spatial overlap between the electric field and the displacement gradient $\frac{\partial u(z)}{\partial z}$, and weighted by the photo elastic constant $p(z)$. A particular case take places when the scattering process occurs in an optical cavity. Under double optical resonance conditions, both input and scattered fields E_i and E_s are resonant in the cavity and can be expressed as the same standing wave given by $E_i = E_s = \exp(ik_z z) + \exp(-ik_z z)$ (with $k_z = \pi/L$ where L is the length of the confinement regions) [39]. Then, the product between the fields in eq. 2.36 become $E_i E_s^* = 2 + (\exp(i2k_z z) + \exp(-i2k_z z))$. Consequently, with an optical cavity in double resonance conditions we can detect both forward scattering (term 2) and backscattering $((\exp(i2k_z z) + \exp(-i2k_z z)))$ contribution from Raman scattering experiments [60].

2.3 Experimental techniques

Longitudinal acoustic phonons in *GaAs* and *AlAs*, however, vibrate at the range of gigahertz up to terahertz. In this range, typical oscillation periods are on the order of few to tens of picoseconds. Phonons beyond several tens of gigahertz fall well beyond the cut-off frequency of any electromechanical or piezo-based microphone currently available.

In order to detect longitudinal acoustic phonons in the few to hundreds of gigahertz range, optical systems have demonstrated suitable [69, 71, 89, 97]. Light can be inelastically scattered by phonons losing or gaining energy in the process [98, 99]. This interaction is mediated by electrons. Propagating along a solid, the electric field of the light perturbs the electronic system. Consequently, the energy associated of the valence electrons is modified which leads to perturbations in the ion core positions resulting in vibrations, i.e. phonons. One approach to detect phonons is by monitoring the energy of scattered photons [96]. While some photons do not lose energy and are elastically scattered (Rayleigh scattering), those which do change their energy due to phonons can be distinguished by spectroscopic means, using diffraction gratings to translate different photon wavelengths to different positions, allowing us to distinguish between the elastic and inelastic contributions [21, 68, 100]. When the phonons oscillate with a common phase, i.e. coherent phonons, a different approach is resolving them in time [74, 75, 101–103]. To achieve this, we need a system operating at a time scale comparable with the phonon oscillation period, such as the experimental realization does not sense an average of these oscillations but resolves different phases of it. Ultrafast lasers enable this kind of technique. Using ultra short pulses with durations on the scale of tens of femtoseconds up to few picoseconds, we can probe time dynamics with frequencies in a range from gigahertz up to terahertz [104]. This detection scheme is known as the pump-probe spectroscopy.

2.3.1 Pump-probe spectroscopy

One research line of this manuscript covers the experimental study of the temporal dynamics of nanostructures engineered as cavities and resonators. These resonant structures were designed to confine phonons in the range between tens and hundreds of gigahertz. In this work we have used ultrashort pulses of light to excite phononic resonators and to study their optical response at different times. This technique, known as pump-probe spectroscopy, uses two ultrashort pulses of light focused on the sample under study [74, 75]. The resulting process can be summarized in three main steps. First, one of the pulses, termed the pump, is focused on the sample surface. This pulse generates an impulsive response of the system by perturbing the lattice structure through one or more different processes like thermoelasticity, deformation potential, electrostriction and inverse piezoelectric effect [73]. This response generates phonons on the time scale of the ultrashort pulses. Consequently, phonons generated by ultrafast laser action vibrate with a common phase (as long as the phonon period of oscillation is significantly larger than the pulse duration) i.e. coherent phonon generation. Processes that occur on longer time scales than pump pulse duration also produce phonons. In contrast with those produced during the partial absorption of the pump pulse, these phonons are incoherent. Processes that lead to the production of incoherent phonons are for example the increase in temperature of a sample due to consecutive pump pulses focusing on it and the recombination of electron-hole pairs originally produced during the pump excitation. These incoherent phonons might have effects in the measured signals from pump-probe spectroscopy experiments but do not manifest in the phononic spectrum that can be extracted from them. The second step of the pump-probe technique consists of a second pulse, termed the probe, being focused in the same area where the pump was focused before. During its reflection, the probe pulse senses the (almost) instantaneous optical reflectivity of the sample. Consequently, when the probe reflects from the sample it senses an index of refraction that has been modulated therefore altering the reflected amplitude of the probe beam. This technique used to detect coherent phonons is also known as time-domain Brillouin Scattering (TDBS) [103], a name that emphasize that photons are being scattered by phonons. The amount of photons being scattered varies as the phase of the coherent phonons generated changes over time. Then, the probe power after being reflected from the sample varies periodically at the frequency of the coherent phonons present in the sample. This results in a modulation in the sample reflectivity depending on the

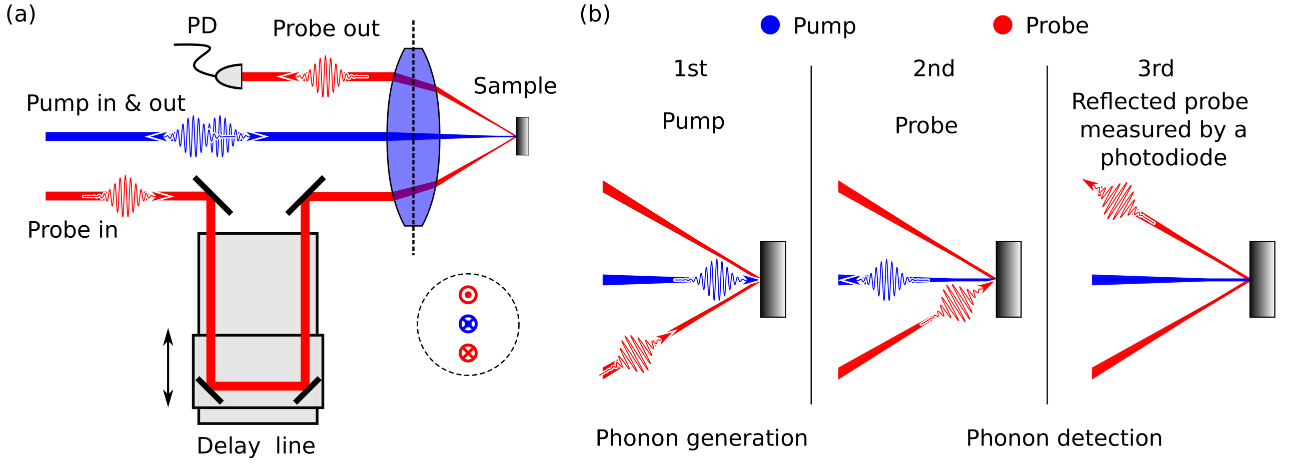

Figure 2.5: (a) Sketch of a pump and probe optical setup. A mechanical delay line is used to control the delay between the pump and the probe pulse arrival on the sample. On the bottom right, a front view of the focusing lens shows the direction of the three beam trajectories passing through it. (b) Description of the pump and probe technique for phonon detection. First a pump pulse focused on the sample impulsively generate phonons. Secondly, the probe is focused on the same sample spot. Thirdly and finally, the probe, carrying information about the phonon population and phase upon reflection, is redirected into a photodiode.

phonons oscillation phase at the moment of the probe reflection. By controlling the time-delay between pump and probe using a mechanical delay-line, the probe reflection can sense different reflectivity conditions as a function of time-delay. The third and final step of the pump-probe technique is to extract the probe reflected beam and focus it on a photodiode. Figure 2.5 (a) and (b) present a schematic representation of the optical setup and of the three steps described for the pump-probe technique to detect coherent phonons.

When the pump pulse is focused on a solid structure, there are four mechanisms through which phonons can be coherently generated: deformation potential, thermoelasticity, the inverse piezoelectric effect and electrostriction [73]. Their contribution to the dynamics of the system can be taken into account by describing their effects as a stress applied along the structure. Then, the wave equation describing the elastic system can be reformulated by introducing $\sigma(z,t)$ the photoinduced stress as

$$\frac{\partial^2 u(z,t)}{\partial t^2} - v^2 \frac{\partial^2 u(z,t)}{\partial z^2} = \frac{1}{\rho}\frac{\partial \sigma(z,t)}{\partial z} \tag{2.37}$$

where v is the sound velocity in the media and $\sigma(z,t)$ is the result from adding all the mechanisms contributions through which light induces a stress in the lattice. The photoinduced stress is a force that acts along the full structure. As a consequence of its presence the ion cores move from their lattice positions, which can be modeled as a continuous strain $\eta(z,t)$ along the structure. It is a direct consequence of the light inducing stress in the solid. From equation 2.37, for a semi-infinite system and considering a free surface condition, the strain spectrum induced by the pump can be calculated as a function of the photoinduced stress [73]

$$\tilde{\eta}(z,t) = -\frac{i\omega}{2\rho v^3}\left[\hat{\tilde{\sigma}}\left(\omega, i\frac{\omega}{v}\right) - \hat{\tilde{\sigma}}\left(\omega, -i\frac{\omega}{v}\right)\right] \tag{2.38}$$

where $\hat{\tilde{\sigma}}$ is the result after Fourier and Laplace transforming (in that order) the photoinduced stress [73, 102, 105]. This result analytically states the dependence of the strain spectrum on the photoinduced stress spectrum. It directly states how the pump beam induces a strain field along the lattice structure. This induced strain is what allows the probe beam to detect the effect of coherent phonons generated by the pump. Calculating the optical reflectivity of a

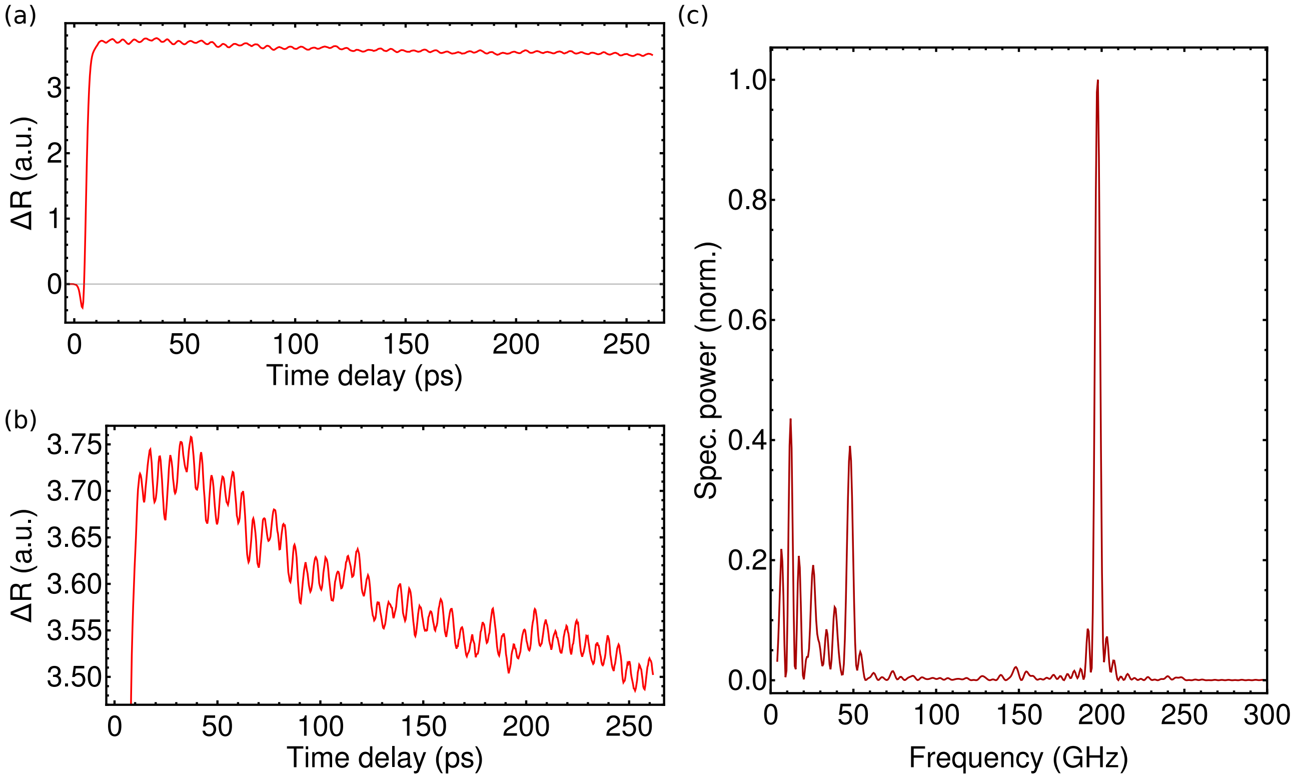

Figure 2.6: (a) Time resolved reflectivity trace obtained from a pump-probe spectroscopy setup. At zero delay, a rapid change of the instantaneous reflectivity is the result of the pump pulse ultrafast action on the sample. (b) Zoom into the time resolved reflectivity trace shown in panel (a). The oscillations in reflectivity in this plot are the result of coherent phonons modulating the sample's optical reflectivity. (c) Phononic spectrum obtained after Fourier transforming the reflectivity time trace. At 200 GHz the main resonance of the structure is detected. Additional peaks on both sides of the main peak at 200 GHz are distinguished and are caused by the multilayer structure acting as a resonator. At 50 GHz a strong peak appears corresponding to the Brillouin frequency of the materials used and altered by the overall structure multilayer.

semi-infinite structure considering strain field η the following expression is obtained [73, 106]

$$\Delta r/r = -2ik_0u(0,t) + \frac{4ik_0n}{1-n^2}\frac{\partial n}{\partial \eta}\int_0^{\infty}\eta(z,t)\exp(2ink_0z)dz \tag{2.39}$$

where k_0 is the wavevector of the probe beam, $u(0,t)$ is the free surface displacement of the sample, n is the material refractive index and $\frac{\partial n}{\partial \eta}$ is the photoelastic coefficient. The first term in equation 2.39 accounts for the changes in reflectivity caused by the displacement of the interface through which the probe beam is focused. The second term accounts for the modifications of the refractive index due to the presence of strain and, as shown in equation 2.38, it depends on the photoinduced stress. Consequently, when we measure the instantaneous reflectivity of the sample with the probe pulse we are able to detect the coherent phonons generated by the pump. In typical pump-probe experiments, the second term in equation 2.39 is much larger than the first one. If we neglect the first term, we observe that phonons can be detected as long as the integral along the structure does not vanish. This imposes an important condition on the two factors present within the integral $\eta(z,t)$ and $\exp(2ink_0z)$. Because the strain function has the periodicity of the phonons wavevector q, we can state that a sufficient condition for a not vanishing integral is given by $q = 2k_0$. Figure 2.6 (a) presents an example of the reflectivity traces measured through pump-probe spectroscopy. These time resolved reflectivity traces are acquired while the delay line position is changing. Note that the pump-probe is a stroboscopic technique where we collect the average of several pump and probe pulses focused on a photodiode without resolving each pair. In figure 2.6 (a), near zero delay there is a rapid (few picoseconds) change in the optical reflectivity of the sample under study. Then, in the following hundred of picoseconds we see how the system relaxes back to equilibrium. The overall process of relaxation takes several nanoseconds, but within the first few hundred picoseconds we observe oscillations in the time resolved reflectivity traces. These oscillations are the signature of the presence of coherent phonons modulating the optical properties of the sample on the picosecond scale. Figure 2.6 (b) shows a zoom in the oscillations shown in panel (a) and uses the same ordinate units. We can see how these oscillations show a periodic modulation of the sample reflectivity and, by processing, we can extract a phononic spectrum associated to the sample presented in figure 2.6 (c). In the example presented in Fig. 2.6, we measured an acoustic resonator operating at 200 GHz using pump and probe powers of 100 and 20 mW, and pulses with duration of 2 ps at a wavelength of 865 nm. Besides the example presented in Fig. 2.6, all experimental realizations done in this thesis were done in hybrid opto-phononic resonators. In hybrid structures featuring confinement of both acoustic and optical waves we can approximate the detection efficiency in pump-probe experiments as a function of the phonon frequency ω as

$$D(\omega) \propto \int E^2(z) p(z) \sigma_{Raman}(\omega) \frac{\partial u(z)}{\partial z} dz \tag{2.40}$$

where $E(z)$ is the laser electric field along the structure, $p(z)$ is the material-dependent photoelastic constant, $\frac{\partial u(z)}{\partial z}$ is the strain gradient along the structure and $\sigma_{Raman}(\omega)$ is the Raman cross-section [71].

There are multiple challenges that can affect pump-probe spectroscopy experiments. Commonly, optical setups are designed to optimize stability by reducing their footprint and mechanically fixing all optical pieces. Given how fast is the speed of light, a pump-probe detection scheme requires long delays implemented by long trajectories for the optical beams and a set of movable pieces mounted in a delay line stage. These two requirements are directly opposed to the ideal scenario for robust measurements. Consequently, the main challenges commonly faced on these experiments are stability and reproducibility. In addition, high optical powers are used, typically in the range of several milliwatts, in order to ensure enough light being detected carrying the phonon induced signal. This range of powers is a limiting factor for example when dealing with biological samples and quantum dots typically incapable of supporting such powers without compromising their integrity. The present manuscript describes the work done to reduce or remove these detrimental factors.

2.4 Multilayer structures

Multilayer structures allow us to control the propagation of acoustic and optical waves by engineering the media through which they propagate. If waves propagate through a periodic structure, i.e. formed by identical groups of layers, called unit cells, concatenated one after the other, a band structure describes the sustained modes of the structure. These structures are called superlattices, and their band structures exist in direct analogy and in addition to the periodicity in solid-state materials imposed by their crystal lattice structure. Superlattices are a powerful tool for the engineering of nanophononic structures. In this section, we describe three cases of multilayer structures based superlattices: distributed Bragg reflectors (DBRs), optical cavities and acoustic resonators.

2.4.1 Distributed Bragg reflector

Let us consider a superlattice formed by two materials A and B with mass density ρ_A and ρ_B, respectively. Sound velocity through each of the different materials is given by v_A and v_B for materials A and B, respectively. Figure 2.7 presents a schematic representation of such a multilayer structure. From equations 2.27, considering the boundaries conditions (equations 2.28 and 2.29) and from Bloch's theorem we obtain a homogeneous system of equations. Solutions

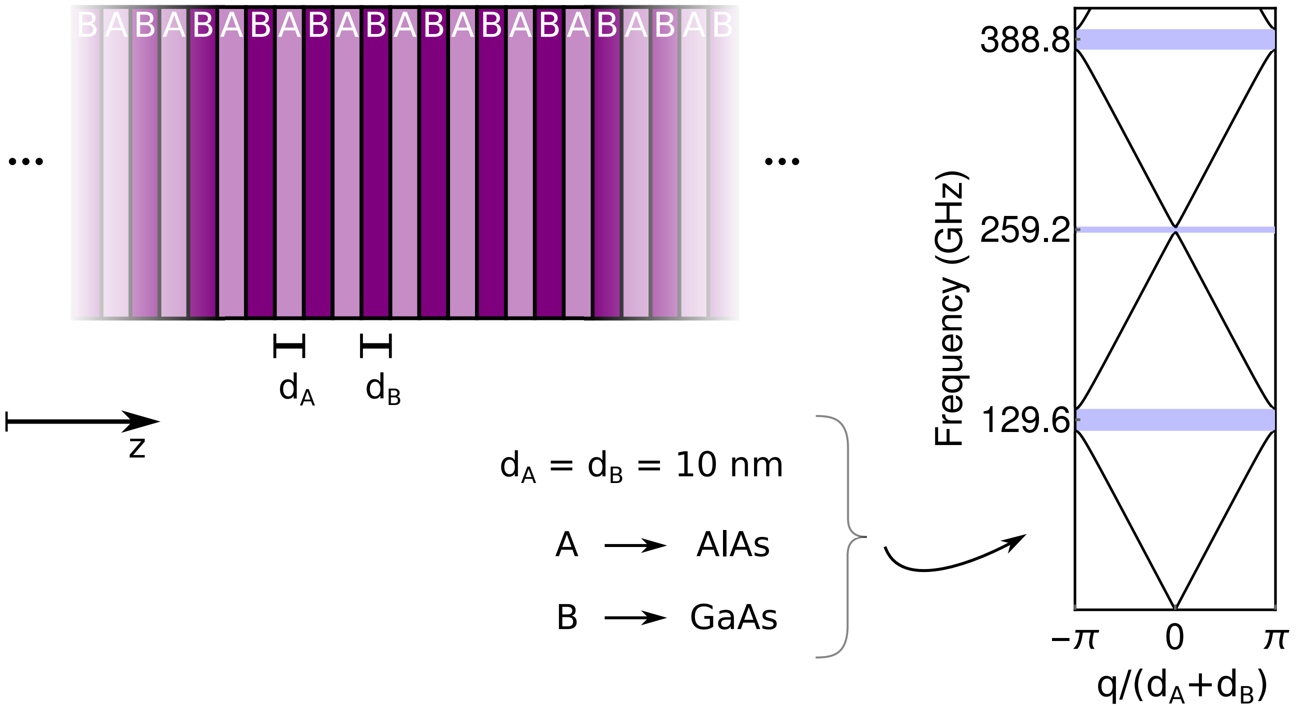

Figure 2.7: Left: Superlattice formed by concatenating layers of material A and B, alternating between them. Each layer of material A and B has a thickness d_A and d_B. Right: Dispersion relation calculated for longitudinal acoustic phonons in a superlattice form of *GaAs* and *AlAs* with layers of thickness $d_A = d_B = 10$ nm. Light blue boxes mark the minigaps opening between the different bands.

for it are found by solving for ω the equation given by its determinant equal to zero. From it, the dispersion relation of superlattice is obtained

$$\begin{aligned}\cos(qd) &= \cos\left(\frac{\omega d_A}{v_A}\right)\cos\left(\frac{\omega d_B}{v_B}\right)\\ &\quad -\frac{1}{2}\left(\frac{\rho_A v_A}{\rho_B v_B}+\frac{\rho_B v_B}{\rho_A v_A}\right)\sin\left(\frac{\omega d_A}{v_A}\right)\sin\left(\frac{\omega d_B}{v_B}\right) \qquad (2.41)\end{aligned}$$

where q is the wavector and the thicknesses of the layer A, B and the whole unit cell are given by d_A, d_B and d, respectively [63, 94]. Figure 2.7 present the solutions of this equation for a superlattice formed by alternating layers of 10 nm thickness of *GaAs* and *AlAs*. The first Brillouin zone is plotted up to 410 GHz and shows bands and, between them, gaps spanning along different bandwidths. The gaps resulting from superlattice structures are typically called minigaps, highlighting their small scale in contrast with the gaps emerging from the crystal lattice structure. Using the transfer matrix method algorithm described in this section, we can simulate the reflectivity of finite versions of superlattices. Figure 2.8 presents plotted in yellow (blue), the acoustic reflectivity as a function of phonon frequency for a multilayer structure formed by 10 (20) identical cells as described in figure 2.7. This type of periodic structures is known as a distributed Bragg reflector and is used as a building block for more complex structures like resonators. While we have described reflectors for acoustic waves, optical waves can also be treated in an analogous approach and optical DBRs, also referred as dielectric mirrors, are common in modern optics laboratories.

Superlattices band structures offer a platform for the study of acoustic phonons in nano-engineered devices designed to control them. As we have showed, minigaps open and within them only evanescent solutions appear. These are associated to stop bands i.e. high reflectivity spectral regions that effectively act as mirrors for phonons. In the following sections we will address the use of these as part of cavities and resonators designed to confine longitudinal acoustic phonons and photons, respectively.

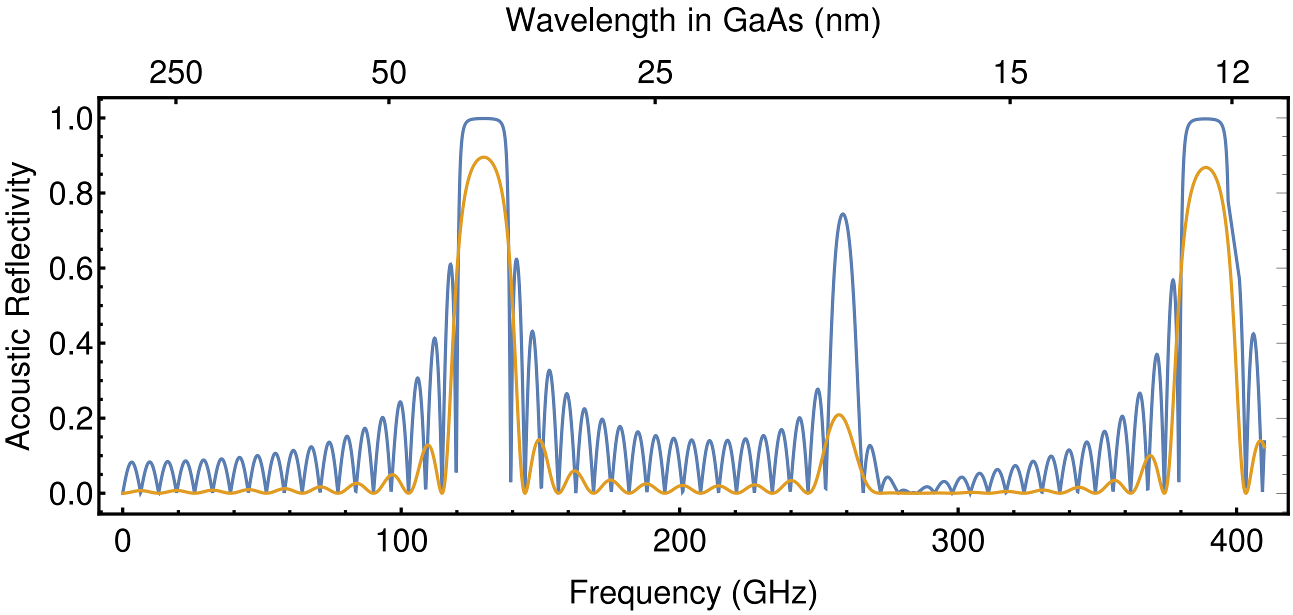

Figure 2.8: Plotted in yellow (blue): Acoustic reflectivity of a distributed Bragg reflector of 10 (20) unit cells each one formed by two layers of 10 nm thickness of *GaAs* and *AlAs*.

2.4.2 Optical cavities

Optical cavities based on DBRs fabricated at the micro- and nano- scale have demonstrated several applications in modern technologies [55, 107–111] Molecular beam epitaxy (MBE) allows the fabrication of multilayer devices operating as optical cavities featuring layers thicknesses on the nanometric scale and with practically atomically flat interfaces [112]. In this work, we have used multilayer structures fabricated by MBE for the implementation of optical cavities operating in tandem with acoustic resonators and enhancing the phononic signals measured from them. Such enhancement is done by engineering devices where the Raman scattering cross section is maximized by increasing the overlap between the electric field and the strain at the resonant frequencies we aim to detect as demonstrated in previous works [60, 69–72, 100].

Figure 2.9 (a) presents a schematic representation of a Fabry-Perot cavity as a multilayer structure. It is formed by two optical DBRs surrounding a spacer region between them. If the spacer has a length multiple of $\lambda/2$ when light propagates in it gets trapped inside, reflecting back and forth as depicted by the red arrows [66, 107, 108]. In this work, we have engineered *GaAs*/*AlAs*-based nanostructures working as Fabry-Perot cavities. Using these structures we have confined light, enhancing the measured signals in pump-probe experiments [38, 113].

The TMM can be used to simulate the propagation of light through multilayer structures like Fabry-Perot cavities and to compute their reflectivity as a function of wavelength. As an example, let us consider the case represented in 2.9 (a) where two distributed Bragg reflectors of 12 layer pairs each surround a spacer in the middle. Only two materials are used in the structure, *GaAs* and *AlAs*. The used DBR design is formed by layers with thicknesses of 65.6 and 75.9 nanometers for *GaAs* and *AlAs*, respectively, which opens a stop band around 900 nm. In between the two reflectors, a *GaAs* spacer is placed with a thickness of 254.4 nm matching the size of one wavelength (in *GaAs*) of 900 nm wavelength light in free space. All these thickness are chosen in order to confine this color of light in the spacer region. The overall thickness of the cavity is approximately 3.6 μm. Figure 2.9 (b) presents the optical reflectivity of the Fabry-Perot cavity in a *GaAs* medium computed using the TMM. Due to the presence of a DBRs, a high reflectivity region appears around 900 nm, but, distinctively, at that wavelength a dip in the curve where the reflectivity drops to practically zero can be distinguished. Reflectivity dips like this one are the signature of the presence of a confined mode. In order to visualize the simulated confined mode, using the TMM we compute and plot the electric field amplitude as a function of position for the simulated reflectivity conditions.

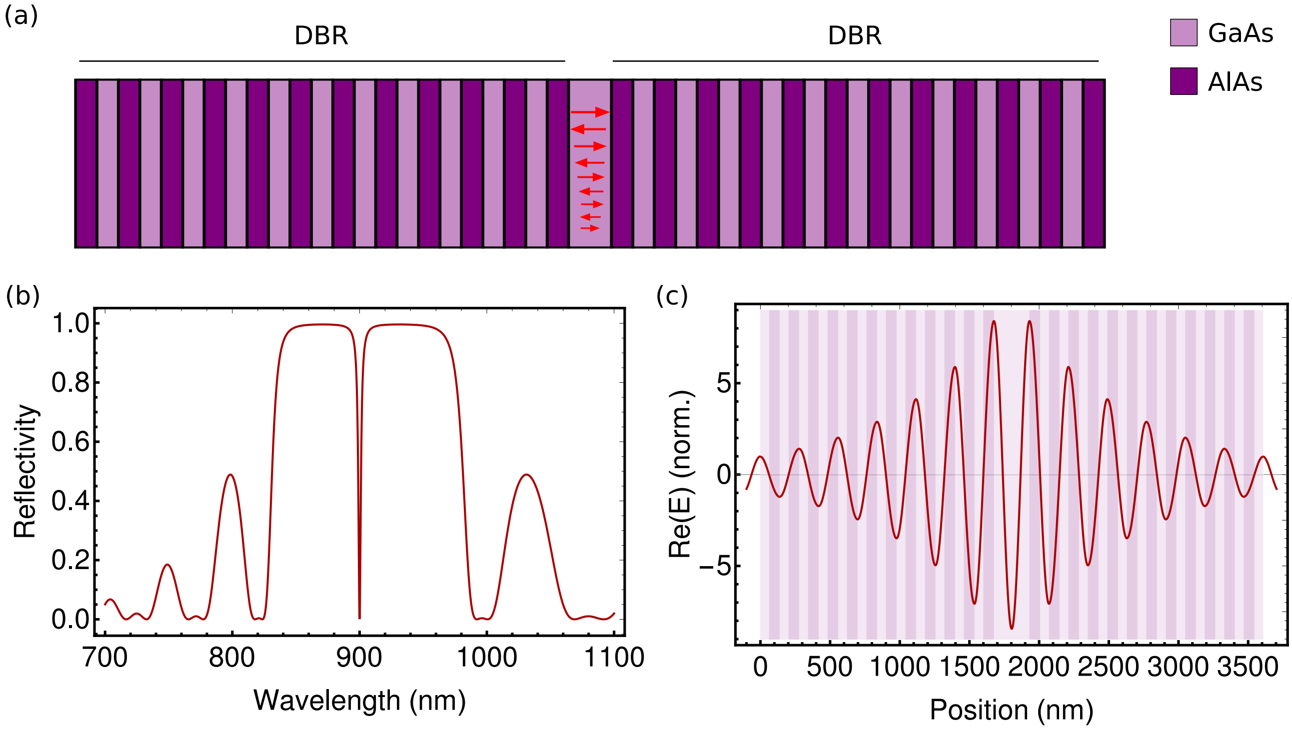

Figure 2.9: (a) Schematic of a Fabry-Perot cavity formed by two distributed Bragg reflectors (DBR) around a solid spacer. The red arrows represent the multiple internal reflections between the two reflective multilayer structures. (b) Optical reflectivity of a Fabry-Perot cavity computed using the TMM to simulate a plane wave incident from left to right. At 900 nm, a reflectivity dip shows the presence of a confined mode. (c) Plot of the electric field as a function of position along the full structure. The background inset represent the multiple layers of the structure with the lighter (darker) color corresponding to $GaAs$ ($AlAs$).

Panel (c) show the real part of this complex amplitude plotted for the full extension of the structure (normalized to the incoming field at the input interface i.e. at the left extreme of the structure). Behind the curve, insets in form of boxes represent the layers thicknesses of the structure with respect to the field. The design parameters allow the largest amplitude at the spacer, reaching values over eight times larger than the input field amplitude. In addition, we observe how the field at the spacer spans along one full wavelength accordingly to the structure design.

The example presented in figure 2.9 constitutes an ideal case of a Fabry-Perot cavity multilayer structure. The structure is symmetric and, moreover, all simulations were done considering it is surrounded by a uniform $GaAs$ medium. The real structures to be experimentally studied are measured in different conditions. Letting aside the possibility of errors on the fabrication procedures that may alter the layers' nominal thickness, we must take into account that the multilayer structure is grown on a substrate. As a consequence of this, the two opposing sides of the structure are exposed to different conditions during an experiment. One side is adjacent to the substrate while the other to the ambient. Then, the difference in reflectivity at the extreme interfaces affects the balance between the two reflectors confining light in the spacer. Using the TMM we can simulate how this imbalance affects the cavity reflectivity and the field amplitude along the structure. Figure 2.10 (a) presents the optical reflectivity of the symmetric structure considered for figure 2.9, but in this case embedded in a non uniform ambient. On the right extreme of the multilayer structure the cavity is adjacent to a $GaAs$ substrate while on the opposed extreme (left) to air. Light propagates from left to right, entering the structure through the air-$GaAs$ interface. Distinctively from the balanced case, the optical reflectivity does not drop to almost zero at the reflectivity dip associated to the cavity mode. This result, shows how an unbalanced cavity limits the amount of power that can be injected into it. Panel (b) presents the electric field as a function of position along the structure. While the mode

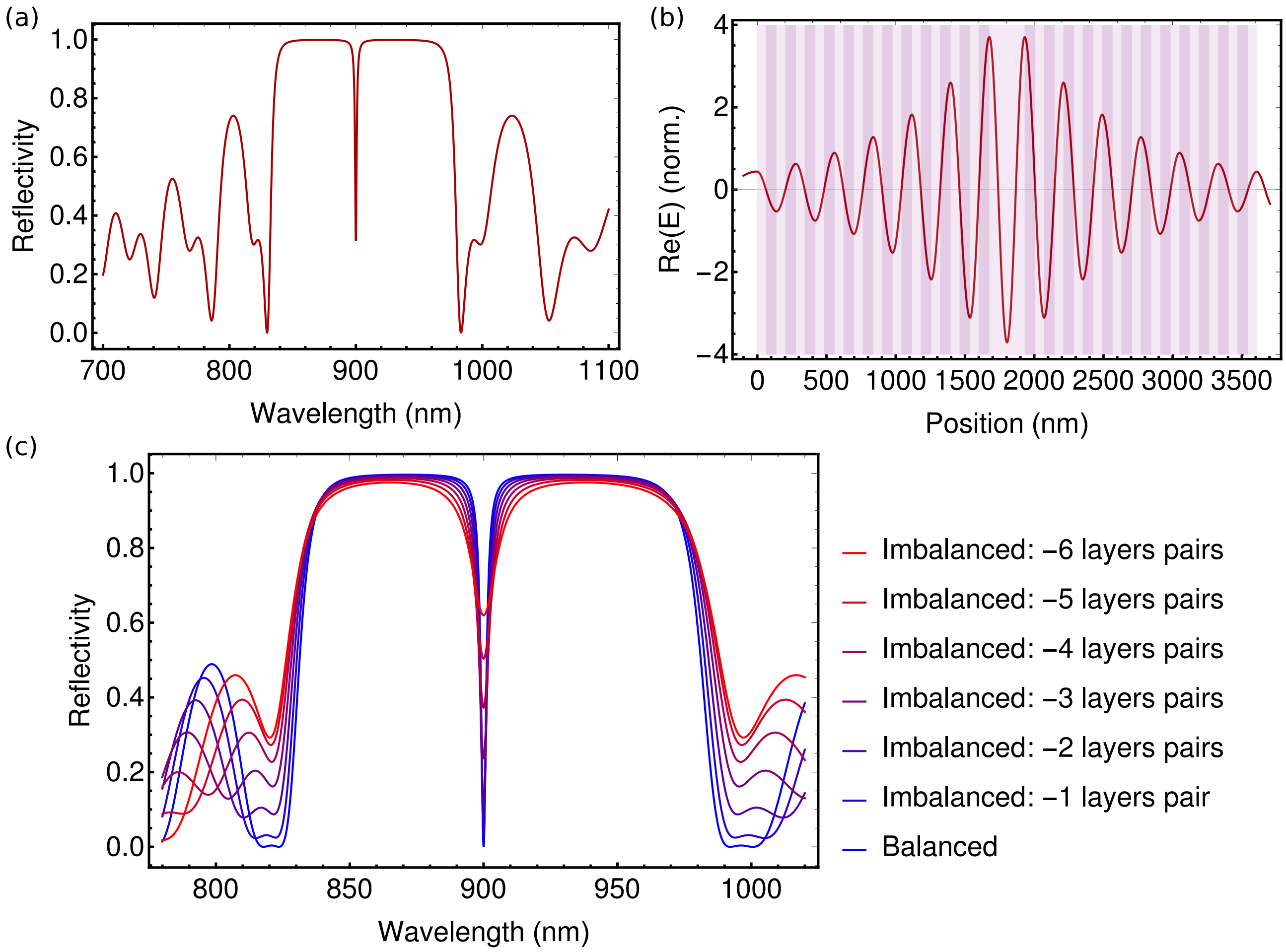

Figure 2.10: Panels (a) and (b) present the optical reflectivity and electric field of a symmetric Fabry-Perot cavity embedded in an unbalanced ambient. The simulated structure is the same as the one considered in figure 2.9 but with one of its extremes (the right one) being adjacent to a *GaAs* substrate, while the other extreme (the left one, from which light inputs the structure) being adjacent to air. The background inset represent the multiple layers of the structure with the lighter (darker) color corresponding to *GaAs* (*AlAs*). (c) Optical reflectivity curves of Fabry-Perot cavities formed by two DBRs while their number of layers pairs variate. The structure is embedded in a balanced ambient, i.e both extremes adjacent to *GaAs*. The imbalance comes from the lack layers pairs affecting causing different reflectivity on each side of the spacer. As can be seen in panels (a) and (b), the presence of an imbalance between these reflectivities, result in an increment of the minimum value obtained at the reflectivity dip.

looks practically the same as in the balanced case, we can notice a reduction in the maximum values reached by the field in the spacer. Another approach to model an unbalanced cavity is to consider an even ambient, but a different number of layer to each side of the structure spacer. Panel (c) presents how the optical reflectivity varies while the number of layers is reduced from the right side of the structure. As shown in the case of the unbalanced ambient conditions, the reflectivity dip start to vanish while we increase the unbalance, i.e. limiting the amount of light that can be coupled to the cavity mode.

In real experimental implementations the boundary conditions of Fabry-Perot cavities, the ambient is commonly uneven i.e. on one side there is a substrate while on the other either air or vacuum. In order to compensate this intrinsic imbalance, a typical strategy is to vary the number of layer of the DBRs forming the cavity in order to compensate the boundary conditions. Figure 2.11 presents the case of a Fabry-Perot cavity formed by the same unit cells as in the previous examples embedded in an uneven ambient. In order to compensate the ambient effect, on the substrate side of the structure there are 12 unit cells, while in the other extreme only 8. The extra four unit cells increase the reflectivity on the substrate side, with the

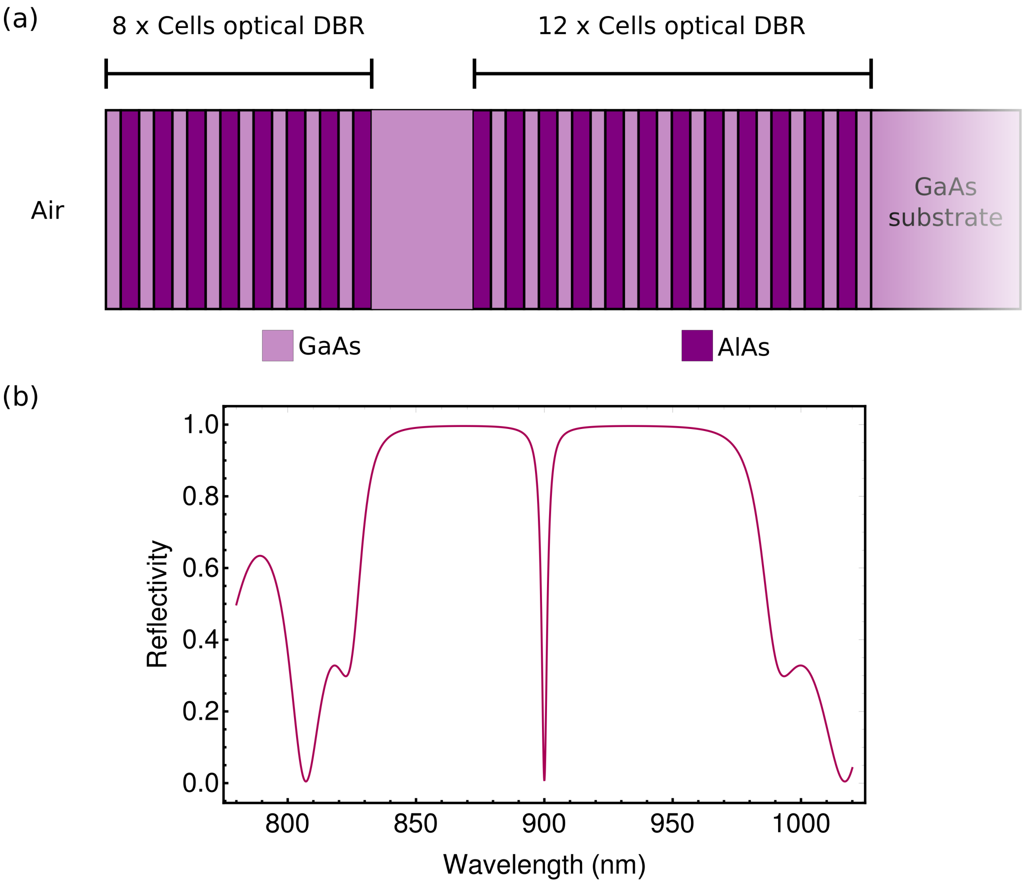

Figure 2.11: (a) Schematic representation of a Fabry-Perot cavity in an unbalanced ambient. The unit cells used are the same as those of figure 2.10 and 2.9. The cavity design features four less unit cells in the DBRs adjacent to the ambient, in order to balance the optical reflectivity on each side of the spacer. (b) Optical reflectivity computed for the structures presented in panel (a). We can see how the different DBRs used compensate the unbalance due to the boundaries condition allowing the reflectivity dip corresponding to the confine optical mode decrease down to practically zero.

intention to compensate the large reflectivity between the structure materials and air. Panel (a) presents a schematic representation of the described cavity. We plot the optical reflectivity of the sample using the TMM and present it in panel (b). We can see how the reflectivity dip, even in the presence of the unbalanced ambient drops to practically zero. This is the result of using four extra unit cells on the substrate side of the cavity and it is a common practice to balance the reflectivity at different extremes of cavities.

The Fabry-Perot cavities presented in this section are examples of how distributed Bragg reflectors can be used to confine optical modes. In the following section and in direct analogy to the designs presented here, Fabry-Perot resonators are described using the same principles to confine acoustic vibrations.

2.4.3 Fabry-Perot resonator

Fabry-Perot resonators operate in the same way as Fabry-Perot optical cavities, but confining acoustic waves [60, 66, 100]. In fact, the same structure described for figure 2.11 acts also as an acoustic resonator. Using the TMM we can simulate the propagation of acoustic waves through the structure presented in figure 2.11 (a), however, we must remark some differences from the case of optical waves. In contrast with photons, phonons do need a medium to propagate. Moreover, at frequencies in the order of several gigahertz, mechanical waves are not sustained in air. Consequently, we must change the way we model phonons propagating through a multilayer structure with air (or vacuum) on one of its extremes. For this purpose,

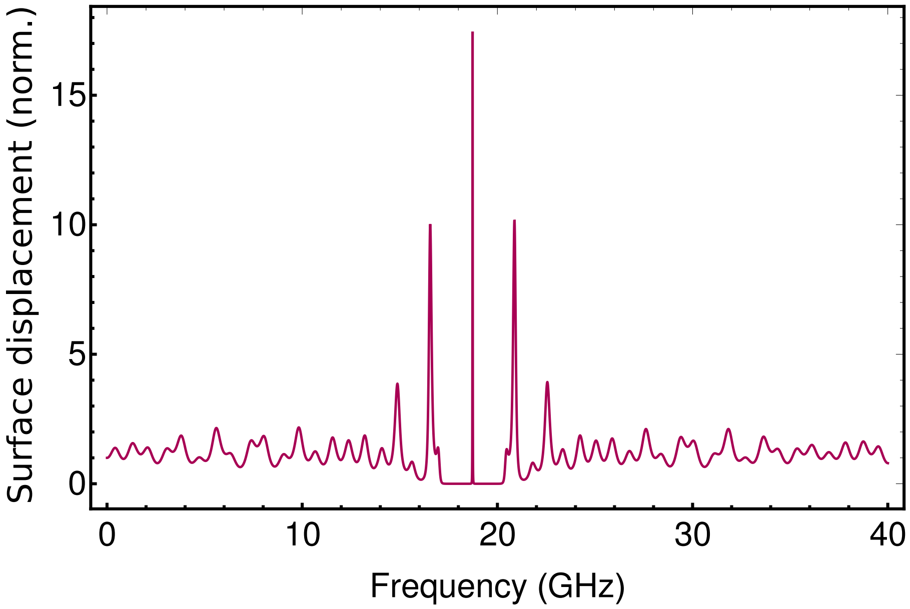

Figure 2.12: Surface displacement intensity computed for the structures presented in figure 2.11 panel (a). The result is normalized to the incident displacement coming from the substrate side. We can see a maximum at the resonant frequency of the structure around 18.7 GHz.

we made two changes in the algorithm used to simulate the propagation of phonons for this kind of structures. First, we consider phonons incident in the structure from the substrate side, i.e. from right to left as shown in figure 2.11 (a). Second, we impose a zero stress boundary condition at the interface between the structure and air. The zero stress condition implies that all phonons incident to the interface between the structure and air (or where the condition is applied) are reflected back into the multilayer structure. As a result, the structure reflectivity is equal to one. Then, in order to evidence the presence of a confined mode in the multilayer structure from figure 2.11 (a) we compute the normalized surface displacement using the TMM with the zero stress condition imposed at the air interface. Figure 2.12 shows a the surface displacement intensity as a function frequency. In contrast with the reflectivity calculations, in this case we see a high peak at the resonant frequency around 18.7 GHz. On both sides of the resonant peak, a flat region with values equal to zero appears associated to the DBRs minigap. Figure 2.13 presents the plot of the displacement field as a function of position at the resonant frequency. As in the case of the optical cavity, most of the field is located at the spacer of the Fabry-Perot resonator.

Fabry-Perot resonators operation can be described in a direct analogy to their optical cavities counterparts. Acoustic waves do not penetrate them when their frequencies are in the minigaps associated to acoustic band structures. Uneven boundary conditions lead to a reduction of the amplitude of the acoustic field confined at the spacer region and different amount of layers can reduce this unbalance. Nevertheless the fact that phonons do not propagate in air results in a system impossible to balance completely. For the simulations presented in this manuscript we consider that phonons propagate towards the structure from the substrate side, i.e. the right side in figure 2.11 panel (a). In real implementations, the generation process of phonons can occur at different parts of the structure. For example, if a metallic layer is placed on the air side of the structure, light focused on it will cause a thermoelastic response, generating phonons that originate in the left most side of the structure, and penetrate it from left to right. In the absence of a metallic layer, when using semiconductors materials their energy gaps can be targeted by the photon energies and electron hole pairs can be created, leading to a coherent phonon generation process due to deformation potential. In addition to this and in any solid, electrostriction can also coherently generate phonons.

Acoustic resonators are an important building block for nanophononics. In the following chapters we will come back to this type of structure operating at different frequencies. Moreover,

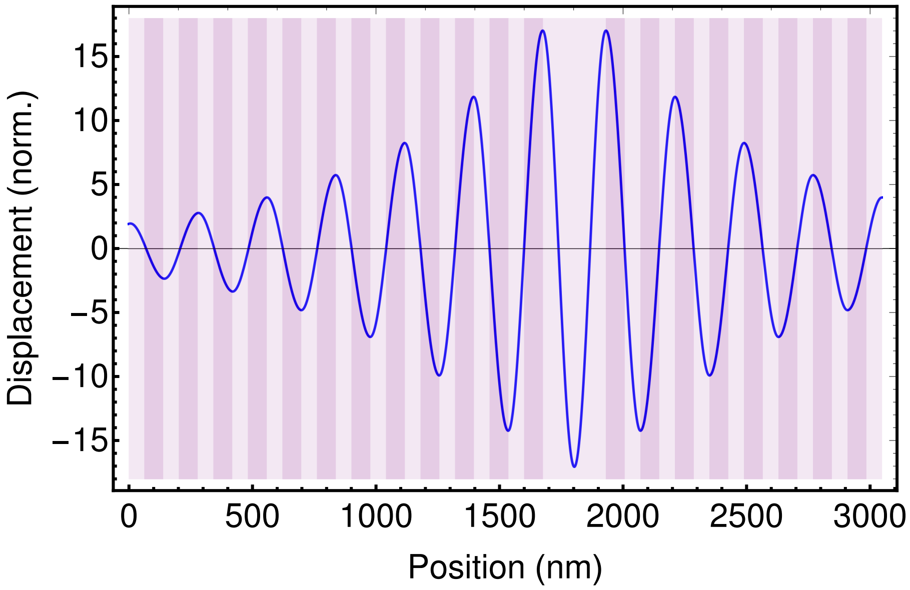

Figure 2.13: Displacement field as a function of positions plotted along the multilayer structure presented in figure 2.11 panel (a) at the resonant frequency ≈ 18.7 GHz. The result is normalized to the incident displacement coming from the substrate side. The background inset represent the multiple layers of the structure with the lighter (darker) color corresponding to *GaAs* (*AlAs*).

it will serve as a departing point for novel types of confinement, based not only in DBRs and spacers, but on quasiperiodic structures that modulate the acoustic properties of multilayer devices.

Chapter 3

Nanophononic engineering with superlattices

Nanotechonologies have revolutionized the world in which we are living, with electronic and photonic devices being part of our everyday routine [40, 114–116]. Miniaturization made this possible, but as nanostructured systems scale down below phonon mean free path (MFP), the phonon dynamics of the overall system changes (MFP estimated values for bulk silicon at room temperature are below 300 nm [117]). As a result, heat transfer abandons a diffusive regime and thermal conductivity in nanostructures typically drops [117, 118]. Featuring high integration density producing more heat in smaller volumes, electronic and photonic devices on the nanoscale present more challenges to guide their produced heat away resulting in detrimental effects as a consequence [24, 25, 118, 119]. Nanoengineered structures have demonstrated suitable for dealing with this problem by controlling the propagation of phonons at the nanoscale [26, 28–31]. In addition to heat transport applications, studying the phonon propagation has demonstrated potential for the simulation of complex wave dynamics [50, 51], imaging applications [77, 120, 121] and quantum technologies [41, 42, 45, 122, 123], among other fields [37]. In this chapter, we focus on the engineering of nanophononic structures like phonon mirrors, filters and resonators designed to control the propagation of phonons in one dimension [60, 61, 124]. The main challenges faced when engineering the way phonons propagate lie in the fabrication process. Materials need to be highly pure in order to ensure low or no scattering of phonons due to defects. Interfaces between different materials need to be as flat as possible since their roughness on the scale of high frequency phonon wavelengths can directly impact how phonons propagate. In this sense, molecular beam epitaxy (MBE) constitutes a powerful fabrication technique, capable of achieving practically atomically flat interfaces in heterostructures. The multilayer structures to be introduced in this chapter are designed taking into consideration parameters like layer thicknesses and total number of layers in a structure, such that they remain feasible to fabricate in the state of the art clean room facilities at the Centre for Nanoscience and Nanotechnology (C2N).

In the following section, we propose a set of tools to control the propagation of acoustic phonons in multilayer systems. At the core of these tools are the same band structures emerging from periodic layered systems like distributed Bragg reflectors. In order to control the propagation of phonons, we break the periodicity of these multilayer devices by altering the thicknesses of the layers that formed the periodic structure. By doing so, instead of creating a single superlattice where the band structure is fixed, we propose the use of quasiperiodic structures where the band varies along the multilayers, creating an acoustic local band structure. In contrast to textbook examples of electronic quantum wells in heterostructures where the lattice changes between different parts of a structure, but within each of these regions the unit cells are the same, here, the local bands emerge from collective characteristics within and around each cell. Our approach is based on the idea that, while all cells contribute to create the local bands their contribution is position dependent, the closer a cell is, the larger its contribution to the local band experienced in that particular position is. Thus, by progressively varying these bands

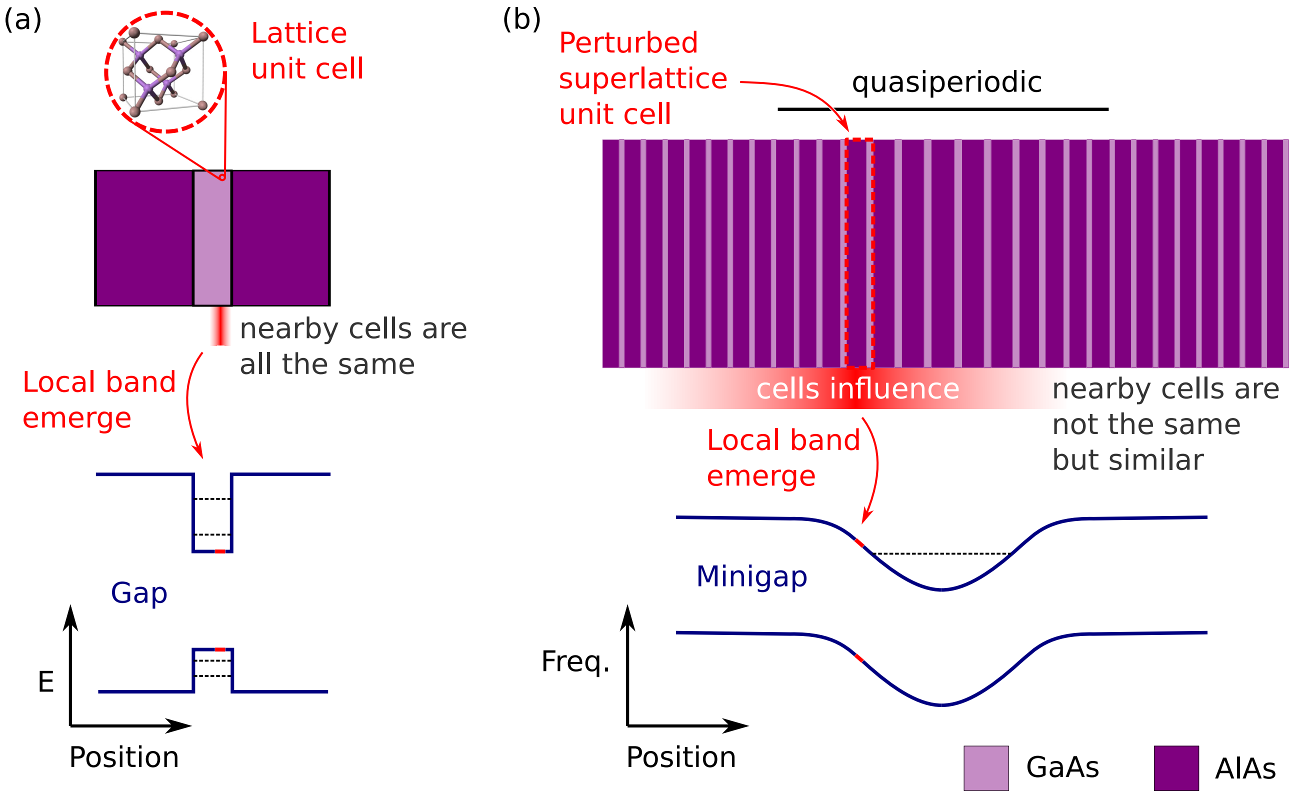

Figure 3.1: (a) Schematic diagram of the electronic local band structure of a GaAs quantum well. The bands are determined by the composition of each layer. (b) Schematic diagram of the phononic local band structure of an adiabatic resonator. The bands are determined by each cell and its neighbors. The farther away from a given position, the less the cells influence the emerging band.

along the multilayers we are able to shape the bands to form an acoustic local band structure. This progressive modulation, not rapid enough to remove the effect of a local band, we called it an adiabatic modulation. In order to quantify how rapid or not the modulation of the local band is along a multilayer structure we define an adiabatic parameter depending on the overlap between consecutive minigaps as $P_{adiabtic} = (\sum_{i=1}^{N_{total}-1} B_i \bigcap B_{i+1})/(\max_i B_i)$ where i is an index identifying each unit cell, B_i is the bandwidth interval of a chosen minigap of the i-th cell local band and N_{total} is the total number of cells in the structure. If the parameter $P_{adiabtic}$ is close to 1, we consider the propagation of phonons along the structure adiabatic. Correspondingly, we call multilayers structures confining phonons by means of an acoustic local band structure adiabatic resonators.

Figure 3.1 panels (a) and (b) present schematic diagrams of an electronic and an acoustic local band structure, respectively. On top of each of these band structures, the multilayer design producing them is represented. These two different devices are both multilayer structures formed by concatenating layers of $GaAs$ and $AlAs$. In panel (a) the electronic local band structures of a quantum well is represented. On top, the schematic of the structures producing these band is shown: a central layer of $GaAs$ surrounded by $AlAs$. On the bottom, the electronic band structure shows the gap edges as a function of position. The difference in the energy level arise from the different lattices $GaAs$ and $AlAs$ have. On the top, a schematic of a zoom in the $GaAs$ layer presents its unit cell, below, marked in red, we represent the different influence nearby unit cells have to the band experienced in a given (local) position. Closer unit cells affect more the emerging band, nevertheless all unit cells are the same, therefore we end up with a fixed local band for all the $GaAs$ layer. In panel (b) the acoustic local band structure of a quasiperiodic resonator (to be introduced in this chapter) is shown. On top, the layers of the resonator are represented (not to scale) showing the particularity of this design where the central cell is 6% larger that those on the extremes. On the bottom, the acoustic local band structure as a function of position is plotted. In this case each unit cell is formed by two layers. Nearby cells affect more than those far away at a given (local) position. As a result, a local band structure emerges at each position, featuring a minigap determined by the characteristics of the region around it. The inverse proportionality between wavelength and frequency makes that a change in thickness of 6% corresponds to a change of roughly the same scale in the minigaps frequencies. The effects of such an alteration are large enough to effectively bend the acoustic band structure along the perturbed region, allowing us to engineer a regions surrounded by minigaps where a confined mode is supported in a similar fashion as in a quantum well.

3.1 Superlattice band structure

In order to introduce the concept of an acoustic local band structure we are first going to address the case of a superlattice band structures. In this section, we describe the dependence of the dispersion relation of periodic structures on the structural parameters defining them. Let us consider a superlattice formed by concatenating layers of *GaAs* and *AlAs*. Given the angular frequency as $\omega = 2\pi f$ and the wavevector q of the superlattice, its dispersion relation given by equation 2.41 and can be expressed as [62]

$$\begin{aligned} \cos(qd) &= \cos\left(\frac{\omega d_{AlAs}}{v_{AlAs}}\right)\cos\left(\frac{\omega d_{GaAs}}{v_{GaAs}}\right) \\ &\quad -\frac{1}{2}\left(\frac{\rho_{AlAs}v_{AlAs}}{\rho_{GaAs}v_{GaAs}}+\frac{\rho_{GaAs}v_{GaAs}}{\rho_{AlAs}v_{AlAs}}\right)\sin\left(\frac{\omega d_{AlAs}}{v_{AlAs}}\right)\sin\left(\frac{\omega d_{GaAs}}{v_{GaAs}}\right) \end{aligned} \tag{3.1}$$

where ρ_{AlAs} and v_{AlAs} (ρ_{GaAs} and v_{GaAs}) are the *AlAs* (*GaAs*) mass density and the speed of sound for LA phonons, respectively [63, 94]. d_{AlAs} (d_{GaAs}) is the geometric thickness of each layer of *AlAs* (*GaAs*) and $d = d_{AlAs} + d_{GaAs}$ the period of the structure i.e. the unit cell thickness. Minigaps can be opened centered at frequencies that fulfill the following condition: the accumulated phase acquired by a wave propagating through each cell is equivalent to half a wavelength or an integer multiple of it. In order to exemplify this, let us consider three superlattices with different cell configurations where depending on the cell characteristics different minigaps are either opened or closed.

Figure 3.2 presents a schematic representation of three different superlattices and their corresponding band structures. In panel (a), the superlattice depicted is formed by concatenated *GaAs* and *AlAs* layers, where all layers have thicknesses such as an acoustic wave traversing each of them acquires the same phase due to propagation i.e. $d_{GaAs}/(v_{GaAs}/f) = d_{AlAs}/(v_{AlAs}/f)$ where d_{GaAs} and d_{AlAs} are the *GaAs* and *AlAs* layer thicknesses, respectively, and f is the frequency of the acoustic wave propagating through the stack of layers. Let us define $f_\lambda = v_{GaAs}/(2d_{GaAs}) = v_{AlAs}/(2d_{AlAs})$ which is the frequency at which an acoustic wave propagating through one unit cell acquire a 2π phase. Then, f_λ is the frequency at which one wavelength fits in each unit cell which is formed of two consecutive layers. As stated above, minigaps can appear at frequencies able to fit multiples of half a wavelength in each cell i.e. for frequencies $\frac{m}{2}f_\lambda$ where m takes positive integer values. On the right side of panel (a), the dispersion relation associated to the superlattice is plotted and we can see minigaps centered at frequencies $0.5f_\lambda$ and $1.5f_\lambda$, while no minigap appeared at f_λ. In order to simplify future discussions, we will identify this kind of superlattice as ($\lambda/2$,$\lambda/2$) [1]. Figure 3.2 panels (b) and (c) present two different superlattices where each unit cell extends along one wavelength at f_λ. In contrast with the ($\lambda/2$,$\lambda/2$) superlattice, for these, the layers forming the cells contribute differently to

---

[1] Notice that the notation used is different from common practices where the ($\lambda/2$,$\lambda/2$) superlattice we have described is named $\lambda/4$,$\lambda/4$ superlattice. This discrepancy comes from the fact that our reference frequency for this notation f_λ is defined relative to the unit cell thickness and not the frequency where the first minigap appears i.e. $0.5f_\lambda$.

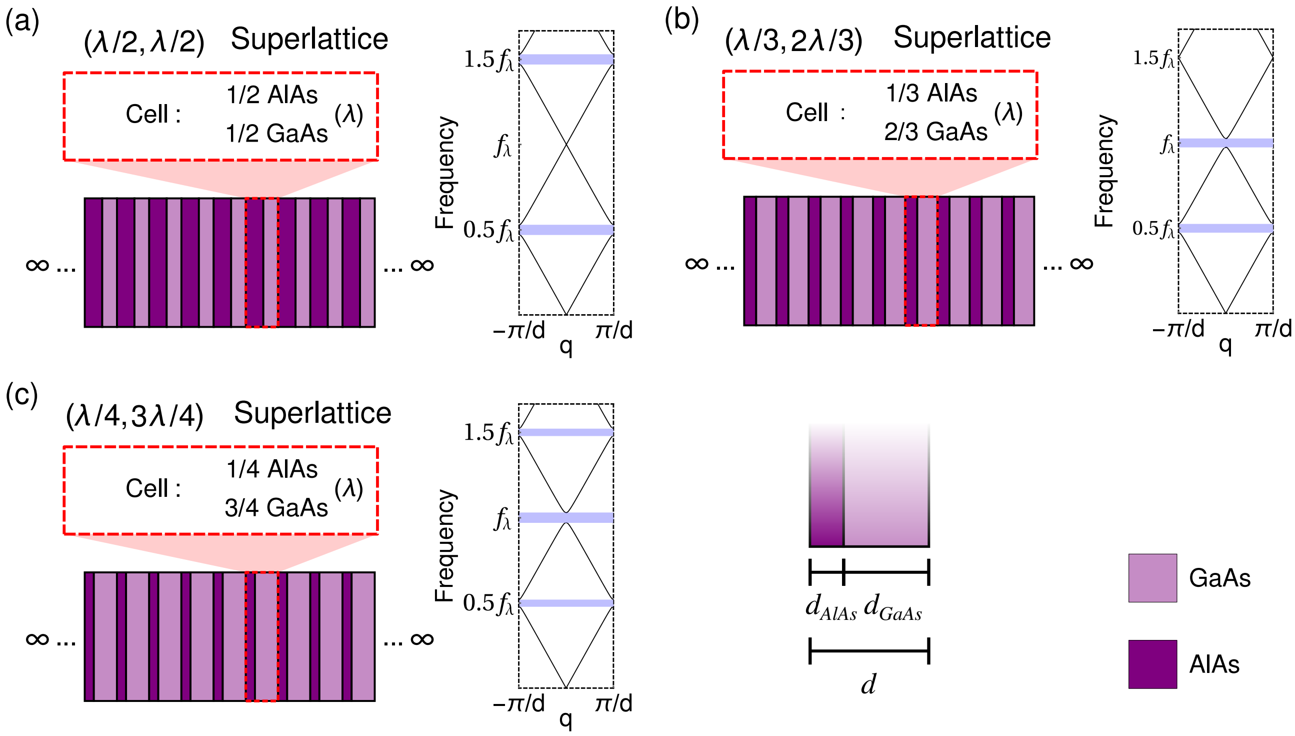

Figure 3.2: (a) Left: Superlattice built of cells formed by $AlAs$ and $GaAs$ layers of 1/2 wavelength thickness each one. Right: Dispersion relation showing how the second minigap at f_λ is closed for this kind of superlattice. (b) Left: Superlattice built of cells formed by $AlAs$ and $GaAs$ layers with thicknesses of 1/3 and 2/3 of a wavelength respectively. Right: Its dispersion relation showing how the third minigap at $1.5f_\lambda$ is closed. (c) Left: Superlattice built of cells formed by $AlAs$ and $GaAs$ layers with thicknesses of 1/4 and 3/4 of a wavelength respectively. Right: Dispersion relation of such a superlattice. Arrows point to single cells showing in red the displacement profile of an acoustic wave propagating at $0.5f_\lambda$, f_λ and $1.5f_\lambda$.

the 2π phase acquired by an acoustic wave traversing each cell. For the superlattices depicted in panel (b), the $AlAs$ layer in each unit cell accounts for a $\frac{1}{3}2\pi$ phase and the $GaAs$ layer for $\frac{2}{3}2\pi$. For panel (c), the $AlAs$ layer in each unit cell accounts for a $\frac{1}{4}2\pi$ phase and the $GaAs$ for $\frac{3}{4}2\pi$. Extending the notation used for the previous case, panel (b) and panel (c) structures correspond to $(\lambda/3,\ 2\lambda/3)$ and $(\lambda/4,\ 3\lambda/4)$ respectively. From the three superlattices presented in Fig. 3.2 we can see how the ratio between the two materials used in each cell controls the opening and closing of all minigaps. The superlattice $(\lambda/3,\ 2\lambda/3)$ band structure in panel (b) presents minigaps centered at frequencies $0.5f_\lambda$ and f_λ while no minigap and instead a band crossing occurs at $1.5f_\lambda$. In contrast, the superlattice $(\lambda/4,\ 3\lambda/4)$ in panel (c) shows minigaps at $0.5f_\lambda$, f_λ and $1.5f_\lambda$. On the right, we can see the sketch of an individual cell of this superlattice showing the parameters d, d_{AlAs} and d_{GaAs} which are the thickness of the unit cell, the $AlAs$ layer and the $GaAs$ layer, respectively.

The notation we have adopted to represent each superlattice is based on the phase a wave acquires by propagating through the layers forming one of its unit cells. This means that for the $(\lambda/4,3\lambda/4)$ superlattice, for example, the phase contribution of the $AlAs$ layer is 1/4 of the total phase acquired along the full unit cell, for a wave at frequency f_λ. This does not imply that the thickness ratio between layers is 1/4 (or 3/4). The reason is that it is not the geometric thickness that matters for this ratio but the acoustic one. For this purpose we define as new variables the acoustic thickness of each of the layers in an $AlAs/GaAs$ superlattice as $D_{AlAs} = d_{AlAs}/\lambda_{AlAs}$ and $D_{GaAs} = d_{GaAs}/\lambda_{GaAs}$ for $AlAs$ and $GaAs$ layers respectively. Then, the superlattice notation adopted can be in general stated as $(D_{AlAs}\lambda, D_{GaAs}\lambda)$. For future references in this work, we maintain the definition of acoustic thickness as already used, i.e. measured in units of the wavelength of an acoustic wave at frequency f_λ.

Following the idea of defining variables in terms of acoustic thicknesses we define two parameters to control the minigaps bandwidth and position independently: The total acoustic thickness of one cell

$$D = D_{AlAs} + D_{GaAs} \tag{3.2}$$

and the ratio between the acoustic thickness of one *AlAs* layer and the total acoustic thickness of one cell

$$r = \frac{D_{AlAs}}{D_{cell}}. \tag{3.3}$$

Using these new parameters we can rewrite equation 3.1 as

$$\cos(qd) = \cos\left(\frac{\omega D}{f_\lambda}\right) - \frac{\epsilon^2}{2}\sin\left(\frac{\omega r D}{f_\lambda}\right)\sin\left(\frac{\omega(1-r)D}{f_\lambda}\right) \tag{3.4}$$

with

$$\epsilon = \frac{Z_{GaAs} - Z_{AlAs}}{(Z_{GaAs}Z_{AlAs})^{1/2}} \tag{3.5}$$

where $Z_{GaAs} = \rho_{GaAs}v_{GaAs}$ and $Z_{AlAs} = \rho_{AlAs}v_{AlAs}$ are the acoustic impedance of *GaAs* and *AlAs*, respectively.

Equation 3.4 gives the dispersion relation for an *AlAs/GaAs* superlattice formed by concatenating identical cells of D acoustic thickness (measured at frequency f_λ) with r as the acoustic thickness ratio of *AlAs* in the unit cell. On its right hand side two terms contribute in different proportion depending on the magnitude of $\epsilon^2/2$. The constant ϵ accounts for the acoustic impedance contrast between the superlattice materials by measuring the difference between their impedances normalized by the geometric average. For *AlAs* and *GaAs* this constant is relatively small with $\epsilon^2/2 \sim \mathcal{O}(10^{-2})$, although this order of magnitude is not uncommon for superlattices made of IV, III-V, or II-VI compounds [62]. As a result, the main contribution on the right hand side of equation 3.4 comes from the first term, independent of ϵ and r. Taking this into consideration and neglecting the second term we obtain

$$\cos(qd) = \cos\left(\frac{\omega D}{f_\lambda}\right) \tag{3.6}$$

$$qd = \pm\frac{\omega D}{f_\lambda} + \nu 2\pi \qquad \text{for} \qquad \nu = 0, \pm 1, \pm 2 \ldots \tag{3.7}$$

as a rough approximation of the dispersion relation accounting for the superlattice periodicity while neglecting the effects of the impedance mismatch between materials. Figure 3.3 (a) shows both the band structure corresponding to this approximation (dashed orange) and the real one (solid black). As can be seen, the minigaps appears as a consequence of the impedance mismatch [62].

We can further analytically study the minigap opening by solving equation 3.4 at the Brillouin zone center and edge using a second order approximation. For this purpose, we consider $\omega = \Omega + \Delta\Omega$ where $\Omega = \frac{m}{2} f_\lambda$ with m being a positive integer and corresponding to the minigaps central frequencies ($0.5f_\lambda$, f_λ, $1.5f_\lambda$, ...). The dispersion relation thus reads [62]

$$\eta = \cos\left(\frac{(\Omega+\Delta\Omega)D}{f_\lambda}\right) - \frac{\epsilon^2}{2}\sin\left(\frac{(\Omega+\Delta\Omega)rD}{f_\lambda}\right)\sin\left(\frac{(\Omega+\Delta\Omega)(1-r)D}{f_\lambda}\right) \tag{3.8}$$

where η is $+1$ for the zone center solutions and -1 for the edge ones. Keeping only terms up to the second order on $\Delta\Omega$ we obtain

$$\Delta\Omega \approx \frac{f_\lambda}{D}|\sin(m\pi r)|\epsilon \tag{3.9}$$

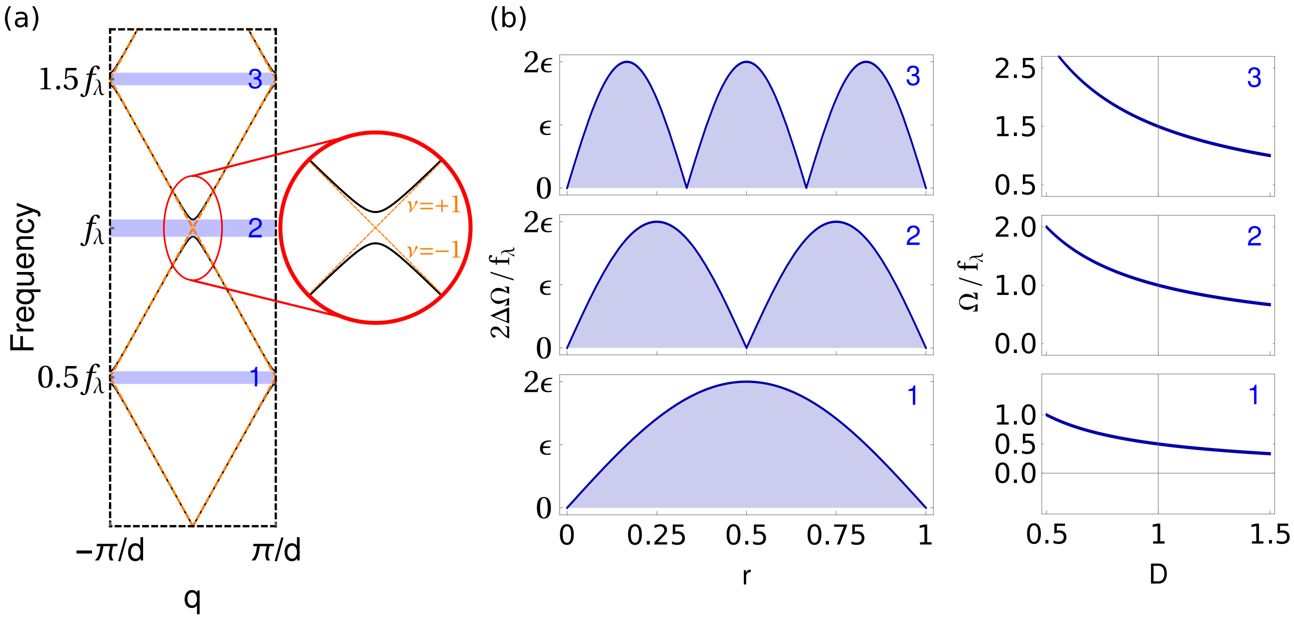

Figure 3.3: (a) Dispersion relation (black) and its approximation only considering periodicity (orange) for a $(\lambda/4, 3\lambda/4)$ superlattice. Highlighted in red, a zoom in the second minigap at f_λ shows the values of ν around it. (b) Left: Minigaps bandwidth normalized to f_λ as a function of the parameter r. Right: Minigaps center frequency normalized to f_λ as a function of the parameter D [62, 125].

where m is an integer that labels the minigaps taking odd (even) values at the zone edge (center). Figure 3.3 (b) left panel shows the first, second and third minigap opening and closing by plotting their bandwidth $2\Delta\Omega$ as a function of r for a superlattice with unit cell thicknesses of one wavelength at f_λ, i.e. $D = 1$. If instead we focus on the minigap central frequency, we can show it shifts as a function of the parameter D since it scales the whole system proportionally. Figure 3.3 (b) right panel presents the minigap central frequency Ω as a function of D.

As we have seen, the parameters r and D allow us to tune the bandwidth and position of the minigaps. They serve as knobs and let us control the propagation of phonons along multilayered structures. Until here, all the structures considered have been periodic with both r and D parameters fixed. In the following section we describe structures where these parameters change along the multiple layers. These devices are similar to superlattices in the sense that phonon propagation is controlled by band structures, but distinctively they are not periodic nor do they present a single band structure.

3.2 Local band structure

The study of phonons propagation plays an important role for several fields like nanoelectronics [126–128], cavity optomechanics [70, 129, 130] and quantum technologies [131, 131, 132]. Designing resonators capable of confining phonons offers the possibility to control their density of states and allows us to shape the spatial profile of the confined modes to engineer the interaction between phonons and other particles like photons and electrons [22, 122, 133]. In this section we introduce the control of phonon propagation by designing quasi periodic structures where the unit cell parameters r and D are modulated adiabatically along them. As a quantitative reference we designed structures with an overlap between consecutive local minigaps above 90% (with our design of a band structures we always target a specific minigap for which $P_{adiabatic} > 0.9$). We show through simulations how, by introducing an adiabatic modulation perturbing a superlattice design, we can control the propagation of phonons and engineer acoustic resonators. We propose that band structures are present even if we relax the

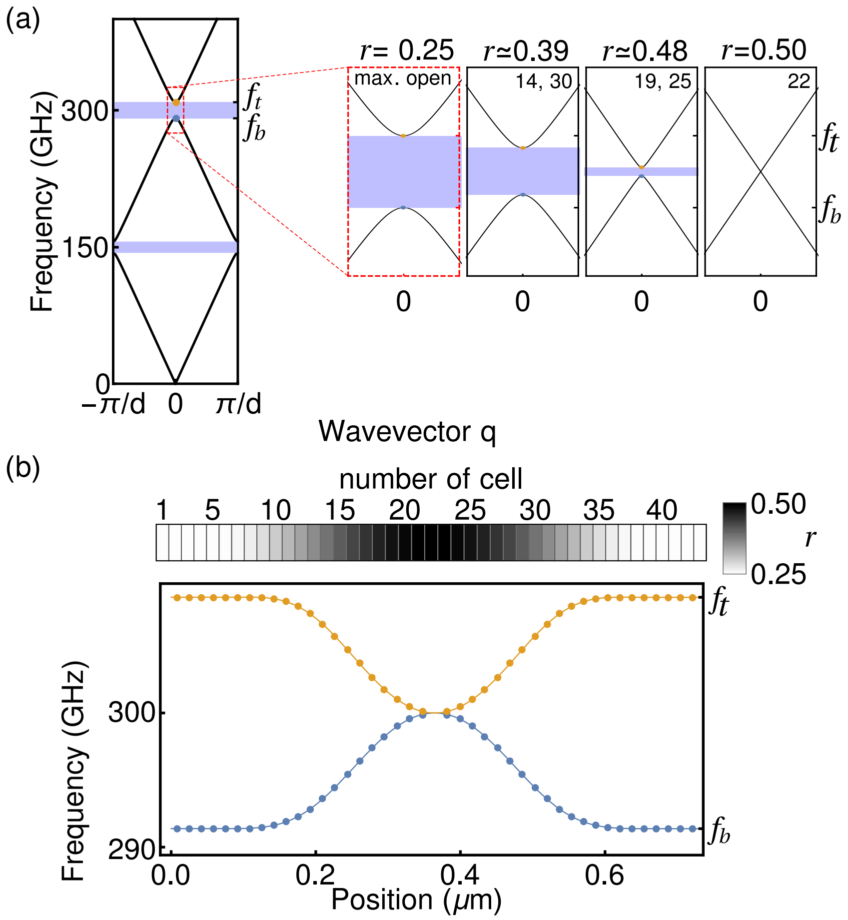

Figure 3.4: (a) Left: Acoustic band structure for an $r = 0.25$ and $D = 1$ superlattice at $f_\lambda = 300$ GHz (i.e. $(\lambda/4, 3\lambda/4)$). Right: Zoom-in around the band structure second minigap (dashed red rectangle). Next to it on the right, zoom-ins in the same region, but showing how the minigap changes for $r \approx 0.39$, $r \approx 0.48$ and $r = 0.5$ corresponding to the cells 14 and 30, 19 and 25, and 22 of the adiabatic structure in panel (b), respectively. (b) Top: Schematic of the adiabatic structure cell parameter (r) modulation. The minigap goes from maximally open ($r = 0.25$) to a completely closed ($r = 0.5$) in the middle and then back ($r = 0.25$) along the structure following a $\sin^2$ shape. Bottom: Local band structure of the presented adiabatic resonator. The minigap edges for each cell are plotted as a function of position. Each vertically aligned pair of dots corresponds to the minigap edges associated with each cell and plotted at each cell center. The solid curves show the continuous trajectory targeted for each edge.

condition of all unit cells being the same in a superlattice. Each of these local band structures is defined by the unit cell parameters of the cell to which the local band structure is assigned and those of its nearby cells (see figure 3.1). Whether this is a strong assumption or not depends on how progressive is the modulation of the unit cells parameters. This is in some sense analogous to the fact that superlattice band structures are present in real multilayer devices under the assumption that there is a large enough number of unit cells with the same parameters. The equations we are using are formulated under the assumption of an infinite multilayer structure. To account for this, real implementations of superlattices like DBRs need to use a sufficiently large number of cells to control the propagation of phonons due to multiple interference phenomena. The total number of cells required for this purpose may vary depending on the application, but DBRs with less than 20 cells are not uncommon. Motivated by such a strong relaxation of an assumption (from infinite unit cells to 20 periods) we propose to relax the periodicity assumption by progressively changing the unit cell parameters along the structure. We implement an adiabatic tuning of the parameters r and D along the unit cells of a superlattice. The resulting structure is quasiperiodic, but designed such as for each cell there is a large enough amount of similar cells nearby producing a locally tuned superlattice behavior, i.e. a local band structure.

To construct the adiabatic structure we consider a superlattice and target our design to one of its minigaps. Let us take the $(\lambda/4, 3\lambda/4)$ superlattice structure as the starting point having unit cells with one wavelength of thickness at the frequency $f_\lambda = 300$ GHz. This corresponds to unit cell parameters $r = 0.25$ and $D = 1$ at $f_\lambda = 300$ GHz. Our design will target its second minigap. Figure 3.4 (a) left shows the acoustic band structure for this superlattice, in red we see a zoom in around the second minigap which for this set of parameters ($r = 0.25$) is maximally open (see figure 3.3 (b) middle left panel). Blue and orange dots mark are the top and bottom edges of this minigap at frequencies $f_t \approx 309$ GHz and $f_b \approx 291$ GHz, respectively. On the right of the zoomed in region we show three more cases for values of $r \approx 0.39$, $r \approx 0.48$ and $r = 0.5$.

We start with a 33 cells $(\lambda/4, 3\lambda/4)$ DBR and then break its periodicity by progressively altering its cell parameters along the full structure. Figure 3.4 (b) top shows a schematic of how this progressive modulation varies along the cells. For this particular example, we consider an adiabatic structure where we alter only the parameter r while leaving D unaltered. The modulation is done such that r varies from $r = 0.25$ (second minigap maximally opened) on one extreme to $r = 0.5$ (closed) in the middle and then back to $r = 0.25$ (maximally opened again) in the other extreme resulting in a symmetric structure. The modulation of the parameter r is done progressively following a $\sin^2$ shape. Additionally, five unaltered cells are added on the modulation extremes such that all cells throughout the structure have enough cells with similar parameters nearby. With this addition to the group of 33 altered unit cells (odd quantity so we have a closed minigap in the middle) we end up with a 43 unit cell structure. Figure 3.4 (b) bottom shows the local band structure for this device. The figure is built by plotting the top an bottom (second) minigap edges for each cell along the structure, the solid line shows the analytical expression for the targeted continuous variation, notice how at the center cell the minigap is completely closed therefore no points are plotted.

The resulting local band structure shares similarities with its electronic counterpart for the case of a quantum well (see figure 3.1 (a)). In a quantum well, confinement occurs at a region surrounded by band gaps that forbid the propagation of electrons for a given range of energies. These gaps appear as a consequence of the crystal lattice structure of solid-state materials. By concatenating layers of different materials i.e. different kinds of crystal lattices, quantum wells can be fabricated. In the acoustic local band structure presented in figure 3.4, minigaps are present at the extremes of the structure while absent in the middle following a progressive closure towards it. The acoustic local minigaps result from a collective behavior of nearby cells at each specific position of the structure. In the following section, we show how this approach to shape a local band structure along a device can be used for confinement purposes i.e. for the engineering of acoustic phononic resonators.

3.3 Phonon confinement in adiabatic structures

In this section, we present a phenomenological approach to confine acoustic phonons in adiabatic structures. The resulting resonators are studied by using a transfer matrix method algorithm to simulate the acoustic reflectivity and displacement distribution. The idea of an adiabatic alteration in a periodic structure for confinement purposes is not new. In optics, this approach has been demonstrated in different platforms for the design of optical cavities that 'gently' couple light into a confined mode exhibiting high quality factors while maintaining low modal volumes [134–138]. The structures presented in this chapter, are inspired by the work of Fabrice Lamberti et al. [72] to extend the adiabatic confinement approach to the acoustic domain at extremely high frequencies.

In the previous section, we have demonstrated how to tune the local band structure along a superlattice by varying its unit cell parameters r and D to control the bandwidth and position of a chosen minigap. In this section, we will deal with adiabatic structures where only one of the unit cell parameters is changed, either r or D. The resulting local band structures in one case maintain fixed the center of the minigap while changing its bandwidth and in the other shift its center while approximately preserving its bandwidth.

3.3.1 Acoustic potential wells

In semiconductor physics, quantum wells and superlattices have been largely exploited for multiple applications like light emitting diodes [139, 140], cascade lasers [141] and photodetectors [142–144]. The capabilities to design a structure where contiguous regions have different electronic bandgap energies have provided control over the emission wavelength in semiconductor optoelectronic devices [145]. In this section, we present a phononic adiabatic structure engineered to mimic the behavior of a quantum well potential. Phonons do not have charge, but the acceleration effect proper of a potential is implemented by adiabatically tuning the unit cells of a superlattice modifying the local group velocity along the structure. The adiabatic structure operates as a resonator featuring two confined modes in a similar fashion as electron and holes are trapped in semiconductors quantum wells.

In order to clarify the comparison between the different resonators of this chapter, in addition to its description, we will summarize the design parameters and its main characteristics in one table per structure. Table 3.1 presents the 43 cells adiabatic structure, where the central 33 cells follow a $\sin^2$ modulation of the r parameter while for the other 10 outer cells it remains constant (as for a DBR). Along the modulated region the minigaps vary from being maximally open to closed and then reopened again in the same way as they were closed. The acoustics thickness D of each cell remains constant and equal to 1 along the full structure. Unless otherwise stated, the working frequency of all the studied resonators in this chapter is $f_\lambda = 300$ GHz and the targeted minigap is the second one, i.e. the first one appearing at the superlattice Brillouin zone center. The resulting structure has an overall size of $\approx 0.73\ \mu$m with layers thickness varying between 4.72 nm to 11.95 nm.

We simulate the acoustic response of the multilayer at different frequencies. The simulation is done using a standard transfer matrix method modeling the propagation of acoustic waves in the structure as presented in section 2.2.1.

We have chosen centro-symmetric unit cells with a central layer of $GaAs$, in contrast with previous examples showing bi-layer unit cells (see figure 3.2). This change of unit cell design is done to ensure having a programmatic way to compare symmetries of different confined modes. Note that both the original superlattice as well as the design parameters are independent from this cell characteristic. Figure 3.5 (a) right presents the reflectivity as a function of frequency.

Acoustic potential wells (43 cells)			
	Region 1	Region 2	Region 3
Number of cells (N)	5	33	5
r	0.25	$0.25(1+\sin^2(\frac{n}{N+1}\pi))$ for $n \in [1, N]$	0.25
D	1	1	1
Minigap bandwidth	Maximal	Modulated	Maximal
Minigap center	Fixed	Fixed	Fixed
Is periodicity broken?	No	Yes	No

Table 3.1: Summary of the design used for the 43 cells acoustic potential wells structure. The index n corresponds to the number of cell in a given region counted from left to right, in this case varying from 1 to 33. The n dependent function in region 2 gives the r value for the n-th cell in this region.

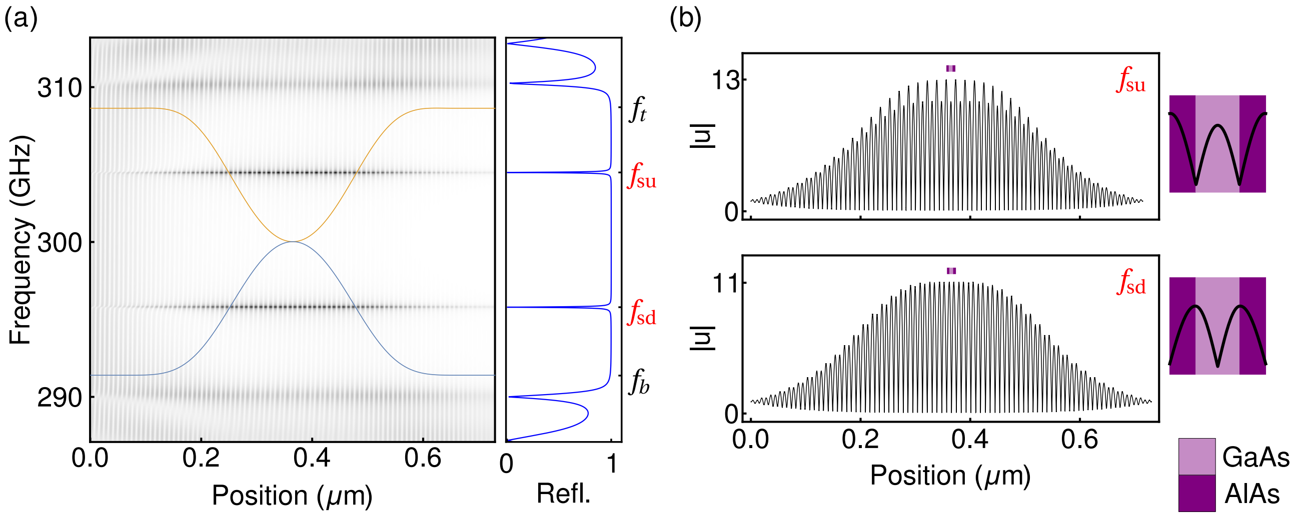

Figure 3.5: (a) Left: Color coded displacement amplitude as a function of position and frequency for the acoustic potential wells resonator. Over it, its local band structure is plotted. Right: Resonator acoustic reflectivity. Top and bottom edges of the maximally opened minigap are labeled as f_t and f_b, respectively. Two reflectivity dips corresponding to acoustic resonances at f_{su} and f_{sd} are identified. (b) Top: Displacement amplitude as a function of position plotted for the resonant frequency f_{su}. Bottom: Displacement amplitude as a function of position plotted for the resonant frequency f_{su}. Right: For each resonant frequency the displacement amplitude in the central cell is shown.

The original ($\lambda/4$,$3\lambda/4$) superlattice stop band can be identified as the high reflectivity region spanning from f_b to f_t, the bottom and top edges of the original minigap, respectively. As signature of confined modes, two reflectivity dips can be identified at frequencies $f_{sd} \approx 295.8$ GHz and $f_{su} = 304.4$ GHz with quality factors of ≈ 3200 and ≈ 3800, respectively[2]. Figure 3.5 (a) left shows in a grayscale the amplitude of the displacement field as a function of both the position along the structure and the frequency of the acoustic wave propagating through it. We can see how large displacements occur at the resonant frequencies f_{sd} and f_{su}. On top of the color map, the local band structure is shown as solid lines, using them as a guide to the eye we notice that at the resonant frequencies the mode is confined within the modulated region. Horizontal slices of the color map are plotted for resonant frequencies in figure 3.5 (b) top and bottom panels. These are the displacement profiles $|\mu|$ at frequencies f_{sd} (bottom) and f_{su} (top). In both cases, the mode appears confined in the modulated region with exponentially decaying tails towards the exterior. While both modes have a similar envelope function their overall spatial function presents opposite symmetries. These mode symmetries coincide with the symmetries of the Bloch modes at the minigap edges confining the mode. In order to evidence these opposed symmetries, the displacement along the central cell is depicted on the right of each plot in panel (b). The usage of a the three-layer cells allow us to systematically compare the symmetries of the modes by monitoring the displacement value at the middle of the central cell. Its position with respect to displacement profile shown in panel (b) is shown by the inset on top of each curve plotted.

The acoustic potential well features a similar behavior as a quantum well in the sense that there are two confined modes, one on each side of the local band, however, we must remark that in the current case both are phononic modes, i.e. they trap the same (quasi) particle. In contrast, its electronic counterpart traps electrons on one side and holes in the other one. In addition, the charge of both electron and hole attract each other, an aspect completely absent for phonons in acoustic potential wells, where the distinctive factor beside the frequency of confinement is the spatial symmetry of the mode. The considered resonant

---

[2] Quality factors are calculated by dividing the resonant frequency by the FWHM associated to the resonant reflectivity dip.

frequencies around 300 GHz imply wavelengths on the scale of tens of nanometers (in *GaAs* roughly 16 nm). Consequently, the layers of the acoustic potential well structure are extremely thin in comparison with near infrared optical wavelengths. These multilayer devices thus act as an effective medium for light in such spectral range which make them compatible with already demonstrated so-called Matryoshka structures, where the acoustic resonator acts as a spacer for an optical cavity, enhancing optomechanical interactions [60, 72, 146].

3.3.2 Acoustic single-sided potential well

Adiabatic structures offer a 'gentle' way to couple acoustic waves into a confinement region. This approach has been exploited using optical waves too. For example, micropillar cavities have been fabricated where, by scaling a few unit cells within a central region of a multilayer structure, losses through the sides have been reduced [136, 147, 148]. The design principles used in this chapter are compatible with multilayers structures grown by MBE and then shaped into micropillar or similar three dimension structures by inductively coupled plasma etching. In this section we present an adiabatic resonator featuring an acoustic adiabatic band structure resulting from altering the unit cell acoustic length D while maintaining the acoustic ratio between materials r constant along the structure. As in the previous resonator, this different acoustic structure also creates a region surrounded by local minigaps. This is achieved by shifting a fully opened minigap at the center of the structure and results in an adiabatic resonator supporting a confined acoustic mode. Fabrice Lamberti et al. [72] experimentally demonstrated the presence of confined modes at frequencies around 350 GHz through Raman spectroscopy. Here, we include the description of this resonator using the variables r and D. We simulate the resulting structure and, in the following chapter, we experimentally investigate the resonator using a pump and probe technique.

The design parameters for this resonator are presented in table 3.2. A central region of 13 modulated cells is surrounded by two regions of 8 unperturbed cells each. The cells in the modulated region scaled up towards the center of the structure. Its central cell is the thickest one with 6% more acoustic thickness than the original superlattice cell. This size modulation is done progressively following a $\sin^2$ shape as shown in table 3.2 (D row, region 2 column). The parameter $r = 0.25$ remains unaltered along the full structure. The total size of the structure is ≈ 0.49 μm and layer thicknesses range from 4.72 nm to 12.63 nm.

Figure 3.6 (a) right shows the reflectivity as a function of frequency of the adiabatic structure. A stop band between f_b and f_t is distinguished, in it, a dip in reflectivity at $f_a \approx 300$ GHz shows a confined mode with a quality factor ≈ 1400. On the left, the displacement as a func-

Acoustic potential one-sided well (29 cells)			
	Region 1	Region 2	Region 3
Number of cells (N)	8	13	8
r	0.25	0.25	0.25
D	1	$(1 + 0.06\sin^2(\frac{n}{N+1}\pi))$ for $n \in [1, N]$	1
Minigap bandwidth	Maximal	Maximal	Maximal
Minigap center	Fixed	Modulated	Fixed
Is periodicity broken?	No	Yes	No

Table 3.2: Summary of the design used for the 29 cells acoustic potential one-sided well structure. The index n corresponds to the number of cell in a given region counted from left to right, in this case varying from 1 to 13. The n dependent function in region 2 gives the D value for the n-th cell in this region.

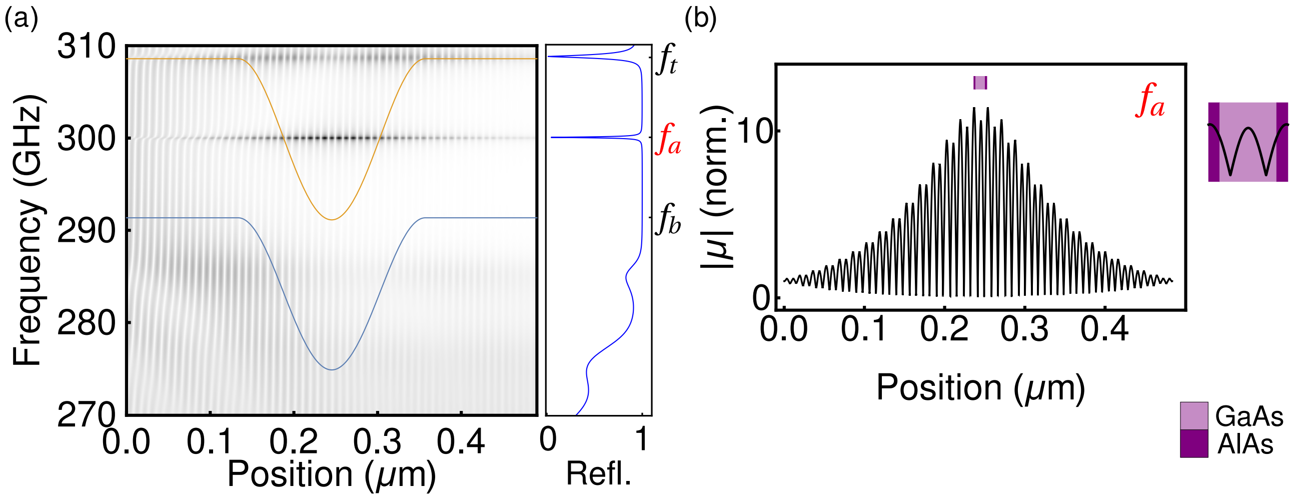

Figure 3.6: (a) Left: Color coded displacement amplitude as a function of position and frequency for one-sided well adiabatic resonator. Darker regions represent higher intensities of displacement. Over the color map, the local band structure is plotted. Right: Resonator acoustic reflectivity. Top and bottom edges of the maximally opened minigap are labeled as f_t and f_b, respectively. One reflectivity dip corresponding to an acoustic resonances at frequency f_a is identified. (b) Left: Displacement amplitude as a function of position plotted for the resonant frequency f_a. Right: The symmetry of the confined mode is evidenced by plotting it displacement profile within the central cell.

tion of position and frequency is plotted in grayscale. As in the case of the previous resonator (acoustic potential wells structure), the confined mode appears localized in the modulated region. Plotted on top, the local band structure shows that the modulation up to 6 % in acoustic cell thickness results in a shift of around one full bandwidth of the minigap creating a one-sided well. Figure 3.6 (b) left panel presents the displacement amplitude $|\mu|$ as a function of position for an acoustic wave propagating at the resonant frequency f_a. On the right, the displacement amplitude in the central cell is plotted. As a guide to the eye, on top of the full displacement profile, the central cell is depicted with its thickness scaled accordingly to the position axis. The symmetry exposed in the displacement profile within the central cell matches the one of the Bloch modes at the minigap high frequency side (yellow) of the local band structure, i.e. the side confining the resonant mode.

The adiabatic resonator acts in a similar way as a potential well. The deeper we make the perturbation, the more modes enter the confinement region. Actually, for this set of parameters, we can see in figure 3.6 (a) how a dip at high frequencies (approximately at f_t) appears near the minigap region. While not shown here, if the perturbation is increased (reduced) from 6% we would see the dip near f_t shifting towards lower (higher) frequencies, entering (leaving) the high reflectivity region.

The acoustic potential single-sided well structure introduced here is an example of how we can engineer local band structure for confinement purposes in different ways. In the adiabatic resonators the local band structure can be tuned not only in bandwidth but also spectrally.

3.3.3 Acoustic potential wells by band inversion

The adiabatic structures introduced here are based on the engineering of Bloch waves in superlattices [136–138, 149]. Here, we introduce a third resonator based on the modification of the parameter r along the adiabatic structure. Similar to the potential mimicking a quantum well, its local bands present two potential wells, one on each side of the local band (high and low frequency sides). In contrast, here we are going to modify the symmetry of the Bloch modes associated to their edges. The resulting local band structure has a very similar design to the acoustic potential wells structure since only the minigap bandwidth is modulated down to the closing point and then reopened towards the extremes of the structure. The distinction lies in the fact that the minigap is not reopened in the same way as it was closed. Instead, the ratio between materials is exchanged causing an exchange of the spatial symmetries of the Bloch modes on the minigap edges known as band inversion [150–152]. The election of targeting our adiabatic design to the second minigap is motivated by the fact that, as can been seen in 3.3 (b), there are two values of the unit cell parameter r for which this minigap is maximally opened, $r = 0.25$ and $r = 0.75$. These minigaps have the same central frequency and bandwidth, but their Bloch modes at the edges have opposed spatial symmetries. Recent works have demonstrated how resonators can be engineered by concatenating acoustic periodic structures with opposed symmetries in their Bloch modes [125, 153, 154]. Here, we introduce an adiabatic resonator where the acoustic ratio of the unit cells r of a superlattice varies progressively from $r = 0.25$ to $r = 0.75$, resulting in a local band structure where band inversion occurs progressively along the device.

Table 3.3 presents the design parameters for the resonator. Here, we have split the modulation along two regions, region 2 and 3. Along their cells the minigap closes and reopens. While similar to the acoustic potential wells structure, here the minigap reopening is implemented by a change in the acoustic ratio r from 0.5 (closed) up to 0.75 (opened). The parameterization of r along the structure is done using a $\sin^2$ function and ensuring continuity along all the regions. Regions 1 and 4 surround the modulated regions and have constant parameters matching the modulation regions extremes. The resulting structure, has the parameter r varying, from left to right, from 0.25 up to 0.5 in the middle cell and then keeps increasing up to 0.75 at the right extreme. At the design frequency $f_\lambda = 300$ GHz the total thickness of the structure is approximately 1.1 μm and the layer thicknesses vary from 3.98 nm to 14.15 nm.

Figure 3.7 (a) right presents the acoustic reflectivity of the structure. The high reflectivity region spanning from f_b to f_t presents now three reflectivity dips at frequencies $f_{ad} \approx 292.4$ GHz, $f_{am} \approx 300$ GHz and $f_{au} \approx 307.7$ GHz with quality factors of ≈ 10700, ≈ 298600 and ≈ 10400, respectively. On the left panel, the displacement amplitude as a function of position and frequency is plotted in grayscale. The modes confined at the upper (f_{au}) and lower (f_{ad}) sides of the local band structure are similar to those already presented in the two previous resonators. In contrast, the third mode (f_{am}) in the middle has a different nature. Figure 3.7 (a) left panel presents the local band structure as solid color lines. The color codes are used to represent the symmetry of the Bloch modes at the edge of the local minigaps. By doing so, we are including information that allows us to distinguish between the two cases when the minigap is maximally opened, i.e. for $r = 0.25$ and $r = 0.75$. When the r parameter transits between these two values the band edges swap symmetries, effectively resulting in an

Acoustic potential wells by band inversion (65 cells)				
	Region 1	Region 2	Region 3	Region 4
Number of cells (N)	16	17	16	16
r	0.25	$0.25(1+\sin^2(\frac{n}{N}\frac{\pi}{2}))$	$0.25(3-\cos^2(\frac{n}{N}\frac{\pi}{2}))$	0.75
D	1	1	1	1
Minigap bandwidth	Maximal	Modulated	Modulated	Maximal
Minigap center	Fixed	Fixed	Fixed	Fixed
Is periodicity broken?	No	Yes	Yes	No

Table 3.3: Summary of the design used for the 65 cells structure where acoustic potential wells including band inversion. The index n corresponds to the number of cell in a given region counted from left to right, in this case varying from 1 to 17 (16) for region 2 (3). The n dependent functions in region 2 and 3 give the r value for the n-th cell in these regions.

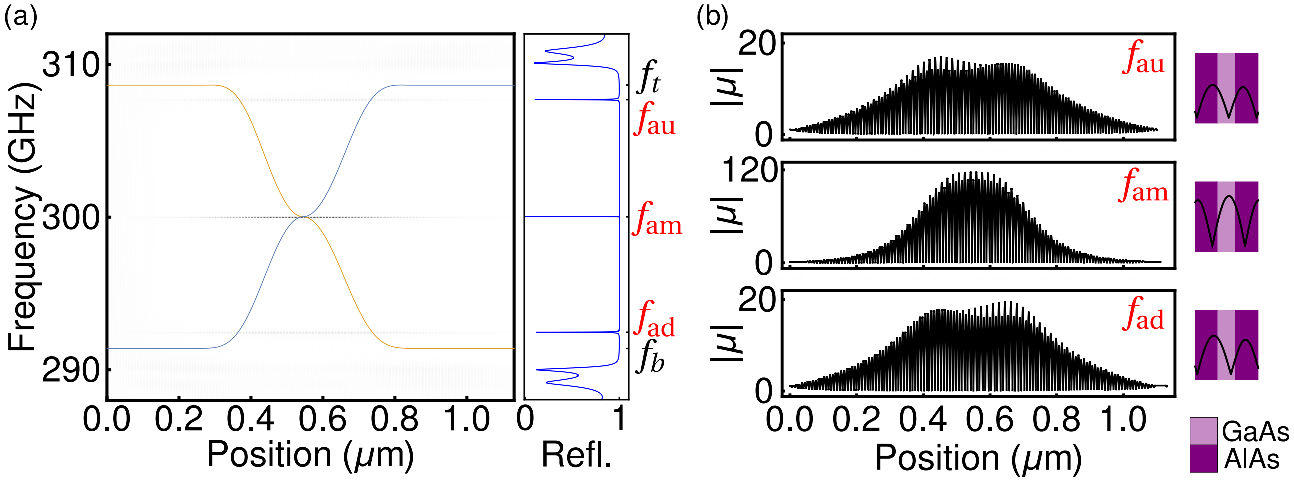

Figure 3.7: (a) Left: Color coded displacement amplitude as a function of position and frequency for the acoustic potential wells by band inversion structure. Over it, its local band structure is plotted. Right: Resonator acoustic reflectivity. Top and bottom edges of the maximally opened minigap are labeled as f_t and f_b, respectively. Three reflectivity dips corresponding to acoustic resonances at f_{au}, f_{am} and f_{ad} are identified. (b) Top: Displacement amplitude as a function of position plotted for the resonant frequency f_{au}. Middle: Displacement amplitude as a function of position plotted for the resonant frequency f_{am}. Bottom: Displacement amplitude as a function of position plotted for the resonant frequency f_{au}. Right: For each resonant frequency the displacement amplitude is plotted in the central cell.

addition frequency for which the resonance condition is fulfilled. In this case the mode is not located in a spacer, but it spans along the modulated region because the band inversion, which causes the resonance, is happening progressively along the structure. This, however, is not a necessary condition and previous works have demonstrated interface states resulting from the abrupt exchange of symmetries [125, 154]. Figure 3.7 (b) left presents from top to bottom the displacement amplitude profile along the structure for the resonances at f_{au}, f_{am} and f_{ad}. We can distinguish how the confined mode at f_{am} is different from the other two. The mode is confined in the modulated region while exponentially decaying towards the outside. The other two resonances at f_{au} and f_{ad} have envelopes with two local maxima, contrasting with the single one of the f_{am} mode. In addition, we observe a difference between the peaks near different local maxima of the envelope function. For the mode at f_{au} the left side shows high but less dense peaks in contrast with the right side of the mode. For the mode at f_{ad} the same can be distinguished but inverted from left to right. The reason for this difference is related to the modes symmetries. As we saw for the acoustic potential wells structure, the modes inherit symmetries of the local band edge that confines them. In this case, each side of the confinement region presents a different symmetry, resulting in a competition between these two symmetries along the structure (compare against 3.5 (b)). On the right of each plot in 3.7 (b) the displacement amplitude is plotted in the central cell. A common characteristic among the three cases is a shift of the central (anti) node towards the right, this can be attributed to the imbalance caused by not having a symmetric structure. Apart from this slight shift of the displacement profiles, the mode at f_{am} can be identified as symmetric and the other two (f_{ad} and f_{au}) as antisymmetric based on the central layer hosting either a node or antinode (see Fig. 3.7 (b) right).

The acoustic potential well by band inversion shares common characteristics with an electronic quantum well. Confinement occurs on both sides of the local band structure as in the case of electron and hole trapping. In the acoustic case an additional confined mode appears at the center of the minigap caused by the band inversion along the structure. It has been shown that the band inversion concept is closely related to a change in topological invariants associated to superlattices bands [150, 151]. Interface states confined in a similar way have

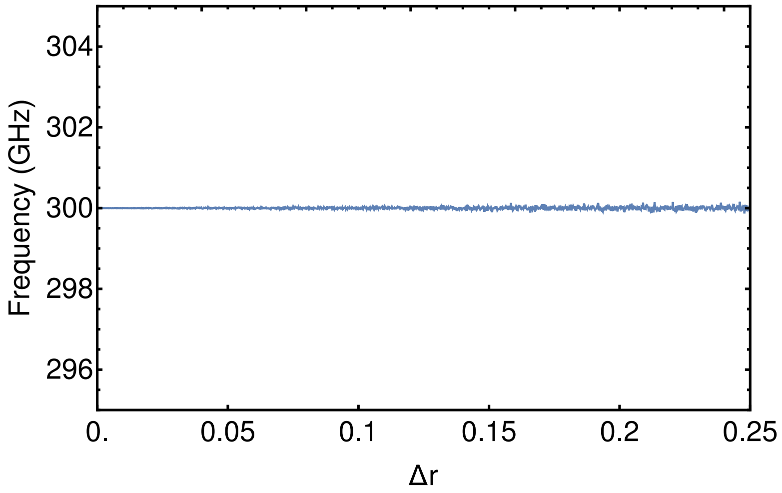

Figure 3.8: Evaluation of the adiabatic resonator by band inversion under the presence of noise in the acoustic ratio of each cell r. Each cell was subject to an alteration of its parameter r by a random number going from 0 to Δr. The plot presents the central resonant frequency f_{am} of the perturbed adiabatic resonators as a function of Δr.

shown robustness to random fluctuations that locally change the bandwidth of the minigap confining it, but leaves its central frequency fixed [125]. We evaluated the robustness of the adiabatic resonator introduced in this section under the presence of the same kind of noise, i.e. by modulating the acoustic ratio of $AlAs$ r. For the presented adiabatic structure, the main difference with respect to these previous reports is the fact that the band inversion is implemented progressively rather than abruptly at a single interface. We simulated perturbed versions of the adiabatic resonator where we vary the acoustic ratio r in each cell by a random parameter randomly chosen from a uniform distribution going from 0 to Δr. We increase the Δr from 0 to 0.25 in order to always remain with cell with realistic parameters, i.e. to ensure that the r parameter of each cell always remains between 0 and 1. Figure 3.8 presents the central resonant frequency f_{am} of the perturbed adiabatic resonators as a function of Δr. The confined mode by band inversions remains almost unperturbed at the resonant frequency of 300 GHz with variation below 0.06%.

The confined modes by band inversion have demonstrated robustness under a particular kind of noise. However, such kind of noise, that affects the bandwidth of the superlattices minigaps but leaves unaltered its cells acoustic thickness is a very particular one. Unless specifically fabricated with those characteristics, multilayer structures like those grown by MBE suffer from unrestricted random noise where the geometric thickness of each layer vary altering both minigaps bandwidth and central frequency. This idea motivates the study of the designed structure under random noise altering each layer thickness. For comparison purposes two further multilayer structures are designed with the same number of layers as the adiabatic resonator obtained by band inversion. The first one is a Fabry-Perot resonator formed by a λ layer of $GaAs$ surrounded by $(\lambda/4, 3\lambda/4)$ distributed Bragg reflectors. The second one is a resonator confining acoustic modes by band inversion at the interface between two distributed Bragg reflectors of the form $(\lambda/4, 3\lambda/4)$ and $(3\lambda/4, \lambda/3)$ [3] as reported in [125]. In order to perform a comparative analysis of the resonators' robustness, we study the shape of the reflectivity dip varying while we keep increasing random noise in each layer thickness. We do this by fitting a Lorentzian function to different sets of randomly perturbed structures. This is done systematically by generating a total of 5000 sets of random thickness variations for each layer. The amplitude of these variations progressively goes from 0 up to 1.0 nm in a progressive way while going from the set $j = 1$ which corresponds to the unperturbed structure, up to $j = 5000$ where

---

[3] Note that the adopted notation is $(D_{AlAs}\lambda, D_{GaAs}\lambda)$ where D_{AlAs} and D_{GaAs} are the acoustic thicknesses of the $AlAs$ and $GaAs$ layers in each cell, respectively. Then, a $(\lambda/4, 3\lambda/4)$ superlattice is formed by unit cells with a $3\lambda/4$ layer of $GaAs$ while a $(3\lambda/4, \lambda/4)$ superlattice by unit cells with a $\lambda/4$ layer of $GaAs$.

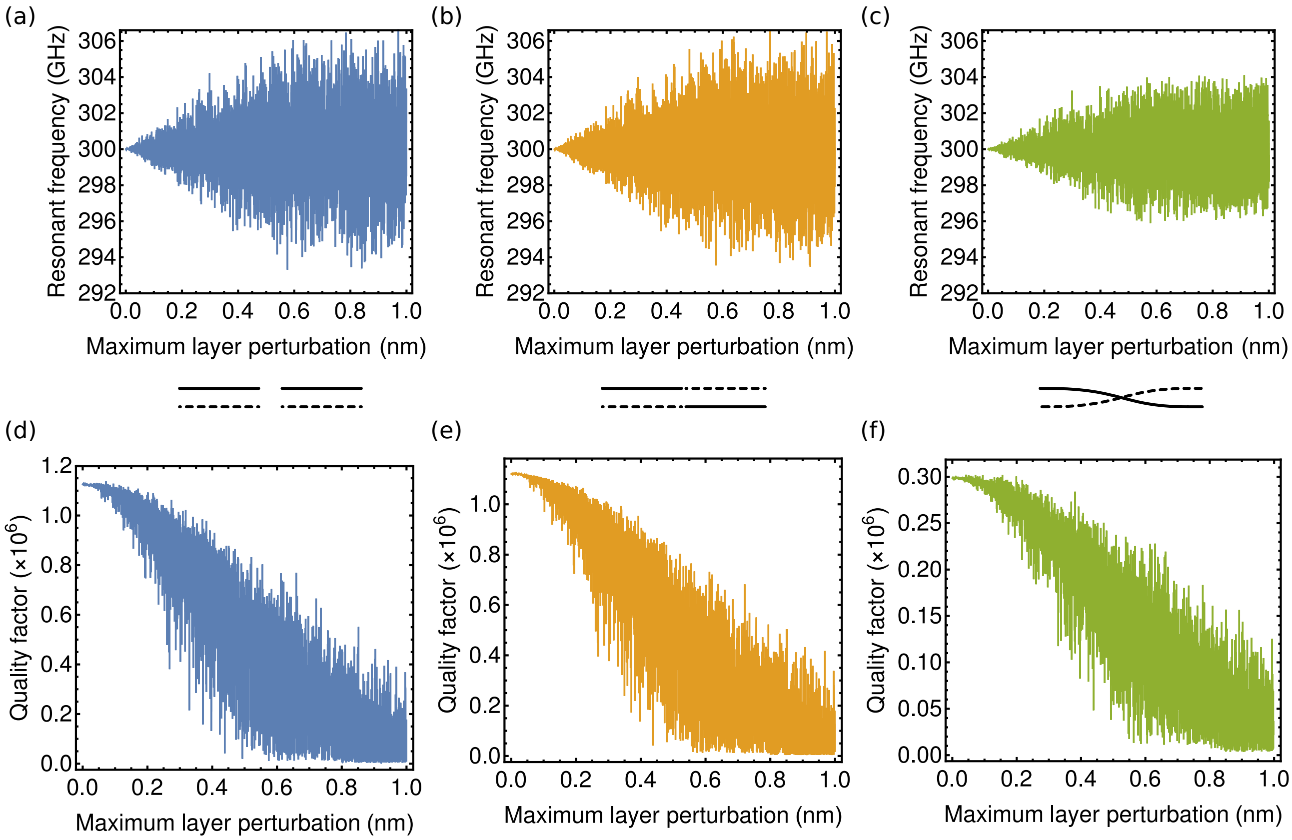

Figure 3.9: Three resonators were subject to the same kind of random noise in their layers thicknesses: a Fabry-Perot resonator, a resonator by band inversion formed by two concatenated superlattices and the adiabatic resonator by band inversion. All designs with no added noise feature a confined mode at 300 GHz. Panels (a), (b) and (c) present the resonant frequency of the perturbed Fabry-Perot resonator, resonator by band inversion and adiabatic resonator as a function of maximum layer perturbation. The non adiabatic designs show resonant frequency variations in the same range of magnitudes, but for the adiabatic resonator we can see how the confined mode tends to be located closer to its nominal resonant frequency. Panels (d), (e) and (f) present the quality factor of the perturbed versions of the Fabry-Perot resonator, resonator by band inversion and adiabatic resonator as a function of maximum layer perturbation. Unperturbed quality factor for non adiabatic resonators are on the same order around 1.1×10^6. The adiabatic resonator original design has a lower quality factor around 0.3×10^6. Nevertheless, it appears more robust under the random noise than their non adiabatic counterparts. In particular, at larger perturbations, despite starting with much higher quality factors, they reduce down to the order of magnitude of the adiabatic resonator quality factor.

each layer thickness deviates from its nominal value by a random length between −1.0 nm and 1.0 nm.

From fitting the reflectivity dip we can follow the deviation from the original resonant frequency and quality factor while increasing the noise level. Figure 3.9 panels (a), (b) and (c) present plots of the central frequency of the resonance reflectivity dip for the perturbed versions of the Fabry-Perot resonator, resonator by band inversion and adiabatic resonator as a function of maximum layer perturbation, respectively. In panels (a) and (b) we can see how both non adiabatic structures show a similar behavior. In panel (c) in contrast, for all noise levels the adiabatic resonator appears closer to the nominal resonant frequency than the others. In order to quantitatively compare the three resonators we compute the standard deviation from the obtained resonant frequencies. The values obtained for the Fabry-Perot, topological and adiabatic resonators are approximately 1.89, 1.89 and 1.41, respectively. Thus, we have evidenced through simulations a reduction of how disperse these values are when the nominal design is perturbed. Panels (d), (e) and (f) present the quality factor varying as a function of maximum layer perturbation for the perturbed versions of the Fabry-Perot resonator, resonator by band inversion and adiabatic resonator as a function of maximum layer perturbation, respectively. As the non-adiabatic structure features distributed Bragg reflectors with higher reflectivity than their perturbed counterparts, the non adiabatic resonators depart from higher quality factors, approximately 1.1×10^6. The adiabatic resonator, in contrast, has a quality factor of approximately 0.3×10^6. Nevertheless, while increasing the layer perturbation parameter the plot shows how the non adiabatic resonators are more sensitive to perturbations than the adiabatic resonator. For the maximum layer perturbations simulated, the quality factor of the two non-adiabatic structures is reduced down to values that are similar to the adiabatic resonator quality factors. We must consider that not all perturbed structures lead to a confined mode. From the total 5000 perturbed structures designed for each of the three resonators, approximately 200 did not feature a confined mode for the non adiabatic cases while only 100 for the adiabatic structure, with most of them ($\approx 70\%$) appearing at the maximum perturbation range between 0.8 and 1.0 nm. Considering the span of different quality factors seen for the perturbed non adiabatic structures, figure 3.9 (b) suggests that at the maximum perturbation conditions we have more chances to have a confine mode for the adiabatic case.

Simulations indicate that different designs for one dimensional multilayer structures might be engineered where a random alteration of the layer thickness affects in a less drastic manner the performance of the acoustic resonators. While out of the scope of this work, there is a vast space of parameters and designs possibles where acoustic local band structures might be engineered for this purpose.

3.4 Generalized acoustic potentials

We have demonstrated how by engineering a local band structure along multilayer devices we can control the propagation of acoustic phonons and engineer acoustic resonators. As a consequence of implementing a local band structure varying along a device, different frequency-dependent group velocities are imposed at different positions of the device. This gradient of velocities for a given frequency acts as an acceleration field and therefore allows to replicate the effect of an effective potential landscape. While phonons have neither charge nor mass, we can engineer multilayer structures that shape the medium through which they propagate such that an effective acceleration takes place. This capabilities, open the door to engineer structures that replicate the behavior of single-particle dynamics in the presence of a potential landscape. For example, previous works have pointed out the advantages of using nanophononic structures as simulation platform for complex electronic dynamics [155, 156]. In comparison with optical simulation platforms, nanophononic systems can be much smaller and offer the advantage of phonons having a slow speed of propagation and long coherence time [89]. These characteristics allow the study of wave dynamics in quasi-infinite systems and on time scales much smaller than the mechanical oscillation period. Previous implementations of phononic structures that mimic potentials were based on the use of coupled nanocavities [155], the phononic equivalent of coupled resonant optical waveguides (CROWs) [157]. Coupled nanocavities potentials are based on a tight-binding model to replicate the effect of potentials. In this section, we exploit the versatility in the design of adiabatic structures to implement generalized acoustic potentials.

In this section, we shape the local minigaps of an adiabatic structure to mimic the effect of a given potential by tuning the unit cells along the device. In the adiabatic resonators already introduced, we have altered only one of its unit cells parameters per resonator, r to control the minigap bandwidth and D to control the minigap central frequency. These two are independent from each other and form a complete set of parameters to control the shape of the local band structure. The maximum bandwidth is $2\epsilon f_\lambda$ (see equation 3.9) and is the only limiting factor, given by the impedance mismatch between the used materials (expressed in the constant ϵ). Both parameters, will vary from cell to cell creating a local band structure with its local minigap edges placed according to a chosen design.

We target the second minigap of a ($\lambda/4$,$3\lambda/4$) at $f_\lambda = 300$ GHz superlattice. In order to design a local band structure mimicking nanomechanical potentials we limit the problem to a particular case. In this case, all the local minigaps vary within the boundaries given by the top (f_t) and bottom (f_b) edges of the maximally opened minigap. Additionally we fix the bottom edge at f_b along all cells acting as the deepest part of the potential. To this end, let us rewrite the dispersion relation of a superlattice (equation 3.4) as

$$1 = \cos\left(\frac{2\pi f_b}{f_\lambda}\right) - \frac{\epsilon^2}{2}\sin\left(\frac{2\pi f_b r}{f_\lambda}\right)\sin\left(\frac{2\pi f_b(1-r)}{f_\lambda}\right) \tag{3.10}$$

Here we have set $\cos(qd) = 1$ since our target minigap is the second one, i.e. the first at the zone center ($q = 0$). We have also set $D = 1$, because, while being a useful parameter to describe the scaling of a cell, we can fix it and vary f_λ instead. Taken f_b as the bottom of the potential, we vary f_λ following the middle of the potential curve we want. This results in the top edge f_t following the same shape but scaled by a factor of two, defining the potential. Then, solving equation 3.10 for r give us the all the parameters needed to implement multilayer structures working as nanomechanical potentials.

3.4.1 Parabolic potential

The first potential to replicate in a nanomechanical system is the parabolic potential. In quantum mechanics, this potential is related to particles trapped by a linear restoring force, being the quantum counterpart of a harmonic oscillator. When considering trapped particles with a rest mass, the resulting energy levels are equidistant following a linear dependence with n_{mode} the mode number. This, however, depends on the particle dispersion relation. Electrons have a quadratic dispersion relation and therefore a linear dependence on n_{mode} is obtained. In our case, phonons have a linear dispersion relation and thus we expect non-equidistant energy levels following an $n_{mode}^{2/3}$ dependence.

There have been previous implementations of this kind of potential in different physical systems. In the optical domain, two dimensional photonic crystals have been used to achieve similar effective potentials by tuning its (2D) cell parameters near the confinement region [158]. In nanoacoustics, there has been an alternative approach where instead of cells being modulated there were coupled acoustic resonators changing their resonant frequencies according generating a parabolic potential in a tight-binding model fashion [155].

In this work, by modulating the cell parameters we design a nanoacoustic multilayer structure mimicking a parabolic potential of the form

$$V(x) = V_0 x^2. \tag{3.11}$$

Here, the variables V and x will correspond to the bandwidth of the local minigap and the position along the structure, respectively. The position is given in the unitless variable x which is normalized to go from -1 to 1, from the leftmost to the rightmost cell of the structure. The constant V_0 corresponds to the maximum bandwidth $V_0 = f_t - f_b$ and sets the maximum of the potential. Then, the local bandwidth varies from its maximum value at the extremes ($V = V_0$, i.e. minigap maximally opened) to zero at the middle ($V = 0$, i.e. minigap completely closed) in a parabolic way.

In this section we have considered feasible structures from the point of view of growth techniques. This is done by designing multilayer structures with no more than 403 layers and individual layer thicknesses not below 2 nm. Additionally, we kept the number of cells high enough to maintain an average overlap between local minigaps above 93%. The parabolic potential resonator is built by concatenating $N = 101$ cells. The parameters for each cell are obtained from numerically solving for r the N equations given by the set of f_λ values for each cell and equation 3.10.

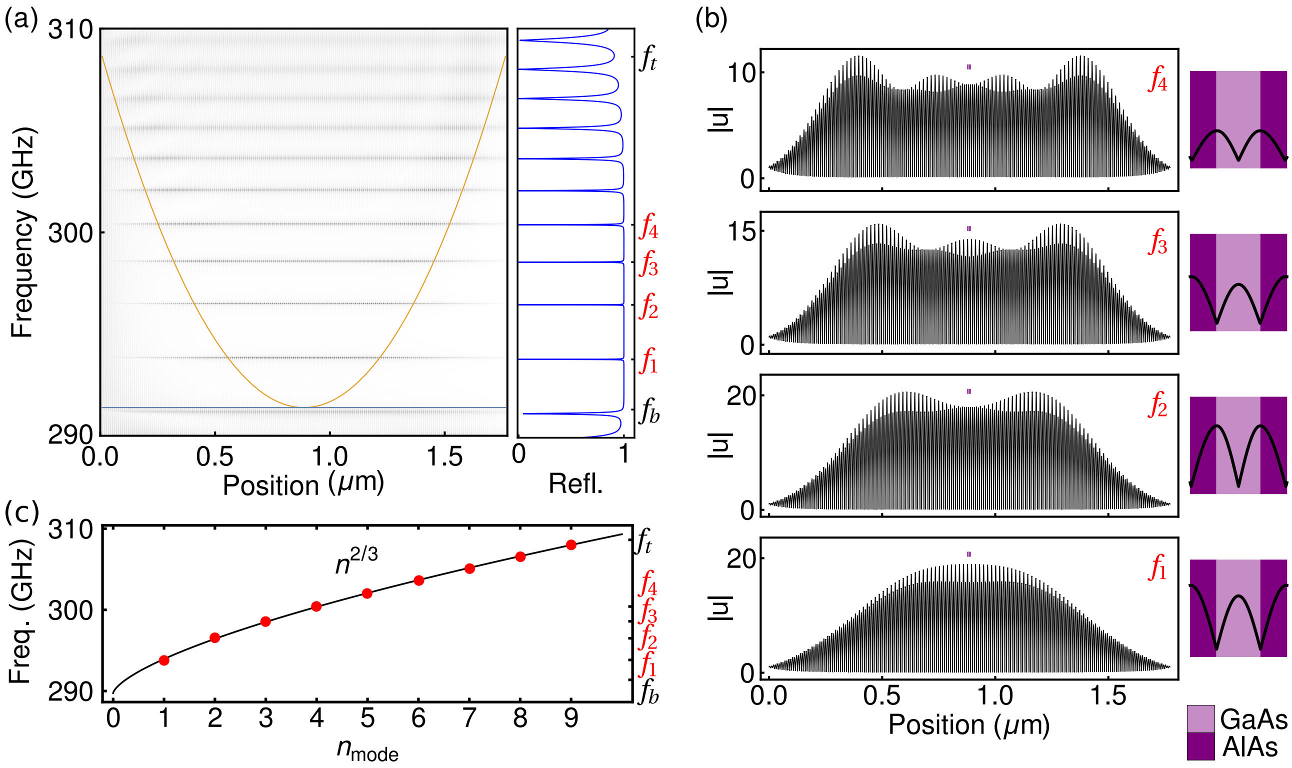

Figure 3.10: (a) Left: Color coded displacement amplitude as a function of position and frequency for the parabolic nanomechanical potential resonator. On top, its local band structure is plotted. Right: Structure acoustic reflectivity. Top and bottom edges of the maximally opened minigap are labeled as f_t and f_b, respectively. Up to nine reflectivity dips corresponding to acoustic confinement within the parabolic potential are identified. The first four modes at frequencies f_1, f_2, f_3 and f_4 are identified. (b) Left: Displacement amplitude as a function of position plotted for the first four resonant frequencies. Right: Zoom in the central cell displacement amplitude for the same frequencies f_1, f_2, f_3 and f_4. (c) In red points the acoustic resonances as a function of n_{mode} the mode number are plotted. The solid black curve correspond to a fit following the expected n^2_{mode} dependency.

Figure 3.10 (a) top left panel presents in grayscale the displacement amplitude as a function of position and frequency for the parabolic resonator. The structure is excited with an acoustic wave of unit amplitude impinging from the left. We can count up to nine of the horizontal lines corresponding to confined modes due to the parabolic nanomechanical potential. On the right, we plot the acoustic reflectivity. The first four confined modes at frequencies f_1, f_2, f_3 and f_4 are labeled, as well as the top f_t and bottom f_b edge of the maximally opened minigap and associated to the deepest and highest part of the potential. The spacing of the modes is not equidistant, but follows a $n^{2/3}_{mode}$ dependence on the mode number. Figure 3.10 (a) bottom presents in red points the nine acoustic resonances found and their corresponding mode number n_{mode}. The solid black curve behind is a fitted function following a $n^{2/3}_{mode}$ dependency. To further characterize these confined modes, in figure 3.10 (b) left we plot the displacement amplitude as a function of position for the four lowest frequency resonances. We see that some qualitative characteristics of the quantum harmonic resonator are replicated. First, the envelope function of each of the modes has n_{mode} local maxima for the resonance at frequency $f_{n_{mode}}$. The envelope function follows this trend because the Bloch theorem stands in this structures with broken periodicity. The adiabatic modulation of the cell parameters causes that if we consider Bloch waves propagating through the structure, their periodic part gets adiabatically modulated, becoming also quasiperiodic. On the right of each displacement plot, Figure 3.10 (b) presents the acoustic displacement amplitude in the central cell of the structure. As in the case of symmetric resonators, we can see that the lowest energy mode shares the symmetry of the edges confining it. The second replicated characteristic from a quantum harmonic resonator is that these symmetries are opposed between consecutive modes. As a guide to the eye, the central cell position is depicted as an inset in each full displacement amplitude curve (figure 3.10 (b) left).

The parabolic resonator structure produces the effect of a parabolic potential for phonons. Nevertheless, there are important differences. We can see in the displacement amplitude along the structure how for the first four confined modes the decay tails leaking out of the confinement region get shorter, while they keep increasing for the last five modes. This happens because the potential we implemented is different in nature from what we usually consider for harmonic potentials. Usually, there is a mass or a charge which gets attracted or repelled towards a particular direction, changing its velocity, acting as an acceleration which is the manifestation of a scalar potential. In this case, the potential is emerging from collective characteristics of structure cells. The adiabatic tuning of the local band effectively accounts for changing the propagation speed, and this is the way we replicate the effect of acceleration of particles, in this case phonons which lack of mass or charge. Taking this into consideration we can understand the non-monotonic change of the confined modes decay tails. What happens is that the penetration depth of phonons at a given frequency inside a minigap does not depends only on the minigap bandwidth, but also on its spectral position within the gap. At a given bandwidth, the decay length decreases the closer to the minigap center the acoustic wave frequency lies. In the nanomechanical parabolic potential structure, non-monotonic change occurs in the decay length of the confined modes because, while going from bottom to top of the potential, competing effects of the local minigaps modulate the decay lengths. First, decreasing while getting closer to the middle, and then increasing while the potential opens. In addition in the quantum harmonic potential the parabola extends to infinity while in this case we are limited to the height of the maximum bandwidth and the size of the structure. This last characteristic, anchors the decay tail end to the extremes of the structure, in contrast to the ideal case where it extends left and right to infinity.

3.4.2 Morse potential

The Morse potential serves as a model to describe the dynamics of a diatomic molecule. In this case, the quantum harmonic oscillator fails to consider the possibility that bounds between the atoms in such molecules can be broken. Taking into account this characteristic, the Morse potential presents an asymptotic behavior towards a constant energy value to one of its sides. This constant value, known as the disassociation energy, corresponds to the energy needed to break the bound between the two atoms. The method presented in this section enables us to implement such potentials for phonons.

As in the previous case, the parameters for each cell are obtained from solving equation 3.10 for r at each cell. Each cell f_λ value is chosen such that the top edge of the local minigap follows the Morse potential function given by

$$V(r_M) = V_0 \left\{ \frac{1 - \exp[a\ (r_e - r_M)]}{1 - \exp[a\ r_e]} \right\}^2 \tag{3.12}$$

where the parameters V_0, a and r_e determine the depth, width and dip position of the potential, respectively. The position along the structure is parameterized by r_M, a unitless variable that goes from 0 to 1 from the leftmost extreme towards the rightmost one. The parameter V_0 is set to $V_0 = f_t - f_b$ such as that potential spans along the full spectral range of the maximally opened minigap. Finally, the constants $a \approx 3.95$ and $r_e \approx 0.26$ are chosen to properly visualize the potential in the structure domain (i.e. $r_M \in [0, 1]$). The resulting curve has a higher slope than the parabolic case, thus requiring more cells to maintain the adiabatic condition. A total of $N = 201$ cells are considered to build the Morse potential resonator.

Figure 3.11 (a) left shows the amplitude displacement as a function of position in the structure and frequency of the acoustic wave propagating through it. The local band structure is

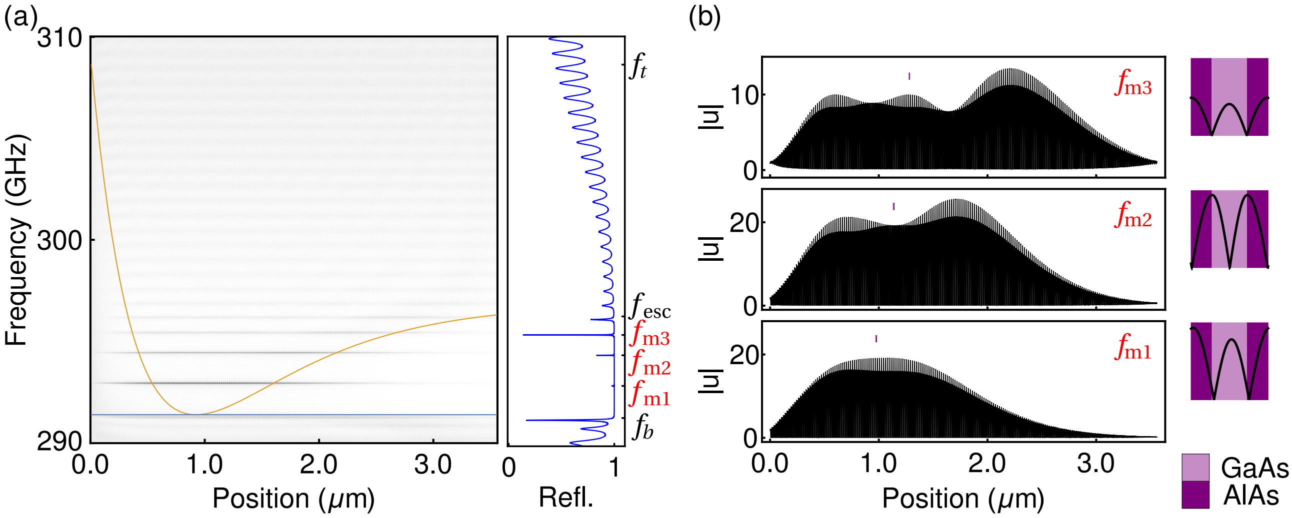

Figure 3.11: (a) Left: Color coded displacement amplitude as a function of position and frequency for the Morse potential structure. On top, its local band structure is plotted. Right: Structure acoustic reflectivity. Top and bottom edges of the maximally opened minigap are labeled as f_t and f_b, respectively. Up to four reflectivity dips corresponding to acoustic confinement within the Morse potential dip are identified. The first three modes at frequencies f_{m1}, f_{m2} and f_{m3} are labeled. (b) Left: Displacement amplitude as a function of position plotted for the first three resonant frequencies. Right: Zoom in the central cell displacement amplitude for the same frequencies f_{m1}, f_{m2} and f_{m3}.

plotted in colored solid lines. The top edge (yellow) follows the targeted trajectory $V(r_M)$. While theoretically the potential domain spans from $-\infty$ to $+\infty$, in our resonator it is limited by the size of the structure. Then, instead of an asymptotic approach to a disassociation energy, the potential ends in the extreme of the structure at a frequency given by the bandwidth $f_{esc} - f_b$ of the local minigap at the rightmost extreme. On the leftmost extreme, the maximum of the potential is reached and it corresponds to the bandwidth of the maximally opened minigap. From the color map we can already distinguish confined modes below the f_{esc} frequency, i.e. within the potential dip. Figure 3.11 (b) right shows the acoustic reflectivity of the Morse potential structure. The first three confined modes are labeled on the right at frequencies f_{m1}, f_{m2} and f_{m3}. We can notice how the reflectivity dips associated to these three modes go from shallow to deeper while going from lower to higher frequencies. This effect appears as a consequence of breaking the symmetry of the full structure. By doing so, we have created confinement regions surrounded by uneven local minigaps, prompting the escape of the confinement in one particular direction. This imbalance is what limits the minimum reflectivity reached by the dip. Towards higher frequencies the balance starts to be recovered with the mode at f_{m3} being the closest to experience a balanced confinement. Above this frequency one extra mode appears before f_{esc}, and we can see how the deepness of the dip is reduced again. All these four modes below f_{esc} correspond to bound states in the dip of the Morse potential. Above it, unbound modes appear corresponding to the ripples in the reflectivity curve. Figure 3.11 (b) left presents the displacement amplitude along the structure. The envelope function linearly increases its number of local maxima following the mode number n_{mode}. As the imbalance between different sides of the confinement region varies along the local band, the decay length of the envelope tails vary from case to case. Once again, we can show the alternation between symmetries of the overall mode. To do so, we need to define a central cell, but since the structure is not symmetric this is not fixed at the middle. Instead, we choose the middle local maximum or minimum of the envelope function and compare the cell corresponding to it. Figure 3.11 (b) right shows the displacement amplitude at each of these cells, starting with the symmetry of its band edge and alternating between consecutive modes.

3.4.3 Double-well potential

The final potential we mimic is a double-well potential. In contrast to the two previous potentials, the double-well features two dips separated by a potential barrier. Taking into account these two minima in the potential and the possibility of tunneling between them, this model can be applied to study the energy level of complex molecule dynamics as well as other physical systems that features this characteristic [159, 160]. The eigenstates of this potential extend along both wells, tunneling through the barrier. This results in hybridized modes featuring symmetric and antisymmetric modes alternating, with the lower one being symmetric. The height of the barrier separating the two wells determines the splitting between the hybridized eigenstates.

To obtain the design parameter we solve equation 3.10 for r at each cell so the trajectory of the top edge of the local minigap is shaped as the double-well potential function

$$V(z) = V_0\left[(\lambda' z^4 - kz^2) + \frac{k^2}{4\lambda'}\right]. \tag{3.13}$$

The two constants λ' and k are positive parameters determining the position and depth of both wells. The variable z is unitless and parameterizes the position in the multilayer structure going from -1 in the leftmost extreme to $+1$ in the rightmost one. We choose $V_0 = f_t - f_b$ to have the potential spanning along the maximal bandwidth, with the maximal opened minigap on the extreme. We choose $\lambda' \approx 2.39$ and $k \approx 1.69$ in order to have relatively shallow wells (compared to the maximum bandwidth) within the structure. A total of $N = 201$ cells is used to ensure the adiabatic condition along the full structure.

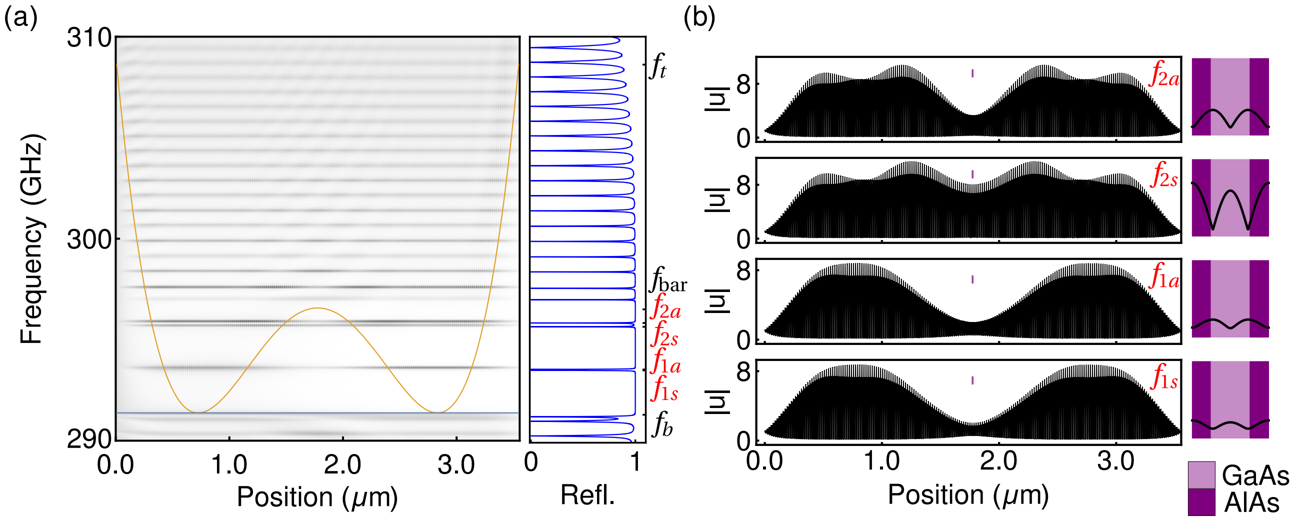

Figure 3.12: (a) Left: Color coded displacement amplitude as a function of position and frequency for the double-well potential structure. Over it, its local band structure is plotted. Right: Structure' acoustic reflectivity. Top and bottom edges of the maximally opened minigap are labeled as f_t and f_b, respectively. Up to four reflectivity dips corresponding to acoustic confinement within the double well potential barrier at f_{bar} are identified. These four modes at frequencies f_{1s}, f_{1a}, f_{2s} and f_{2a} are labeled on the right axis. (b) Left: Displacement amplitude as a function of position plotted for the four resonant frequencies. Right: Zoom in the central cell displacement amplitude for the same frequencies f_{1s}, f_{1a}, f_{2s} and f_{2a}.

Figure 3.12 (a) left shows the displacement amplitude as a function of position and frequency. We also plot, the double-well shaped local band structure. Inside the wells, high intensity displacement profile at specific frequencies extending along both wells are identified. These displacement profiles correspond to confined modes, that are analogous to the hybridized eigenstates of a quantum double well potential. These modes are able to tunnel through the central barrier, thus, causing the splitting of the confined states. On the right, the acoustic reflectivity of the structure is plotted. At the right axis we have labeled the top f_t and bottom f_b frequencies of the maximally opened minigap. Additionally, the central barrier of the potential is marked by f_{bar}. The high reflectivity region appears below this frequency f_{bar}. At lower frequencies, dips in the reflectivity appear as a signature of the hybridized confined modes at frequencies f_{1s}, f_{1a}, f_{2s} and f_{2a}. We can distinguish the splitting in the mode in the color map for the resonances at f_{2s} and f_{2a}, but for f_{1s}, f_{1a} the splitting is indistinguishable. At the reflectivity plot a similar trend occurs, but nevertheless, the split modes are resolved. Figure 3.13 (b) left presents the acoustic displacement amplitude for each of the resonant frequencies. We can see how each pair of hybridized modes share similar envelope functions, with their local maxima increasing linearly with the mode number. A detailed analysis however shows that each pair of hybridized modes corresponds to a symmetric and an antisymmetric state. On the right, a zoom in the central cell shows the acoustic displacement in the middle. As in the previous structure, we can see how the symmetries of the modes manifests there, starting with a symmetric state, and then alternating towards higher frequencies. We notice that the middle of the spatial profile starts to increase towards higher frequencies. This trend is followed because the confined modes transit from being trapped in both wells at the same time below frequency f_{bar}, to not experience at all the wells above this frequency. At higher frequencies than f_{bar}, ripples can bee seen corresponding to modes confined by the potential barriers on the extremes. While the modes are symmetric with respect to the full structure, if we see them with respect to each well they are not. This is similar to what can be seen in the Morse potential, where the envelope function appears to promote the escape towards the lowest barrier side.

3.5 Conclusions

In this chapter, we have introduced the concept of acoustic local band structures in multilayer devices. This type of adiabatic structures features a customizable local band structure that can be tuned by altering the unit cell parameters of a superlattice along it. Exploiting its properties, acoustic structures that mimic quantum wells have been designed and simulated. Three different kind of quantum wells have been studied. First, an acoustic potential well structure trapping phonons in a similar way as electrons and holes get trapped in quantum wells have been demonstrated. Second, a resonator where, by only increasing its unit cells size in its central region, acoustic phonons get confined. Third, an acoustic potential well structure featuring band inversion along its cells with a mode confined at the minigap center. These three adiabatic resonant structures are different from previous implementations of acoustic resonators like the well-known Fabry-Perot resonators [38, 60, 100, 161] or like the resonator by band inversion [125]. First, the confinement does not take place in a region (spacer or interface) surrounded by fixed reflectors (DBRs), but it occurs along a region where the reflectors starts to progressively appear as the local band transits from a closed minigap to an open one (like the one of a DBR). Second, adiabatic resonators typically feature quality factors below the values of a Fabry-Perot structure with the same amount of layers. Third, for the particular case of the acoustic potential well by band inversion, we show through simulations how one if its confined modes presents an better robustness to noise altering its nominal resonant frequency than the non-adiabatic resonators. Although we addressed only confinement in one-dimensional systems, adiabatic structures following similar design principles as the one used in this chapter has demonstrated suitable to implement high quality factor confinement in three dimensional structures, demonstrating relevance in several fields and potential for future applications [72, 134–136, 162–164].

Equipped with the same design tools used to engineer adiabatic resonators, we propose a method to generate customized local band structures allowing us to mimic, in principle, arbitrary potential landscapes. Previous implementations of nanophononic potentials relied on the use of coupled resonators following a tight-binding model [50]. Each of these coupled acoustic resonators is formed by several layers. The final potential landscape is achieved by tuning each of the resonators to a targeted frequency resulting, in general, in thick samples. Here, we have demonstrated how nanophononic potentials can be implemented using individual unit cells as the building blocks instead of full resonators. Consequently, the scale of the structure, and number of layers needed for implementing a potential is significantly reduced. Exploiting this advantage we have engineered structures mimicking three different potentials: a parabolic, a Morse and a double-well potential. The parabolic potential served as a replica of a text book example demonstrating the capabilities of the approach taken to simulate potentials. The Morse potential addresses the case of non-symmetric nanophononic potentials. A characteristic of the Morse potential is a limit in the energy at which modes are confined. Above this limit unbounded modes capable of escaping the confinement are evidenced. Finally, the double-well potential addresses the case of coupled confined modes where a hybridization of the modes is present. These examples demonstrate the feasibility of using nanophononic structures for complex wave dynamics simulation and experimentation exploiting the advantages phononic systems present in contrast with optical (large and fast in comparison with phononic counterparts) and electronic systems (fast and small in comparison with phononic counterparts). Given the characteristics of nanophononic systems, it is possible to experimentally access the full wavefunction of the supported modes of the replicated potentials.

The design strategies presented in this chapter have not considered the effect of losses in the multilayer structures. In general, we assumed pure materials and perfectly flat interfaces (i.e. no losses due to scattering from defects). Losses have been omitted for practical reasons since samples have been fabricated with similar characteristics and have been experimentally demonstrated suitable for working as acoustic resonators [89]. In the following chapter, we address the experimental study of multilayered structures with similar amount of layers in laboratory conditions. While the scope of this work focuses on acoustic structures at extremely high frequencies, it is important to remark that the design concept behind the adiabatic resonator is not limited to this range or field. The generation of a local band associated to varying superlattices relies on Bloch wave engineering. The introduced approach then can be extended to other types of wave phenomena like photonic and electronic multilayer structures. Finally, we can consider also the case of other quasiperiodic structures like Fibonacci arrays or Cantor-like structures, and study how these can been engineered by progressively altering their structural parameters. By doing so, we can study different length and temporal scales difficult to access by optical means, but at which structures engineered to control acoustic phonon can access by the approaches presented in this manuscript.

Chapter 4

Experimental study of phonon confinement in one-dimensional structures

The capabilities to coherently control quantum states, store them and transfer them are indispensable requirements for quantum technologies [46, 165–170]. For their physical implementation, different quantum systems are candidates to meet these requirements. Photons, for example, allow robust transport of quantum states over long distances, but as a trade off, making these particles interact between each other requires nonlinear processes that make the transfer of information between them difficult to implement [165]. Ion traps, have demonstrated long coherence time and strong interaction mechanisms, but gate speeds are low compared to other systems and scalability poses a problem [171–173]. Superconducting qubits offer fast gates [174] and are currently at the front line of quantum technologies since the break through demonstration of quantum supremacy [170]. Nevertheless, they have short coherence times compared to other platforms [175] and both reproducibility [176] and scalability [177] are a problem. These systems are just few examples of many other physical platforms that are candidates for quantum technologies [165]. In order to meet all the requirements needed for this, an approach is to build an hybrid platform based on different quantum systems performing different tasks, exploiting the particular advantages each system offers [41, 167, 172, 178, 179]. For solid-state quantum systems, a common characteristic is the strong interaction with their environment [178]. Phonons, i.e. mechanical vibrations, can modify their host structure. Thus, phonons, if uncontrolled, alter the host conditions and constitute a prominent source of decoherence [49, 180, 181]. On the contrary, we can use phonons as part of a quantum architecture that exploits them for application purposes as, for example, information carriers through quantum channels [46, 182, 183], quantum memories [184, 185] and as transducers for quantum states [122, 123, 186]. In this context, structures that confine phonons i.e. resonators, constitute an important building block for quantum applications.

The fabrication of multilayered structures confining phonons at extremely high frequencies requires precise nanometric layers thicknesses and high quality flat interfaces [187]. The expertise in the fabrication of multilayer structures by state of the art molecular beam epitaxy (MBE) allows growing layers with thicknesses with a resolution down to the atomic monolayer [188]. Such degree of control, allows the engineering of resonators confining acoustic phonons in the range from tens to hundreds of gigahertz [21, 23, 60, 70, 72, 124]. In addition, the possibility of shaping these multilayer structures into three dimensional devices like micropillars [21, 70], waveguides [189], or more complex three dimensional designs [55, 190], opens new degrees of freedom to control quantum systems.

In order to transduce the phononic response of nanoengineered multilayered structures into an electronic signal and vice versa, an intermediate step is required. During the mid 1980s, using a pump-probe technique, ultrafast optical pulses were used to generate and detect coherent phonons in thin layers of semiconductors [74], organic molecular crystals [191] and metals [75]. This technique known as time-domain Brillouin scattering (TDBS) [77, 102], opened the door to experimentally access phenomena occurring at picosecond and femtosecond time scales [104, 192], showing potential for applications in a vast variety of fields. Living organisms have been imaged and their mechanical properties studied [193–195], nanowires have been characterized by acoustic means [196, 197], it has been used for depth profiling of inhomogeneous materials [198] and for the study of nanoporous thin films [199], plasmonic systems [97], dielectrics [200, 201] and semiconductors [202, 203]. In addition, TDBS allows to experimentally study acoustic phonons in multilayer one dimensional nanostructures like phononic resonators and optomechanical cavities [38, 66, 100].

In this chapter, we present the experimental results obtained from the study of acoustic resonators and optomechanical cavities by means of TDBS. The collection of structures used in this chapter were fabricated by the group of Aristide Lemaître in the clean room facilities at the Centre for Nanoscience and Nanotechnology (C2N). The high quality of the samples provided were indispensable for all the experimental realization covered in this work. In the following sections, we introduce the experimental implementation of the time-domain Brillouin technique used for the study of various resonators. We present the main challenges from this kind of experimental setup and the strategies adopted to overcome them. Then, we present results of the measurements performed on four different multilayers structures featuring confinement of both phonons and photons. Finally, we present a summary of the results and conclusions.

4.1 Laser ultrasonics: Time-domain Brillouin scattering

In chapter 1, we described the transient reflectivity coherent phonon generation pump-probe spectroscopy. In the context of picosecond ultrasonics, recent works have opted to rename this technique as time-domain Brillouin scattering (TDBS) [77, 103]. TDBS is a pump-probe technique where ultra short laser pulses are used to generate and detect coherent acoustic phonons [73–77, 101, 204]. Pairs of pulses, coming from one or more ultrafast lasers [205], are focused onto a sample where a first pulse, the pump, perturbs the system impulsively generating phonons in the process. This can be achieved by different mechanisms like thermoelasticity [206, 207], deformation potential [208, 209], inverse piezoelectric effect [210, 211] and eletrostriction [212, 213]. These generation processes typically occur within the time scale of the pulse duration, that is between tens of femtoseconds up to a few picoseconds. Then, acoustic phonons with oscillation periods larger than or on the scale of the pulse duration (tens of gigahertz up to few terahertz) are generated sharing the same phase, i.e. coherent phonon generation [73]. In order to detect the generated phonons, a second pulse, the probe, is focused onto the sample under study. The reflection of the probe pulse depends on the sample condition when the probe was reflected. Given the short pulse duration of the pulse, this technique allow us to measure an almost instantaneous reflectivity of the sample. TDBS allows us to identify the presence of coherent phonons because these contribute all in the same way to the sample reflectivity. By varying the time delay between pump and probe, and by using ultrashort pulses we are able to reconstruct point by point the time resolved reflectivity trace of the sample after the pump excitation and therefore reveal the presence of coherent phonons. These, usually manifest as periodic variations of the measured reflectivity as a function of the time delay between pump and probe. The control of the delay time can be implemented by using a mechanical delay line that physically changes the distance traveled by the probe pulse. An asynchronous approach is possible too, where different ultrafast lasers sending pulses at different repetitions rates result in a time delay scan without the need of modifying the probe trajectory [205, 214]. This approach is known as the asynchronous optical sampling (ASOPS) technique and, by removing the use of a mechanical delay line, offers enhanced stability and fast data acquisition.

The intensity of light coming back from the sample in TDBS experiments depends on many parameters, like the sample reflectivity, the cavity mode dynamics [215, 216], the overlap between acoustic and optical fields imposed by the sample structure, etc. Due to the usually small signals measured in TDBS a synchronous detection scheme is used. For this purpose, the pump pulse is usually modulated in time by an acousto-optic modulator, imprinting a modulation frequency on it which will act as reference. By collecting the probe light with a photodiode, we can electronically demodulate the reference frequency from it using a lock-in amplifier. This synchronous detection scheme, allows us to discriminate the effects of the pump on the probe in order to increase the signal to noise ratio and detect the presence of coherent acoustic phonons [192, 217].

The implementation of a time-domain Brillouin scattering experiment presents different challenges. We can identify three as the most critical ones: the mechanical stability of the optical elements, the filtering of the pump from the probe collection and the spatial overlap between pump and probe on the sample. The stability of the optical setup is a critical factor when using a mechanical delay line to achieve the delay between pump and probe. Typical setups that require stability and movable pieces are interferometers. In order to deal with stability issues these are typically built with a small footprint and the movable pieces do not need to translate more than few micrometers therefore small robust stages or even only piezoelectric actuators are used to achieve this kind of movement. For a pump-probe technique the scenario is different. Just delaying the probe from the pump by half a nanosecond requires around 15 centimeters of extra optical path for the probe. This in general rules out the use of micrometer stages or piezoelectric actuators for displacing optical pieces and directly place a constraint on the minimum footprint the delay system can have. The second critical factor is the pump filtering from the probe detection. What we need to detect are the pump effects on the probe signal. To extract this information a synchronous detection schemes is used where the pump is modulated and the probe is demodulated at the same frequency. Then if the pump is not filtered from the detected signal, being entirely modulated, it passes by the demodulation system and contaminate the measured probe signal. The third critical factor is the spatial overlap of pump and probe spots on the sample. This is related to the mechanical stability of the setup, but it is not enough to have a stable setup. The spatial mode of the beams plays a role as well. In general, Gaussian beams are used and special care is taken to preserve the quality of the Gaussian profile. When using an optical delay system, the beam's intrinsic divergence needs to be taken into account. For this purpose, a common strategy is to expand the beam and therefore reduce its intrinsic divergence. The trade off is that larger beams require larger optical elements in order not to not restrict their cross-section, which has a negative impact on the stability. During the course of this work we addressed each of these challenges using novel strategies to reduce their negative effects on the measurements.

A sketch of the setup we implemented is depicted in figure 4.1 (a). The optical and electronic elements from the setup are grouped in four modules according to the functions each one has and are marked by transparent colored boxes. The four modules together with the ultrafast laser constitute the full experimental setup. For all experiments presented in this chapter the laser used is a Titanium-sapphire laser (Spectra-Physics Tsunami in picosecond configuration) producing an horizontal polarized beam of light at wavelengths between 780 and 940 nanometers. Each pulse has a duration between 2 and 4 picoseconds, coming out of the laser at a 80 MHz repetition rate.

The delay system module receives the laser beam and splits it into two, one formed by the pump pulses with horizontal polarization and one by the probe pulses with vertical polarization. The splitting is implemented by rotating the linear polarization of the laser using a half wave plate and then a 5 mm polarizing beam splitter cube where the pump is transmitted and the probe is reflected. After the cube, the probe pulses follow a path through a folded optical delay system [218]. This system is built using three retroreflectors: two small ones and a large one of 1 and 2 inches aperture, respectively. The two small retroreflectors are mounted on the movable stage of a 60 cm mechanical delay line controlled from the experiment computer (PC). The large retroreflector is mounted in a vertical rail in front of the delay line and the polarizing beam splitter. Figure 4.1 (b) shows the folded retroreflector configuration used and a schematic of the sequence of reflections through each of them. This configuration features stability (reducing the beam pointing in contrast to the use of individual mirrors) and leads to a total of six passes along the delay line. By translating the stage, the probe trajectory length can be modified by up to 3.6 meters corresponding to roughly 12 nanoseconds of delay. Such a long delays are chosen in order to measure most of the reflectivity trace after the pump arrives (given the laser repetition rate of 80 MHz, consecutive pulses are separated in time by approximately 12.5 ns). At the output of the delay line system module, two beams come out one corresponding to the pump and one to the probe pulses. Then, the pump beam is sent to the acousto-optic modulator (AOM) module.

The AOM module works as a $1:1$ telescope formed by two lenses of 50 cm focal distance and an AOM at the telescope focus. The AOM (MT200-A0,2-800) operates at 200 MHz producing a diffraction pattern with most of the light being diffracted at the -1 order (see Fig. 4.1 (b)). The telescope is formed by placing a first lens focusing the pump beam at the AOM and then a second lens collimating the diffracted (-1 order) beam. The AOM controller (MODA200) is driven by a 800 kHz square signal, effectively turning on and off the diffracted beam at the driving frequency. Then, the collimated output beam at the output of the AOM module is formed by sequences of 50 pulses at 800 kHz.

After the probe pulse exits the delay system module and the pump pulse the AOM module, both pulses enter the coupling and collection module. There, both pump and probe trajectories are merged in a polarizing beam splitter and, from there, remain overlapped following the same trajectory towards the sample. On its path, the pump and probe beams pass by a non-polarizing beam splitter which is used to collect the beam upon reflection on the sample at the cost of losing half of the power. The last optical piece before the sample is a 20× objective with numerical aperture of 0.3. It is used to focus at normal incidence both pulses into a 5 μm diameter spot on the sample. By placing the objective at the focal distance from the sample (approximately 2 cm), it collimates the reflected beams. The beams coming back from the sample are extracted using the non-polarizing beam splitter. Then, the pump beam is filtered out by means of a polarizer. Finally, the probe is focused on a photodiode (10 MHz Silicon detector, 2051-FS-M) and its signal is sent to the electronics module.

The electronic elements that control the full experiment are grouped in the electronics module. The measured probe signal is demodulated using a lock-in amplifier (MFLA Zurich Instruments). As the reference signal, the lock-in amplifier takes as an input the 800 KHz square signal driving the AOM controller. This reference allows to demodulate the effects of the pump on the sample reflectivity at the instant the probe pulse is reflected on it. The demodulated signal (complex valued: $X + iY$) is then sent to an acquisition card connected to the experiment computer (See figure 4.1 (a) electronics module. Acquisition card is not included but considered as part of the experiment computer PC). Having the delay line controlled by the same computer, the experimental procedure is implemented and interfaced with LabView. The full experiment works as follows: first, a command to move the delay line at a fixed velocity is sent. The delay line stage accelerates and only once the constant velocity is reached a flag triggers the acquisition of the demodulated signal. Finally, when reaching the end of the movement the constant velocity condition is not fulfilled anymore, triggering another flag that stops the acquisition. Having the sampling ratio and the delay line velocity we are able to retrieve the instantaneous reflectivity as a function of delay between pump and probe pulses.

An example of a time resolved reflectivity trace is depicted in figure 4.2. The measured structure works both as an acoustic resonator at 18 GHz and as an optical cavity at 915 nm [69]. Panel (a) shows the trace of one scan of the delay line reaching up to 8 ns of delay after the pump pulse reached the sample. The vertical axis corresponds to the demodulated real component X while the horizontal to the time delay between pump and probe arrival to the sample. At zero delay, both pump and probe are reflected simultaneously from the sample. The excitation of the pump perturbs the electronic system which results in a rapid blue shift of the sample's optical reflectivity within the first few picoseconds. As a result, the instantaneous reflectivity signal drastically changes, first decreasing and then rapidly increasing above 0.4 V. After this

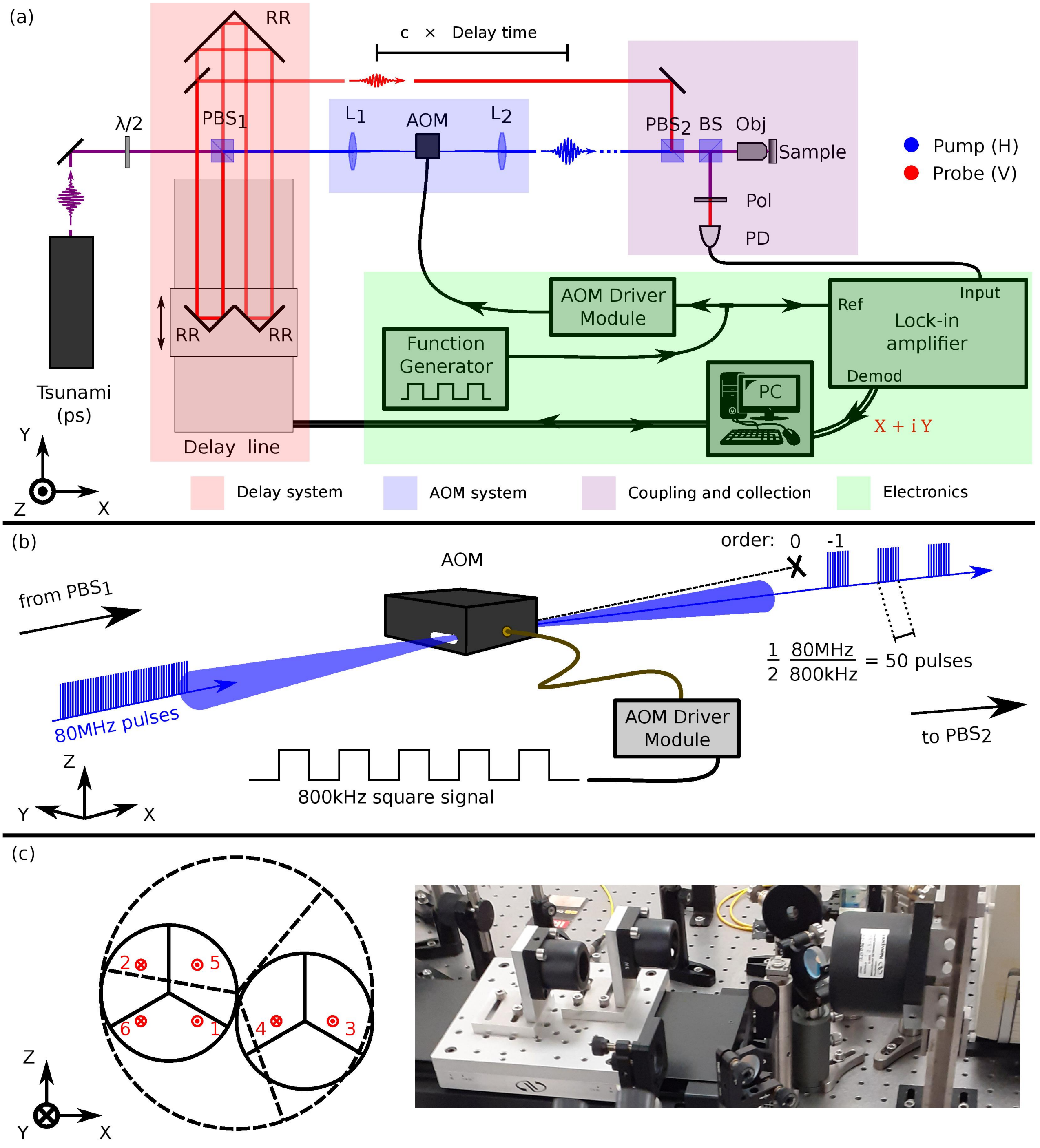

Figure 4.1: (a) TDBS setup sketch. A Tsunami laser generates picosecond optical pulses. A half waveplate ($\lambda/2$) and a polarized beam splitter (PBS_1) splits the laser in pump and probe pulses with horizontal (H) and vertical polarization (V), respectively. A mechanical delay line together with three retroreflectors (RR) are used to control the delay time between pump and probe pulses arrival on the sample. Along the pump trajectory, an acousto-optic modulator (AOM) in the middle of a two lenses (L_1 and L_2) 1:1 telescope modulates the pump to allow a synchronous detection. Then, both pump and probe trajectories are merged at PBS_2 and coupled to the sample using an objective (Obj). A non-polarizing beam splitter (BS) is used to collect the reflected light towards a polarizer (Pol) and a photodetector (PD). (b) The pump acousto-optic modulation system receives 80 MHz pulses and produces a diffraction pattern. Driving the AOM on and off with an 800 KHz square signal, trains of 50 pulses are produced. (c) Left: Diagram of the 3 retroreflectors arrangement used to fold the probe trajectory to get up to 3.6 m of path difference. Right: Photo of the actual setup.

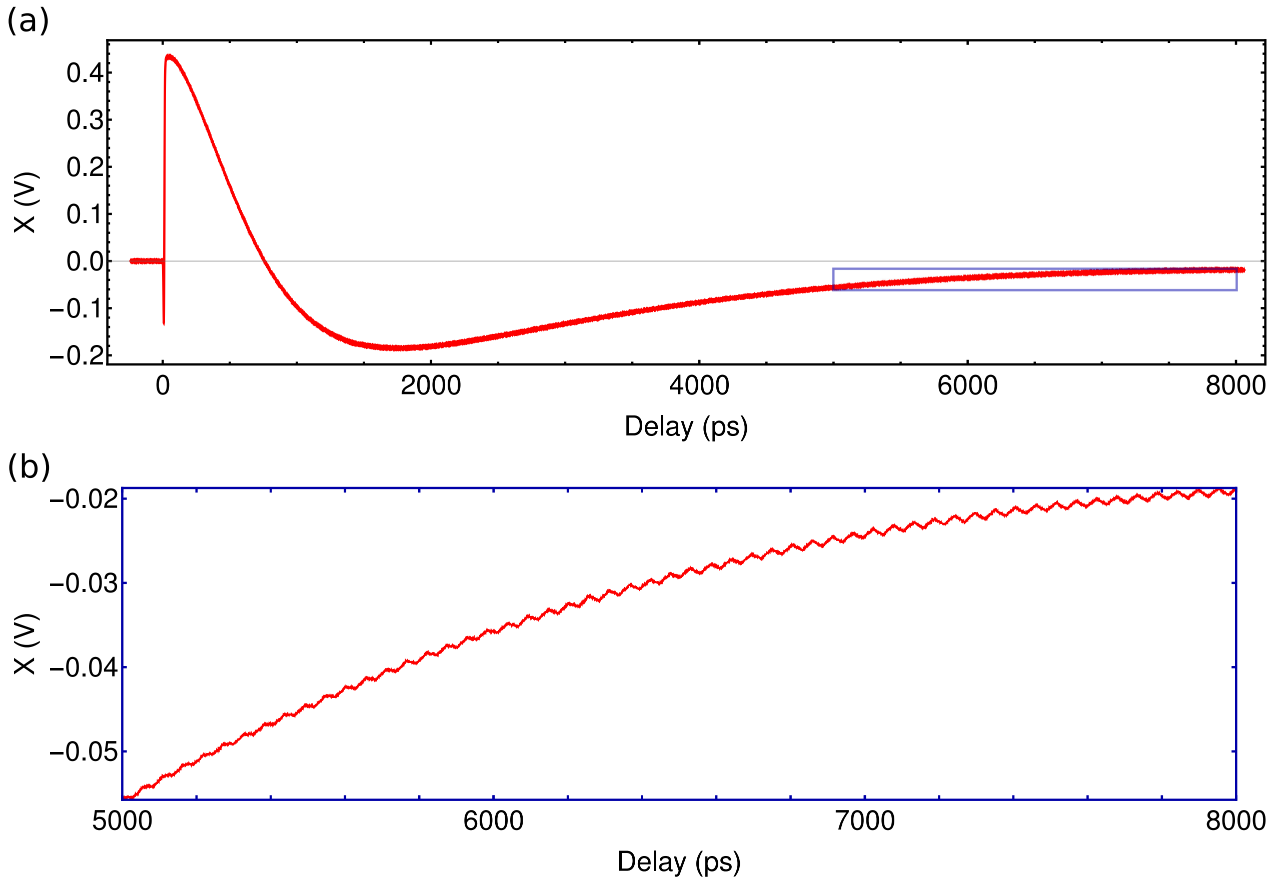

Figure 4.2: Time resolved reflectivity signal measured after demodulation. Only the real part X is plotted. The measurement is done after maximizing the change of X after zero delay. (a) Reflectivity time trace from −250 ps to 8050 ps time delay. (b) A zoom in the interval between 5000 ps and 8000 ps delay reveals oscillations caused by the presence of phonons in a 18 GHz acoustic resonator.

rapid change, the electronic system recovers its equilibrium state prior to the pump reflection in a slower process happening on the nanosecond time scale. Along both these processes, the reflectivity response mixes effects caused by the optical cavity dynamics and due to the presence of phonons. Figure 4.2 panel (b) presents a zoom in the reflectivity trace featuring oscillations due to confined acoustic phonons in the resonator. We note that the plotted signal corresponds to the X component of the demodulated complex value the lock-in amplifier outputs. The global phase of the measured complex value $(X + iY)$ is a free parameter for the demodulation of the electronic signal. In order to fix it in a systematic way, the phase is chosen such that it maximizes the signal just after the $t = 0$ delay. We chose $t \approx 6$ ps as the standard delay to maximize X. For the example trace presented in 4.2, the change in reflectivity follows the same trend as the demodulated X value, i.e. the higher the measured X values are, the more light is being reflected from the sample.

The implementation of the optical delay using a small 5 mm polarizing beam splitter together with the three retroreflector system allow us to reach long (up to 12 ns) delays while maintaining mechanical stability during movement of the delay line stage. The system is aligned using a CCD camera and monitoring the beam pointing after propagating more than 10 m. The beam pointing remains stable without the need of frequent realignment (typically, the setup remains stable over the course of weeks). Regarding the filtering of the pump beam from the collection photodiode, a critical factor is to place the polarizing beam splitters cubes such that the pump is the transmitted beam. These cubes are optimized to extinguish (extinction ratio 1000:1) the vertical polarization in the transmitted beam, but are not as good to extinguish the horizontally polarized beam from the cube reflection (extinction ratio 100:1). By only transmitting the pump beam, we ensure that it preserves a pure polarization. One of the drawbacks of the setup is the spatial mode of the pump beam diffracted by the AOM not being Gaussian. This results in a non-symmetric spot when focused on the sample surface. In contrast, the probe beam remains Gaussian during its full trajectory, but since the overall path length changes significantly by the movement of the delay line (up to 3.6 meters), the beam diameter changes drastically due to the intrinsic beam divergence. This results in a delay dependent probe spot size on top of the sample. The standard strategy to reduce the divergence angle of the beam is to expand it before entering an optical delay system. However, given the small dimensions of the cube (needed to ensure stability) and the constraints imposed by the retroreflectors apertures, expanding the beam is not feasible.

Motivated by the challenges encountered, we tested different strategies to reduce the drawbacks of the introduced optical setup. This, resulted in different versions of the setup by modifying, in particular, the coupling and collection module. These variants enhance both the stability of the optical elements and the pump beam quality by filtering the beams' spatial modes, maximizing the overlap between pump and probe, and fixing the probe spot size on the sample.

4.1.1 Spatial mode filtering by single-mode fiber

Single-mode fibers work as waveguides that allow the propagation of Gaussian modes along them. By coupling light into a single-mode fiber, it is possible to reject all contributions other than the fundamental Gaussian mode from any complex wavefront at the input [219]. In this section, we introduce a different variant of the TDBS setup using single-mode fibers as mode filters for both pump and probe. The new setup features a high quality Gaussian beams being focused on the sample and a fixed spot size for the probe. This approach directly addresses two of the challenges present in the original version of the setup: the spatial overlap and the filtering of the pump from the probe path towards the photodiode. The new version of the setup ensures high quality Gaussian beams and a fixed probe size on the sample. Regarding the filtering of the pump, this version of the setup requires new polarization optical elements to recover the cross polarization measurement scheme.

Figure 4.3 presents the optical setup. The coupling and collection module has been modified to receive both pump and probe beams and send them through two independent sets of quarter ($\lambda/4$) and half waveplates ($\lambda/2$) before coupling them into two single-mode fibers using fixed focus collimators. These waveplates are placed to compensate the polarization changes induced by the single-mode fibers. On the probe path, a 2×2 fiber coupler is used to send the probe pulses into the sample and then collect the outgoing probe signal simultaneously. At the sample output, a fixed focus collimator sends the probe beam to a polarizing beam splitter cube. The output of the pump single-mode fiber is collimated in the same way and sends the pump beam to the same polarizing beam splitter cube. In that cube, both pump and probe trajectories are merged and the beams are then focused on the sample. An extra polarizer is placed in the probe trajectory to improve the pump extinction in the collection. The first advantage of this configuration is the intrinsic robustness of the pump and probe spots on the sample. The cost of using this approach comes as a new dependency of the amount of probe power reaching the sample as a function of delay. At the output collimator at the end of the fiber facing the sample, the probe power variation due to this effect is typically below 10%. For the probe, being at low powers, variations within the detectable range is not a problem since we depart from the premise that the probe has negligible effects on the physics governing the ultrafast phonon generation by the pump. The second advantage of the improved version of the setup is adding a spatial discrimination stage to the collection procedure. While most of the pump removal is done by using a polarizing beam splitter together with a polarizer, adding this extra stage turned out to be more effective and simpler than other filtering approaches, e.g. using pump and probe on separated trajectories, focusing on the sample from different angles of incidence (see figure 4.4). Using a single-mode fiber in the setup allows a spatial mode matching between the mode focused on the sample and the mode collected by the fiber. In the configuration

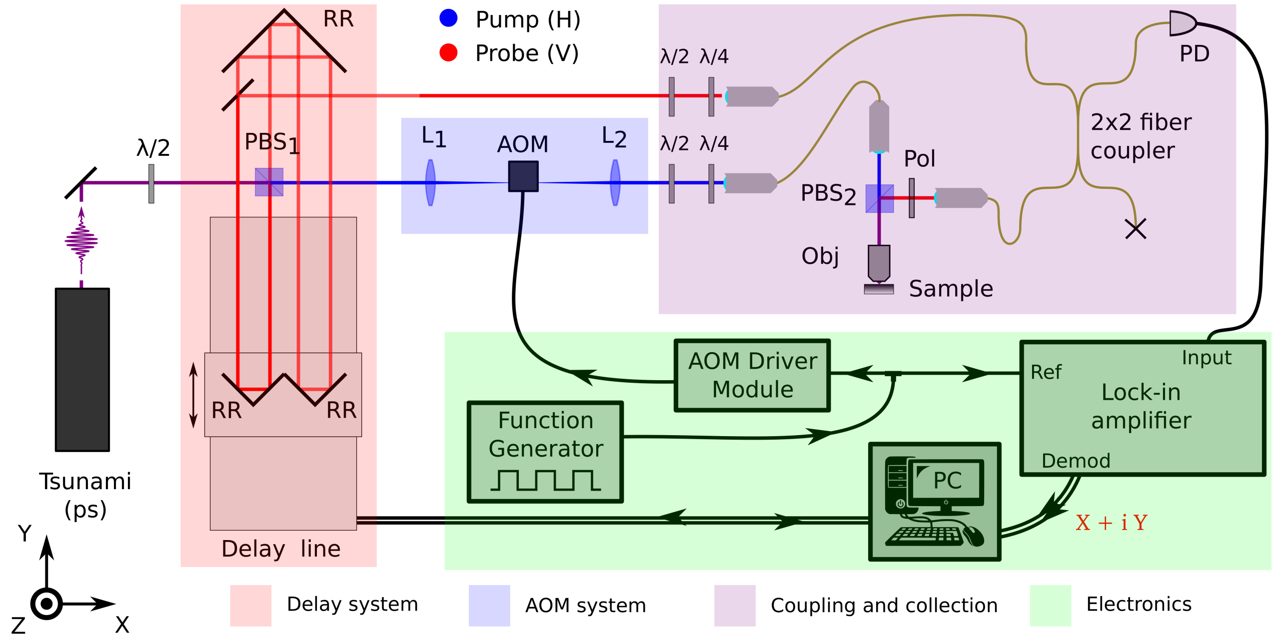

Figure 4.3: TDBS setup featuring spatial mode filtering by single-mode fibers. A Titanium-sapphire laser (Spectra Physics Tsunami pumped with Millennia 10W) generates picosecond optical pulses. A half waveplate ($\lambda/2$) and a polarizing beam splitter (PBS$_1$) split the laser in pump and probe pulses with horizontal (H) and vertical polarization (V), respectively. A mechanical delay line together with three retroreflectors (RR) are used to control the time delay between pump and probe pulses on the sample. Along the pump trajectory, an acousto-optical modulator (AOM) in the middle of a 1:1 telescope (L$_1$ and L$_2$) modulates the pump to allow a synchronous detection. Then, both pump and probe are coupled into separate single-mode optical fibers. After the probe passes a 2 × 2 fiber coupler which simultaneously sends the light towards the sample an collects its reflection both pump and probe merge in PBS$_2$ and are coupled to the sample using an objective (Obj). A polarizer (Pol) is used to compensate for the poor extinction ration of the PBS upon reflection.

presented in figure 4.3, a drawback is that the polarizing beam splitter (PBS$_2$ in reflection) and polarizer in the probe path alter the spatial mode of the beam, limiting the maximum mode matching we can achieve between input and output beams at the probe fixed focus collimator. An advantage of this mode match optimization is that the spatial mode of the pump beam coming back from the sample and reaching the probe collimator (unwanted) has a substantially different wavefront from the collected probe wavefront since it comes from a different collimator and it passes by the PBS (PBS$_2$) in transmission (in contrast with using it in reflection as the probe beam does). Then, the optimization alignment results in a spatial mode filtering of the pump beam.

4.1.2 Towards fiber integrated nanoacoustics

We introduce an alternative approach where both pump and probe beams are placed on the sample surface by bonding a fiber to it [220]. We will address the experimental procedure to implement TDBS in such fibered devices.

The fiber bonding to the samples was done by Quandela SAS [221]. The fiber connected samples were manufactured by an adhesive bonding procedure. Figure 4.5 (b) presents a picture of one optical fiber before (left) and after (right) bonding. We can see how, before applying the glue, the end of a ceramic ferrule used for mechanical stability extends in a conical shape. At its tip, the core and cladding of the fiber extends beyond the ferrule. We used samples operating as optical cavities and optimized the coupling of light into them. In order to do such optimization, the visibility of reflectivity dip associated to the confined mode is monitored

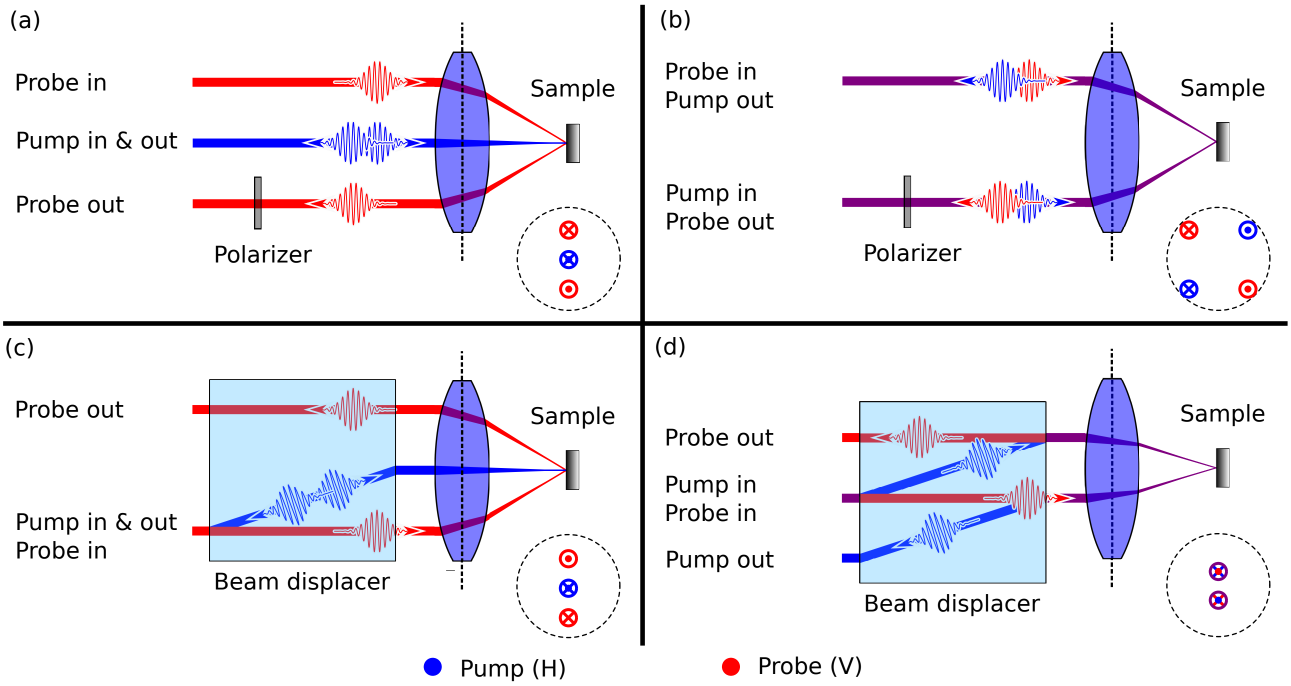

Figure 4.4: Different configurations tested to discriminate pump from the probe both spatially and by polarization. At the bottom right of each panel a schematics shows the position of the beams in the plane of the lens. (a) The pump passes through the center of the lens and is then focused on the sample at normal incidence. The probe passes the lens off center and is focused on the sample at an angle. (b) Both pump and probe pass the lens off center and are focused and collected at a fixed angle. (c) The incident pump and probe are overlapped and pass a calcite beam displacer. The pump is the extraordinary beam and gets deflected towards the center of the lens, focusing on the sample at normal incidence. The probe passes the lens off center and is focused on the sample at an angle. (d) Pump and probe are overlapped and pass a calcite beam displacer. The pump is the extraordinary beam and gets deflected off the center of the lens. Both pump and probe are focused on the sample at an angle, swapping trajectories.

during the gluing proceed such that it is maximized. The reflectivity is monitored through the fiber while maintaining it fixed and moving the chip under it using a 3D piezo motor stage with submicron precision. Once the coupling optimized, glue (UV-curing glue Norland NOA 81) is applied all around the fiber. During the curing process minor changes in the cavity mode central wavelength are seen ($< 0.1\%$).

In order to measure TDBS from fiber connected samples, a third variant of the experimental setup was implemented. Sending pump and probe through the same single-mode fiber grants a perfect overlap between pump and probe and a Gaussian mode on the sample. However, by sharing the same fiber, both pump and probe pulses change their polarization. For connected devices (effectively) we use only one single-mode fiber guided both pump and probe beams. In single-mode fibers stress induces anisotropic changes of the index of refraction, inducing polarization rotations in the Poincaré sphere [222]. Since both pump and probe polarization states experience the same rotations, at the fiber output the resulting states will preserve the orthogonality of the input states, horizontal and vertical. Then, regardless of which elliptical states come out of the fiber, we are always able to transform both pump and probe back to linear states, and to filter the pump with a polarizer.

Figure 4.5 (a) presents the optical setup for the TDBS setup for connected devices. A 2×2 fiber coupler is used to redirect the light onto the sample. Both pump and probe pulses are merged before entering the fibers, following the same trajectory along them. Upon reflection, they both propagate together and are coupled out using a fixed focus collimator. The beam containing both pump and probe passes a quarter, a half waveplate and a polarizer in front of a photodiode. These two plates are used to modify the polarization of pump and probe back

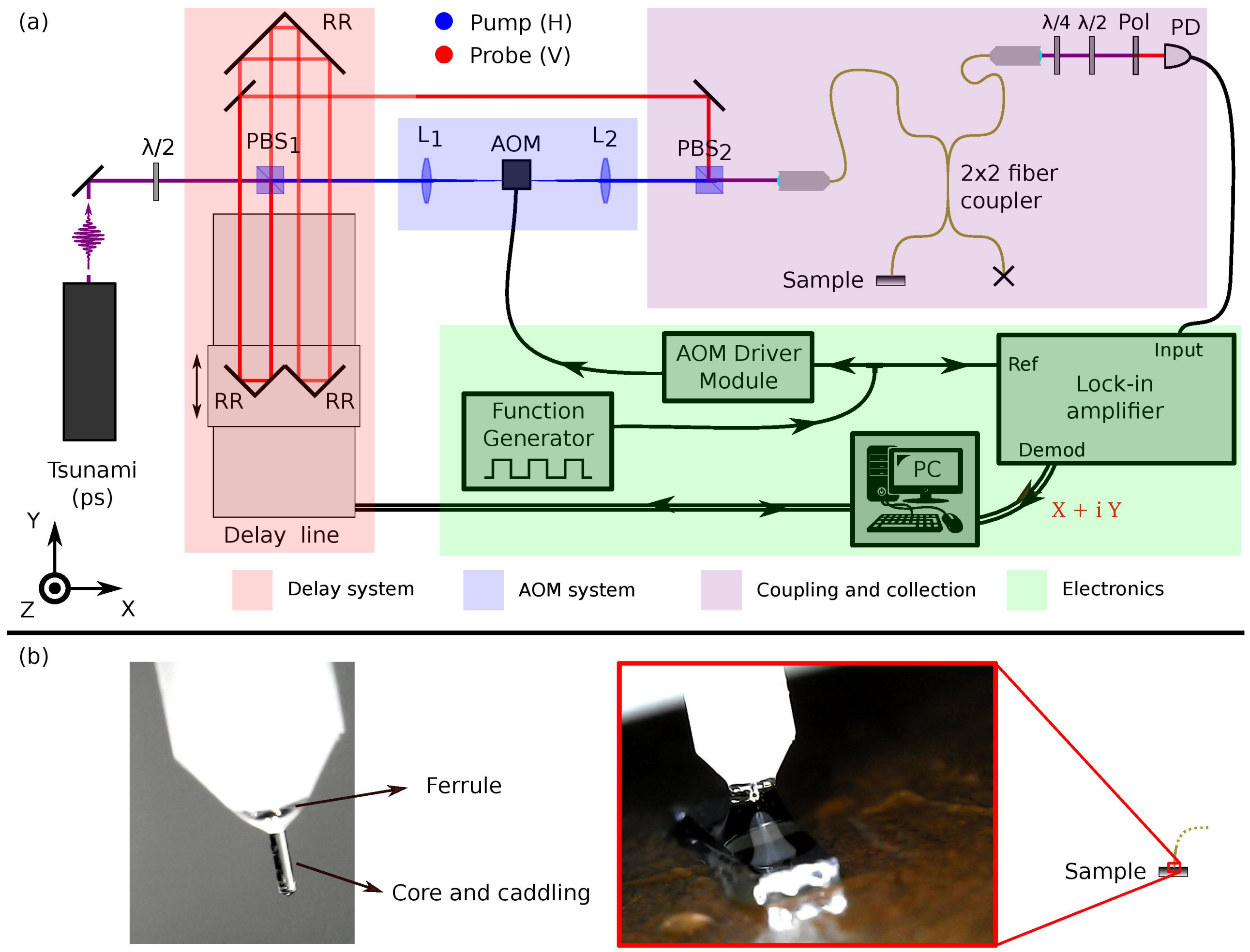

Figure 4.5: (a) TDBS experimental setup for connected devices. An ultrafast laser generates picosecond pulses that enter the setup. A half waveplate ($\lambda/2$) and a polarizing beam splitter (PBS_1) split the laser in pump and probe pulses with horizontal (H) and vertical polarization (V), respectively. A mechanical delay line together with three retroreflectors (RR) are used to control the delay time between pump and probe pulses on the sample. Along the pump trajectory, an acousto optical modulator (AOM) in the middle of a 1:1 telescope modulates the pump to allow a synchronous detection. Then, both pump and probe trajectories are coupled into a single-mode optical fiber connected to a 2×2 fiber coupler which simultaneously sends the pulses towards the sample and collects the reflection from it sending it to the photodiode (PD). Both pump and probe are coupled to the sample by having a fiber bonded to it. Prior to detection, the pulses pass a quarter ($\lambda/4$) and a half ($\lambda/2$) waveplates which transform both pump and probe polarization to linear. Finally, a polarizer (Pol) filter the pump. (b) Left: Photo of the fiber tip prior to being bonded to the sample. Its core and cladding can be seen extending beyond a ferrule used for stability. Right. The same fiber tip after bonding. The adhesive completely surrounds the fiber tip.

to two orthogonal linear states in order to filter out the pump with the polarizer.

The TDBS setup with connected devices offers a novel approach to easily study nanophononic multilayer structures. Its lack of alignment requirements and intrinsic overlap between pump and probe makes its experimental realization quite simple and yields highly reproducible results.

4.2 Acoustic resonator by band inversion at 200 GHz

The concept of band inversion in periodic lattices is related to topological invariants of their different bands. It is suitable to explain the electrical properties of polymers described by

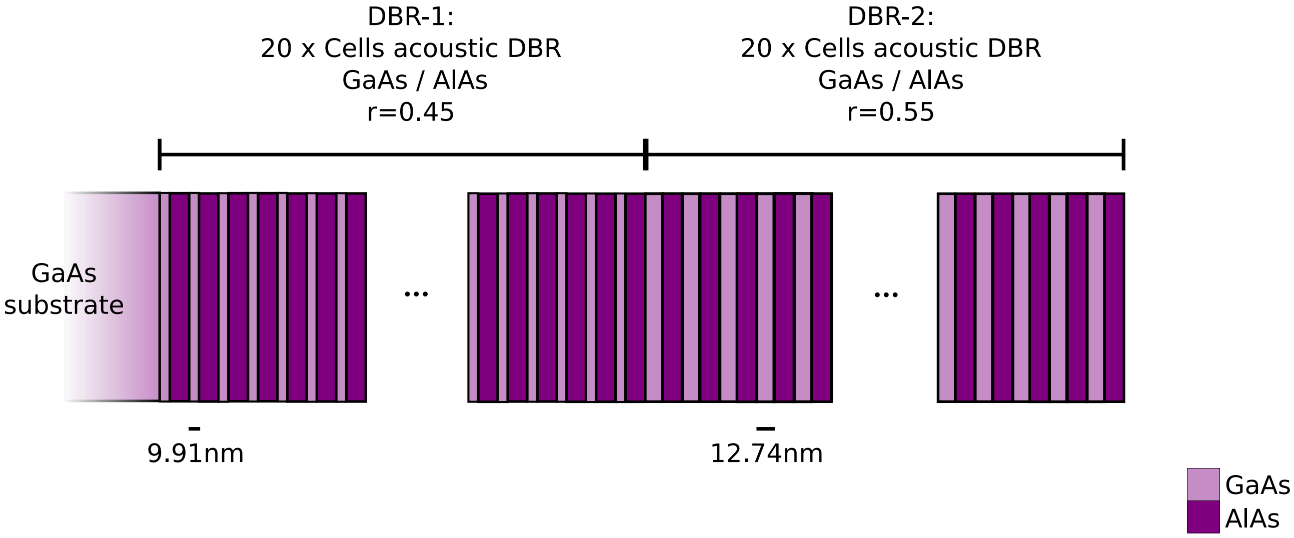

Figure 4.6: Schematic of the resonator by band inversion full structure. The 200 GHz resonator is a purely acoustic device formed by two acoustic DBRs (no optical DBRs is present in the multilayer structure). As an example of the scale acoustic structure two layer thicknesses are depicted, one per acoustic DBR, corresponding to the smallest layer thickness of each DBR.

the Su-Schrieffer-Heeger (SSH) model [223–225]. Extending the concept to superlattices, band inversions have been used to engineer confined interfaces modes between distributed Bragg reflectors by geometric phases associated to their different bands [125, 151]. In one dimensional periodic systems like superlattices, a topological invariant associated to these bands is known as the Zak phase [226]. In general, the study of geometric phases and how these can be used to engineer robust states have been studied in many platforms like photonics, phononics and electronics systems [125, 227–234]. In nanophononics, previous works have demonstrated the presence of confined interfaces states by band inversion using Raman spectroscopy experiments [21]. Complementing these results, we demonstrated interface modes confined by band inversion through TDBS experiments with higher spectral resolution with an asynchronous optical sampling (ASOPS) technique using 50 femtoseconds laser pulses in two color experiments [154]. In this section, we use the free-space TDBS experimental setup presented above for the study of a resonator confining 200 GHz acoustic phonons by band inversion. The 200 GHz resonator by band inversion is a planar multilayer structure from the same wafer used in the TDBS experiments with the ASOPS technique. In contrast with this previous realization, here, we perform one color experiments using only one utlrafast laser (Spectra-Physics Tsunami) operating in a picosecond configuration.

4.2.1 Acoustic confinement in superlattices by band inversion design

The resonator by band inversion confines 200 GHz longitudinal acoustic phonons at the interface between two distributed Bragg reflectors (DBRs). The multilayer planar resonator is a purely acoustic structure. This acoustic structure served as a first test to demonstrate the capabilities of the experimental setup to detect acoustic phonons [68, 125].

The resonator was fabricated by the group of Aristide Lemaître in the clean room facilities at C2N using molecular beam epitaxy (MBE). Two concatenated GaAs/AlAs DBRs were grown on a (001) *GaAs* substrate. A schematic of the structure is presented in figure 4.6. The first DBR (DBR-1) was grown on the substrate side and it is formed by 20 $GaAs/AlAs$ bi-layer unit cells with nominal thicknesses of 13.15 nm/12.74 nm. The second DBR (DBR-2) was grown on top of the first one and it is formed by 20 $GaAs/AlAs$ bi-layer unit cells with nominal thicknesses of 10.76 nm/15.57 nm. Using the two superlattice parameters introduced in the previous chapter [1]: For both DBRS, at the resonant frequency $f = 200$ GHz, the cell's acoustic thickness is $D = 1$, meaning that each cell has a total thickness of one acoustic wavelength. The first DBR (DBR-1) has an acoustic ratio $r = 0.45$ and the second DBR (DBR-2) $r = 0.55$ [2]. Each band has a Zak phase of 0 or π associated to it. The transition between these two values occurs at the closing point of each minigap, for the second minigap this happens at $r = 0.5$. Then, we know that the band of DBR-1 is inverted with respect to the band of DBR-2. The Zak phase value determines the reflection phase of phonons incident on a DBR with frequencies within each minigap. This can be evidenced by the displacement profile at the minigap edges where acoustic displacement function swap nodes by antinodes when the bands are inverted. By concatenating both DBRs with their bands inverted into a single multilayer structure, the resonant condition $\phi_{left} + \phi_{right} = 2m\pi$ with m an integer, is fulfilled directly by the reflection phases of the two DBRs [68, 125]. As a result, an interface acoustic mode is present in the structure, resonant approximately at the central frequency of the minigap i.e. at 200 GHz. Note that given the scale of the multilayers, the resonator acts as an effective medium for light.

4.2.2 Resonator by band inversion experimental results

The experimental study of the resonator by band inversion confining phonons at 200 GHz was done using pump and probe pulses with a duration of 2 ps at a wavelength of 865 nm. We used the TDBS setup coupling and collecting light from the sample in free space. In order to discriminate the pump light from the probe one we used a cross polarization scheme together with a spatial discrimination as presented in figure 4.4 (b) such that both pump and probe are focused onto the sample at the same azimuthal incident angle but coming from different directions, i.e. different polar angles. Pump and probe powers were 100 and 20 mW, respectively.

The measurement covered a small section of the full delay line with 1000 repetitions of the motion over the course of approximately 2 hours. The time delay between pump and probe covered by the delay line movement reached from -4 up to 260 ps relative to the simultaneous arrival of pump and probe pulses on the sample at $t = 0$. Figure 4.7 (a) presents the time resolved reflectivity trace of the measurement. At zero delay we can see a rapid variation first slightly lowering the reflectivity and then rapidly increasing as a consequence of the electronic and thermal response of the sample. Once reaching its maximum, the reflectivity starts to slowly decrease while the system relaxes back to equilibrium. During the relaxation process, we can see small oscillations caused by coherent phonons in the nanoacoustic resonator (see figure 4.7 (c)). The processing of this data is done in three steps. First, a segment of the reflectivity trace between 10 and 260 ps is extracted, i.e. a segment covering only the relaxation process. Secondly, a parabola is fitted in order to replicate the slow variations associated to the relaxation process. Thirdly, the fitted parabola is subtracted from the experimental curve and the result is process using a Lomb-Scargle periodogram [235, 236] to estimate the spectral density of the signal. The use of a periodogram instead of a fast Fourier transform (FFT) was done in this case because the speed of the delay line was not assumed to be a constant. Instead, the position of the delay line as a function of time was directly recorded. The resulting unevenly spaced data as a function of time delay was incompatible with using an FFT. A disadvantage of this approach is that the computation time for processing the data is significantly larger (at least an order of magnitude) than alternative methods using an FFT. For future realizations, this was overcome by modifying the delay line movement configuration parameters in order to safely assume a constant delay line speed and therefore obtain evenly spaced data, suitable for the FFT algorithm. The spectral density obtained after the application of a periodogram on the subtracted time trace is presented in figure 4.7 (b). An intense peak at 200 GHz is

---

[1] From now on we drop the subscript $AlAs$ from the acoustic ratio parameter and, in general, we refer to the $AlAs$ acoustic ratio r_{AlAs} in a cell or a DBR as r, i.e. $r = r_{AlAs}$.

[2] The parameter r used in this manuscript is related to the paramter δ used in reference [154] by the equation $\delta = 2r - 2$.

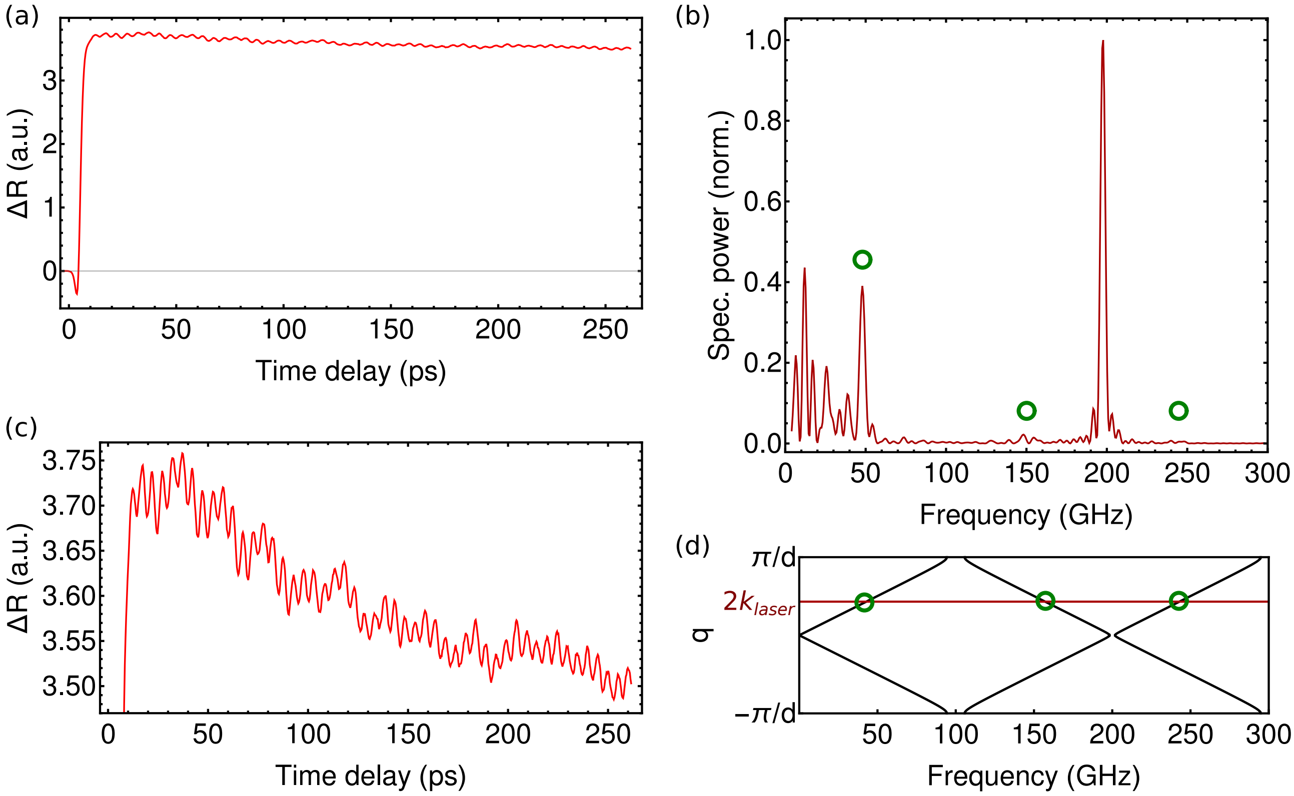

Figure 4.7: (a) Experimental results of the TDBS setup coupling and collecting light in free-space from the 200 GHz resonator confining acoustic phonons by band inversion. At zero delay, a rapid change of the instantaneous reflectivity is the result of the pump pulse ultrafast action on the sample. (b) Phononic spectrum obtained after processing the reflectivity time trace. At 200 GHz the main resonance of the structure is detected. Additional peaks at 50 GHz and on both sides of the 200 GHz resonant peak are seen corresponding to the crossing of the band structure with the $q = 2k_{laser}$ scattering condition (green circles). (c) Zoom in to the time resolved reflectivity trace shown in panel (a). The oscillations in reflectivity in this plot are the result of coherent phonons modulating the sample's optical reflectivity. (d) Dispersion relation of the superlattice on the cap side of the structure, i.e. with an $AlAs$ acoustic ratio $r = 0.55$. An horizontal line in dark red marks the position of the $q = 2k_{laser}$ scattering condition (green circles).

clearly distinguished corresponding to the confined interface mode of the acoustic resonator. In addition, at lower frequencies a Brillouin scattering peak of the full structure is identified around 50 GHz corresponding to the first crossing of the band structure fulfilling the $q = 2k_{laser}$ condition (see figure 4.7). Additional peaks can be distinguished at both sides of the resonant 200 GHz peak also from the $q = 2k_{laser}$ scattering condition (green circles).

The experimental results presented in figure 4.7 demonstrated the capabilities of our TDBS setup to detect coherent phonons in the range of hundreds of gigahertz. In the following sections, we will present different resonators designed to maximize the inelastic scattering of light due to phonons in order to enhance the measurement signal. In addition, we will show how the use of single-mode fibers allowed us to improve the signal to noise ratio such that we are able to reduce the measurement time by at least one order of magnitude.

4.3 Adiabatic resonator at 390 GHz

We proceed to study an adiabatic resonator featuring confined modes at 350 GHz. The experimental study was done by using the second variant of the TDBS setup, i.e. we used single-mode fibers to separately filter the spatial modes of pump and probe, and coupled the beams into the cavity mode using a free-space optical setup. This particular resonator has already been experimentally studied by Fabrice Lamberti et al. using Raman scattering to show the presence of confined phonons at 350 GHz [72]. In this section we complement those results with time resolved measurements.

4.3.1 Adiabatic resonator design

The adiabatic resonator sample operates both as an acoustic resonator and as an optical cavity. The design presents features at two different scales to achieve this behavior. The acoustic resonator was designed with a nominal resonant frequency at 350 GHz and has layers with thicknesses on the scale of the acoustic wavelength at this frequency, roughly 14 nm for $GaAs$ and 16 nm for $AlAs$. In contrast, the optical cavity is formed by two distributed Bragg reflectors with bilayers on the scale of the optical wavelength of light within the structure. For $GaAs$ and $AlAs$ this corresponds to approximately 258 nm and 308 nm, respectively. These two different scales for optics and acoustics, allow to engineer an optical Fabry-Perot cavity with an acoustic resonator working as the spacer between two optical DBRs [60, 89].

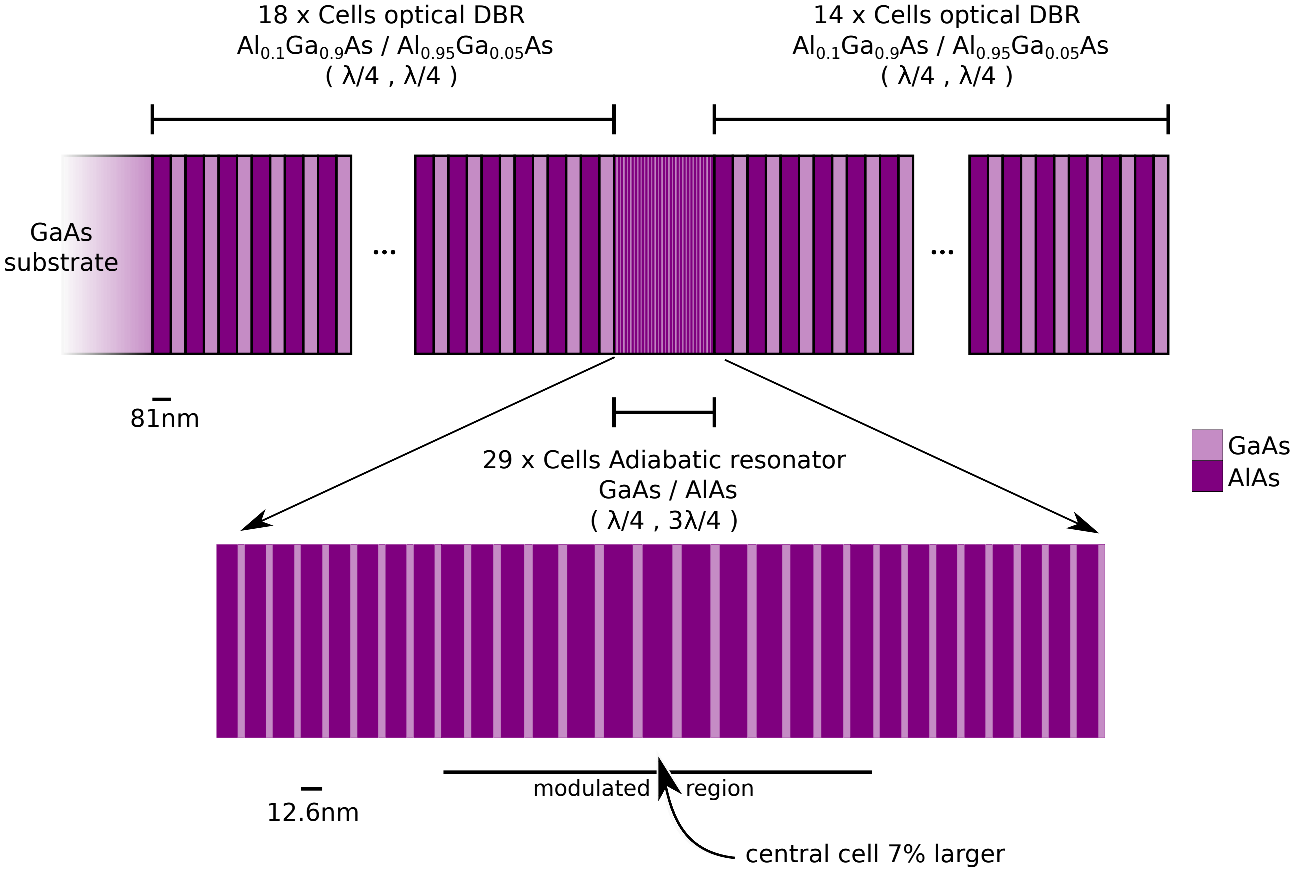

Figure 4.8: Schematic of the adiabatic resonator's full structure. The 350 GHz adiabatic resonator is embedded between two optical DBRs. As an example of the scale difference between the optical and the acoustic structure one layer thickness of each one is depicted, varying from 81 nm at the optical DBR to 12.6 nm in the acoustic resonator.

Figure 4.8 presents a schematic of the multilayer structure design. The full structure was grown by molecular beam epitaxy (MBE) on a (001) $GaAs$ substrate. The optical distributed Bragg reflectors correspond to a $(\lambda/4, \lambda/4)$ design and it is formed by $Al_{0.1}Ga_{0.9}As/Al_{0.95}Ga_{0.05}As$ bilayers cells. Its layers' nominal thicknesses are 64.5 nm and 77.0 nm for $Al_{0.1}Ga_{0.9}As$ and $Al_{0.95}Ga_{0.05}As$, respectively. The bottom (substrate side) reflector has 18 unit cells while the top one (cap side) has 14 unit cells. The difference of four extra cells on the bottom side compensates the different optical reflectivity of the two DBRs due to the difference in refractive index at the interface with the substrate and air, respectively. The acoustic resonator between these two optical DBRs is a quasiperiodic structure formed by 29 unit cells. Its design corresponds to a $(\lambda/4, 3\lambda/4)$ acoustic distributed Bragg reflector with a modulated region in the center, with increased layers thicknesses. The nominal layer thicknesses without modulation are 3.4 nm for the $GaAs$ layer and 12.1 nm for the $AlAs$ layer of each cell. The adiabatically modulated region within the resonator increases all layers thicknesses following a $\sin^2$ shape, increasing the layer thickness up to 7% in the center of the structure. This modulation extends along the central 25 layers of the structure. The full 29 unit cells resonator constitutes a $3\lambda/2$ optical spacer. The design is targeted to an optical wavelength of $\lambda = 913$ nm and an acoustic frequency of 350 GHz but is grown with a spatial gradient, allowing the optical wavelength to vary from 775 nm to 1000 nm. This gradient scales the full structure without altering the proportion between its layer thicknesses. A piece of this sample, in the region where the structure scales down to its smallest thicknesses, was used for the TDBS experiments. As a result, the optical cavity mode of the sample piece is a blue shifted of the optical cavity mode and a higher frequency for its acoustic resonance.

4.3.2 Adiabatic resonator experimental results

The experimental results on the adiabatic resonator were acquired working at room temperature and using pump and probe pulses of 2 ps duration at a laser wavelength of 775 nm. Pump and probe powers were 100 mW and 20 mW, respectively. The sample used for the experiments was taken from an extreme of the full sample wafer. This extreme corresponds to the position where the gradient in layer thickness results in the thinnest layers. Because of the scaling down of the multilayer structure, the expected resonant frequencies are higher than the nominal resonance at 350 GHz. The measurement was done moving the stage at 3 mm/s and covering from -160 ps to 1030 ps of delay with zero delay corresponding to the coincidence of pump and probe pulses. A total of 100 traces were recorded, 50 traces in each direction of movement of the delay line. Figure 4.9 (a) presents a measured reflectivity time trace. Just after the pump arrival, the instantaneous reflectivity drastically increases, followed by an exponential decay while the system recovers the equilibrium. To extract the phonon spectra from these signals we implemented a processing algorithm consisting of three steps. First, a region of interest along the trace is selected, for this case it corresponds to the first half nanosecond after $t = 10$ ps. The second step consists in differentiating the signal in a discrete way by subtracting consecutive values. Taking as an input this resulting trace, the third and final step is a fast Fourier transform (FFT). For practical reasons, we treat each group of 50 traces for the two directions of motion independently. The delay line stage, although very stable, works by mechanically rotating a large screw to translate the stage. Therefore, mechanical noise affects both directions of movement differently. We average both spectra for the final dataset. Figure 4.9 (b) presents the measured spectrum coupling light into the optical cavity mode using a free space configuration. The coupling into the cavity mode and filtering of the pump was implemented using the configuration presented in figure 4.4 (b). The spectrum measured presents, a noisy spectrum at frequencies below 120 GHz. As a result of the rapid change at lower delays within the processing window, below 20 GHz the spectra drastically increase. At higher frequencies where we expect the phononic signal to appear the spectrum is empty except for a intense peak around 389.9 GHz. This peak has a full width at half maximum of 2.9 GHz ($Q \approx 134$) and corresponds to the acoustic mode of our adiabatic resonator. Figure 4.9 (c) presents a zoom in around the resonant peak.

We demonstrated confinement of acoustic phonons in an adiabatic resonator. These results are complementary to previous work done on the same sample using a continuous wave spectroscopy technique. Here, the experiment was performed in the temporal rather than spectral domain, demonstrating in a different experimental platform the confinement capabilities of the adiabatic resonator. This difference allows us to resolve the confined mode with higher resolution. The coherent phonons in the spacer of the optical cavity effectively modulate the reflected signal at the resonant frequency. This result serves also as an upper limit on the frequencies we

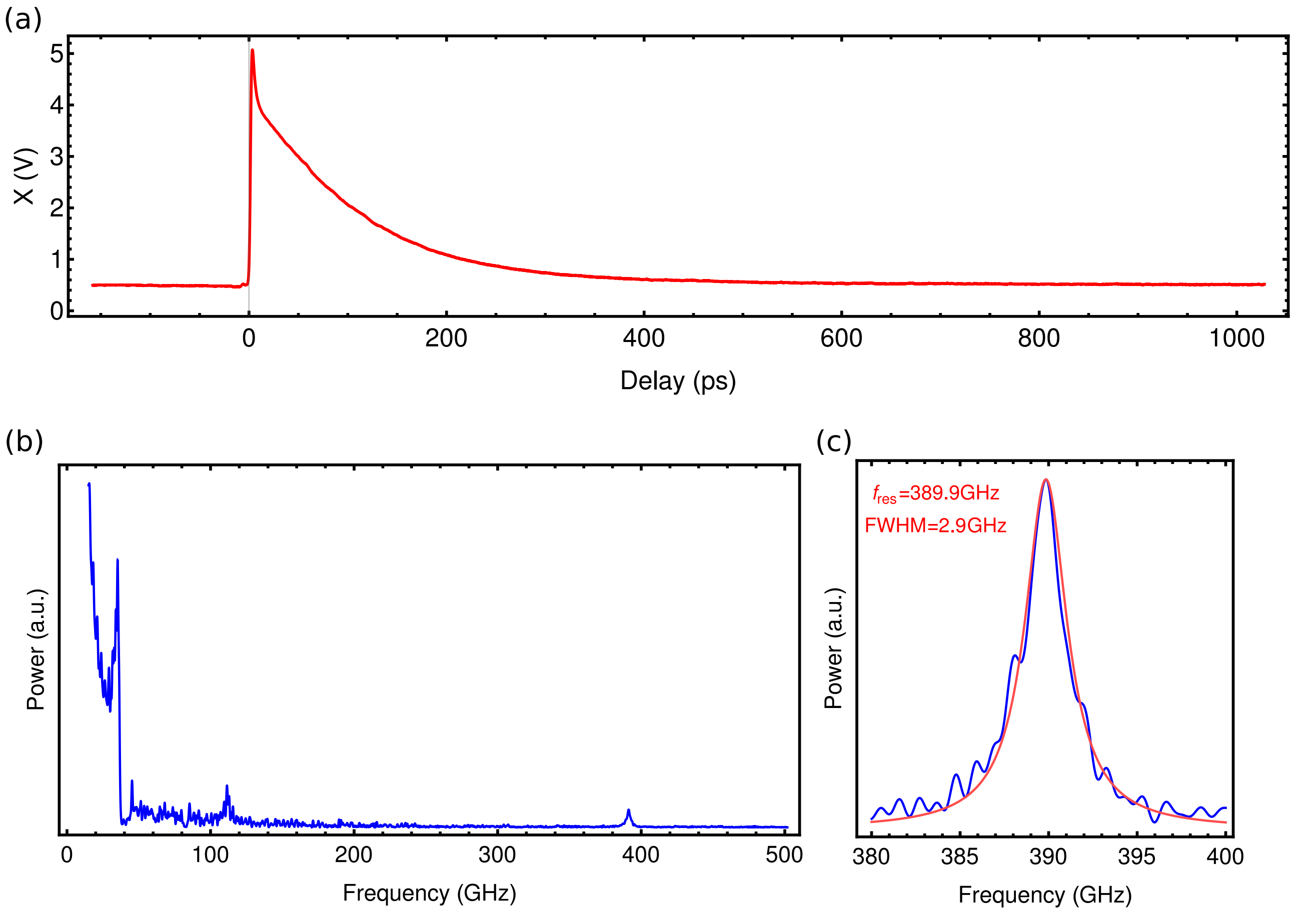

Figure 4.9: (a) Time resolved reflectivity trace measured from the adiabatic resonator. At zero delay, due to the pump pulse arrival the reflectivity drastically changes, then decays backs to equilibrium. (b) Fourier transform of the averaged differentiated trace between 10 ps and 510 ps of delay. *GaAs* substrate Brillouin scattering signal expected at $\approx$ 43 GHz. Resonant peak appears at 389.9 GHz. (c) Zoom in the resonant peak around 389.9 GHz corresponding to the confined mode in the adiabatic resonator showing a FWHM of $\approx$ 2.9 GHz.

have detected with the developed TDBS setups using picosecond pulses of light. The shorter pulses we use, the higher the maximum detectable frequency. This depends on the efficiency to generate phonons and to detect them. To efficiently generate phonons of a given frequency, the ultrashort pulse duration needs to be at most half its period. In the same way, the probe senses the reflectivity variation within its pulse duration due to an averaging effects.

4.4 Hybrid resonator by band inversion at 18 GHz

Multilayer systems like the $GaAs/AlAs$ heterostructures used in this work can be engineered to confine interface states between concatenated distributed Bragg reflectors [125, 154]. An example of such a structure was presented in the previous chapter where, by exploiting the symmetries of the different bands in a superlattice Brillouin zone, a mode confined by band inversion [150–152] was sustained between two perturbed Bragg reflectors. In section 4.3, we have presented experimental results on the study of a resonator by band inversion confining acoustic phonons at 200 GHz. In general, the engineering of confined interfaces modes exploiting geometric phases has been investigated in different fields of physics [125, 227–234]. Nevertheless, most experimental demonstration have so far target a single kind of excitation. In this section, we present the experimental results of the study of a hybrid resonator by band inversion featuring simultaneous confinement of phonons and photons. Embedded structures like the one presented in the previous section allow to confine both light and sound taking advantage on the different scales, but imposes constraints on the scale of the acoustic wavelengths relative to the optical wavelengths which need to be at least an order of magnitude smaller. In addition, the spatial profile of acoustic and optical fields partially overlap. Taking this into consideration, an optomechanical platform where the overlap between strain and electric fields is maximized would constitute an interesting platform for the study of photon-phonon interactions. Moreover, if the confined modes are obtained by band inversion between different superlattices the robustness shown for purely acoustic devices in previous works should be present as well [125].

All multilayer structures experimentally studied were formed by layers of $GaAs$ and $AlAs$ (or their alloys). These materials present a very particular relationship between their optical and acoustic properties. First, the ratio between the speeds of light in the two materials is approximately the same as the ratio between the speeds of sound in the same materials $c_{GaAs}/c_{AlAs} \approx v_{GaAs}/v_{AlAs} \approx 1.2$. Second, the same approximation holds for the ratios between the index of refraction and acoustic impedance $n_{GaAs}/n_{AlAs} \approx Z_{GaAs}/Z_{AlAs} \approx 0.82$. Because of this coincidence of nature one can design a multilayer structure that confines both light and sound simultaneously [69, 237]. This type of structure works both as an optical cavity and as an acoustic resonator confining acoustic and optical modes of the same wavelength ($\lambda_{optics} = \lambda_{acoustic}$). This is in contrast with the previous approach (see section 4.3) were the wavelengths of optical and acoustic wavelength confined differed by more than one order of magnitude ($\lambda_{optics} \gg \lambda_{acoustic}$), allowing to embed an acoustic structure within an optical cavity as its spacer.

4.4.1 Hybrid resonator by band inversion design

In this section we present the design of an acoustic resonator confining both photons and phonons in an interface mode by band inversion. The design concept was the same as from previous implementations [125, 154] but it targeted acoustic phonons at frequencies allowing simultaneous confinement of acoustic and optical modes. Approximately at 18.3 GHz the acoustic wavelengths in $GaAs$ is equal to the optical wavelength of light at 925 nm in free space. For these frequency and wavelength values, two distributed Bragg reflectors were designed and grown one on top of the other. The sample was fabricated by molecular beam epitaxy (MBE) and grown on a (001) $GaAs$ substrate.

The acoustic and optic multilayer structure was grown by alternating layers of $Al_{0.95}Ga_{0.05}As$ and $GaAs$. First, a $(3\lambda/4, \lambda/4)$ distributed Bragg reflector (DBR) at 18.3 GHz with 16 unit cells was grown. Layer periods were 195.1 nm and 76.9 nm for $GaAs$ and $Al_{0.95}Ga_{0.05}As$, respectively. The $Al_{0.95}Ga_{0.05}As$ acoustic ratio of all cells $r = 0.25$ together with equation 3.9 indicates that this design corresponds to a superlattice with its second minigap (centered at 18.3 GHz) maximally opened. On top of it, a second DBR is grown with 14 cells and $(\lambda/4, 3\lambda/4)$ at 18.3 GHz. Layer periods were 65 nm and 230.7 nm for $GaAs$ and $Al_{0.95}Ga_{0.05}As$, respectively. With $r = 0.75$, this DBR also corresponds to a superlattice with its second minigap maximally opened, but its band edge symmetries of the Bloch modes are inverted with respect to the bottom DBR. The resulting structure features a confined 18.3 GHz acoustic interface mode between the two concatenated DBRs.

The resonator and cavity structure was fabricated using unit cells formed of three layers and centered in the $Al_{0.95}Ga_{0.05}As$ layer. By doing so the full multilayer structure is symmetric and the confined interface mode appears at the centered of the engineered minigap (instead of red shifted from the minigap center [125]). The cell design for the bottom DBR (on the substrate side) then corresponds to $(\lambda/8, 3\lambda/4, \lambda/8)$, where we have extend the nomenclature used to represent bilayer unit cells to represent cells formed of three layers of $GaAs$, $Al_{0.95}Ga_{0.05}As$ and $GaAs$, respectively. Using the same notation, the top DBR is formed by $(3\lambda/8, \lambda/4, 3\lambda/8)$ cells, also centered in the $Al_{0.95}Ga_{0.05}As$ layer. The selection of this kind of symmetric cells leads to unit cells with boundaries that are not interfaces between materials. In particular, the boundary between the two DBRs occurs inside a $GaAs$ layer. Then, the acoustic confined mode at 18.3 GHz for which we design our structure is supported at the interfaces between the

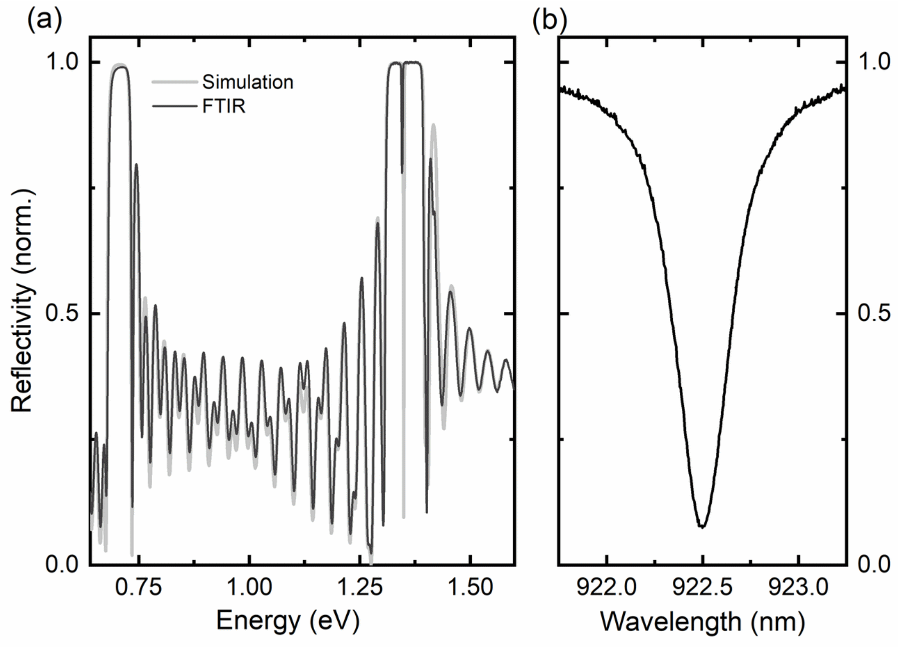

Figure 4.10: Optical reflectivity of the hybrid resonator by band inversion. (a) The measured optical reflectivity showing a high reflectivity region associated to the DBRs of the resonator and, in the middle of it, a dip signature of a confined optical mode. (b) Zoom-in the optical reflectivity spectrum showing the confined mode centered at 922.5 nm (1.34eV).

two DBRs but not at an interface between different materials.

4.4.2 Hybrid resonator by band inversion experimental results

The hybrid resonator by band inversion features the co-localization of optical and acoustic modes with Q-factors of around 2000. The presence of a confined optical mode was experimentally probed by Fourier-transform infrared spectroscopy (Bruker Equinox 55 with Hyperion Microscope, halogen lamp illumination). Figure 4.10 presents the reflectivity spectrum of the sample, and a zoom in (panel (b)) shows the optical cavity mode centered at around 922.5 nm. For the experimental demonstration of acoustic confinement, we detected acoustic phonons in TDBS experiments where we tuned the ultrafast laser wavelength along the optical cavity mode of the hybrid resonator. By doing so, we investigate the optical cavity dynamics, the role it plays in the detection of coherent phonons in TDBS experiments when pump and probe pulses are simultaneous tuned (or detuned) from the optical cavity mode and its impact on the measured phononic spectra. In addition, both optical and acoustic modes confined are resulting from band inversion between superlattices and therefore should feature the same robustness shown for the acoustic case demonstrated through in previous works [125].

By means of the TDBS technique we study the sample working as an acoustic resonator at 18.3 GHz and optical cavity at around 922.5 nm simultaneously. The experimental setup featured a spatial mode filtering stage using single-mode fibers and a free-space coupling into the cavity mode (see section 4.1.1). The laser pulses used during the experiment had a duration of 3.4 ps and approximately matched the optical cavity mode width (full width at half maximum of ≈ 0.5 nm). With such a spectral resolution we were able to study the resonator by tuning the laser wavelength across the cavity mode. This can be easily implemented by taking advantage of the sample gradient[3]. The power of the pump and probe beams were 50 mW and 10 mW, respectively. A total of 12 ns delay between pump and probe is scanned, covering almost the full laser repetition period. The reflectivity trace after the pump and probe simultaneous arrival

---

[3] Samples fabricated with a gradient feature a 30% variation in all layers nominal thicknesses along the full wafer (51 mm). Consequently the acoustic and optical resonant wavelengths vary in 30% as well.

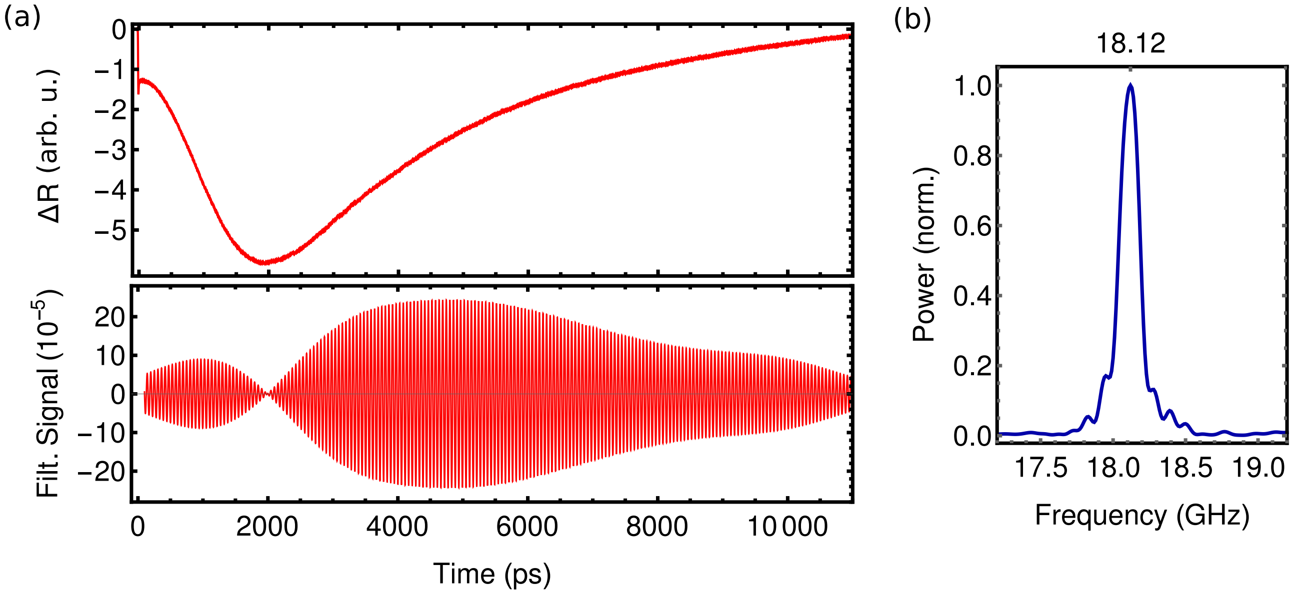

Figure 4.11: (a) Top: instant differential reflectivity time trace as a function of time delay between pump and probe for a $\lambda - \lambda_{cav} \approx 0.79$ detuning. Bottom: Instantaneous reflectivity signal after differentiation and using a bandpass filter between 17.97 GHz and 18.25 GHz. (b) Spectra obtained from the FFT of the time trace showing a resonant confined mode at 18.12 GHz.

spans 11 ns, within this window the trace is differentiated and Fourier transformed to obtain the acoustic spectrum of the hybrid resonator.

Figure 4.11 presents the measured results with the laser tuned on the blue slope of the cavity mode of the structure. Panel (a) top plot presents the time trace recorded in this structure. First, at zero delay the pump pulse is focused on the sample and triggers an electronic response of the system, electron-hole pairs are produced and the reflectivity response of the system blue shifts. Then, a slower evolution on the nanosecond time scale sends back to the equilibrium state of the system prior to the pump excitation while electron-hole pairs recombine. In the process we see a change in the direction the reflectivity changes induced by the dynamics of the cavity mode returning to its position before zero delay. Near 2 ns after the pump arrived to the sample we see a minimum in reflectivity which marks the moment at which the cavity reflectivity dip minimum is sensed at the probe arrival. After differentiation and Fourier transforming the time trace, information about the resonant modes of the studied structure is obtained. Figure 4.11 (b) presents the measured spectral peak associated to the interface state between DBRs. To show how this mode manifests while the system goes back to equilibrium we apply a Savitzky-Golay filter [238] at our differentiated time trace signals. By doing so, we are able to see the reflectivity oscillations induced by the phonons in our sample. Figure 4.11 (a) bottom panel shows the plot resulting after using a filter between 18.97 GHz and 19.25 GHz on the reflectivity time trace. When the probe arrives to the sample and its cavity mode is aligned with the laser wavelength, we see the oscillations disappear near 2 ns after the pump arrival.

The results from measuring at different detunings from the cavity mode central wavelength are presented in figure 4.12. On the left, the reflectivity spectrum is plotted around the cavity mode. The spectrum is cut below detunings $\lambda - \lambda_{cav} \approx 1.1$ nm since we are presenting an interpolated function aiming to reproduce the dip shape, not its full vicinity. Next to the curve, a series of 12 points are plotted marking each detuning value where measurements took place. These are plotted top to bottom from the most red-shifted to the most blue-shifted. On the right of figure 4.12 and in the same order from top to bottom, we show the Fourier transform obtained at each detuning. The dashed vertical line serves as a guide to the eye marking the region of interest where the presence of confined acoustic phonons manifest. While most of the spectra features a single peak associated to our sample's resonant frequency, there are three spectra showing a splitting with two peaks in the region of interest. In order to understand this behavior

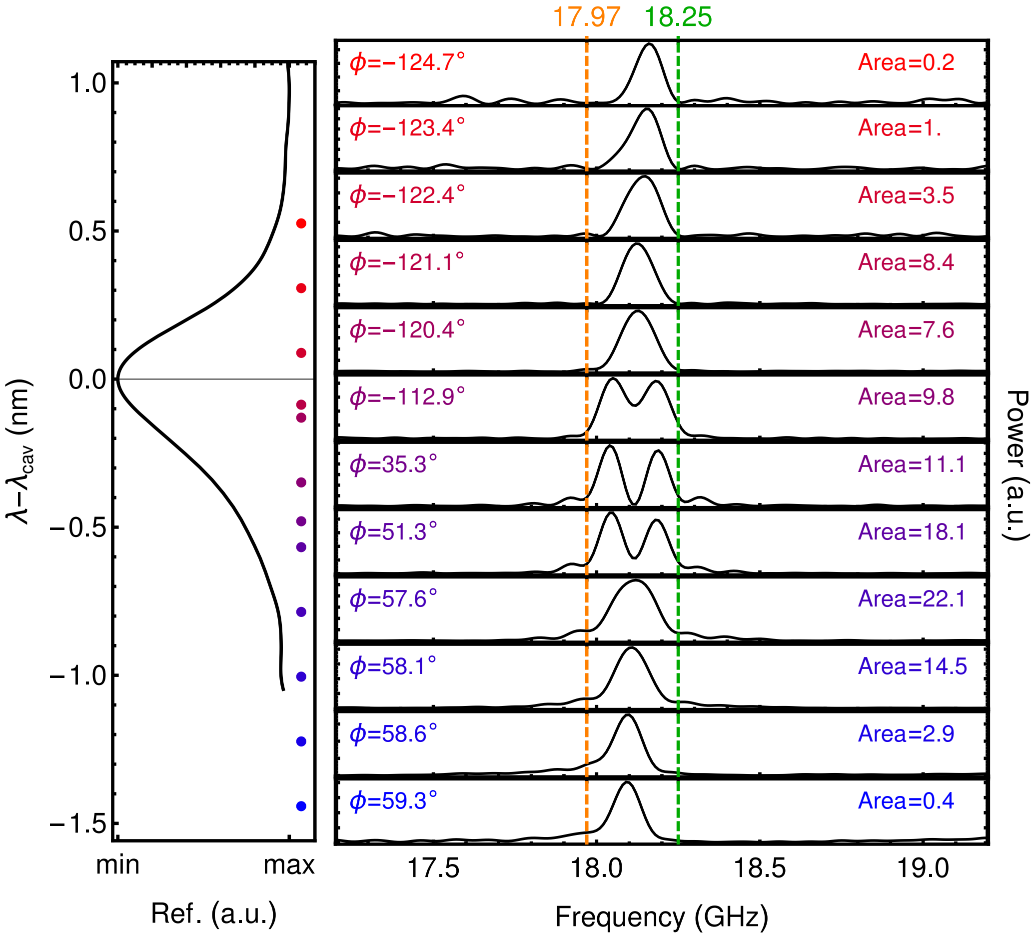

Figure 4.12: Left: Reflectivity curve showing the cavity mode of the topological resonator as function of the cavity detuning $\lambda - \lambda_{cav}$. Colored points indicate measurement positions marking the central wavelength of both pump and probe pulses. Right: Fourier transform of the entire 0-11000 ps experimental time window for each of the measurements. Ordered from top to bottom from the most red-shifted towards the most blue-shifted detuning. Left insets indicate the phase (ϕ) used to maximize the demodulated signal at 0 ps. Right insets indicate the area under the plotted curve.

we have to consider the cavity dynamics involved in the phonon detection. Immediately after the pump pulse arrives at the sample there is a rapid electronic response of the system. This response effectively blue-shifts the cavity mode and places the probe wavelength at a new position with respect to the reflectivity dip i.e. at a different detuning. After this rapid change, the system red-shifts going back to its equilibrium position slowly, meaning on a nanosecond time scale. In this time-resolved scheme to detect phonons, the more sensitive the sample reflectivity is to detuning the better. This happens because the presence of phonons acts as a tiny modulation in the detuning at the phononic frequency. Then, the larger the slope in the reflectivity spectrum is at a given detuning the greater the phononically induced reflectivity oscillations. Furthermore, depending on which side of the cavity mode the detection takes place there is a sign change in the oscillations amplitude given by the difference between a positive and negative slope [215]. This will become key to understanding the splitting seen in the spectra.

In order to ease the description of the detection process let us consider three regimes corresponding to different detunings. The first regime corresponds to large blue-shift detunings $\lambda - \lambda_{cav} < -0.6$ nm. In these conditions the rapid electronic change is not large enough to reach the reflectivity minimum of the cavity mode with the probe. Then, only one side of the mode is dynamically probed during the scan of the delay line i.e. only one slope is sensed while the system goes back to equilibrium. This type of dynamics results in the four spectra

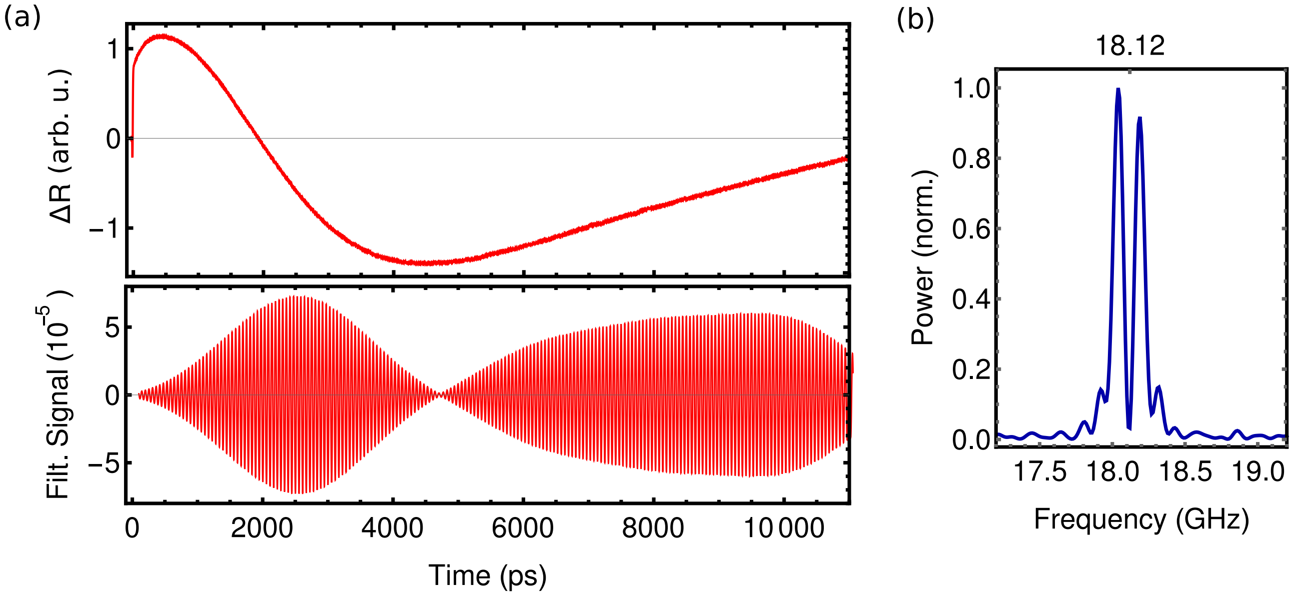

Figure 4.13: (a) Top: instant differential reflectivity time trace as a function of time delay between pump and probe for a $\lambda - \lambda_{cav} \approx 0.48$ detuning. Bottom: Instantaneous reflectivity signal after differentiation and using a bandpass filter between 17.97 GHz and 18.25 GHz. (b) Spectra obtained from the FFT of the time trace showing a resonant confined mode splitted in two near at 18.12 GHz.

shown in the bottom of figure 4.12 right panel. For the second scenario let us consider the first five cases in this figure with detunings $\lambda - \lambda_{cav} > -0.2$ nm. In these five cases the Fourier transform presents a single peak too, because (mainly) only one side of the cavity mode is sensed while the system goes back to equilibrium. In this case, the slope of the cavity mode on the red side is the one sensed, then, we expect an opposite sign in the reflectivity phononic induced oscillations with respect to the previous scenario. Finally, the third scenario lies between the two previous cases with detunings -0.2 nm $> \lambda - \lambda_{\text{cav}} > -0.6$ nm. In this condition, the rapidly induced shift passes by both slopes of the cavity mode causing that, while the system goes back to equilibrium, the reflectivity senses both the positive and negative slopes with comparable contributions over the course of a full delay line scan. This behavior can be modeled as a signed amplitude modulation of the phonon induced reflectivity oscillations. As a direct consequence of this, while the phonons are present at the resonant frequency only, they cause a reflectivity modulation whose Fourier transform splits this peak in two. We can reproduce this behavior by considering a periodic signal with an amplitude modulation of the form $s(t) = \cos(w_{amp}t)\exp(-iw_{phonon}t)$ where t represents the time delay between pump and probe reflection on the sample. Taking the Fourier transform (FT) of this modeling function we obtain $FT(s(t)) = S(w) = \sqrt{\pi/2}(\delta(w-(w_{phonon}-w_{amp})) + \delta(w-(w_{phonon}+w_{amp})))$. The result shows a splitting of $2w_{amp}$ around the w_{phonon} resonant frequency modeled by the periodic function. The reflectivity time trace presented in figure 4.13 (a) exhibits this behavior. It was measured at a detuning $\lambda - \lambda_{cav} \approx -0.48$ nm, farther away from the central wavelength of the cavity mode before the arrival of the pump one the sample. At a time delay of 4.2 ns we see how the system's cavity mode passes by the minimum in reflectivity. Since the expected oscillation in reflectivity depends not only on the presence of phonons but also on a sensitivity function from the cavity, phonons cancel their contribution to the reflectivity change. This is shown in figure 4.13 (a) presenting the differential reflectivity time trace after applying a bandpass filter between 17.97 GHz and 18.25 GHz. The zero sensitivity region reduces the amplitude of the oscillations to zero near 4.5 ns time delay. The shift of 4.5 ns − 4.2 ns = 300 ps between the total extinction of phonons and the minimum in reflectivity can be explained by the asymmetry of the cavity mode. Figure 4.13 (b) presents the spectrum obtained from that measurement. Two peaks as expected from the probe sensing both cavity slopes are identified. The obtained

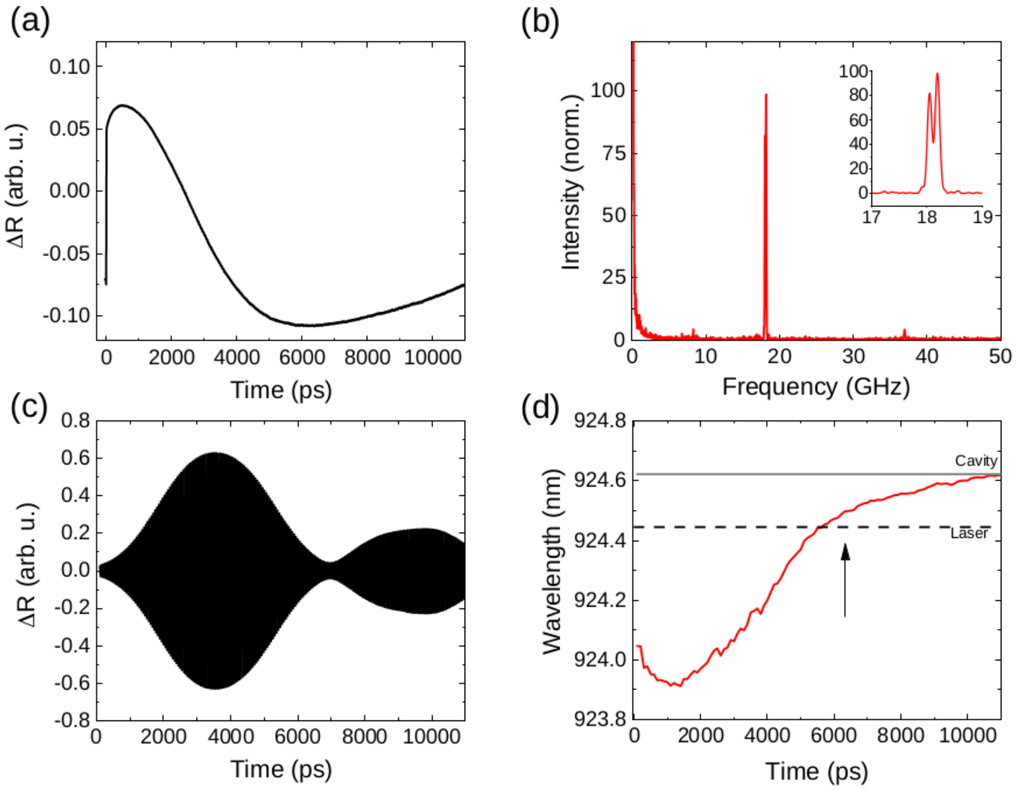

Figure 4.14: (a) Time resolved reflectivity trace for which an splitting in the phononic spectrum is observed. (b) Phononic spectrum obtained from the resonator by band inversion. A mode at 18.12 GHz is observed. The inset presents a zoom in the resonant peaks showing a split with a separation of 140 MHz. (c) Reflectivity time trace from panel (a) after passing a bandpass filter (17.97 GHz to 18.25 GHz). Coherent phonon oscillations are visible and present envelope modulated over time delay. (d) The envelope in panel (c) is the result of the effect of the optical cavity dynamics while the system relaxes to equilibrium after the pump excitation. The red line indicates the center of the cavity mode as a function of time delay. The dashed line marks the laser wavelength (fixed). The grey line indicates the optical cavity wavelength before the pump excitation. The arrow indicates the moment when the laser passes by the cavity mode making the probe signal insensitive to phonons.

results demonstrate the dynamic interaction between the photonic interface mode, determining the sensitivity to the present phonons, and the confined phononic mode by band inversion, which is at the origin of the modulated signal in the gigahertz range.

In order to validate the hypothesis of the optical cavity mode varying position and therefore affecting the phononic spectrum, we proceed to measure the spectral cavity mode as a function of delay. We first reproduce the measurement conditions where we expect a split in the resonant peak of the structure. Then, instead of focusing the probe signal at a photodiode, we use it as an input in the double Raman spectrometer. In this configuration, we are able to track the center of the optical cavity mode as a function of time delay. The measurement was not done within the same day of the previous scan and slightly different conditions used. First, since the sample has a gradient and the measurement position was not exactly the same, the optical cavity mode was now located at 924.62 nm. Pump and probe powers used were 50 and 8 mW, respectively and the pulse duration was 3.4 ps. The laser was tuned at 924.44 nm such as pump-probe measurements were obtained where a resonant splitted peak was observed. Figure 4.14 presents the results of this experiment. Panel (a), (b) and (c) show the time resolved reflectivity trace, the phononic spectrum and the filtered time trace (17.97 GHz to 18.25 GHz). In panel (d) we present the trajectory followed by the center of the optical cavity mode as a function of time delay. We can observe how the change in the reflectivity time trace is correlated to the optical cavity dynamics shifting the cavity center. The arrow marks the position of the laser and when the optical cavity passes through it, we can see in panel (c) how the envelope of the phononic oscillations reaches a minimum. In addition, at delays below 1 ns the cavity keeps blue shifting as a result from thermal effects. This spectral scan validates the role the optical cavity dynamics play in the measured phononic spectrum in TDBS experiment in samples with optical cavities. We can not assume that the phononic spectrum is a direct observation of only the phonons present in the sample, but also of the interplay between them and the cavity dynamics.

4.5 Hybrid Fabry-Perot resonator at 18 GHz

In this section we tested the capabilities of the TDBS setup for fibered nanophononic devices. In order to do so, we exploited again the co-localization properties of $GaAs$ and $AlAs$ by performing experiments on hybrid resonators engineered following a Fabry-Perot design. The co-localization on hybrid structures, as shown in the previous section, offers a suitable platform for TDBS experiments when measuring coherent phonons with laser light tuned at the optical cavity mode of the structure. These experiments allowed us to characterize the hybrid Fabry-Perot resonator, study its corresponding phononics spectra and, by doing so, asses the capabilities of the fibered TDBS setup. As a results of the versatile setup to perform TDBS experiments, we investigate the optical cavity dynamics as a function of pump power. The detected time resolved reflectivity traces unveil information about the cavity dynamics and phononic spectra with varying pump powers over more than five orders of magnitude.

4.5.1 Hybrid Fabry-Perot resonator design

We designed an optical Fabry-Perot cavity made of two $Al_{0.1}Ga_{0.9}As/Al_{0.95}Ga_{0.05}As$ distributed Bragg reflectors around a $\lambda/2$ $GaAs$ spacer. Here, λ represents the wavelength of both optical and acoustic waves to be confined in the structure ($\lambda = \lambda_{optics} = \lambda_{acoustic}$). The sample was fabricated by molecular beam epitaxy (MBE) and grown on a (001) $GaAs$ substrate. The first distributed Bragg reflector (substrate side) was formed of 18 unit cells, followed then by a spacer of half a wavelength, finally, on top of it (cap side), the second distributed Bragg reflector formed of 14 unit cells. Both optical and acoustic waves are confined in this structure and have wavelengths of the same size. Confinement occurs for light of 915 nm wavelength in free space and for sound waves at a frequency of 18.4 GHz, both corresponding to a roughly 260 nm wavelength in $GaAs$.

Figure 4.15 presents a schematic of the Fabry-Perot structure doubling as both optical cavity and acoustic resonator. On the bottom left and right the acoustic and optical reflectivities are plotted, respectively. In the case of the acoustic reflectivity we considered the case where the resonator is surrounded by a uniform ambient of GaAs. This uniform boundary condition for the acoustic case ensures a reflectivity different from zero (as it would be the case with the air interface) which unveils the presence of a confined mode in the reflectivity simulations. In both reflectivity plots, high reflectivity regions appear as expected from the DBR structures and, in the middle, a dip associated with the confined acoustic and optical modes. In the GaAs spacer between the DBRs, both modes spatially overlap. We can see this by simulating a displacement wave and an optical wave propagating towards the structure. In the middle of figure 4.15 we see a zoom in the spacer and plotted over it the acoustic displacement (u) and electric field (E) in this region. The overlap between both fields is almost perfect given the simulated scenario. Note that while the overlap between displacement and electronic field is almost perfect, it is the strain field which is the relevant quantity for the Raman cross section (equation 2.36). Figure 4.16 presents the displacement amplitude ($|u|$) as a function of position along the full structure. The maximum in amplitude coincides with the spacer of the structure, region where the greater contribution to the probe signal comes from experiments. The TDBS experiment in hybrid structures with co-localized modes allows us to retrieve information about the acoustic

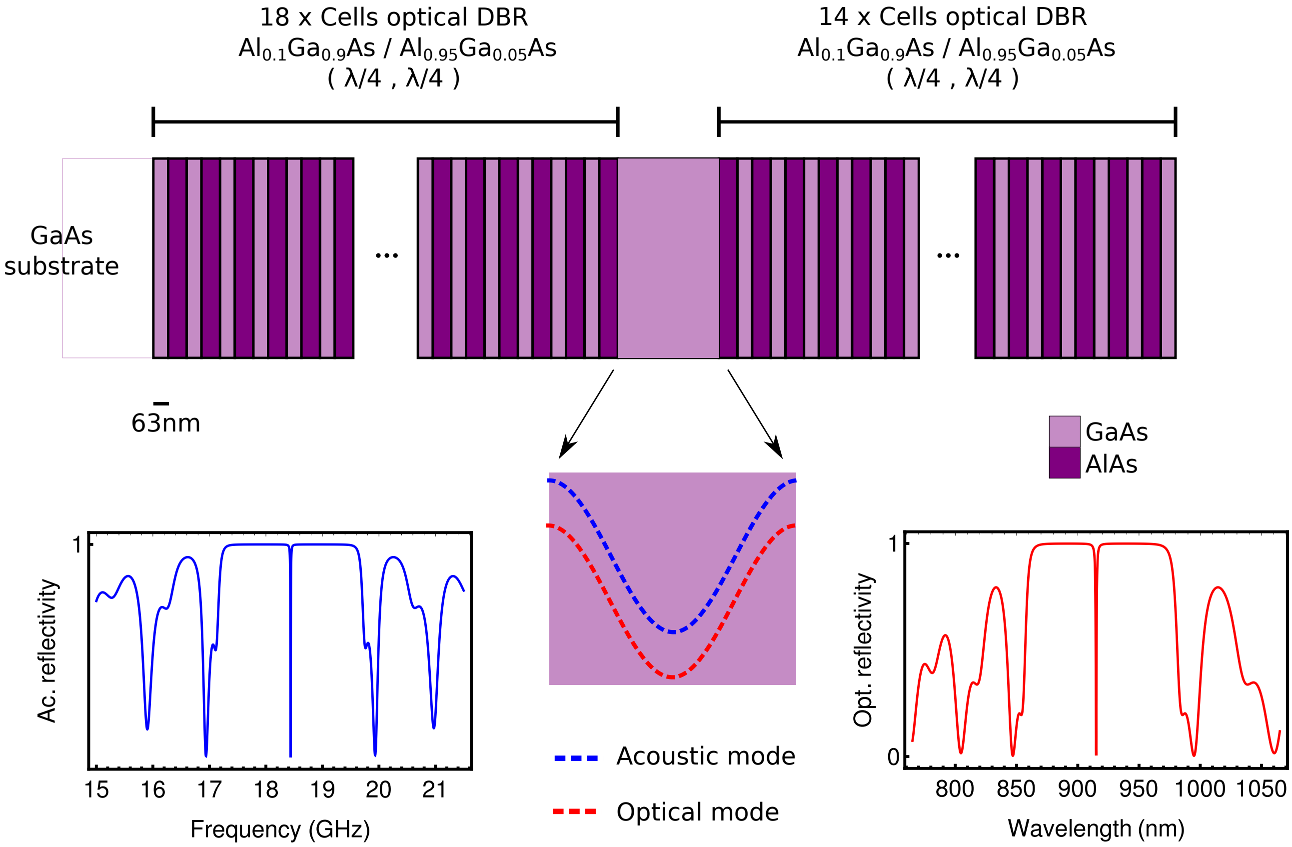

Figure 4.15: Schematic of the hybrid Fabry-Perot resonator structure. Two DBRs doubling as both acoustic and optical mirrors confined light and sound in a *GaAs* spacer. The results is both a cavity at 915 nm and a resonator at 18.4 GHz. A zoom in the central spacer shows the optical (red) and acoustic (blue) confined fields in it. We can see the high level of overlap between them given the double coincidence between *GaAs* and *AlAs* properties. The simulated acoustic and optical reflectivity is plotted at the bottom left and right, respectively. For the acoustic case, we considered the structure surrounded by *GaAs* for the reflectivity TMM simulation.

modes and how they manifest when the structure doubles as an optical cavity.

4.5.2 Hybrid Fabry-Perot resonator experimental results

Quandela SAS glued the hybrid Fabry-Perot featuring confinement of optical and acoustic waves to a single-mode fiber. The fiber integrated sample can be seen in pictures provided by Quandela SAS before and after the adhesive bounding. Figure 4.5 (b) presents a picture of the fiber before (left) and after (right). Using the TDBS experimental setup for connected devices we measure time resolved reflectivity traces from the Fabry-Perot resonator and cavity. A total of 60 time traces were recorded with the delay line moving at 10 mm/s. At this speed, we could cover the entire delay line range for our measurements in approximately one minute, and complete the full set of traces in half an hour. Approximately 11.5 ns of delay between pump and probe were covered for each trace. The two remarkable features the fiber connected resonator presents are that no alignment is required on the sample and the coupling into the cavity mode is much more efficient than in a free space coupling scheme. This measurements were done working with the laser wavelength at 917.58 nm i.e. in resonance at the cavity mode, the pump power was only of 1 mW and the probe 200 μW. In free space, the powers commonly used are at least one order of magnitude larger [239, 240].

Figure 4.17 (a) shows one of the reflectivity time traces recorded during the experiment. As in the case of the adiabatic resonator there is a drastic change in the reflectivity of the sample upon the arrival of the pump. By having the laser wavelength tuned at the center of the cavity mode, when the pump pulse reaches the sample, the electronic response of the system results

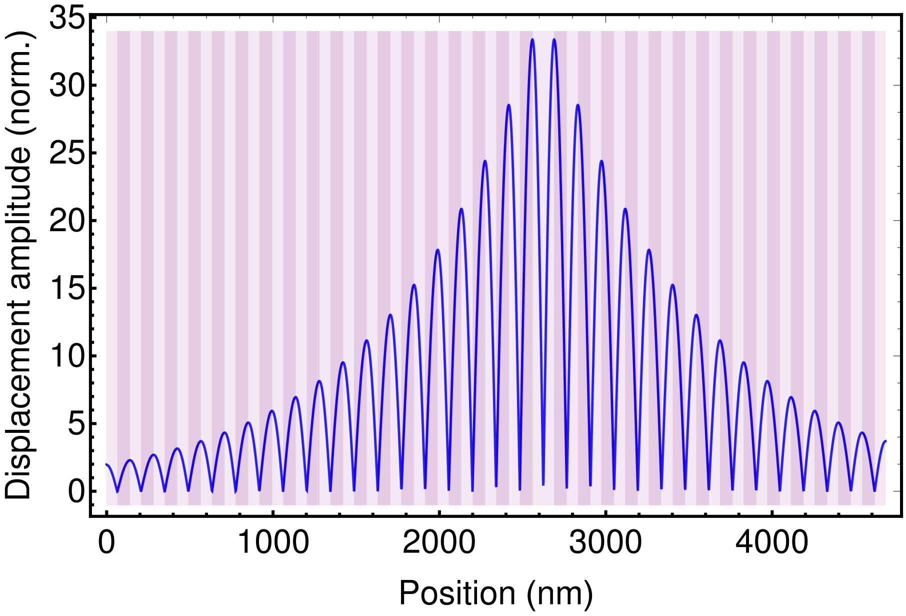

Figure 4.16: Normalized displacement amplitude ($|u|$) as a function of position along the hybrid Fabry-Perot resonator. The normalization is done with respect to the input acoustic field coming from the substrate side (position below zero).

in an increase in the amount of light absorbed. Then, the sample relaxes back to equilibrium reaching the same reflectivity as the one measured before the pump was reflected. The phonons, generated by the pump, are then sensed by the optical reflectivity of the probe as a function of delay. To reveal the effect of phonons in our time trace we process it by differentiating and applying a Fourier transform over a total window of 11 ns starting 40 ps after the simultaneous arrival of pump and probe (this serves the purpose to remove the rapid variation component just after zero delay). In figure 4.17 (b) we present the spectrum obtained, two main peaks are clearly distinguished at 18.3 GHz and 54.9 GHz corresponding to the first and third harmonic of our resonator. The intensity of the peaks and the fact that only odd harmonics are visible in the spectrum results from the dependence of the Raman cross section on the overlap between strain and light fields. The optical and acoustic fields have an outstanding overlap at the spacer at the cavity mode (915 nm) and the resonant frequency (18.3 GHz). From the photoelastic model, at multiples of the resonant frequency the overlap between acoustic and optical fields can be not null. This is the case when both strain and electric modes share parity, which for a $\lambda/2$ spacer of the studied structure is odd. This is, however, a simplified picture of the system. In the experimental realization, the detected signal will depend on the distribution of the field along the full structure. Figure 4.17 (b) presents multiple peaks around the second harmonic at 36.6 GHz. We need to take into a account the full structure to comprehend the origin of these peaks. Using the transfer matrix method together with the photoelastic model presented in chapter 2, we simulate both optical and acoustic fields and compute the expected pump and probe detection spectrum presented in figure 4.18 (a). In contrast with our experimental results each harmonic presents features at different scales. Because of this, a zoom window of ×100 is used up to 25 GHZ and then a second ×10 zoom from 25 GHz to 50 GHz. While the relative power between the first and third harmonic is drastically different, the shape with multiple peaks at the second harmonic now appears from the simulation results as well. Figure 4.18 (b) shows from left to right, a zoom in at the first, second and third harmonics of both experimental and simulated spectra, respectively. The main features present in the experimentally obtained spectrum are mostly reproduced by the simulations. However, the alignment between peaks is not ideal and a splitting in each peak is visible which might result from the optical cavity playing a role in the detection process. The disagreement might be related with the assumption that all layers have the same photoelastic constant, which is not true in the real case. Nevertheless, we have to remark that the parameter used for all the three panels in figure 4.18 (b) are the

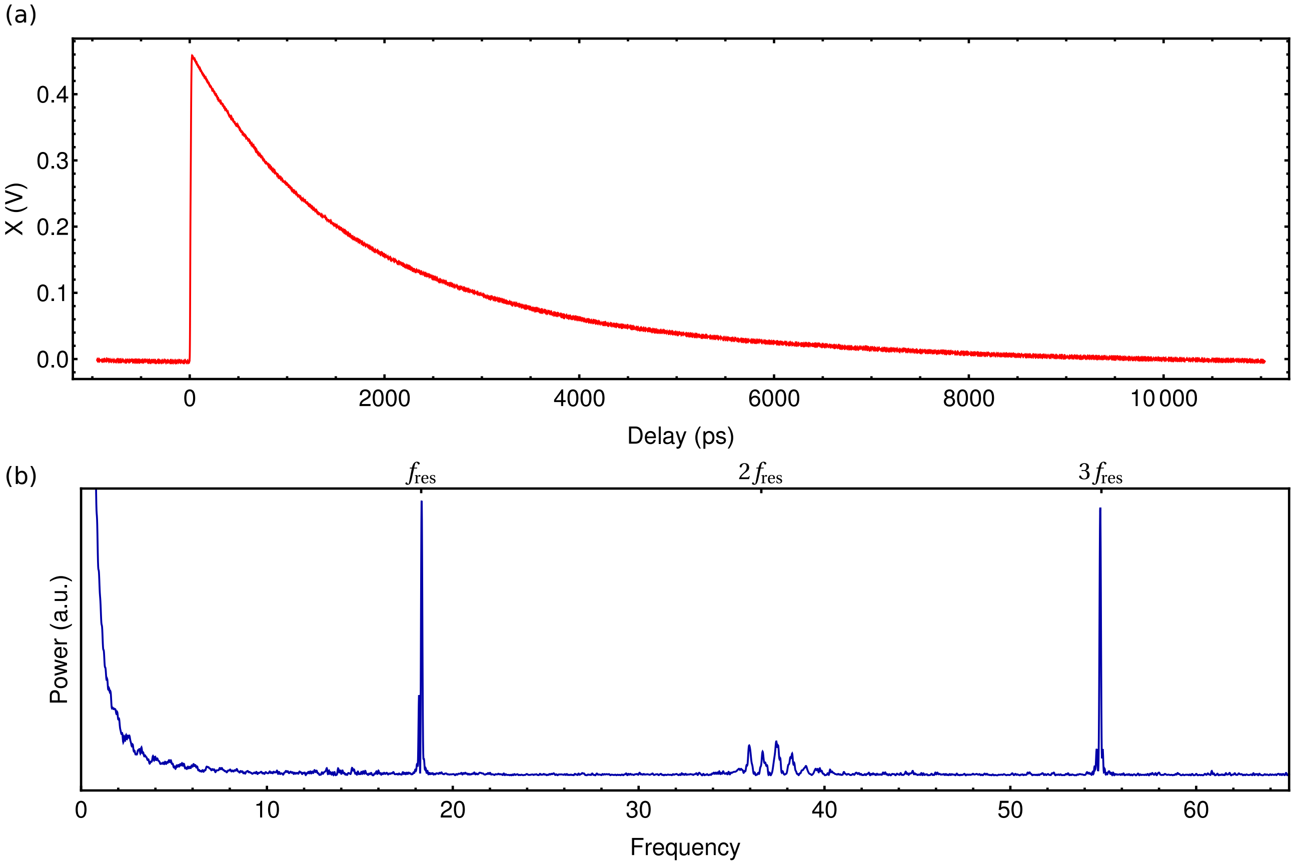

Figure 4.17: (a) Instantaneous reflectivity as a function of time. After the pump strike the sample the reflectivity changes drastically varying the amount of probe being reflected. Then, they system and its reflectivity with it go back to its equilibrium. (b) Fourier transform of the differentiated signal. A window from 40 ps to 11040 ps was used.

same, therefore, despite small shifts, the alignment seems remarkable for frequencies working at different scales (the acoustic wavelength in *GaAs* at 18.3 GHz is approximately 261 nm while for 54.9 GHz is 87 nm).

The experimental characterization of the fiber integrated hybrid Fabry-Perot resonator allowed us to resolve up the third harmonic resonant in the structure. Using the TDBS technique, we were able to obtain the spectrum presented in figure 4.17 after accumulating 60 time resolved reflectivity traces in an experiment that lasted approximately 30 minutes. Motivated by the good results obtained, we proceed to perform a systematic study of the integrated Fabry-Perot resonator at different pump powers. In order to avoid a change in the laser conditions during the power scan it is critical that the experiment is done in the shortest period of time. The use of the fiber integrated device allowed us to accomplish this by performing fast measurements where we can obtain an individual phononic spectrum after only five minutes of integration i.e. after accumulating 20 time resolved reflectivity traces each one covering up to 10 ns of delay. The experiment was done by fixing the probe power at 700 μW while varying the pump power from 1 μW up to 20 mW. The complete power scan covered a total of 24 different pump powers: 0.001, 0.002, 0.005, 0.010, 0.025, 0.050, 0.1, 0.3 and 0.5 mW, from 1 to 10 mW in steps of 1 mW, and from 12 to 20 mW in steps from 2 mW. The laser was kept pulsing in the same condition during the full experiment delivering pulses of 3.8 ps full width at half maximum. The pulse central wavelength was tuned to the optical cavity mode at 917.58 nm.

Figure 4.19 presents the results of the power scan measurements done in the hybrid Fabry-Perot resonator. Panel (a) presents in a color map the time resolved reflectivity trace as a function of pump power. The color map is built after interpolating along the 24 measured traces. While for all traces at zero delay there is a rapid change in reflectivity, we can distinguish three intervals of power with different behaviors. Up to 10 mW , we see how the drastic change

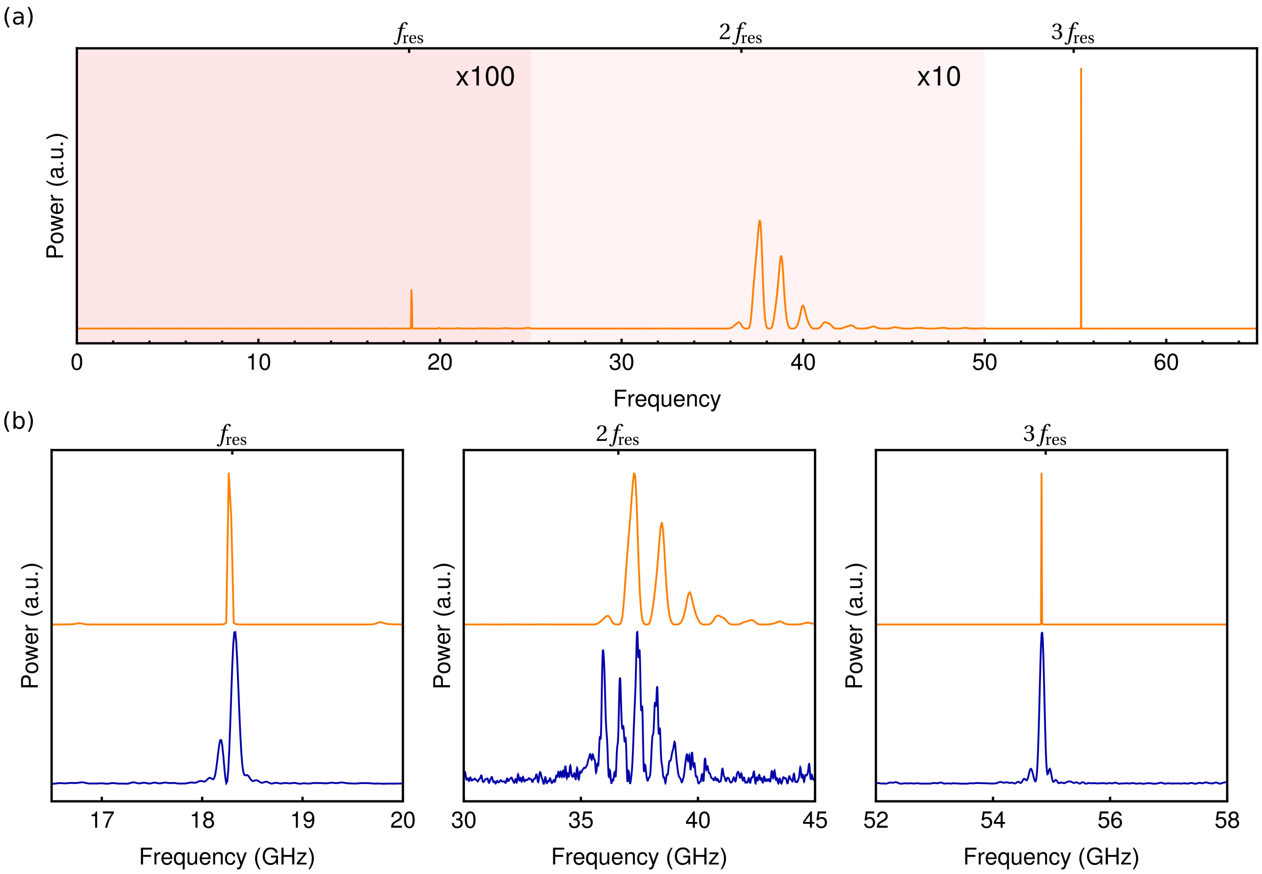

Figure 4.18: (a) Simulated pump and probe detection spectrum obtained for the resonator/cavity design. A ×10 zoom is done from 25 GHz to 50 GHz to visualize the second harmonic peaks. A ×100 zoom is done up to 25 GHz to visualize the resonator mode (first harmonic) peak. (b) The experimental (dark blue) and simulated (orange) spectra are plotted around the first, second and third harmonics.

in reflectivity at zero delay depends on the pump power, reaching its maximum variation at roughly 10 mW. At this limit, we are saturating the electronic response of the system, i.e. reaching a maximum of electron holes production. Between 10 and 15 mW, the time resolved reflectivity trace remains approximately constant within the first nanosecond. After it, we see a shifts towards lower delays of the profile followed by the time trace. Finally, between 15 and 20 mW we can see a clear shift towards lower delays of the time trace curve. We attribute the effects seen in power above 10 mW to the heating effect of the pump power on the sample. While we increase the pump power, there is a point when there is not enough time between consecutive pump pulses for the system to cool down. The results, is that there is accumulation of thermal energy in the sample, effectively red shifting the reflectivity of the resonator. Nevertheless, at the three power intervals we can see traces where oscillations due to the presence of phonons are distinguished. Figure 4.19 (b) present in a color map, the phononic spectrum as a function of pump power. The data for the color map is obtained by processing the time resolved reflectivity traces using a Savitzky-Golay filter [238], substracting each filtered curve from its corresponding time trace and finally Fourier transforming the results to obtain the phononic spectra of the 24 measurements. The color map is then obtained by interpolating along each the full set of spectra. For each power the color map presents an intense peak around the resonant frequency. At high power, the intensity of the resonance increases so much it reduces the contrast of the peaks at lower pump power, therefore a zoom in to the color map between zero and 6 mW is presented in panel (d). Tracking the resonant peak in the zoomed area we see how it reaches its maximum values at 3 mW and then reduces in intensity when the power keeps increasing. In panel (b) we see how this peak appears to splits in two between 6 and 15 mW. Towards higher values, more peaks are distinguished on

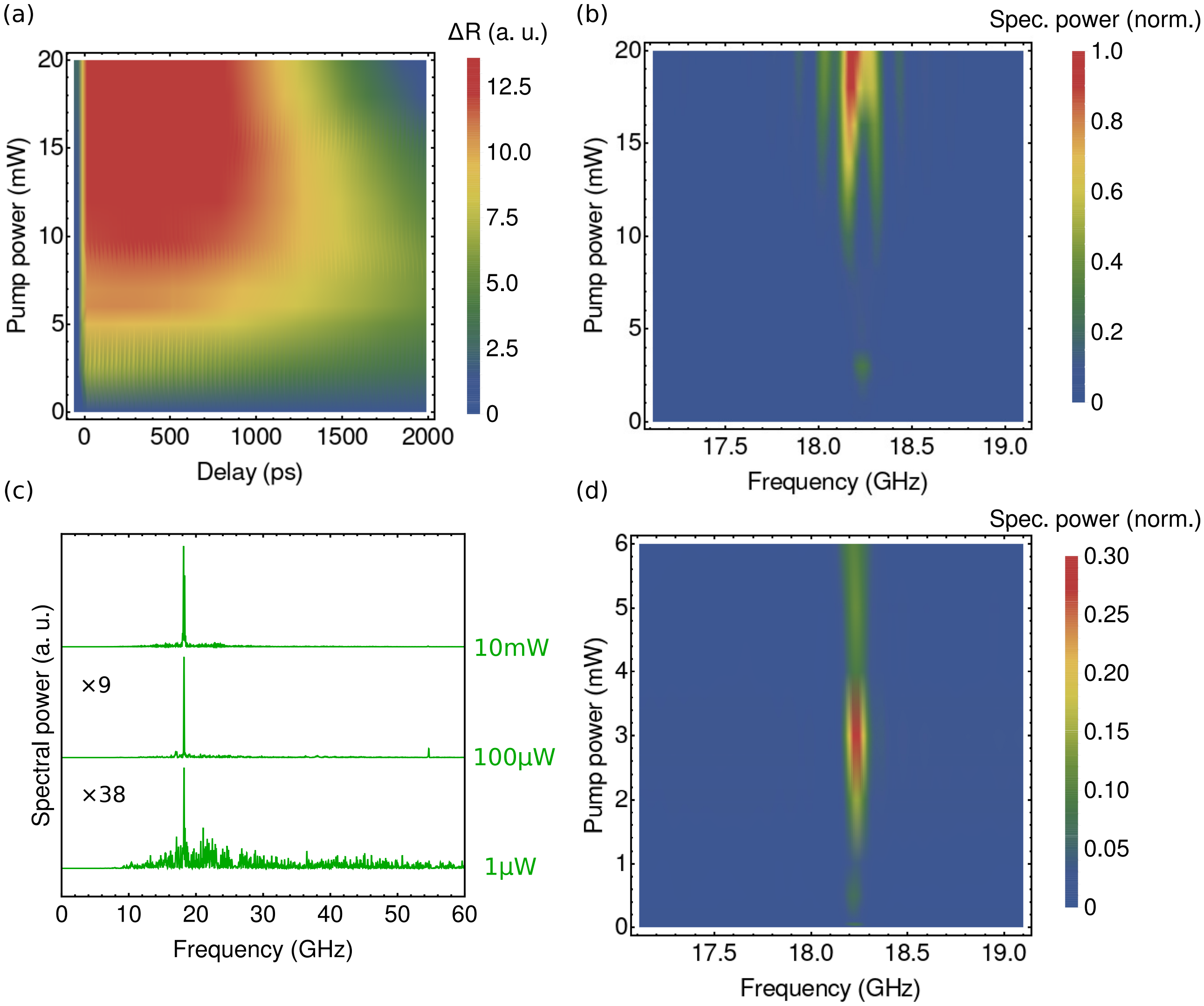

Figure 4.19: Figures from the power scan in the hybrid Fabry-Perot resonator. (a) Color map showing the first 2 ns of the time resolved reflectivity trace obtained from TDBS measurements maintaining the probe power fixed at 0.7mW while varying the pump powers to: 0.001, 0.002, 0.005, 0.010, 0.025, 0.050, 0.1, 0.3 and 0.5 mW, from 1 to 10 mW in steps of 1 mW, and from 12 to 20 mW in steps from 2 mW. The color map is obtained by interpolating along the experimental curves. (b) Color map showing the phononic spectra obtained after processing the time traces presented in panel (a). Again, the color map is built interpolating between the experimental curves. (c) Individual phononic spectra obtained at 1 μW, 100 μW and at 10 mW showing the resonant peak at 18.3 GHz of the hybrid Fabry-Perot resonator. (d) Zoom in the color map presented in panel (b) for the range between 0 and 6 mW of pump power.

the side and finally at 20 mW one main peak remains dominant. We consider this behavior is caused by the thermal response of the system playing a role in the optical cavity dynamics undergone during the relaxation process. As discussed when presenting the variation of the time resolved reflectivity trace as a function of power, when the pump power increase there is a heating effect red shifting the optical cavity mode. This results in an alteration in the way we detect the presence of coherent phonons caused by sensing different slopes of the optical cavity reflectivity dip. The oscillations are caused by strain altering the reflectivity of the sample. Given that this change is fixed, if we change from a positive reflectivity slope to a negative one there is sign change in the oscillations detected. This corresponds to a π phase change of the reflectivity oscillation which in the end affects the detected spectrum [215]. Regardless of this effect, we have been able to measure coherent phonons with pump powers varying over 5 orders of magnitude from 1 μW up to 20 mW. Figure 4.19 (c) presents the spectra at three different pump powers featuring an intense peak at 18.3 GHz corresponding to the resonant frequency. The results, demonstrate the possibility to perform TDBS experiments at extreme low power which shows potential for applications where this condition is a critical factor, like for biological applications for example.

4.6 Conclusions

In this chapter, we have presented the experimental techniques developed for the study of phonons in one-dimensional structures. We presented three variants of optical setups to perform TDBS experiments. Two of these variants features spatial mode filtering steps based in the use of single-mode fibers. One variant was developed to perform TDBS experiments in fiber integrated devices by means of a polarization discrimination scheme. We have used this experimental tools for the study of different acoustic resonators, confining phonons in the range of tens and hundreds of gigahertz. The studied resonators were *AlGaAs* heterostructures fabricated by molecular beam epitaxy. The high quality of the fabricated samples allowed us to test different schemes for confining acoustic modes in structures with layers thicknesses in the range of few to hundreds of nanometers.

Four different acoustic resonators were experimentally studied featuring different confinement mechanisms. First, we used the developed TDBS free space setup for the study of a resonator by band inversion confining acoustic phonons at 200 GHz at the interface between DBRs. The experiment took place using only one laser tuned at 875 nm with a cross polarization scheme and we obtained a resulting phononic spectrum showing an intense peak at 200 GHz. For the second and third resonator we used a TDBS setup featuring spatial mode filtering by using single-mode fibers. The second resonator was an adiabatic resonator designed with the tools presented in chapter 3. In this resonator, the local band structure is tuned along the structure, resulting in measurements showing confinement of acoustic phonons at 390 GHz. In contrast with previous experimental studies of the same sample using Raman spectroscopy, the spectrum obtained here presents an increased resolution showing a resonant peak with a full width at half maximum of 2.9 GHz, a factor of two smaller [72]. The third experimentally studied resonator was a hybrid resonator confining acoustic phonons and photons in the interface between two DBRs. Using our TDBS setup we were able to demonstrate the presence of 18.12 GHz confined phonon modes at the interface between the two reflectors. In addition to oscillations due to the presence of confined phonons, the instantaneous reflectivity trace captures the response of the optical cavity dynamics while the system relaxes back to equilibrium. This effect manifests itself in both the reflectivity trace and in the spectrum obtained from it. To the best of our knowledge this is the first realization of a system confining states by band inversion operating on two physical systems of different nature simultaneously. Finally, the fourth resonator studied was a Fabry-Perot working as both cavity and resonator confining phonons at 18.3 GHz and photons with wavelengths of 915 nm. The usage of *GaAs* and *AlAs* is exploited for this structures where we can design almost perfect overlap between acoustic and optical confined fields. Working in collaboration with Quandela SAS we implemented a fibered cross polarization scheme to filter out the pump in order to perform TDBS experiments in connected devices. By this means we measure acoustic phonons confined at 18.4 GHz in the connected acoustic resonators. Furthermore, we have access to the spectral features expected for its second and third harmonic. The use of the fiber integrated device allowed us to perform a set of 24 measurements of the phononic spectra at different pump powers. This was possible given the short time required for each of the measurements, taking 5 minutes each and accumulating only 20 time resolved reflectivity traces. Furthermore, we were able to demonstrate the coherent generation of phonons for a set of pump powers varying over 5 orders of magnitude going from 1 μW up to 20 mW.

The whole collection of measurements offers high resolution spectra compared to Raman scattering experiments in the frequency domain. Furthermore, the use of a time-resolved technique like TDBS, brings a different view of the system response to an impulsive photo-induced phonon generation process. By following this response, a better understanding of the spectra measured using a pump and probe detection scheme can be obtained. The experiments presented in this work demonstrated confinement of longitudinal acoustic phonons from 18.4 GHz up to 390 GHz. With these realizations we demonstrate that the design concepts introduced in the previous chapter can be experimentally accessible. In the following chapter, we use the same experimental setup but target a different kind of system: three-dimensional multilayer structures.

Chapter 5

Experimental study of phonon confinement in micropillars

In chapters 3 and 4 we studied one-dimension multilayer structures theoretically by simulations and experimentally by means of a time-domain Brillouin scattering (TDBS) technique. Experimental results were obtained studying $GaAs/GaAlAs$ heterostructures grown as planar layered systems working both as optical cavities and acoustic resonators. This type of layered planar samples can be etched into three dimensional structures [110] preserving the multilayer design, but imposing a boundary given by the shape of the structure. Its surface acts as a reflector for both optical and acoustic waves due to the impedance mismatch between the device and the environment resulting in three-dimensional confinement. In this chapter, we investigate phonon confinement in hybrid opto-phononic micropillars.

Micropillar multilayer structures appear as a promising platform for the development of quantum technologies featuring capabilities to work as optical cavities and to host semiconductor quantum dots within their structure [55, 241–245]. The strong dependence of these quantum systems on the electromagnetic three-dimensional host environment motivates the study of phonons in this type of structures. In addition, the capability to work simultaneously as an optical cavity and as an acoustic resonator makes these three dimensional devices attractive as an optomechanical platform [21, 68, 70, 216, 246]. In this chapter, we apply the experimental tools developed for time-domain Brillouin scattering (see chapter 4) for the study of three-dimensional confinement in micropillar structures. We study how phonon confinement is altered as a function of the micropillar size and the effect of coherent phonon generation by ultrafast laser action on the optical cavity dynamics of micropillars on the picosecond time scale. We follow two experimental approaches for the study of micropillars using a TDBS technique. First, in section 5.2 we present the study of hybrid micropillars using a free-space scheme in order to couple pump and probe beams. By optimizing the spatial mode matching between the beams used and the micropillar optical modes we investigated micropillars of 2 and 5 μm diameter. As a second approach and motivated by the results obtained for fibered devices in one-dimensional structures, in section 5.4 we study micropillar resonators working as fibered devices. The fiber-integrated micropillars were fabricated in collaboration with Quandela S.A.S.

In this chapter we show the experimental results from the study of micropillars working both as acoustic resonators and optical cavities at ≈ 18 GHz and ≈ 915 nm (in vacuum), respectively. The free-space and fibered approaches to perform TDBS experiments in micropillars were used for this purpose. All micropillars presented in this chapter were obtained from MBE-grown wafers through e-beam lithography and inductively coupled reactive ion etching. This step of the sample fabrication was performed in the group of Isabelle Sagnes.

5.1 Micropillar resonator at 18 GHz

The micropillar structures investigated in this chapter were fabricated in the clean room facilities of C2N. The fabrication process involved two main stages. First, on a *GaAs* substrate the group of Aristide Lemaître grew an *AlGaAs* heterostructure by molecular beam epitaxy. This planar layered structure working both as an optical cavity and an acoustic resonator was designed as a Fabry-Perot cavity where two distributed Bragg reflectors surround a spacer. Due to the particularity in the material properties of *AlAs* and *GaAs* (see section 4.3), this Fabry-Perot design works for both optical and acoustic modes, leading to simultaneous confinement of photons and phonons in the spacer of the structure [69]. On a second stage of the fabrication process, micropillars were obtained by electron beam lithography and inductively coupled plasma etching of the planar sample by the group of Isabelle Sagnes. The resulting sample contained arrays of hundreds of micropillars of systematically varying diameters. The growth of the multilayer structure by MBE was done with a spatial gradient linearly varying all layers thicknesses over 30% along the 2" wafer. Consequently, the resonant optical wavelength and acoustic frequency vary gradually along the gradient axis on the sample. In this chapter, we studied micropillars with sizes between 2 μm and 5 μm diameters. Devices on this scale have been vastly studied in photonics and they are a promising platform for the development of quantum technologies featuring capabilities to work as optical cavities and to host semiconductor quantum dots within their structure [55, 109, 241–245]

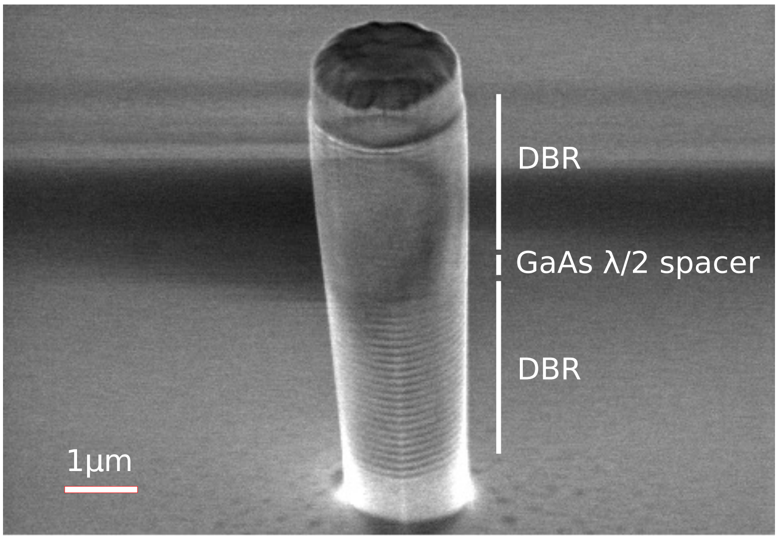

Figure 5.1: SEM image of a micropillar resonator experimentally studied by TDBS. On its bottom half, the multilayer structure of a distributed Bragg reflector (DBR) is visible. On the top half, these features are not resolved due to charge accumulation at the electron beam focus. The micropillar top surface, where the beam is focused to couple into the device, has a diameter of approximately 2 μm.

The micropillar was formed by (starting from the bottom) 22 bilayers of $Ga_{0.05}Al_{0.95}As$ and $Ga_{0.9}Al_{0.1}As$ with thicknesses to form a $(\lambda/4, \lambda/4)$ DBR for photons and phonons. On top of it, a pure *GaAs* layer of thickness of $\lambda/2$ was grown as the spacer of the cavity/resonator. Finally, a second DBR was grown with 18 bilayers of $Ga_{0.05}Al_{0.95}As$ and $Ga_{0.9}Al_{0.1}As$ with thicknesses also forming a $(\lambda/4, \lambda/4)$ DBR. The difference of 4 extra bilayers on the bottom side compensates for the different boundary conditions on the top (against the surrounding environment, i.e. air or vacuum) and bottom side (*GaAs* substrate) of the micropillar.

Figure 5.1 presents an image of one of the studied devices obtained using a scanning electron microscope (SEM). In general, these etched devices operate at two different scales depending of the dimensions we consider. Along the growth direction (central axis of the micropillar in figure 5.1) we have the multilayer structure. Alternating layers of *AlAs* and *GaAs*, this structure features layers thicknesses on the scale of tens of nanometers that have been engineered to

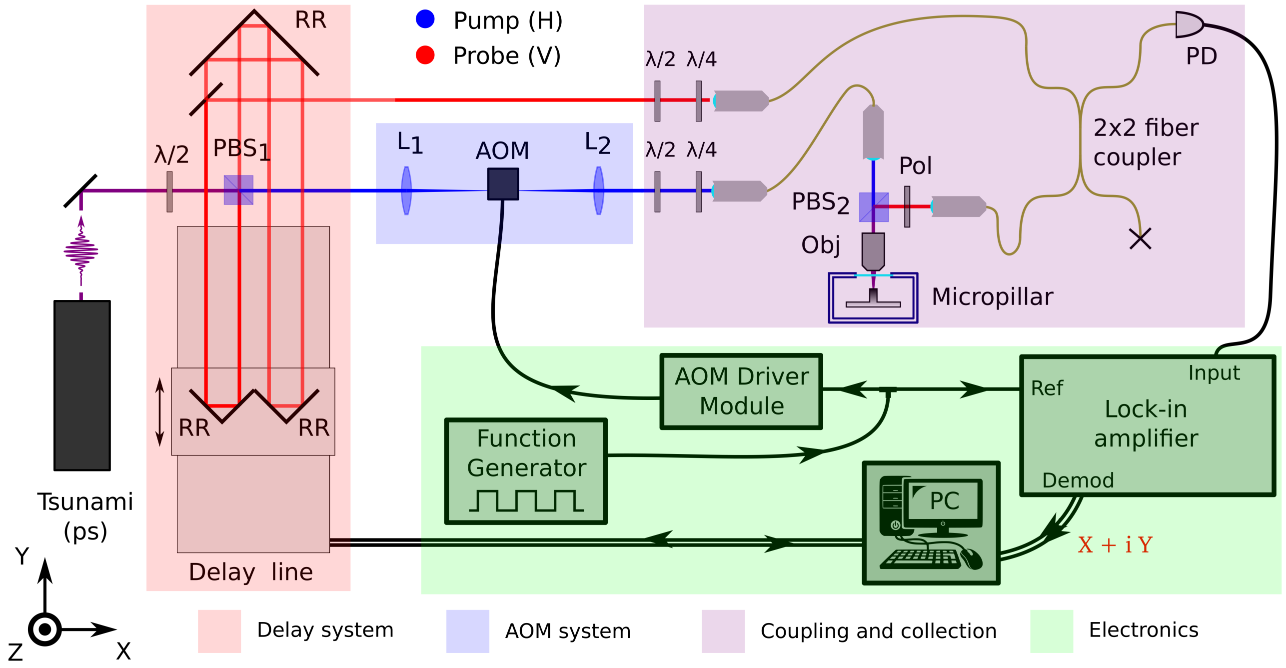

Figure 5.2: Optical setup for TDBS measurements. Picosecond pulses pass by a half waveplate ($\lambda/2$) and a polarizing beam splitter (PBS_1) where two beams of pulses output for a pump and probe detection scheme. Then, the probe enters an optical delay system. The pump is focused through an optoacoustic modulator system where an 800 kHz modulation is imprinted on it. Both pump and probe beam are coupled to two single-mode fibers where their spatial modes are cleaned. At the output of the fibers, pump and probe trajectories are merged and focused onto the pillar. By controlling the delay between pump and probe and demodulating the effects of the pump on the sample at the instant the probe is reflected from it, we are able to resolve in time the Brillouin scattered signal from the micropillar resonator.

confine optical and acoustic modes at its *GaAs* spacer. On the scale of the three dimensional micropillar shape (micrometers scale), photons and phonons are contained within its boundaries by the impedance mismatch between the micropillar materials and the environment. This contrast in scales leads to a different treatment on the optical waves when modeling it radially and vertically. Radially the micropillar acts as a single-mode fiber [247]. Vertically, the multilayer structure acts as an optical microcavity [66].

The experimental study of these micropillars requires optical setups that let us couple and collect light into and from their cavity modes, respectively. In the following section we present two approaches for this purpose and the experimental results obtained from each one using a TDBS technique.

5.2 Micropillar resonator experimental study in free-space

One of the challenges of studying micropillars is to efficiently couple light to their cavity modes. We used a variant of the TDBS setup developed to couple to planar layered samples in free space (see figure 4.3). The setup features spatial mode filtering of the laser beams by the use of single-mode fibers allowing both pump and probe pulses to remain fixed at the top of the micropillar while controlling the delay between pump and probe.

Figure 5.2 presents a scheme of the optical setup used to coherently generate and detect acoustic phonons in micropillars. It corresponds to the same optical setup used for TDBS in planar samples using a cross polarization scheme, but instead of a free space multilayer structure, we have a micropillars inside a vacuum chamber. In order to couple into the micropillar cavity mode a 20× microscope objective focuses pump and probe beams on the top of it.

We selected two micropillars of 2 and 5 μm diameter. Figure 5.3 panel (a) and (b) present

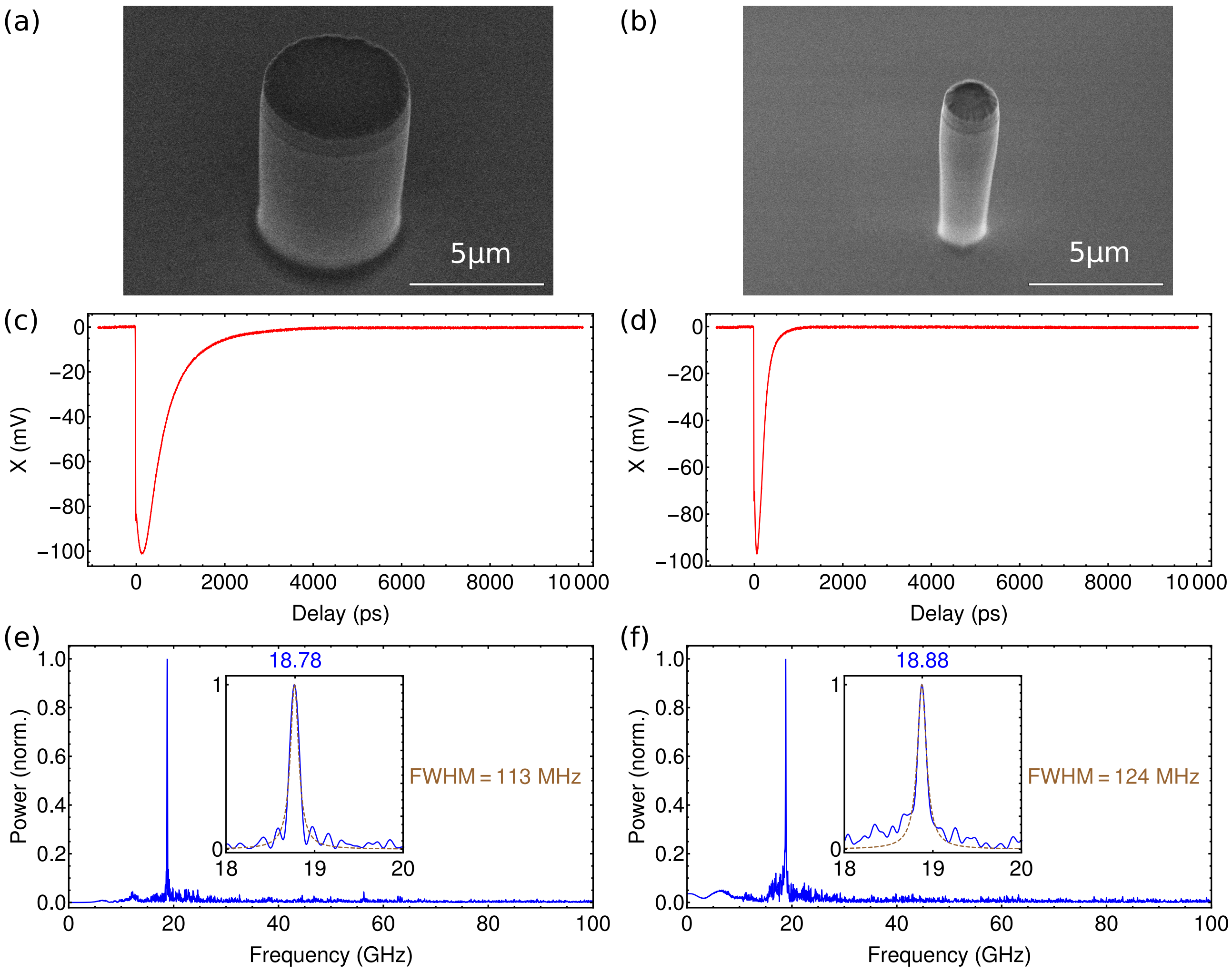

Figure 5.3: Panel (a) and (b) show SEM images of the large (5 μm diameter) and small (2 μm diameter) micropillars. Time traces of the instantaneous reflectivity measured from these devices as a function of delay between pump and probe are presented in panel (c) and (d), respectively. Finally, below these traces their corresponding spectra are presented in panel (e) and (f). They were obtained by subtracting a filtered version of the trace for frequencies below 10 GHz and then applying a Fourier transform. Zoom in the spectra around the peak corresponding to the resonant frequency of both micropillars are presented as insets.

SEM images of the large and small micropillars studied, respectively. The samples are kept inside a vacuum chamber in order to protect the micropillars from the environment conditions that might damage them (like for example due to oxidation of the $AlAs$ layers). Experiments were performed at around 900 nm, allowing a selective excitation of the GaAs cavity spacer [248]. At the spacer, electron holes pairs are produced leading to coherent phonon generation due to deformation potential (all experiments were performed at room temperature). In addition, as in all solid-state structures subject to an electric field, electrosctriction is present and acts as another source of coherent phonon generation.

The ultrafast laser was blue-detuned from the optical cavity mode center, at the higher slope of the reflectivity dip in order to maximize the sensitivity to detect phonons in the resonator [215, 216, 239]. Because of the sample gradient, the micropillar cavity modes were 894 and 892 nm for the large and small micropillar, respectively. For the 5 μm diameter micropillar, pump and probe powers were set at 2.1 mW and 0.65 mW, respectively, while for the 2 μm diameter micropillar 1.3 mW and 0.6 mW, respectively. The laser pulse duration was fixed at 3 ps. Figure 5.3 presents the time resolved reflectivity trace of the probe for the 5 (panel c) and 2 μm (panel d) diameter micropillar. At zero delay, the probe measures the rapid change in the reflectivity induced by the pump. This fast response has two contributions resulting from electronic and thermal effects. While the electronic response results in a blue shift of the optical cavity mode, the warming up of the sample due to the pump counters this effect. Nevertheless, since the micropillars are made entirely of semiconductor materials and at the experimental conditions investigated, the electronic effects are more severe than the thermal ones [73]. As a result, the cavity mode rapidly blue shifts near zero delay and then, while relaxing back to equilibrium, causes the main features seen in the time resolved reflectivity. On top of the reflectivity changes due to the relaxation process, oscillations caused by the presence of coherent phonons appear. To resolve them, we process the time traces using a Savitsky-Golay filter to remove the main contributions below 10 GHz and then performing a Fourier transform of the filtered signal. The resulting spectra can be seen in figure 5.3 panels (e) and (f). At frequencies lower than 10 GHz the response is not representative of the system since the used filter removes most of its contributions leaving only smooth spectral features in this range. At higher frequencies a single peak at approximately 18.8 GHz reaches values well above the noise floor. It corresponds to the coherent acoustic phonons generated in the micropillar by the pump excitation. With the TDBS setup we can achieve long delays between pump and probe; for this measurement we recorded over 10 ns after zero delay. As a result we can report information regarding the lifetime of the phonons measured at the micropillar resonators provided that the phonon detection sensitivity remains constant. The insets at figure 5.3 panels (e) and (f) present a zoom in the spectra around the resonant peak for the large and small micropillar, respectively. Fitting a Lorentzian function we estimate the full width at half maximum (FWHM) of these fits obtaining 113 MHz and 124 MHz. The results indicate the presence of coherent phonons in the micropillar for more than 8 ns after they were generated. Such long life times contrasts with similar experiments where, for square micropillars, shorter life times are observed with a strong dependence on the micropillar size [246].

The main difference between measured time traces of large and small micropillars is the faster decay of the initial electronic response for the smallest device. The effects of scaling the lateral size of micropillars have been studied and experimentally observed for the case of square micropillars [216, 246]. By reducing the micropillar size, electron-hole pairs tend to recombine faster as a result of the greater influence of the $GaAs$ spacer boundaries, i.e. a larger surface to volume ratio (electron-holes tend to recombine in the roughness of the micropillar boundary) [249]. Here, the investigated circular micropillars of 2 μm and 5 μm diameter show the same trend. We modeled the reflectivity time trace as a result of the optical cavity dynamics while the system relaxes back to equilibrium and estimate the relaxation time of the electronic system after zero delay between pump and probe pulses. Figure 5.4 (a) presents in solid green and blue lines the time resolved reflectivity traces while the system recovers. In black dashed lines two curves are presented resulting from modeling the change in reflectivity as a Lorentzian reflectivity dip shifting back to equilibrium in an exponential decay fashion. The model used for both curves is given by

$$f_{model}(A, B, C, D, \Delta, \tau_r) = A + B \frac{\Delta^2}{4\left((C + De^{-t/\tau_r})^2 + \frac{\Delta^2}{4}\right)} \tag{5.1}$$

where A, B and Δ are fitting parameters describing the micropillar optical cavity mode with the latter, Δ, corresponding to the full width at half maximum of the cavity mode reflectivity dip. The parameters C and D determine the start and end point of the relaxation process (from A to B in figure 5.4) The parameter τ_r corresponds to the relaxation time of the optical cavity mode dynamics. Using a spectrometer we recorded both the laser spectrum and the reflectivity curve of the optical cavity mode of both micropillars. Figures 5.4 (b) and (c) present the measured spectra together with Lorentzian fitted curves. The fitted curve corresponding to the laser spectrum is plotted in red while the optical cavity mode of the small and large micropillars are presented in dark green and blue, respectively. From these spectra we obtain the initial condition prior to the pump interaction with the micropillar. Consequently, we know the detuning between the laser and the optical cavity mode that have to be recovered when

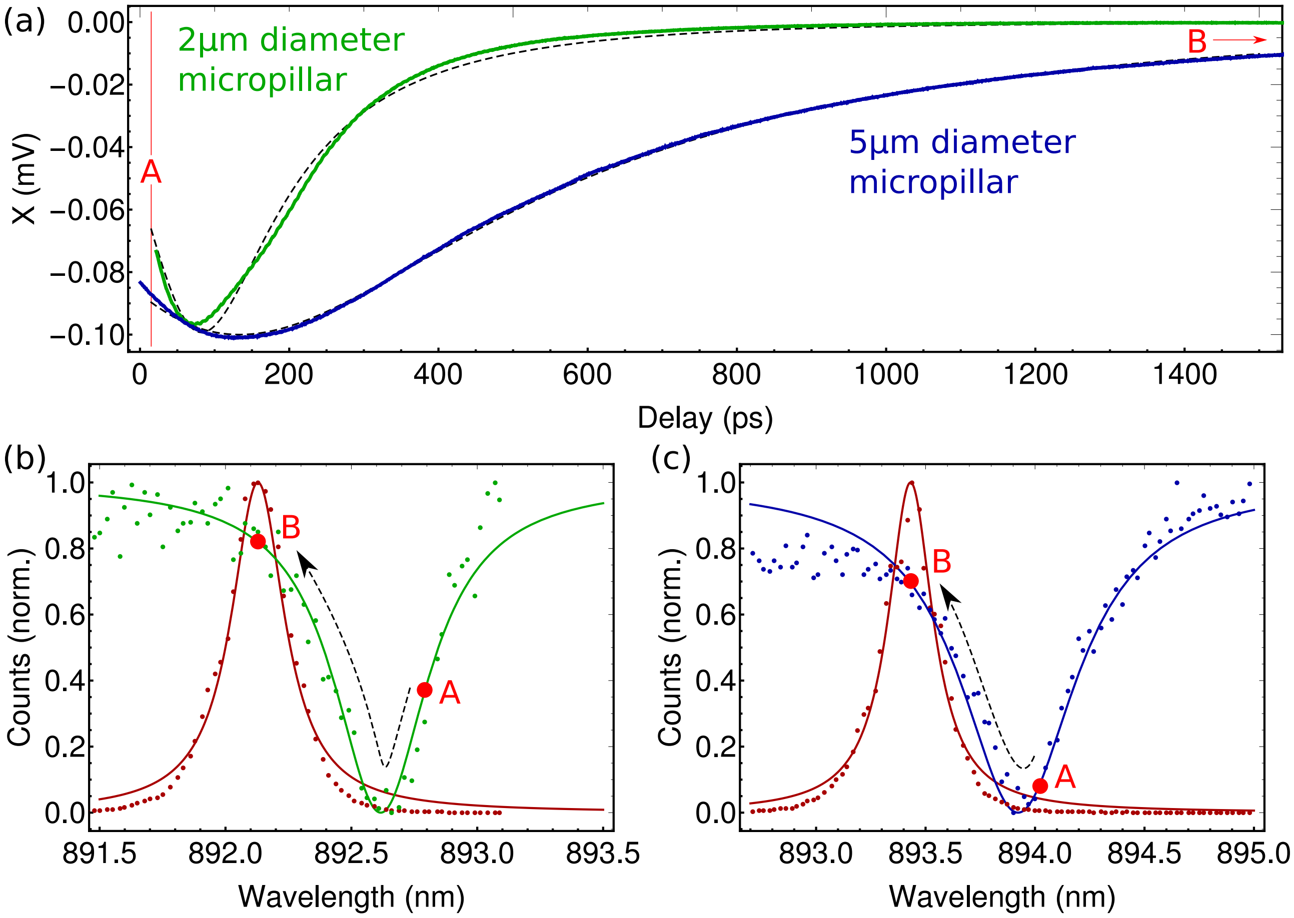

Figure 5.4: (a) Zoom in the reflectivity time trace at the first 1500 ps after pump action. The optical cavity after being perturbed by the pump relaxes back to equilibrium, causing the main changes seen in the curve. The relaxation time between the 2 and 5 μm diameter micropillars is significantly different as can be seen by the rapid recovery of the smallest pillar. The dashed black curves correspond to fits using the proposed model (equation 5.1) for the reflectivity time trace. In panels (b) and (d), the small points and the curves are the experimental and fitted spectral data, respectively, for both micropillar cavity modes used for the TDBS measurements. Solid red curves correspond to the laser fitted while solid green and blue curves correspond to the fitted modes of the 2 and 5 μm diameter micropillar, respectively. From the measured data and fitted model, the start (A) and finish (B) points of the relaxation process are depicted in all panels.

the system fully relaxes (marked by the red B letter in the spectra). As a result the parameter C of the model is fixed by expressing it in terms of Δ. Fitting the reduced model the dashed black curves from figure 5.4 (a) are obtained. Panels (b) and (c) show the start and end point of the relaxation process marked by the red letters A and B, respectively, as obtained from the fitted curves. The dashed arrows represents the relative trajectory followed by the laser with respect to the cavity mode while the system recovers. The relaxation times obtained from the fits are $\tau_r \approx 800$ ps and $\tau_r \approx 270$ ps for the large and small micropillar, respectively.

We have seen how the micropillar size has a significant impact on the cavity dynamics measured on the TDBS signals. It depends on the spectral detuning of the laser from the cavity mode and on the time it takes while the electron hole pairs recombine in the *GaAs* spacer. There is also a dependency on the power used for the measurements. In the previous results, we presented comparable intensities for pump and probe powers (few milliwatts). Now, we present results on the experimental study of the phononic spectra measured using the TDBS setup as a function of pump power.

A third micropillar is chosen for the scan in pump power. The new pillar is a 5 μm diameter circular micropillar with an optical cavity mode at 914.1 nm. The laser pulse duration is set

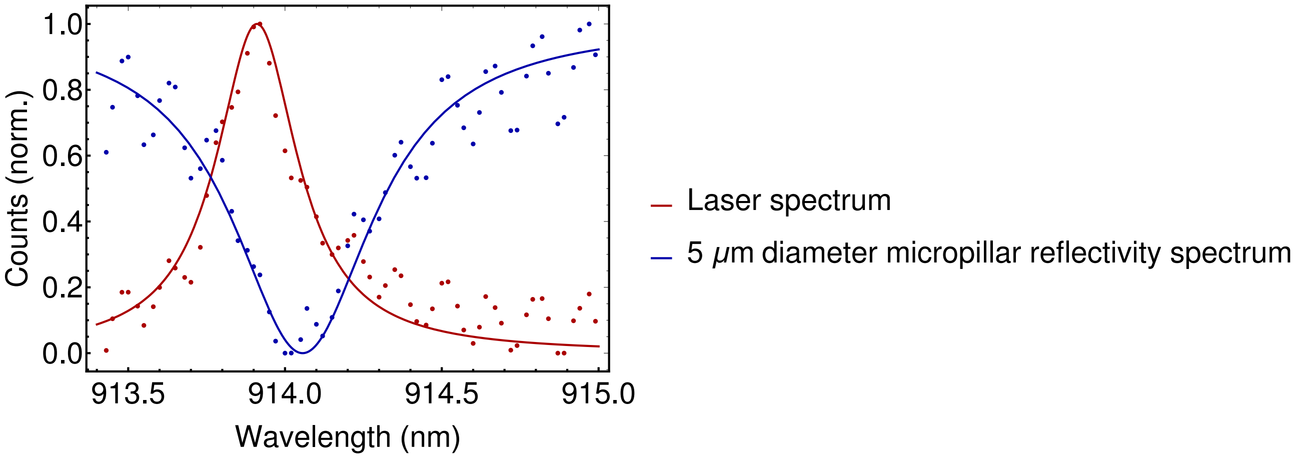

Figure 5.5: Points in dark red and blue present the spectrum of the laser and the reflectivity spectrum of the micropillar cavity mode as measured before for the power scan, respectively. In solid lines of corresponding colors, Lorentzian functions fitted to the experimental points are presented. The laser is slightly shifted to the blue side of the optical cavity mode.

to 4.5 ps and the wavelength is tuned on the blue side of the cavity mode at 913.9 nm as presented in figure 5.5. We measured using total powers up to 17 mW. Figure 5.6 (a) presents as an intensity map the phononic spectra between 17.1 GHz and 19.1 GHz obtained from TDBS measurements as a function of pump power. A total of 11 spectra were measured varying the pump power from 0.5 mW up to 16 mW while maintaining the probe power fixed at 1 mW. The full intensity map results from interpolating between the measured spectra. Panel (c) presents the peak value of the spectra as a function of pump power. We observe a trend increasing the peak resonant power while the pump power increases from 0.5 to 3 mW. Then, the resonant peak starts to vanish at a slower pace while increasing the pump power up to 16 mW. Figure 5.6 (b) shows the spectrum up to 100 GHz obtained at 3 mW of pump power. The resonant mode at 18.3 GHz is observed as well as its third harmonic at 54.8 GHz. Fitting these spectral peaks, we obtained full widths at half maxima of 84 MHz and 90 MHz which indicated that the phonons are present along the full 11 ns recorded after the pump reflection. The corresponding time resolved reflectivity trace is presented in figure 5.6 (d). The cavity dynamics rapidly shifts the reflectivity during the first 3 nanoseconds, then the system reaches its equilibrium and phonons are still present resulting in the spectral peaks showed in panel (b).

The optical cavity dynamics has a direct impact on the time resolved reflectivity trace, as we have seen in the previous cases. Figure 5.7 (a) presents the time resolved reflectivity trace varying as a function of pump power in an intensity map. The 11 measurements performed are plotted and then interpolated to complete the full intensity map presented in panel (a). Panel (b) presents three cross-sections of the intensity map by plotting the time resolved reflectivity traces corresponding to pump powers: 0.5, 3.0 and 16.0 mW. After zero delay, i.e. while the micropillar relaxes, we observe how the minimum in reflectivity for pump power 3.0 and 16.0 mW appears near 640 ps while for a pump power of 0.5 mW it appears near 120 ps. This minimum in reflectivity marks the instant at which the optical cavity center passes by the laser line and serves as a reference on how the optical cavity dynamics changes as as a function of pump power. To visualize this effect, on top of the intensity map at panel (a) we have marked with red points the positions where the reflectivity reached its minimum while the system relaxes. We observe that while pump power increases from 0.5 to 4 mW the minimum in reflectivity is reached at larger delays and from the intensity map we see that the system takes longer times to recover as well. At pump powers higher than 4 mW, the minimum in reflectivity starts to progressively shift towards lower delays. This shift can be explained by an increase in the equilibrium temperature of the micropillar that red shifts the optical cavity mode. The increase of the equilibrium temperature is the result of an accumulation effect due to the subsequent pump and probe pulses arriving to the sample at the laser repetition

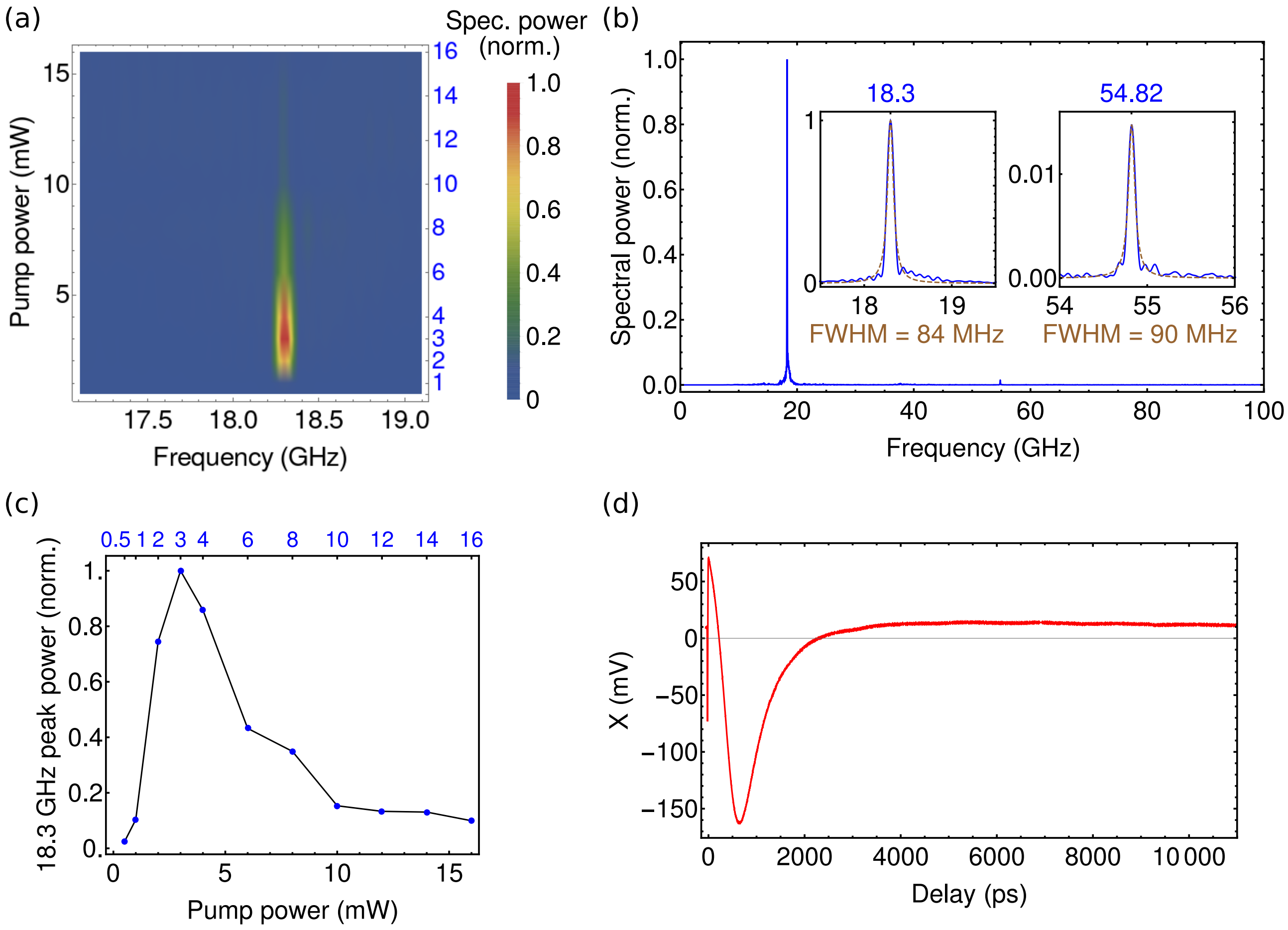

Figure 5.6: Figures from the power scan in a large 5 μm diameter micropillar. (a) Acoustic spectra obtained from TDBS measurements at different pump powers: 0.5, 1, 2, 3, 4, 6, 8, 10, 12, 14 and 16 mW, while maintaining the probe power fixed at 1mW. A zoom in around the resonant peak is plotted (plotted range from 17.1 to 19.1 GHz). The full intensity map results from interpolating between the measured spectra. (b) Spectrum obtained for pump and probe powers of 3 mW and 1 mW, respectively. At this pump power is where the stronger resonant peak at 18.3 GHz was measured. At 54.82 GHz a spectral peak corresponding to the third harmonic of the resonance is observed. Zoom in the first and third harmonic are presented as insets with dashed brown Lorentzian curves fitted to the data. (c) Peak values of the first harmonic as a function of power. (d) Reflectivity time trace from which the spectrum presented in panel (b) was obtained.

rate (80 MHz). On top of the equilibrium temperature reached by the micropillar, there is an increase in temperature each time the pump excites the micropillar. This second thermal effect (happening at a shorter time scale than the one related to the equilibrium temperature) warms up the micropillar above the equilibrium temperature and it manifest in the time resolved reflectivity as an increase on the probe signal before zero delay as shown in figure 5.7 (c). The value X in all plots corresponds to the demodulated signal obtained from the lock-in amplifier and is related to the reflectivity of the sample. The increase of X before zero delay in the time resolved reflectivity traces depicted in panel (a) is the result of the micropillar, after each pump excitation, not being able to leak all its thermal energy before the next pump pulse arrives. Consequently, the demodulated signal is not null before zero delay, since it is capturing the effect of the previous pump pulse to the one exciting the sample at zero delay. Figure 5.7 (d) shows the change in reflectivity just after the pump arrival. Again up to 3 and 4 mW a trend increasing the reflectivity is seen, then it starts to reduce as one would expect from the optical cavity red shifting due to thermal effects. This result indicates a dynamic control of the micropillar optical cavity as a function of pump and probe power. Moreover, the time

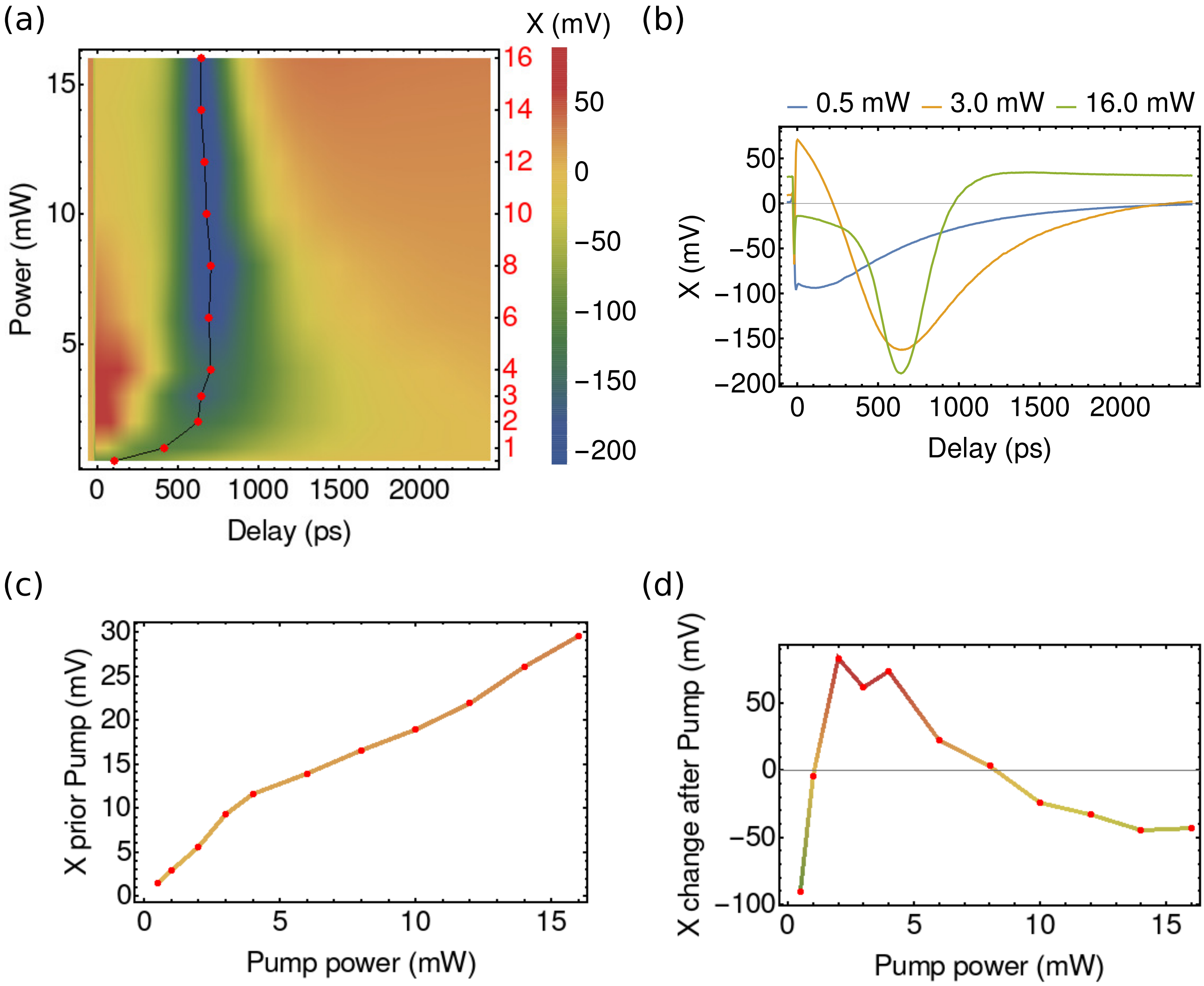

Figure 5.7: Figures from the power scan in a large 5 μm diameter micropillar. (a) Time resolved reflectivity trace obtained from TDBS measurements at different pump powers: 0.5, 1, 2, 3, 4, 6, 8, 10, 12, 14 and 16 mW, while maintaining the probe power fixed at 1 mW. A zoom in around the first two nanoseconds after the pump pulse was reflected from the sample are presented. The full intensity map results from interpolating between the measured curves. The minimum in reflectivity after the pump reflection is marked with red points for each measured time trace and connected by black solid lines. (b) Time resolved reflectivity trace obtained from TDBS measurements at pump powers 0.5, 3 and 16 mW, while maintaining the probe power fixed at 1mW. These traces correspond to cross-sections of the intensity map at panel (a). (c) Reflectivity before the zero delay. (d) Change in reflectivity just after zero delay.

resolved reflectivity traces provide information about the detuning of the optical cavity on the picosecond time scale. Such information could be used to engineer pump schemes where we could excite the optical cavity at different conditions. Moreover, we could engineer multilayer optical cavities with modified cavity modes in order to operate under specific pump schemes and gain optical control of the cavity on the picosecond time scale [250, 251].

We have presented experimental results on three micropillars by coupling into their cavity modes in free space, one of 2 μm and two of 5 μm of diameter. We have compared their spectra and dynamic response upon coherent generation of phonons in the micropillar resonant structure as a function of pump power. The results indicated lifetimes of more than 8 ns of coherent phonons in the studied micropillars. After a systematic study as a function of pump power in the TDBS experiment we were able to optimize the measurement conditions and evidence lifetimes of more than 11 ns in the 5 μm of diameter micropillar. Moreover, we have shown evidence of an optical cavity dynamics resulting from the interplay between thermal and electronic effects in the experiment. Finally we introduce a model to account for the electronic effects which allowed us to extract information of the optical cavity trajectory followed after pump excitation. The challenges of coupling to micropillars in free space constitute a limiting factor for the amount of data that can be collected. In the following section we will address an approach that overcomes these limitations and allows coupling into small micropillar resonators free of alignment.

5.3 Fiber-integrated micropillar resonator

Motivated by the high quality spectra obtained from fibered planar resonators, we applied the same approach to micropillars. This implies gluing a single-mode fiber to the top of a micropillar. This work was done in collaboration with Quandela S.A.S. In the following section we present the results of the experimental study of a fiber-integrated micropillar resonator.

5.3.1 Fiber-integrated micropillar experimental results

For the fiber integration of a micropillar resonator, we used the same sample containing the micropillars studied in free space in this chapter. Here, several arrays of micropillars are present featuring optical cavity modes at around 912 nm. Figure 5.8 (a) presents an SEM image of an array of the micropillars. Using a 3D piezo motor with submicrometer precision, the core of a single-mode fiber (Thorlabs 780HP, core diameter 4.4 μm) was aligned to the top face of

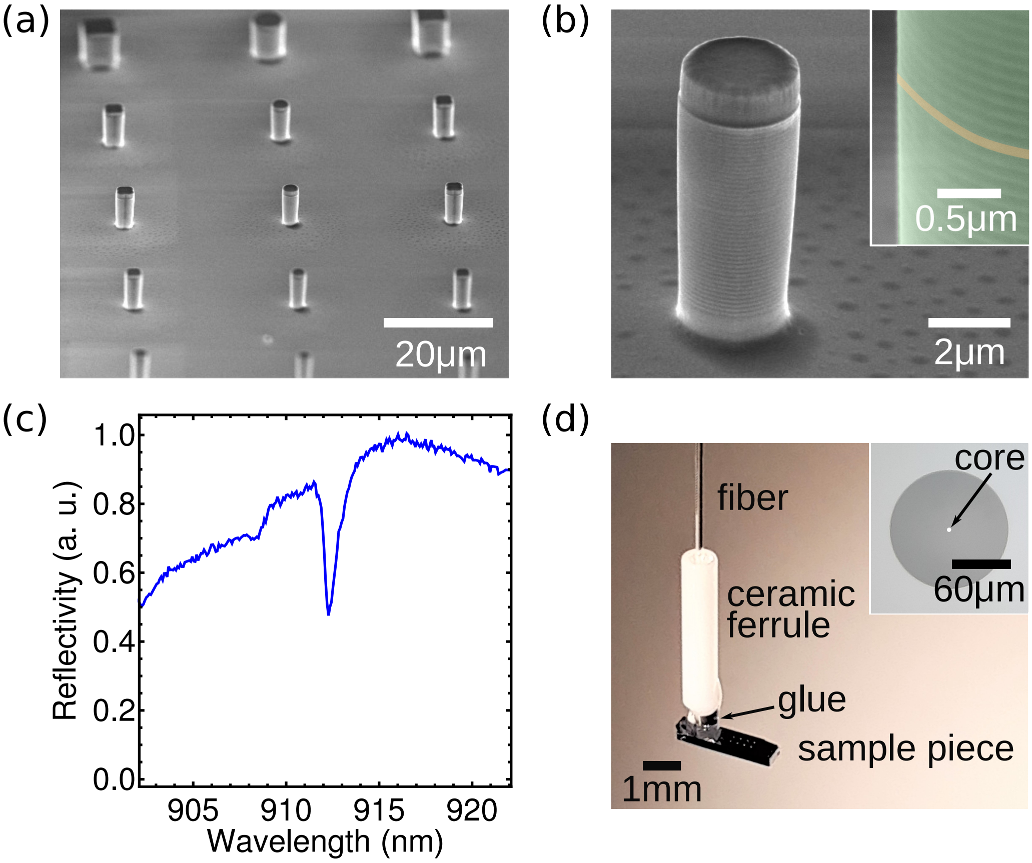

Figure 5.8: (a) SEM image of an array of pillars present in the sample piece used for fiber integration. (b) SEM image of a 2.8 μm diameter micropillar. Inset shows a zoom near the center of the multilayer structure. Transparency and false colors are used to enhance the contrast between layers. (c) Reflectivity spectrum of the fiber-integrated micropillar. The micropillar optical's mode appears as a reflectivity dip around 912.1 nm. (d) Image of the final device. Inset presents a microscopy image of the single-mode fiber where the core can be distinguished.

a 2.8 μm diameter micropillar (see figure 5.8 (b)). With the single-mode fiber connected to a spectrometer, we monitored the reflectivity spectrum of the micropillar cavity mode in order to optimize the injection of light into the micropillar. Once aligned, we permanently glued the single-mode fiber to the micropillar (UV-curing glue Norland NOA 81). The curing process caused minimal shifts of the micropillar cavity mode wavelength (less than 0.1%). Figure 5.8 (c) shows the reflectivity spectrum of the glued micropillar as measured through the single-mode fiber showing a reflectivity dip associated to the micropillar optical mode approximately at 912.1 nm. A ceramic ferrule was placed surrounding the glued region in order to enhance the mechanical stability of the device. Figure 5.8 (d) presents a picture of the final device where we can see the sample piece at the bottom, and distinguish an array of white dots resulting from light scattered at different arrays of pillars.

For the experimental study of fiber-integrated micropillars we used the TDBS setup developed for fibered planar layered structures, as presented in section 4.1.2. The use of fibered devices removes all alignment requirements that are typically challenging to achieve, in particular, for micropillars in a free space configuration, requiring robust micrometer stages together with high magnification objectives. Even at the most stable version of the free space setup, alignment was always required on a day to day basis. In contrast, fibered devices are aligned only once maximizing coupling between the fundamental propagating mode of a single-mode fiber and the micropillar cavity during the gluing process. Lacking free-space alignment, the exchange between different samples requires only disconnecting the planar sample and connecting the micropillar. Then compensation for polarization changes along the fiber using waveplates is performed. Figure 5.9 (a) presents a schematic of the optical setup for fiber-integrated micropillars. In contrast with the free-space coupling into micropillars, we do not need a vacuum chamber to preserve the integrity of the fiber-integrated micropillar since the adhesive effectively seals the micropillar from the environment.

In order to evaluate the amount of power reaching the micropillar, we asses the losses in the optical setup from the single-mode fibers to the micropillar. After coupling both pump and probe beams into the fibered part of the setup, we consider three main sources of losses: the 2×2 fiber coupler, the fiber coupler connector (FC) and the fiber-to-micropillar coupling. Standard values of the 2×2 fiber coupler and the fiber coupler connector (FC) are 50% and 80%, respectively. In addition, the fiber-to-micropillar coupling depends on the single-mode fiber characteristics (core radius and indexes of refraction of the core and cladding). In order to model the spatial profile of the micropillar mode, we treat it as a single-mode fiber with a core of $GaAs$ and vacuum as the cladding [252, 253]. This model has been demonstrated suitable to describe the spatial mode of micropillars of similar dimensions operating as single photon sources [247] and a detailed description of it can be found in appendix A. Once having calculated the spatial profile of the micropillar mode we do the same for the single-mode fiber. For each spatial profile we define a radius for which the mode intensity has dropped to 5% of its maximum value. Then we estimate the geometric overlap between two disks of radii corresponding to the micropillar (≈ 1.19 μm) and the single-mode fiber (≈ 4.75 μm) spatial profiles, obtaining a resulting overlap around 6.24%. Considering the three sources of losses, and that two of them (the two fiber couplers) affect the collected amount of light twice (input and output) we obtain a theoretical estimate of around 1%. We measured a total coupling efficiency of 0.8% where additional losses are possible from potential misalignment between the micropillar and the single-mode fiber.

The main source of losses in the TDBS fibered setup for micropillars comes from the coupling between the micropillar and the single-mode fiber. In order to couple the fundamental mode of the modeled 2.8 μm diameter micropillar to a single-mode fiber, we need the best possible match between both modes. We can treat this problem numerically by fitting the intensity profile of a single-mode fiber to the one of the micropillar. Figure 5.9 (b) presents the radial intensity profile of both the micropillar and a single-mode fiber whose parameters have been optimized to match the spatial mode of a 2.8 μm diameter micropillar. The refractive index of the considered single-mode fiber are approximately 1.59 and 1.45 for the core and cladding, respectively and its core has a radius of 1.175 μm. The selected parameters were obtained by performing a numerical fit of the single-mode fiber spatial mode to the micropillar mode. The fitting of the modeled intensity profile can be computationally demanding if all parameters are left free. For this particular pillar we fixed the cladding refractive index to 1.45, then numerically fitted the core refractive index and radius obtaining the curves shown on the left of figure 5.9 (b). On the right next to the plotted profiles a schematic view of the micropillar mode against the modeled single-mode fiber mode is presented. We show that the overlap between the micropillar and single-mode fiber modes can be optimized by the use of custom optical fibers.

Considering the losses in the setup, using probe powers on the order of hundreds of microwatts enough light reaches our photodiode to be detected ($\sim \mu W$). This stable configuration allowed us to explore different measurements conditions in a systematic approach. As seen for the micropillars in free space, the optical cavity dynamics plays a significant role in the detected signal in TDBS experiments on structures featuring confined optical modes. Previous works have investigated the optical cavity dynamics in micropillars with high quality factors optical cavities relative to the laser excitation (laser line FWHM > cavity mode FWHM) [216]. The case of low quality factors (laser line FWHM < cavity mode FWHM) have been investigated in planar structures [113, 215, 254]. Here, we explore a micropillar resonators in the case of low quality factors by TDBS experiments using a laser line with a FWHM of around 0.22 nm and a micropillar optical cavity mode with a FWHM of around 0.51 nm. We expect that depending on the position of the central laser wavelength with respect to the center of the optical cavity mode the phononic spectrum and the measured time resolved reflectivity trace vary as demonstrated for planar samples in section 4.4.2 and by P. Sesin et al. [215]. We also expect the measured data to change depending on the used pump power, particularly relevant in this realization given that the amount of power coupled into the micropillar corresponds to a significant part of the laser spectrum. Exploiting the stability and lack of free space alignment of the fibered setup, we explore different measurement conditions by coupling light into the micropillar mode at different detunings. We tune the laser wavelength and spectrally scan the mode covering three points: at the cavity mode center, blue shifted and red shifted from it. Given that there are also heating effects due to the laser pulses warming up the sample and causing a spectral shift of the cavity mode, we systematically scan the pump power at each of the three spectral positions selected for the laser.

The fibered micropillar was connected to the TDBS setup and using a spectrometer we recorded the micropillar cavity mode as well as the laser spectra before each power scan measurement series. Note that the micropillar cavity mode spectrum was obtained without either pump and probe pulses on the sample and therefore does not account for the effects resulting from the rise in temperature during the TDBS experiments at high power nor contains information regarding the picosecond time scale optical cavity dynamics due to the pump excitation. At the best, the cavity spectrum measured with the spectrometer serves a reference to identify the equilibrium position of the cavity mode at low pump and probe powers. In the right column of figure 5.10, panels (b), (d) and (e) present the spectral data points from the pillar and laser for each of the three spectral positions measured: the blue shifted (911.84 nm), centered (912.14 nm) and red shifted (912.56 nm) relative to the cavity mode, respectively. At each of the three spectral positions, a scan in pump power was done while maintaining the probe power fixed at 0.7 mW and the results are presented in the following sections 5.3.2–4. Pulses used for all measurements had a duration of 3.9 ps. On the left column of Fig. 5.10, panels (a), (b) and (c) present the time resolved reflectivity traces measured at low powers (pump power: 0.1 mW for panel (a) and (b), and 0.3 mW for panel (c); probe power: 0.7 mW) and corresponding to the spectral conditions depicted in panels (b), (d) and (e), respectively. These measurement conditions correspond to the minimum pump powers of the power scan at each of the spectral detuning conditions. We used the function model f_{model} from eq. 5.1 to fit the measured time resolved reflectivity traces. Figure 5.10 presents these fits as dashed lines in the left panels. Based on the resulting fit parameters and taking into account the measured laser

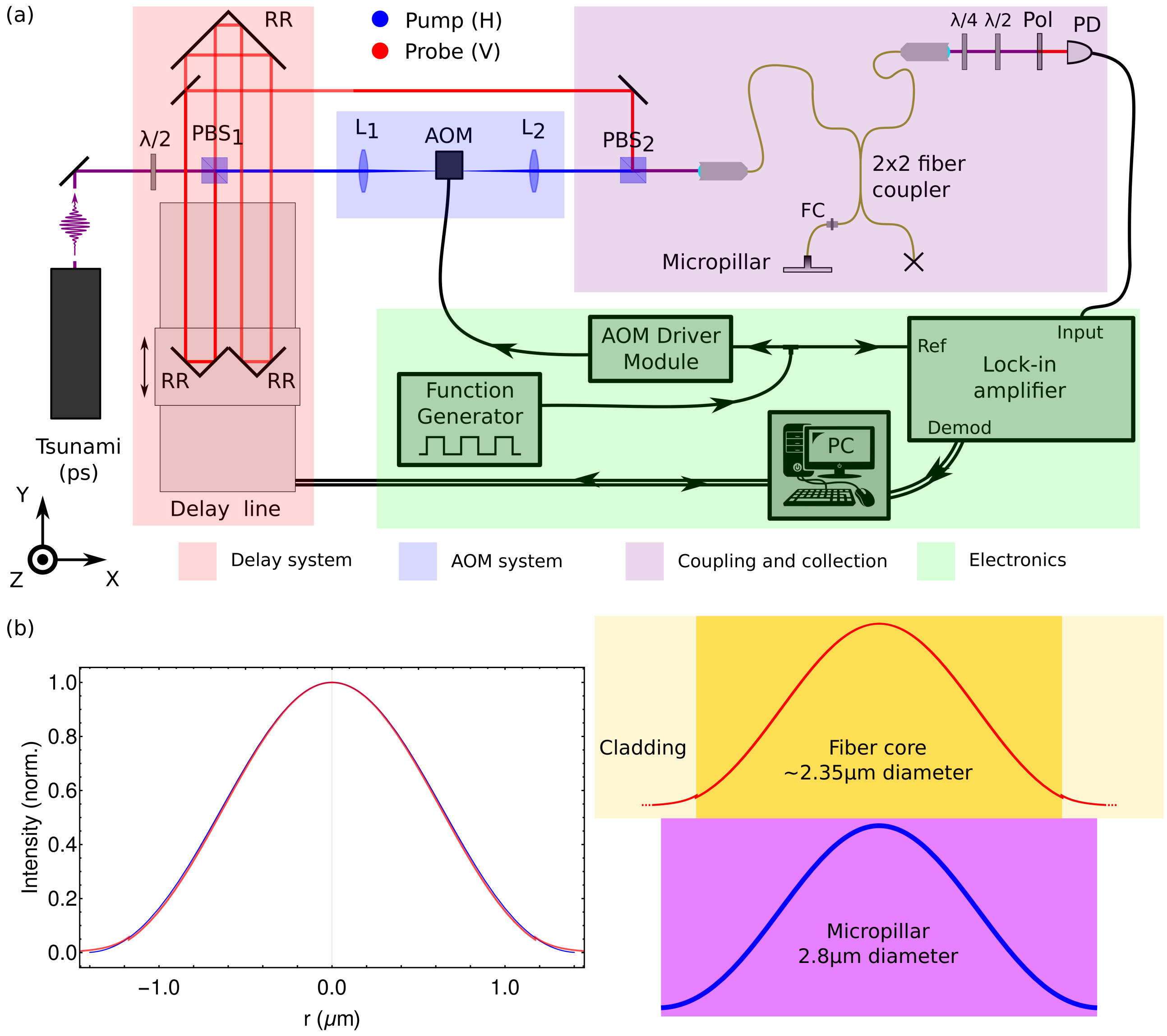

Figure 5.9: (a) Optical setup for TDBS measurements of fiber-integrated micropillars. Picosecond pulses pass by a half waveplate ($\lambda/2$) and a polarizing beam splitter (PBS_1) where two beams of pulses are generated for a pump and probe detection scheme. Then, the probe enters an optical delay system. The pump is focused through an optoacoustic modulator system where an 800 kHz modulation is imprinted on it. Both pump and probe beam are coupled to the same single-mode fiber where their spatial modes are cleaned. By controlling the delay between pump and probe and demodulating the effects of the pump on the sample at the instant the probe is reflected from it, we are able to resolve the Brillouin scattered signal in time. A quarter, a half waveplate and a polarizer are used at the probe collection to extinguish the pump pulses in a cross polarization scheme. (b) Left: Intensity profile of single-mode fiber and 2.8 μm diameter micropillar plotted in red and blue, respectively. The core refractive index and radius were found by fitting these two curves while maintaining the cladding refractive index fixed at 1.450. Right: Schematic showing the micropillar against the single-mode fiber. The intensity profile of fiber and pillar are plotted in red and blue, respectively.

wavelength, we estimate the shift caused by the pump excitation. Figure 5.10 right presents the initial and final spectral position of the relaxation modeled process using red points. We can see how for the blue shifted trace, the pump leads to a drop in the signal. This corresponds to a reduction of the sample reflectivity at the laser wavelength as we have corroborated by using the measured probe signal before demodulation (given that the phase of the complex value measured with the lock in amplifier is a free parameter, this can not be ensured just from the demodulated signal). The measured shift as obtained from the fit parameters is +0.27 nm,

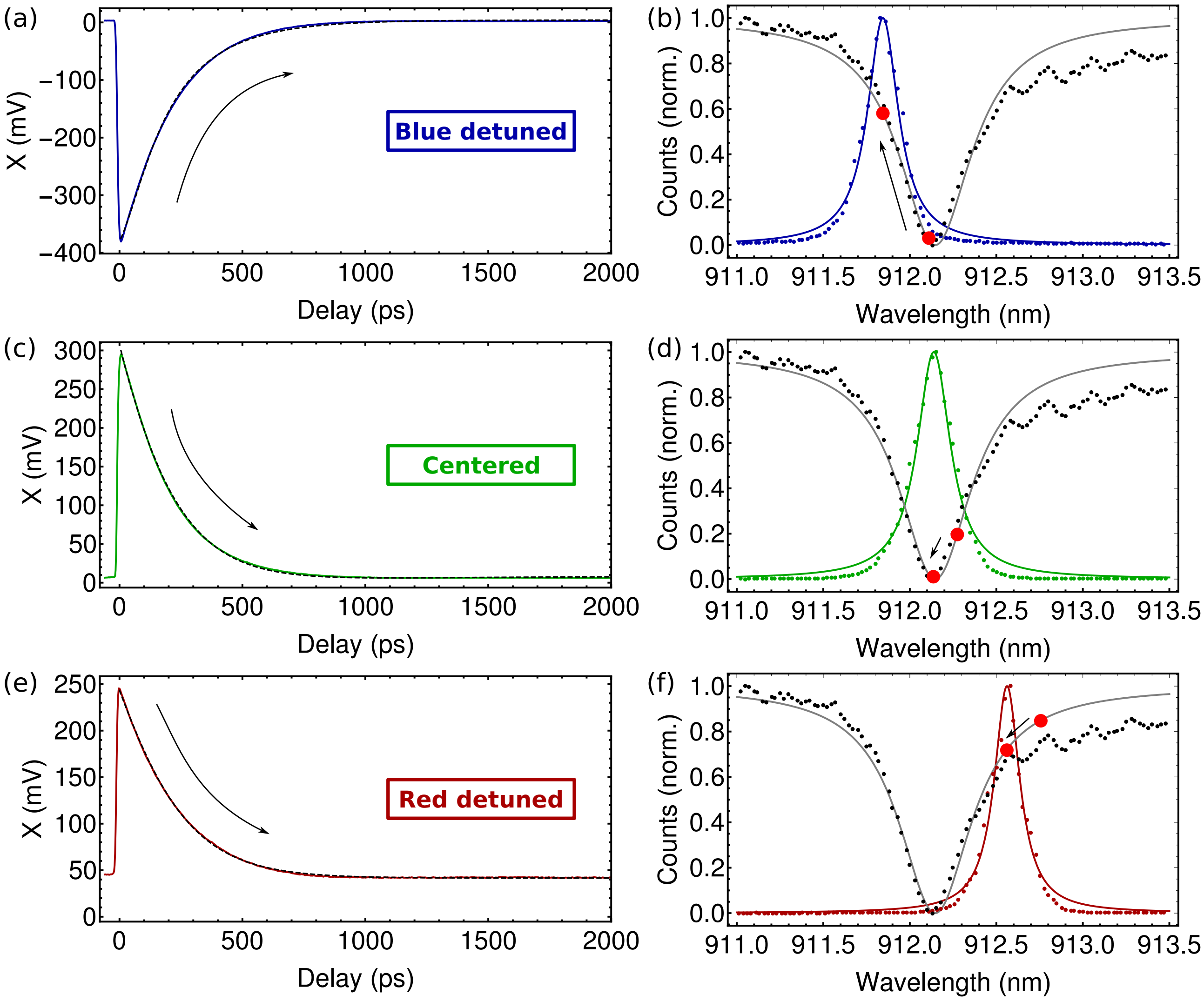

Figure 5.10: Panels (a), (c) and (e) present the reflectivity time traces from the 2 μm diameter micropillar resonator with the position of the central laser wavelength blue shifted, centered and red shifted with respect to the unperturbed pillar cavity mode. Dashed curves correspond to fits of the model given in equation 5.1. Panels (b), (d) and (f) show the spectra from the pillar and laser at each of the spectral positions. As red points the initial and final point of the relaxation process are represented as obtained from the fitted curves. Arrows indicate the direction the optical cavity dynamics changes.

i.e. a shit of -0.27 nm of the optical cavity mode[1]. For the centered and red shifted time traces we note an increase in the reflected probe signal, as expected from the spectral position at which these traces were recorded (see arrows in figure 5.10). The corresponding shifts of the laser lines (optical cavity mode) as obtained from the fitted parameters for the centered and red shifted cases are $+0.14$ (-0.14) and $+0.19$ nm (-0.19 nm), respectively.

The time traces presented in figure 5.10 correspond to measurements that reach up to 4000 ps of time delay between pump and probe. These were processed producing a filtered version of the time traces by means of a Savitsky-Golay filter maintaining all main contributions below 10 GHz. This new curve was subtracted from the raw data and the result was Fourier transformed into the spectra presented in figure 5.11. Panel (a) corresponds to the measurement done at the blue shift side of the optical cavity and is where the resonant peaks appear better resolved with a signal-to-noise ratio around 50. This is related to the laser line being close to the maximum value of the sensitivity function of the system allowing us to resolve the

---

[1] Let us remark that during the experimental realization the laser spectra remains fixed. It is the optical cavity mode that shifts, however, for practical and visualization purposes we treat the problem as if the laser line moves while the optical cavity mode is fixed

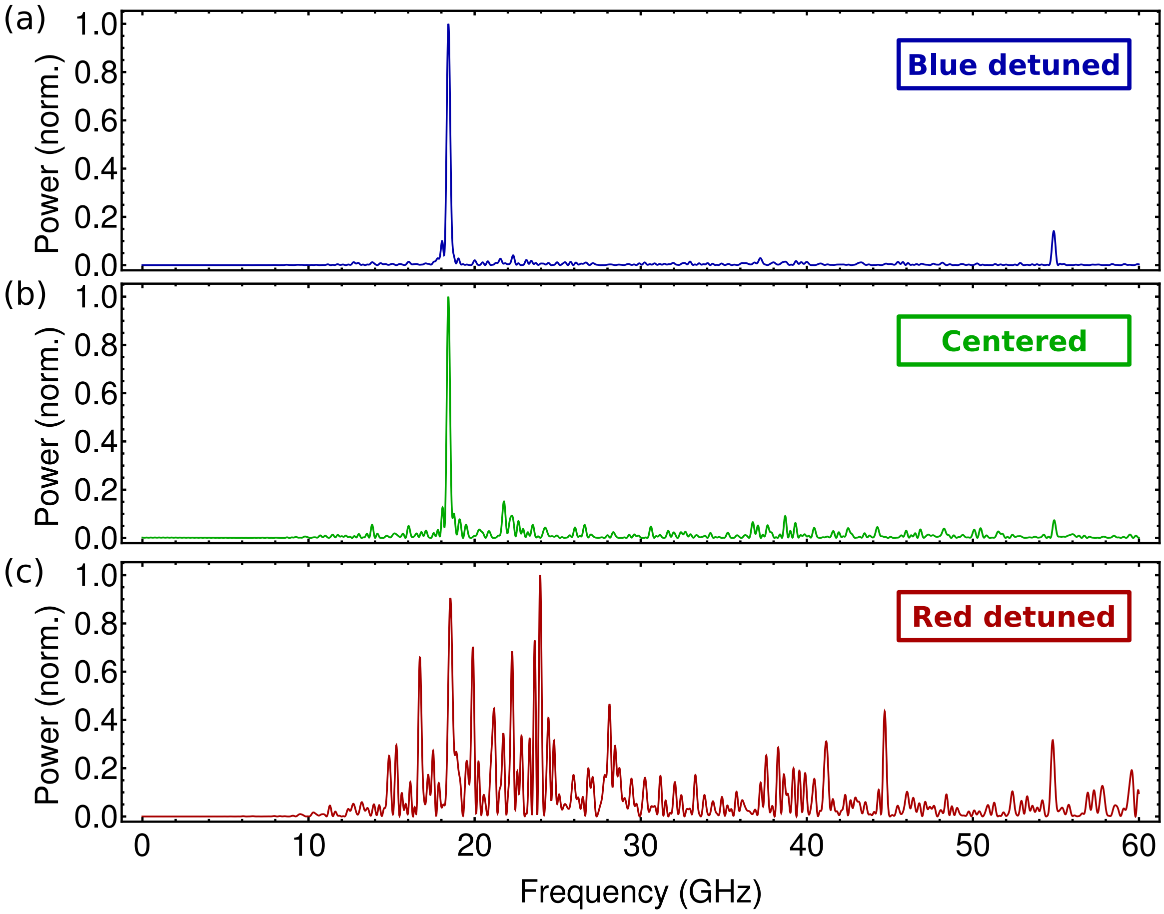

Figure 5.11: Panels (a), (b) and (c) present phononic spectrum from the 2 μm diameter micropillar resonator when blue shifted, centered and red shifted from the pillar optical cavity mode. In all cases, the first and third harmonic of the acoustic resonator are found at 18.42 GHz and 54.87 GHz, respectively. For the red shifted and centered cases the pump power was 0.1 mW. The spectrum obtained at the red side of the optical cavity mode required 0.3mW of pump power to distinguish resonant peaks. In those conditions several unidentified peaks appear around.

presence of phonons. The higher the slope at a given spectral position of the optical cavity, the higher the reflectivity oscillation expected from phonons. The sensitivity to detect phonons at different detunings from the optical cavity mode center is correlated to the derivative of the cavity mode reflectivity [215, 216, 239]. A second factor influencing the maximum signal-to-noise ratio we can obtain in the phononic spectra is the optical cavity dynamics undergone during the relaxation process after the pump excitation. Since the coherent phonons induce mainly a rigid shift of the cavity mode, the probe coupled to opposite sides of the optical mode leads to different signs of the phonon-induced reflectivity oscillations. Consequently, when the probe laser passes through both slopes of the optical cavity mode resonant peaks can be split as has been showed in section 4.4.2. In addition to effects related to phase flips, the electronic response of the micropillar blue shifts the cavity mode increasing or decreasing the amount of light coupling into the cavity. At the blue side, the measurement conditions are typically ideal since the blue shift allows more light to couple into the cavity. Figure 5.11 panel (b) presents the spectrum measured coupling the laser at the center of optical cavity reflectivity dip showing a signal-to-noise ratio of around 10. Conditions are also favorable in this spectral position because more probe light is coupled into the cavity and the blue shift of the optical cavity mode causes the laser line to pass by the high sensitivity region of the spectra resulting in phonon induced oscillations. In both panels (a) and (b), the first and third harmonic of the micropillar resonance are resolved at 18.42 and 54.87 GHz, respectively. Panel (c) presents the spectra obtained when measuring red shifted from the cavity center and low signal-to-noise

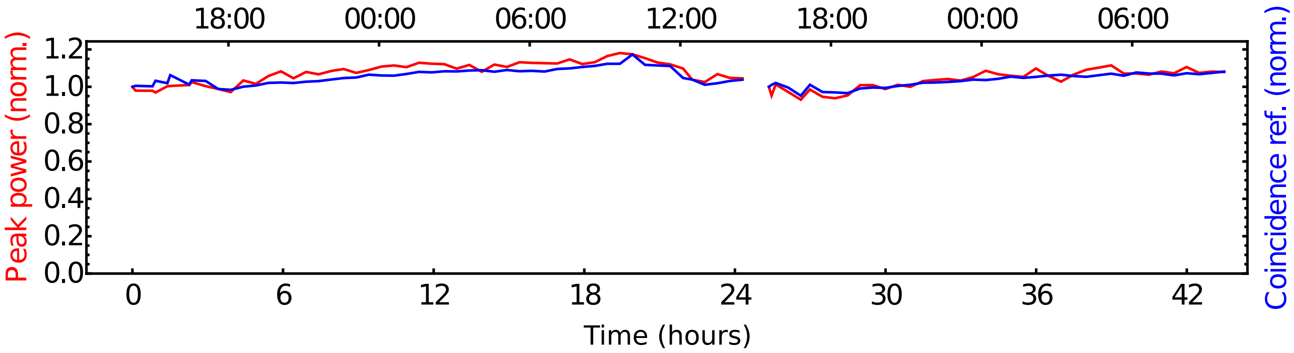

Figure 5.12: Stability of the TDBS experiments on the fiber-integrated 2.8 μm diameter micropillar. The phononic spectrum was measurement over the course of more than 42 hours. Plots present the intensity of the main resonant peak (at 18.43 GHz) and the instantaneous reflectivity after the pump excitation over the course of the full measurement.

ratio of around 1 is observed with the micropillar resonant peaks on the same scale as the noise. More light is needed (0.3 mW) to distinguish the first and third harmonics since the electronic shift of the optical cavity reduces the sensitivity to detect coherent acoustic phonons.

The low pump power values used for the time traces in figure 5.10 and spectra in figure 5.11 were picked to avoid major changes in the micropillar and to just slightly shift its cavity mode. As a result, a monotonous variation in reflectivity is seen during the relaxation process. This, however, can drastically change when increasing the pump power. In the following sections we separately present power scans, reflectivity time traces and the corresponding spectra for each spectral position. All three performed power scans were done within the same day ensuring the same laser condition along the full measurement. For each pump power we accumulated data for 5 minutes. In addition, the changes of pump power take an additional 5 minutes. In total, each measured spectrum thus required a total of 10 minutes. To perform such TDBS experiments in a systematic way we required the experimental conditions to remain constant over the full duration of the scan. To asses the stability of the fibered TDBS setup and sample we proceed to perform a long-term experiment where we measured a phononic spectrum when the laser was detuned on the blue side of the optical cavity mode. Pump and probe powers were fixed at 0.5 and 0.7 mW, respectively. These measurement conditions were chose to obtain a clear resonant peak with a good signal-to-noise ratio, but using pump powers far away from when thermal effects start to appear[2]. We measured the phononic spectra every 30 minutes and we only intervened in between in order to adjust the power (such as they remain fixed at 0.5 and 0.7 mW). The full experimental realization ran over the course of 42 hours and we adjusted the laser due to drifts once after 24 hours of measurement time. Figure 5.12 presents the results of such an experiment were we monitored the main resonant peak at 18.43 GHz and plotted its peak intensity over the 42 hours of the measurement. In addition, we also present in the same figure, the peak value of the instantaneous reflectivity measured after the pump excitation of the micropillar. The plotted curves shows variations of 15% over the full measurement following a cycle of 24 hours imposed by the laboratory conditions (mainly temperature). The results demonstrate a remarkable stability in contrast with free space implementation of TDBS experiments on micropillars. The fixed coupling conditions indicate that, by providing the same laser condition, we can ensure the same experimental results in any other laboratory, making the device a transferable platform for coherent phonon generation and detection experiments. We can also grant comparable results within a single power scan done over the course of hours. Moreover, the fiber-integrated micropillar resonator

---

[2] As it is going to be shown in section 5.3.2, the most intense resonant peak when measuring blue-detuned from the cavity mode, was obtained for pump and probe powers of 0.9 and 0.7 mW, respectively. Thermal effects start to be noted at 1 mW of pump power. For the stability assessment, we choose an intermediate pump power of 0.5 mW where the resonant peak was intense but we maintain the measurement conditions far away thermal effects.

constitutes a plug-and-play device operating in the tens of gigahertz range which, together with the fibered pump-probe setup, results in a versatile approach for nanoacoustic experiments. In the following sections we present the results of the power scan at the three spectral conditions chosen where each measurement had a duration between 4 to 6 hours and was done within the same day.

5.3.2 Micropillar optical cavity dynamics when blue detuned: Dominant electronic response for efficient phonon detection

In this section we investigate the evolution of the time resolved reflectivity traces and the phononic spectrum as a function of pump power when measuring with a laser blue shifted from the micropillar optical cavity mode. We will see how the electronic response of the micropillar is dominant in this condition because its blue shifting of the optical cavity leads to an alignment between the laser central wavelength and the optical cavity mode. Consequently, the time resolved reflectivity traces are strongly dependent of the pump power at low powers (< 1 mW). At high powers (> 1 mW), thermal effects start to play a more significant role altering the measured time traces and reducing the intensity of the resonant peak in their corresponding phononic spectra. TDBS experiments when blue detuned from an optical cavity tend to be considered as the optimum conditions to obtain the best signal-to-noise ratio in phononic spectra resonant peaks [215, 216, 239]. Here we show how different pump and probe power conditions alter significantly the intensity of the measured resonant peaks and how the thermal and electronic effects in play during the experimental realization can be studied by analyzing the time resolved reflectivity traces.

The first series of measurements corresponds to a power scan with the laser blue-detuned (911.84 nm) from the optical cavity mode (see figure 5.10 b). We investigate the electronic response of the system due to the pump excitation of the micropillar as a function of pump power and its interplay with the heating effect caused by the accumulation of thermal energy due to the repeated action of the pump pulses. Figure 5.13 (a) and (b) present color maps showing the evolution of the time resolved reflectivity traces and their corresponding phononic spectra as a function of pump power, respectively. As for all measurements in this section, the probe power was fixed at 0.7 mW. The pump scanned through thirteen values: from 0.1 mW to 1 mW in steps of 0.1 mW, and from 1 mW to 2.5 mW in steps of 0.5 mW. The laser pulse duration was fixed at 3.9 ps. All measurements were done within the same day and using the same configuration for all experimental parameters except for the pump power. The example presented in 5.10 panel (a) corresponds to the trace with the lowest pump power of 0.1 mW from the scan. Figure 5.13 (a) presents the time resolved reflectivity traces as a function of pump power. The full intensity map is completed by interpolating between the measured traces. The scanned pump powers are marked on the plot's right axis by ticks (in some cases the values are written in red next to each tick) From the color map showing the time resolved reflectivity traces we can see how increasing the power changes the reflectivity response, from a rapid change and subsequent monotonous decay for low powers, to a response featuring the optical cavity dynamics with a local minimum. From 0.1 mW to 0.5 mW the minimum in the trace transits from non-existing to appearing closer to zero delay. Above 0.5 mW, the minimum in reflectivity appears clearer while shifting towards larger delays reaching its maximum at around 200 ps for 1 mW and remaining there for up to 2.5 mW.

Figure 5.13 (b) shows as an intensity map the phononic spectra obtained after processing the reflectivity time traces presented in panel figure 5.13 (a). The full map is obtained from interpolating the experimental spectra at different pump powers. The micropillar resonant peak appears at 18.45 GHz and has it highest value at 0.9 mW of pump power. For pump powers of 1 mW and higher, the resonant peak starts to reduce its intensity and eventually blends into the background noise. By comparing both intensity maps in figure 5.13 we notice a correspondence between the highest resonant peak of the phononic spectra and the minimum

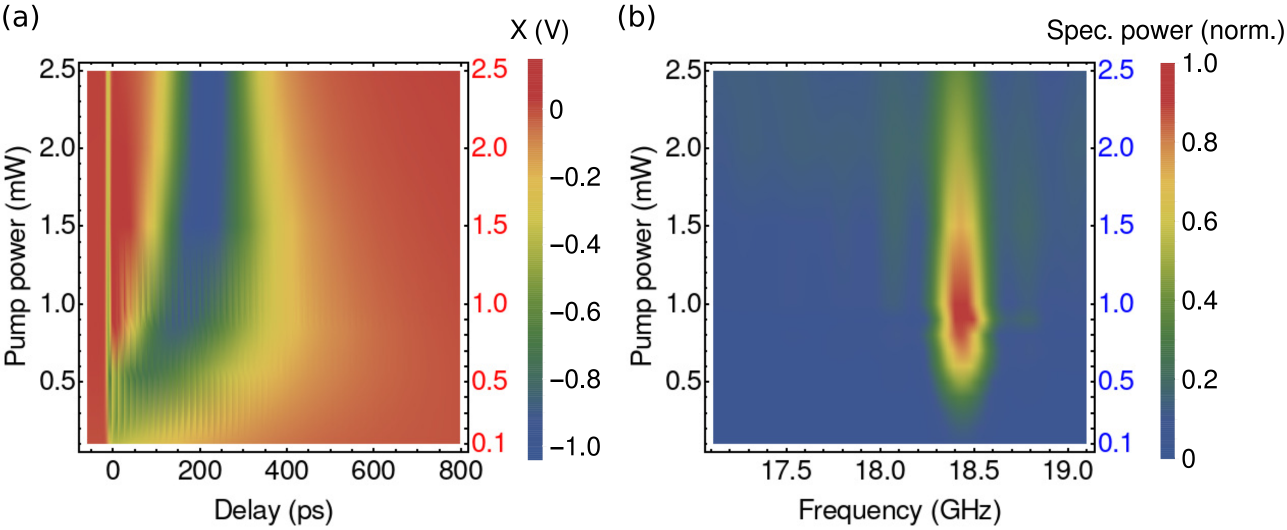

Figure 5.13: Measured with the laser detuned towards the blue side of the optical cavity mode, panels (a) and (b) present the intensity map of the time resolved reflectivity traces and their corresponding phononic spectra as a function of pump power, respectively. The full intensitity map results from interpolating between the recorded experimental data. In panel (b) the resonant peak is centered at 18.45 GHz.

in reflectivity of the time traces reaching its maximum delay position at around 200 ps. The optical cavity dynamics determines the time delay at which the minimum in reflectivity appears. In section 5.1 we propose a model (eq. 5.1) to describe this dynamics and numerically fit it to the time resolved reflectivity traces. Here, using the same model we fit all measured time traces presented in this section. The fit algorithm was implemented using a unique set of seeds for the fitting parameters in order to ensure a systematic implementation of the model.

Figure 5.14 presents as solid blue curves the time resolved reflectivity traces for all pump powers measured with the laser on the blue side of the optical cavity mode (sketch of the cavity mode and laser position presented at the bottom). Time traces are plotted for each of the thirteen measured pump powers. Pump power is indicated in red for each plot. In black dashed lines, curves obtained by fitting the model proposed in eq. 5.1 are shown. For the experimental data (solid blue), we notice how increasing the pump power and therefore shifting the cavity mode further towards the blue side, the reflectivity curve starts to acquire a shape like a cavity reflectivity dip. This is a consequence of the relaxation process acting as a spectral scan of the optical reflectivity. From the fitted curves, for higher powers the model seems to stop reproducing the optical cavity dynamics measured in the experiment, in particular for 1.5, 2.0 and 2.5 mW. More exhaustive attempts to increase the fitting agreement with the experimental failed as a consequence of the thermal effects on the micropillar starting to play a more significant role. The disagreement happens because the model used considers only the electronic relaxation of the sample while it omits the thermal effects that counteract this relaxation process. In particular, the slower change in reflectivity at small delays (below 100 ps of delay) are not reproduced as a consequence of the thermal effects playing a significant role at this stage. For the other ten reflectivity time traces measured with pump powers between 0.1 and 1 mW the agreement is remarkably good.

To understand how the cavity dynamics evolves from the time traces, we separate them in three groups according to how the reflectivity just after the pump excitation varied when increasing power. Figure 5.15 (a) presents a zoom in the first 250 ps after the pump excitation for the measurements done with pump powers going from 0.1 to 0.4 mW in steps of 0.1 mW. At this lower limit, while increasing the pump power, we are increasing the starting shift caused by the electronic response of the micropillar due to the pump action. As a result, and since the optical cavity starts with the laser at its blue side (see sketch in figure), the more the cavity shifts, the more the laser line scans the cavity mode Eventually the laser line reaches

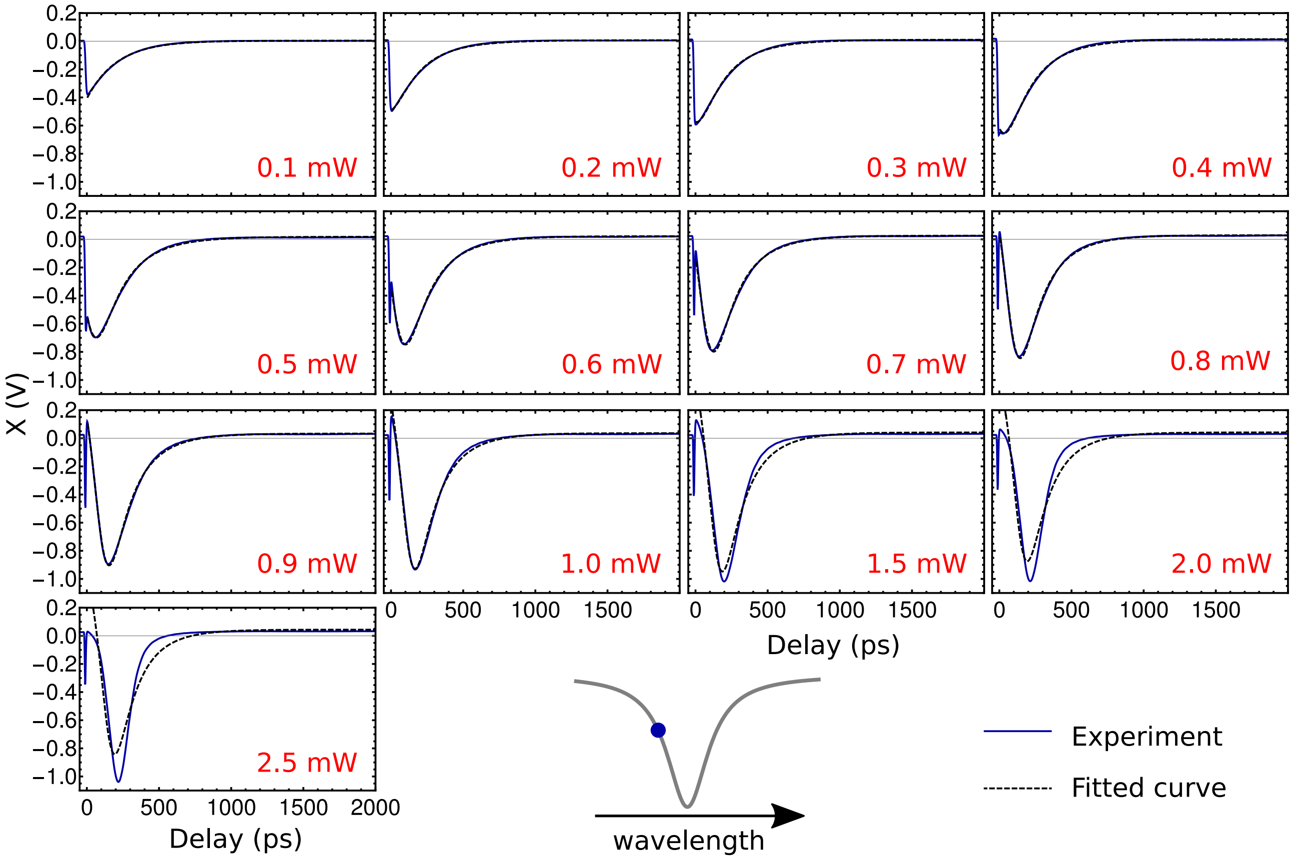

Figure 5.14: Time resolved reflectivity traces measured at the blue side of the optical cavity mode as a function of pump power. Insets in each plot indicate the pump powers going from 0.1 mW up to 2.5 mW. On top of the experimental data a black dashed fitted curve is presented for each time trace. The fit was done using the model given in equation 5.1. For the high pump power limit the fit stops reproducing the measured data. The fit was done systematically for all data using the same conditions (same model and parameters seed). An sketch showing the cavity reflectivity dip and the laser center on its blue side is placed in the bottom.

the minimum in reflectivity and passes to the red side of the cavity mode, increasing the probed reflectivity again. This situation can be already noticed for 0.4 mW of pump power as the slight bump just after zero delay. As a consequence, in this lower limit of pump powers the micropillar's resonant peak is just starting to increase its intensity since the increment of pump power leads to electron hole pairs being created producing phonons by the deformation potential mechanism. In order to use the fitting model as presented in equation 5.1, we redefine the zero delay position to the time delay when the instantaneous reflectivity reached its peak value just after the simultaneous arrival of pump and probe on the micropillar, at the lowest power (0.1 mW). As a result, this simultaneous arrival occurs at slightly negative delays, as can be seen from the initial drastic change in reflectivity around −10 ps. Panel (b) presents the scenario when the pump power is large enough so the laser already passes the minimum reflectivity due to the initial shift induced by the pump. Then, the higher the pump power, the higher the resulting reflectivity since at zero delay the probe is now reflected on the red slope of the optical reflectivity dip. This occurs for pump powers between 0.4 and 1.0 mW. In this range, the delay at which the cavity passes by the minimum in reflectivity during its relaxation process increases up to around 170 ps. This results in the larger shift taking more time to reach this minimum reflectivity conditions. Finally, at high powers between 1.0 up to 2.5 mW, a different behavior is observed during the first hundred picoseconds of delay. The fast changes vary into slower slopes for longer time. If the fast change was caused by the exponential in the proposed model (eq. 5.1), we conclude that a second effect, counteracting the electronic relaxation must be altering the cavity dynamics. We hypothesize that thermal effects can be

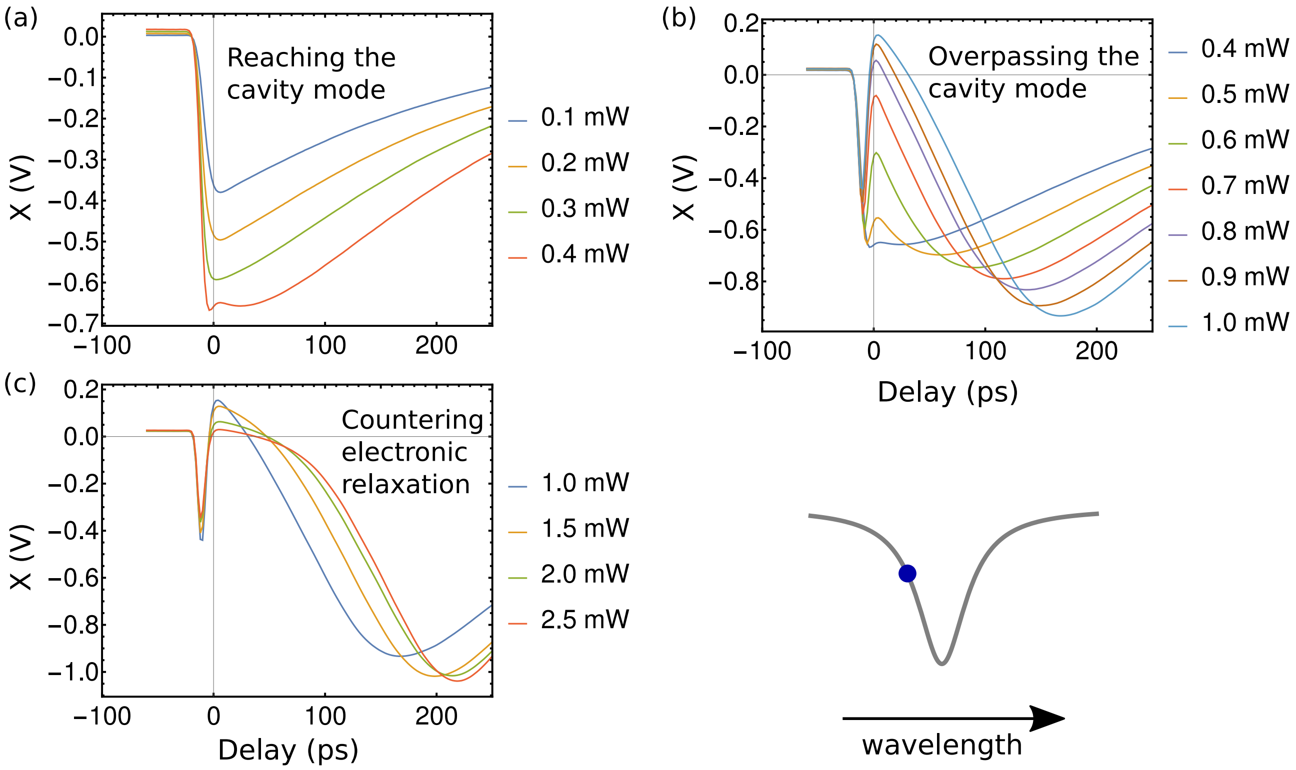

Figure 5.15: Panels (a), (b) and (c) plot the time resolved reflectivity traces measured at the blue side of the optical cavity for pump powers going from 0.1 mW up to 0.4 mW, from 0.4 mW up to 1.0 mW and from 1.0 mW up to 2.5 mW, respectively. (a) Reflectivity drops after pump reflection. While increasing the pump power we increase the blue shift the cavity mode experiences, eventually reaching the minimum reflectivity, i.e. at the cavity mode. (b) After passing the cavity mode, reflectivity starts to increase just after the pump reflection. Also a minimum appears on the relaxation process when passing again by the cavity mode. The higher the power the longer it takes the system to recover. (c) After the coincidence, the electronic relaxation process red shifts the cavity while the thermal response, cooling after the pump action blue shifts it. At the high power limit, the thermal response becomes relevant countering the electronic response. A sketch showing the cavity reflectivity dip and the laser center on its blue side is placed in the bottom right.

responsible for this. While during the relaxation process the optical cavity red shifts, thermal effects induced by the high pump power heats the micropillar. After the pump pulse abandons the micropillar, a cool down process starts which results in a blue shift, effectively countering the electronic relaxation process. Notice that this does not imply a change in the time it takes the system to relax since these two process, thermal and electronic relaxation are occurring simultaneously. The three higher pump powers, where the bending of the reflectivity curve at lower delays changes into a slow slope coincide with a breakdown of the model in equation 5.1, i.e. an effect becomes dominant that is not captured by the model. The thermal effect of the pump on the probe also manifests in the background signal before the pump excitation. As the experiment takes place, pump pulses are being coupled in the micropillar every 12.5 ns. This short period at higher powers and short pulses lead to heating of the sample due to an accumulative effect of the subsequent pulses arriving. As a result, we can notice in figure 5.15 how, while we increase the pump power, the background signal prior to the rapid change in reflectivity near zero delay progressively increases with the pump power indicating heating effects in the fiber-integrated micropillar.

From the optical cavity dynamics we interpret why the maximum resonant peak appears at 0.9 mW of pump power. The sensitivity function to detect phonons depends on the derivative of the micropillar optical reflectivity response. The highest sensitivity occurs at the higher slopes on both the blue and the red side of the optical cavity mode. Since we are starting from

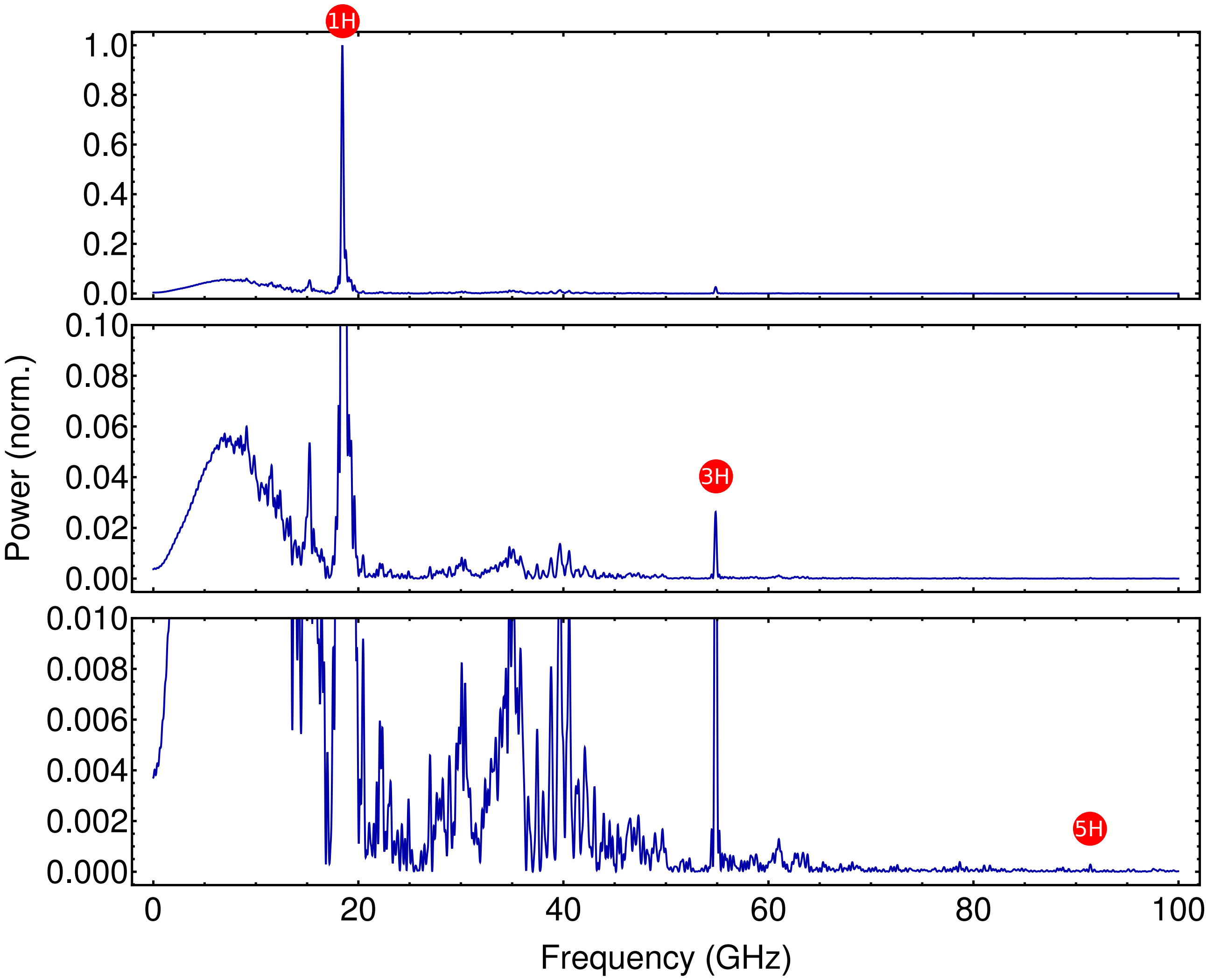

Figure 5.16: Phononic spectrum from the 2.8 μm diameter fiber-integrated micropillar resonator when the laser is blue shifted from its optical cavity mode. Pump and probe power for this measurement were 0.9 mW and 0.7 mW, respectively. Laser pulse duration was fixed at 3.8 ps. Three vertical zoom ins of the same spectrum are presented increasing from top to bottom by a factor of ten on each plot. The first, third and fifth harmonic of the acoustic resonator are found at 18.42 GHz, 54.86 GHz and 91.42 GHz, respectively (and marked by red points with 1H, 3H and 5H accordingly). At the *GaAs* spacer, even harmonics do not contribute to the measured signal since the overlap between electric field and strain change is effectively zero. Nevertheless, at the even harmonics, in particular the second one, a series of peaks resulting from modes spanning along the multilayer mirrors appear as we have already seen when measuring planar cavities (see figure 4.18).

the blue side and shifting the laser relative to the cavity, to the red side, we are able to be in the scenario where we pass by both maxima in sensitivity thus resulting in larger oscillations amplitudes induced by phonons. The power then does not keep increasing since thermal effects start to alter this dynamics. Figure 5.16 presents the spectrum at this scenario i.e. for a pump power of 0.9 mW. Three versions of the same spectrum are plotted with different scales along the vertical axis. At frequencies below 10 GHz we see an increase in the spectral power resulting from the inability of the Savitsky-Golay filter to replicate the rapid changes at the beginning of the time trace. The same effect is seen when processing the data differently, only differentiating and Fourier transforming them, but in this case the effect is much more attenuated due to the filter. The first, third and fifth harmonics of the acoustic resonance are distinguished in the spectrum and marked by the red points with 1H, 3H and 5H, respectively. Only odd harmonics are visible because the overlap between the change of strain and the electric field is maximum.

In contrast, for even harmonics the overlap between acoustic and optical fields is minimum in the *GaAs* spacer. However, the distributed Bragg reflectors present a partial overlap between these two fields at even harmonics. As a consequence, a modulation in reflectivity is induced and manifests in the spectrum at even multiples of the resonant frequency. In particular for the second harmonic, a series of peaks around 40 GHz are distinguished in a similar fashion as seen when investigating colocalized acoustic and optical modes in planar layered samples (see figure 4.18).

We have presented the results obtained from the pump power scan blue-detuned from the optical cavity mode. We have showed how, by increasing the pump power the optical cavity dynamics vary and manifest in the measured reflectivity time traces. In the following sections we will present results on the center and the red side of the cavity mode, and compare the results.

5.3.3 Micropillar optical cavity dynamics when centered at the cavity mode: Electronic and thermal effects leading to two local maxima of phonon detection efficiency

In this section we explore the scenario when the laser is tuned at the center of the micropillar optical cavity mode. Under this condition, most of the pump power is coupled to the optical cavity mode when the pump pulse reaches the micropillar. We perform a pump power scan and show how there are two local maxima of the micropillar resonant peak in the phononic spectrum. These two local extremes of the resonant peak at around 18 GHz are the result of the interplay between thermal and electronic effects. The first local maximum is found at low pump powers and has a similar nature as the one encounter in section 5.3.1, i.e. in conditions where the electronic response is dominant. The second resonant peak maximum is found at higher pump powers where the equilibrium position of the optical cavity is red shifted due to thermal effects. We use the model given by eq. 5.1 in order to evaluate the evolution of the optical cavity from the time resolved reflectivity traces. The results indicate how, when tuned at the center of the optical cavity mode, there are two different scenarios that can be targeted depending of the pump power used.

The second power scan for the fiber-integrated micropillar was done with the laser tuned at its optical cavity mode (912.14 nm. See figure 5.10 (d)). The measurement conditions where the same as in section 5.3.1 and the pump power was set to nineteen different values going from 0.1 mW up to 10 mW.

Figure 5.17 panels (a) and (b) present intensity maps of the reflectivity time traces and phononic spectra as a function of pump power, respectively. The resonant frequency appears centered at 18.45 GHz. The nineteen pump powers used for these measurements were obtained by varying from 0.1 to 1.0 mW in steps of 0.1 mW, then from 1.5 to 3.0 mW in steps of 0.5 mW and finally at 4.0, 5.0, 6.0, 8.0 and 10.0 mW. At the right axis, ticks are placed marking all cross-sections from the maps corresponding to experimental data. From the time traces (panels a) we see a minimum in reflectivity appearing between 200 and 400 ps. Considering the spectral position to which the system relaxes long after the arrival of the pump is at the center of the cavity mode, the proposed model (equation 5.1) is not consistent with the experimental data. The reason for this inconsistency is that the model contains the assumption that the relaxation of the spectral cavity position is monotonous after the initial excursion. Therefore, we should not be able to pass by the micropillar reflectivity dip while relaxing, but this minimum should only be the end point of the electronic relaxation. Experimental data, however, show otherwise. The laser line is passing the cavity dip regardless of starting at the cavity resonance mode. In comparison with the measurements for which the laser was blue-detuned from the cavity mode, this occurs for relatively high powers (the maximum power used when blue-detuned was 2.5 mW. In contrast for the measurements done at the cavity mode we reach up to 10 mW). Thus, taking into consideration what we measured under those conditions, we can expect thermal effects to

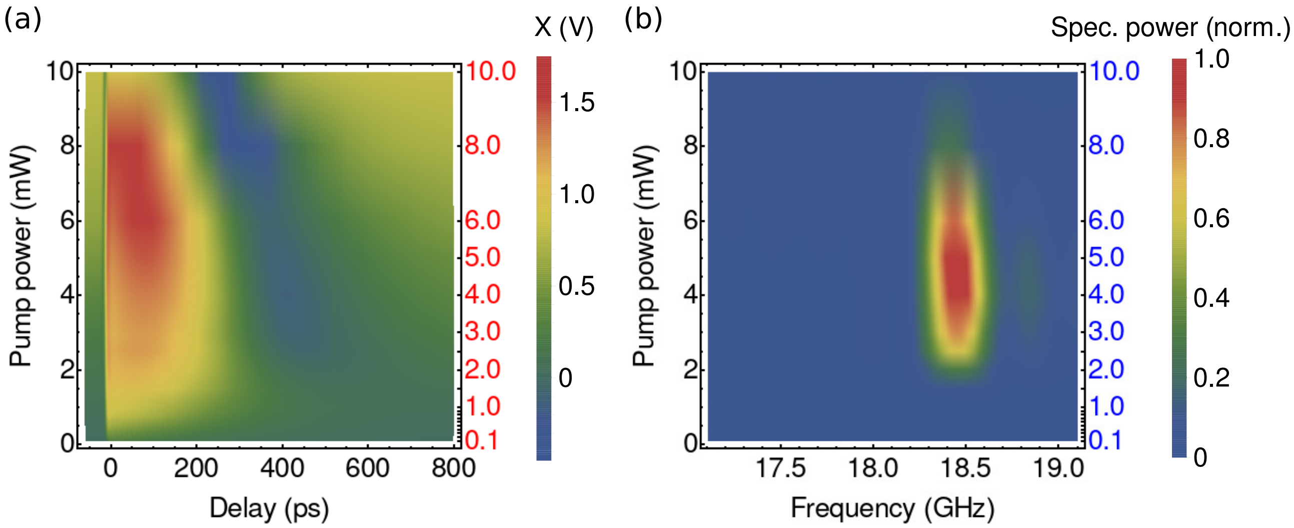

Figure 5.17: Measured with the laser tuned at the optical cavity mode, panels (a) and (b) present the intensity map of the time resolved reflectivity traces and their corresponding phononic spectra as a function of pump power, respectively. From the acquired experimental data, the full intensity maps are interpolated. In panel (b) the resonant frequency occurs at 18.45 GHz.

play a role in the time traces at the high powers where the minimum in reflectivity appears. Then, we hypothesize that the cavity mode prior to the arrival of the pump is already red shifted (and not at resonance as measured without the pulses altering the system) due to the micropillar increasing its temperature because of an accumulation effect of the previous pump pulses being partially absorbed every ≈ 12.5 ns. This effect heats the pillar while increasing the pump power resulting in a red shift of the cavity mode with respect to the laser, positioning the laser out of the cavity mode and effectively placing it again on the blue side. Supporting this hypothesis, the minimum in reflectivity shifts towards lower delays while increasing the pump power. Considering this, we can see how in a similar way as for the spectra measured with the laser blue-detuned from the cavity mode, by comparing panels (a) and (b) we found a correspondence between the highest resonant peak measured at 5.0 mW and the minimum in reflectivity reaching its maximum delay position (around 370 ps).

Figure 5.17 panel (b) shows a single three dimensional peak around 5 mW. However, from processing the data at lower powers we have already seen that resonant phonons can be distinguished at low powers (see figure 5.11 panel b). In order to track how this resonance is varying while increasing the power, we measure using pump powers varying between 0.1 and 1.0 mW in steps of 0.1 mW. With this data we were able to follow the trend of the resonant peak at low powers. Figure 5.18 presents an intensity map showing only a zoom in of the region of low pump powers up to 0.8 mW. The data is organized in the same fashion as in the not zoomed version. Panel (a) and (b) present the experimental time resolved reflectivity traces and corresponding phononic spectra, respectively. Scale factors are preserved as for the not zoomed version but the color levels are scaled to the new range of values. As for the measurements with high pump powers, the resonant peak, now with a peak value for this range at 18.43 GHz, increases and then decreases while varying the pump power. The peak value is measured with the pump at 0.5 mW, and contrasting with both the high power conditions and the measurements blue-detuned from the optical cavity, no minimum appears in the reflectivity time traces, but it changes monotonically while relaxing back to equilibrium. On both sides of the resonance, two peaks start to appear corresponding to the edges of the acoustic minigap from the distributed Bragg reflectors forming the resonator.

The results seen for the pump power scan at the center of the cavity mode show two conditions for which the resonant peak reaches a local maximum. While the first one, at high pump powers, results from the heating effects red shifting the cavity, at the low pump

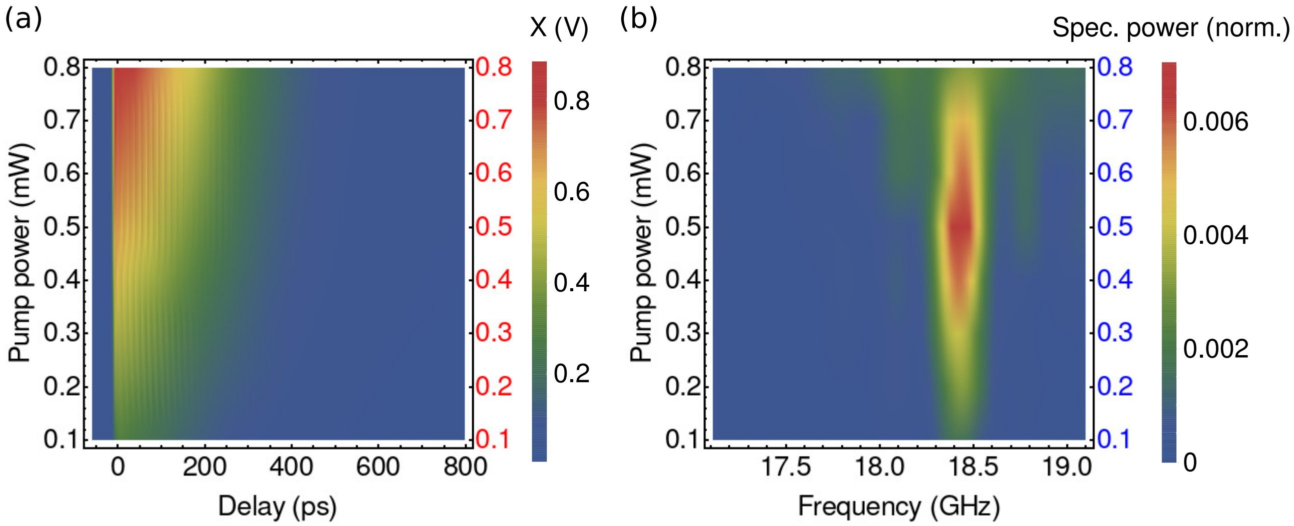

Figure 5.18: Measured with the laser tuned at the optical cavity mode, panels (a) and (b) present the intensity map of time resolved reflectivity traces and their corresponding phononic spectra as a function of pump power, respectively. Only the first eight pump powers (going from 0.1 up to 0.8 mW) are presented in this plot to highlight the spectral changes in this range. The full intensity maps result from interpolation using the experimental data. In panel (b) the resonant frequency in this range has its peak value at 18.43 GHz.

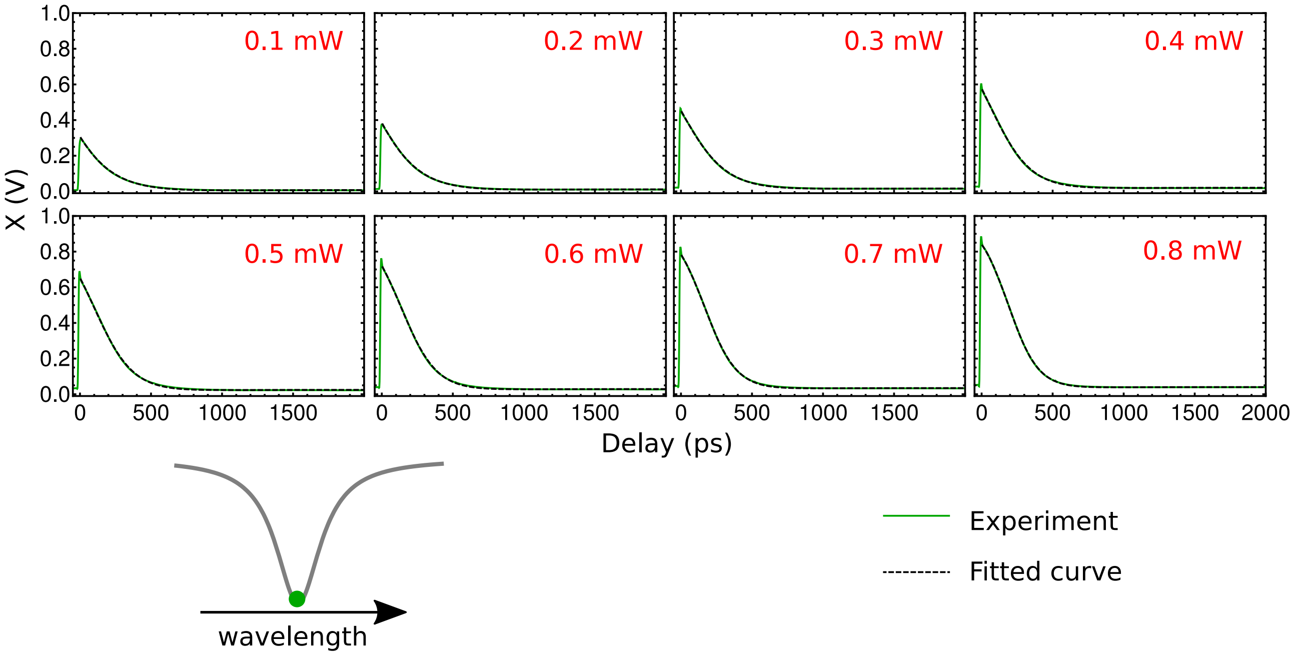

Figure 5.19: Time resolved reflectivity traces measured at the center of the optical cavity mode as a function of pump power. Insets in each plot indicate the pump powers going from 0.1 mW up to 0.8 mW in steps of 0.1 mW. On top of the experimental data a black dashed fitted curve is presented for each time trace. The fit was done using the model given in equation 5.1 and in a systematic way using the same conditions (same model and parameters seed). A sketch showing the cavity reflectivity dip and the laser center is placed in the bottom.

powers the electronic response of the system and its relaxation is the main contributor to the optical cavity dynamics resulting in the measured time traces. To support this hypothesis, we proceeded to fit the measured curves in this range with the proposed model of a shifting Lorentzian dip (equation 5.1).

Figure 5.19 presents in solid green curves the first eight reflectivity time traces measured at pump powers going from 0.1 to 0.8 mW. On top of the experimental data, curves resulting

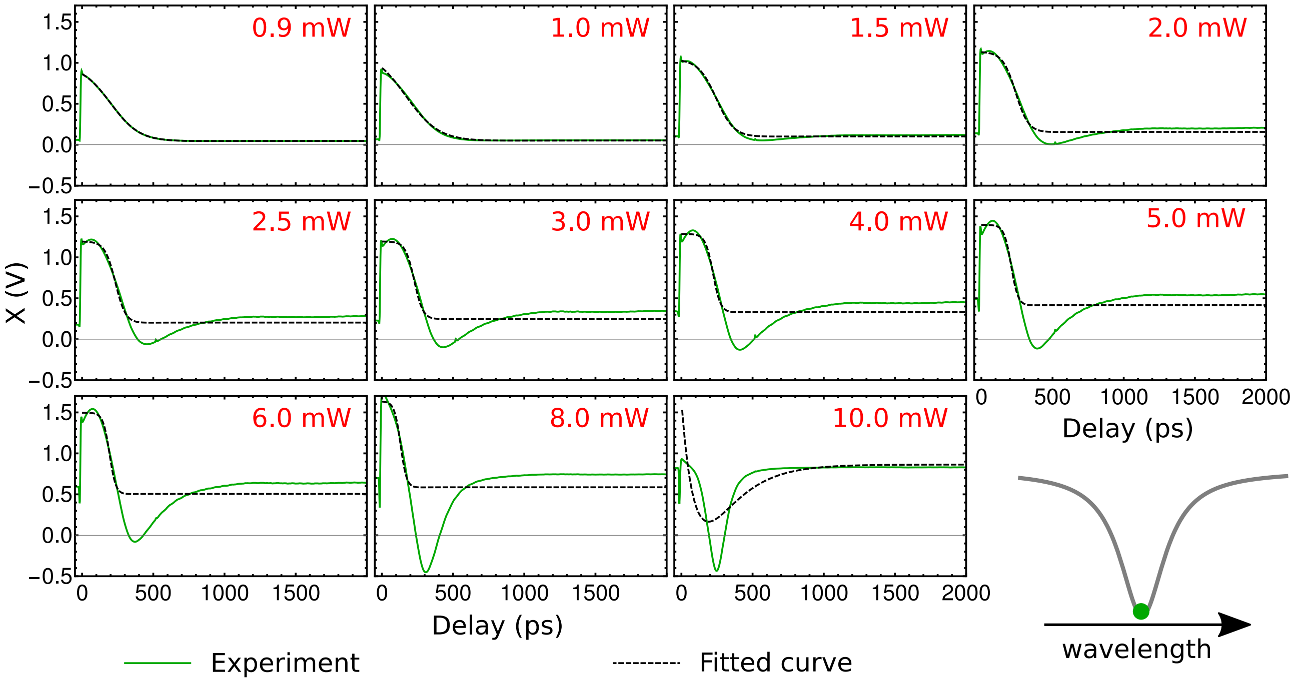

Figure 5.20: Time resolved reflectivity traces measured at the center of the optical cavity mode as a function of pump power. Insets in each plot indicate the pump powers going from 0.9 up to 10.0 mW. On top of the experimental data a black dashed fitted curve is presented for each time trace. The fit was done using the model given in equation 5.1 and in a systematic way using the same conditions (same model and parameters seed). These condition were the same that those used for lower pump powers (below 0.9 mW) An sketch showing the cavity reflectivity dip and the laser center at it is placed in the bottom.

from fitting the model against the measured time traces during the electronic relaxation show good agreement with the experiment. All fitting processes were done systematically, meaning that both the model and the free parameter initialization values were the same for all traces. The trend that is observed in this range is that while increasing the pump power, the shift just after the pump excitation, places the laser up in the reflectivity dip of the optical cavity mode, effectively "climbing" it. We can notice also the effect of heating starting to play a role resulting in a rapid change near zero delay and producing a peak, which becomes distinguishable between 0.5 and 0.8 mW. We attribute this to the sample cooling after the pump action took place, slightly shifting the cavity towards the blue, reducing its reflectivity. From these results, we attribute the resonant peak seen at lower powers (figure 5.18 panel b) to the shift due to the pump excitation placing the laser at the red side of the cavity mode and passing by the high sensitivity region for phonon detection at its highs slope (at 0.5 mW of pump power). Increasing the power beyond this limit leads to a longer time spent within the high sensitivity region during the electronic relaxation.

Figure 5.20 presents in solid green curves the last eleven reflectivity time traces measured at pump powers from 0.9 to 10.0 mW. On top of the experimental data, curves resulting from fitting the model against the measured time traces during the electronic relaxation show good agreement for the first two pump powers (0.9 mW and 1.0 mW). While increasing the power the fitting curve becomes less able to reproduce the experimental data. Two features are not consistent with the proposed model. The first one is the bending of the reflectivity curve just after zero delay, leading to the peak around it and the subsequent increase in signal after it. The second one is the appearance of a minimum in reflectivity between 200 and 500 ps of delay. Our model does not reproduce this because it considers the initial spectral position of the laser to be very close to the optical cavity mode, as it was measured through the use of a spectrometer. The heating due to the accumulation effect caused by the series of pump pulses being coupled into the micropillar changes this condition. Instead, the cavity relaxed position

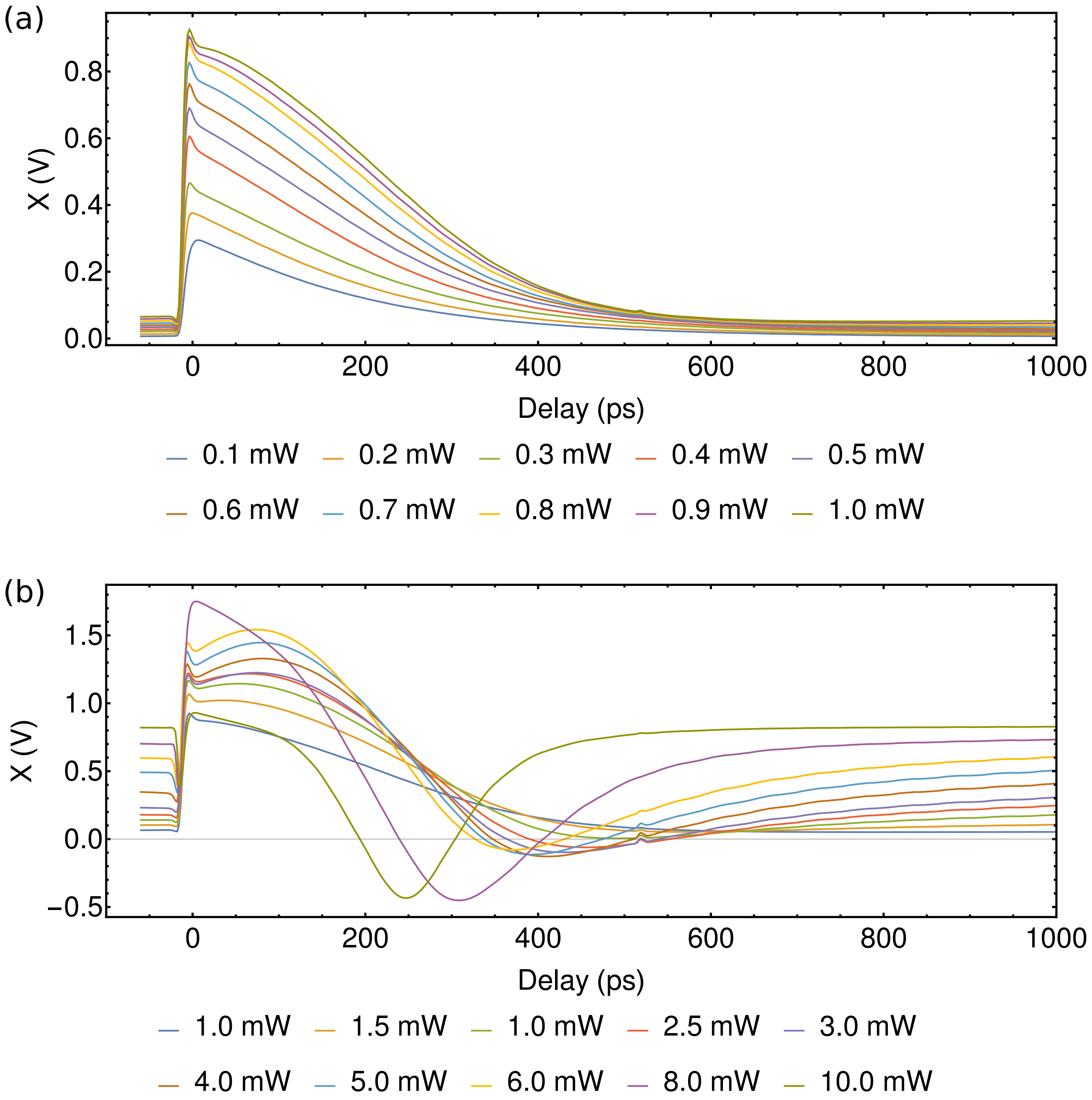

Figure 5.21: Panels (a) and (b) plot the time resolved reflectivity traces measured at the center of the cavity mode for pump powers going from 0.1 mW up to 1.0 mW and from 1.0 mW up to 10.0 mW, respectively. (a) Reflectivity increases after pump reflection. By increasing the pump power we increase the initial blue shift of the cavity mode. As a result from starting at the resonant wavelength, the shift results in an increase in reflectivity. (b) While the micropillar starts to heat due to the pump pulse the rise in temperature counter the electronic response due to the pump excitation. After the pump abandons the micropillar, it cools down counteracting the optical cavity red shift of the electronic relaxation process. At 10 mW, we can see how this results in an effective scan in time of the optical cavity mode.

(before pump action) is red shifted such that, when the pump triggers the electronic response of the micropillar, the blue shifts caused by it results in the laser traversing the reflectivity dip producing traces with minima as can be seen progressively appearing while varying the pump power from 1.5 up to 10 mW.

Figure 5.21 present the measured time traces separated in two groups according to the way they change while increasing the power. A small peak near 570 ps can be distinguished which resulted from an instability in laser pulse at this specific position of the delay line. For all data treatment this was included and not removed in order to preserve consistency between

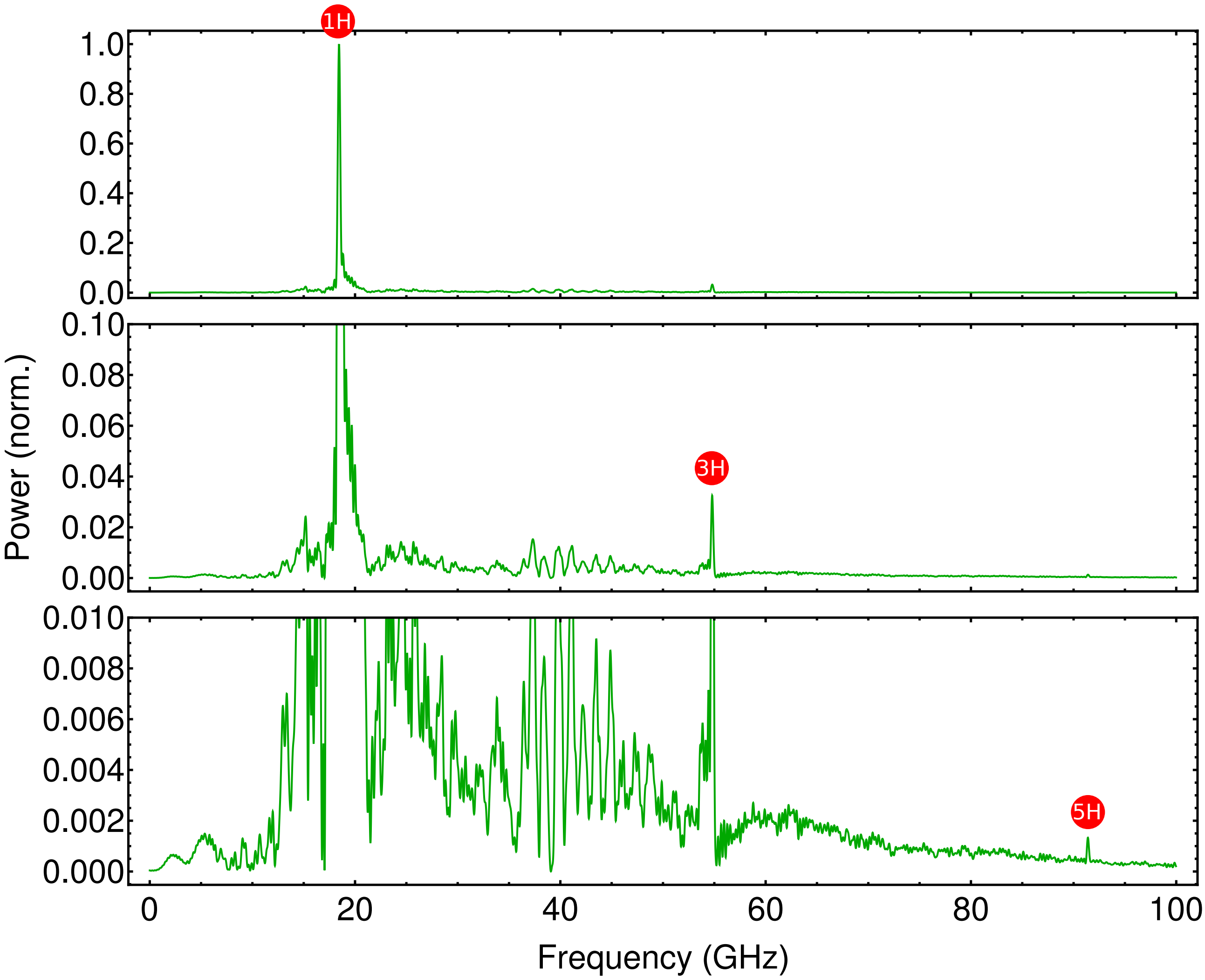

Figure 5.22: Phononic spectrum from the 2 μm diameter micropillar resonator measured with the laser at the optical cavity mode. Pump and probe power for this measurement were 5.0 mW and 0.7 mW, respectively. Laser pulse duration was fixed at 3.8 ps. Three zoom in the same spectrum are presented increasing from top to bottom by a factor of ten on each plot. The first, third and fifth harmonic of the acoustic resonator are found at 18.45 GHz, 54.80 GHz and 91.41 GHz, respectively (and marked by red points with 1H, 3H and 5H accordingly). At the *GaAs* spacer, even harmonics do not contribute to the measured signal since the overlap between electric field and strain change is effectively null. Nevertheless, at the even harmonics, in particular the second one, a series of peaks resulting from modes spanning along the multilayer mirrors appear as have been seen when measuring planar cavities (see figure 4.18).

measurements. Panel (a) presents the measured traces for pump powers going from 0.1 up to 1.0 mW. The signal increase when increasing the pump power, resulting in the time traces appearing ordered from bottom to top. With increasing power also, the peak in reflectivity near zero delay emerges. This peak is the result of the initial pump action producing two competing effects: a blue shift due to the electronic response of the micropillar and a rise in temperature resulting in a red shift of the optical cavity mode, leading to the small decrement in reflectivity that forms the peak. After passing the peak the relaxation process inverts the blue shifts. The electronic relaxation process leads to a red shift causing a drop in reflectivity. The thermal relaxation is a cooling process after the pump leaves the micropillar and counters the electronic effect by blue shifting the optical cavity mode. These two effects together lead to the bending towards higher values of the time traces appearing between 50 and 400 ps. On the negative delay end of the measured traces we can see how the equilibrium reflectivity increase with the pump power as a result of the thermal energy accumulating due to the frequent action of pump pulses. Figure 5.21 panel (b) presents the measured traces for the range of pump powers between 1.0 and 10 mW. We can see how the trend to increase the signal seen at low powers is absent in this case and results in reflectivity traces crossing each other. Again, prior to the pump arrival, we can see an increase in the reflectivity as a result of heating the micropillar with the pump pulses. The two features in the traces that the proposed model is not capable to reproduce and that were identified from figure 5.20 are also present here. First, the bending of the curve just after the peak near zero delay significantly increases. Second, for the last two pump powers of 8.0 mW and 10.0 mW, the peak near zero delay resulting from the pump excitation vanishes. We can understand this by considering the pump excitation causing an electronic and a thermal response during the same time period. For lower pump powers this is not the case. The electronic response is faster and the thermal response is slower therefore producing the peak at zero delay in the process. For high powers, the difference in temperature between the micropillar and its surroundings, results in a larger temperature gradient and therefore a more drastic change of the optical cavity dynamics. The two effects combined when the thermally induced reflectivity variation is faster than the electronic one results in a monotonous but slower change in reflectivity (since the heating effect slows the electronic response). This is visible near zero delay in the traces measured at 8.0 and 10.0 mW where the first drastic change can bee seen decreasing its slope and crossing their low power counterparts. This description of the pump excitation affecting the optical cavity considers the electronic and thermal effects. Nevertheless, these two take place in the same micropillar and on a similar time scale. One can imagine that there might exist a feedback between them. The modeling of such dynamics it is out of the scope of the present work. The second feature that the proposed model can not replicate is the appearance of the minimum reflectivity dip. We can see how it shifts towards lower delays, as if the systems would take less time to reach it while relaxing. While the thermal effects do slow the electronic relaxation bringing back the cavity to its original spectral position prior to the pump arrival, they also shift this starting position. In comparison to the case when measuring blue-detuned from the optical cavity mode, here powers are much higher. At 10 mW the laser is no longer at the cavity mode when the pump reaches the micropillar, but on the blue side due to the red shift of the optical cavity mode caused by the pump heating the micropillar. This indicates the nature of the two resonant peaks found in the spectra obtained as a function of power. The peak at low power (0.5 mW) seen in figure 5.18, corresponds to sensing through the slope on just one side of the optical reflectivity dip. The second peak at high power (ten times more power: 5.0 mW) results from the relaxation trajectory of the optical cavity results in subsequent sensing through the slopes on both sides of the reflectivity dip producing the high resonant peak seen in figure 5.17. Figure 5.22 presents the phononic spectrum measured under these conditions. As in the previous case, when measuring at blue detuning from the cavity mode, the first, third and fifth harmonics of the acoustic resonance of the micropillar can be seen, for this case, appearing at 18.45 GHz, 54.80 GHz and 91.41 GHz, respectively. In contrast with the previous case, the spectrum appears cleaner with the fifth harmonic clearly distinguishable from the background as a result of the higher phonon detection sensitivity. Around 40 GHz, the series of peaks appearing at the second harmonic and resulting from modes spanning along the distributed Bragg reflectors can be distinguished more clearly than for the cleanest spectrum obtained when measuring blue-detuned from the cavity mode (see figure 4.18 and 5.16).

In this section we have presented the experimental results on TDBS measurements done using different pump powers on a 2.8 μm diameter fiber-integrated micropillar with the laser tuned at its optical cavity mode. Resonant phonons were identified and tracked as a function of pump power. By doing so, we have obtained information about the optical cavity dynamics and how it changes due to electronic and thermal effects. Since the sensitivity to detect phonons depends on the tuning with respect to the cavity, we have identified two different conditions resulting in local maxima in the spectral and pump power domain. At low powers, the system is mainly governed by its electronic response and relaxation. When reaching the high sensitivity region one of these local maxima is found. At higher powers a thermally induced shift places

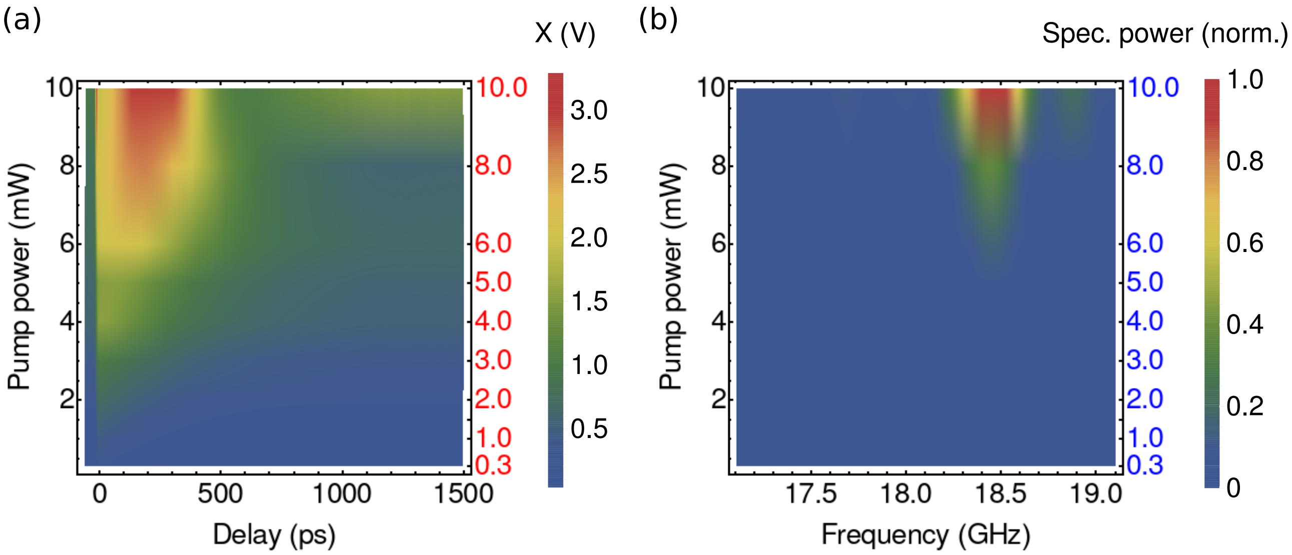

Figure 5.23: Measured with the laser detuned towards the red side of the optical cavity mode, panels (a) and (b) present the intensity of of the time resolved reflectivity traces and their corresponding phononic spectra as a function of pump power, respectively. The full intensity map results from interpolating between the experimental data. In panel (b) the resonant peak appears centered at 18.46 GHz.

the laser blue-detuned from the cavity mode prior to the pump excitation. After the pump pulse leaves the micropillar, the electronic system relaxes, red shifting the cavity mode while the thermal relaxation induces a red shift which counteracts the electronic process. As a result, the second local maximum of the spectra occurs when passing by the two high sensitivity regions for phonon detection. These results are consistent with the proposed model for the time traces (equation 5.1) at low powers. At higher powers the results are not longer fully captured by this model due to the thermal contributions at higher pump powers as expected from the previous measurements. In the following section we present the results when measuring with the laser initially tuned to the red flank of the optical cavity mode.

5.3.4 Micropillar optical cavity dynamics when red detuned: Dominant thermal effects for efficient phonon detection

In this section we experimentally study the optical cavity dynamics of a hybrid micropilar when coupling to it red detuned from its cavity mode. Consequently, we expect less light couples into the cavity than in the previous case in section 5.3.3. In addition, the blue shift of the optical cavity mode due to the electronic response of the system leads to high reflectivity, i.e. less light coupled into the cavity. Therefore, we expect to have low detection efficiency for phonons at low pump powers. However, when increasing the pump power, a red shift of the optical cavity due to the micropillar warming up is expected. Then, more pump power implies more light coupled into the optical cavity. As a result, we will show how at high pump powers the efficiency for detecting phonons starts to rapidly increase. We reach a point where the phonon induced oscillations in reflectivity can be seen by naked eye directly in the time resolved reflectivity traces.

The third series of TDBS measurements of the fiber-integrated micropillar was done with the laser detuned from the optical cavity mode towards its red side (912.56 nm. See figure 5.10 (f)). All measurement conditions were the same as in section 5.3.2 and 5.3.3 while the pump power changed from 0.3 to 10.0 mW.

Figure 5.23 presents the experimental results as intensity maps showing the change of the time resolved reflectivity traces and their corresponding phononic spectra as a function of pump power. Panel (a) presents the measured instantaneous reflectivity as a function of pump

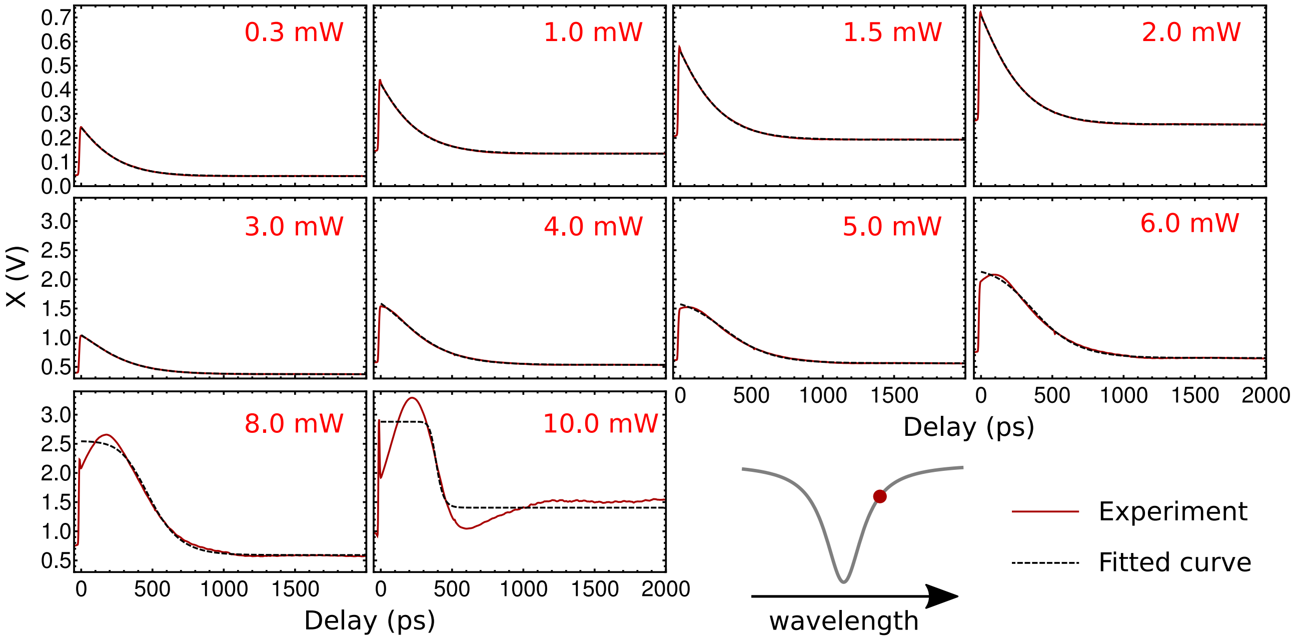

Figure 5.24: Time resolved reflectivity traces measured at the red side of the optical cavity mode as a function of pump power. Insets in each plot indicate the pump powers going from 0.3 mW up to 10.0 mW. On top of the experimental data, a black dashed fitted curve is presented for each time trace. The fit was done using the model given in equation 5.1. For the high pump power limit the fit stops reproducing the measured data. The fit was done systematically for all data using the same conditions (same model and parameters seed). A sketch showing the cavity reflectivity dip and the laser center on its red side is placed at the bottom.

delay in an intensity map resulting from interpolating between the experimental data. For low powers and as for the case when the laser was tuned at the cavity mode, the electronic response of the system upon the pump action blue shifts the reflectivity dip increasing the measured signal at zero delay. Then, it monotonically decreases while the system relaxes back to equilibrium. For higher pump powers this changes and the thermal effects start to become more relevant. As a result, the curve bends while the cooling of the sample counteracts the electronic relaxation. In addition, the peak at zero delay seen in previous measurements starts to rise and at the highest pump power (10.0 mW) it can be clearly distinguished. Under these conditions we can observe that a minimum in the reflectivity appears, a signature that the optical cavity mode has been red shifted due to thermal effects caused by the train of pump pulses being coupled into the micropillar. Remarkably, strong phonon induced oscillations can be distinguished at these high powers. This is the result of the system spending more time in the high sensitivity region as the blue shift of the sample cooling effectively slows the traversing of the optical cavity mode. In figure 5.23 (a) right axis, ticks mark the measured pump powers. Figure 5.23 (b) presents the spectra obtained after processing the traces showing the micropillar resonance at 18.46 GHz. The full intensity map was obtained in the same way as for the previous micropillar measurements i.e. smoothing the transient reflectivity signal below 10 GHz with a Savitsky-Golay filter, subtract the smooth signal from the measured unfiltered version and Fourier transforming the result. The intensity map presented in panel (b) results from interpolating between the obtained experimental spectra. On its right axis the used pump powers are marked with ticks. As shown in figure 5.11 (c), the resonant peak is not very clear at low powers. Nevertheless, we can see how it rises with increasing power. For the highest power of 10.0 mW the signal is so strong that we can distinguish the phonon reflectivity oscillation from the time traces.

Figure 5.24 shows the measured reflectivity time traces in two dimensional plots with the pump powers as insets. The experimental data is plotted in solid red lines. On top of it, using the model given by equation 5.1 the fitted curves are plotted in black dashed curves. As in

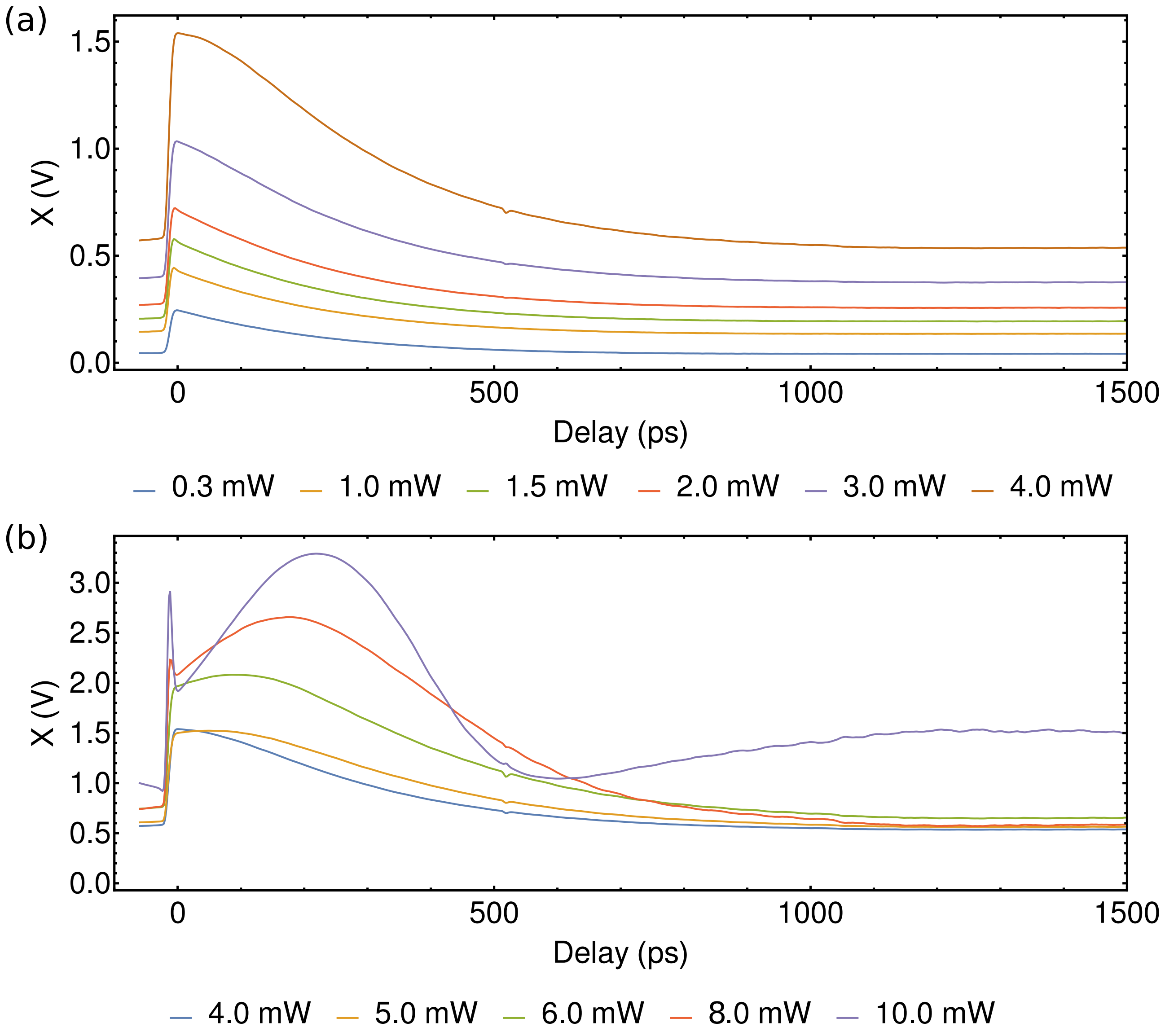

Figure 5.25: Panels (a) and (b) plot the time resolved reflectivity traces measured red detuned from the cavity mode for pump powers going from 0.3 mW up to 4.0 mW and from 4.0 mW up to 10.0 mW, respectively. (a) Reflectivity increases after pump excitation. While increasing the pump power we increase the blue shift of the cavity mode experience. As a result of starting at the resonant wavelength, the shift leads to an increase in reflectivity. (b) While the micropillar starts to heat due to the pump pulse the rise in temperature counter the electronic response due to the pump excitation. In contrast with the previous measurements at different spectral positions, the interplay between the optical cavity dynamics and how much light is coupled into the cavity leads a feedback resulting in drastic changes as a function of power. After the pump abandons the micropillar, it cools down counteracting the optical cavity red shift of the electronic relaxation process.

the previous series of measurements, we can see how the model agrees with the data at lower powers but diverts from it while the pump power increases. Moreover, the signal prior to the pump excitation increases in significantly larger steps compared to previous measurements, suggesting thermal effects contribute more to the TDBS with the laser red detuned from the cavity mode. This results from the fact that in contrast to the two previous spectral position used, by measuring at the red slope of the cavity, the thermal red shift due to the sample heating results in more light being coupled into the micropillar (as the cavity shifts so the laser falls closer to the central wavelength of the cavity mode). The reflectivity peak seen at zero delay only appears at the two highest pump powers used: 8.0 and 10.0 mW. Nevertheless, the visibility of this peak drastically increases between these two values as a result of the heating

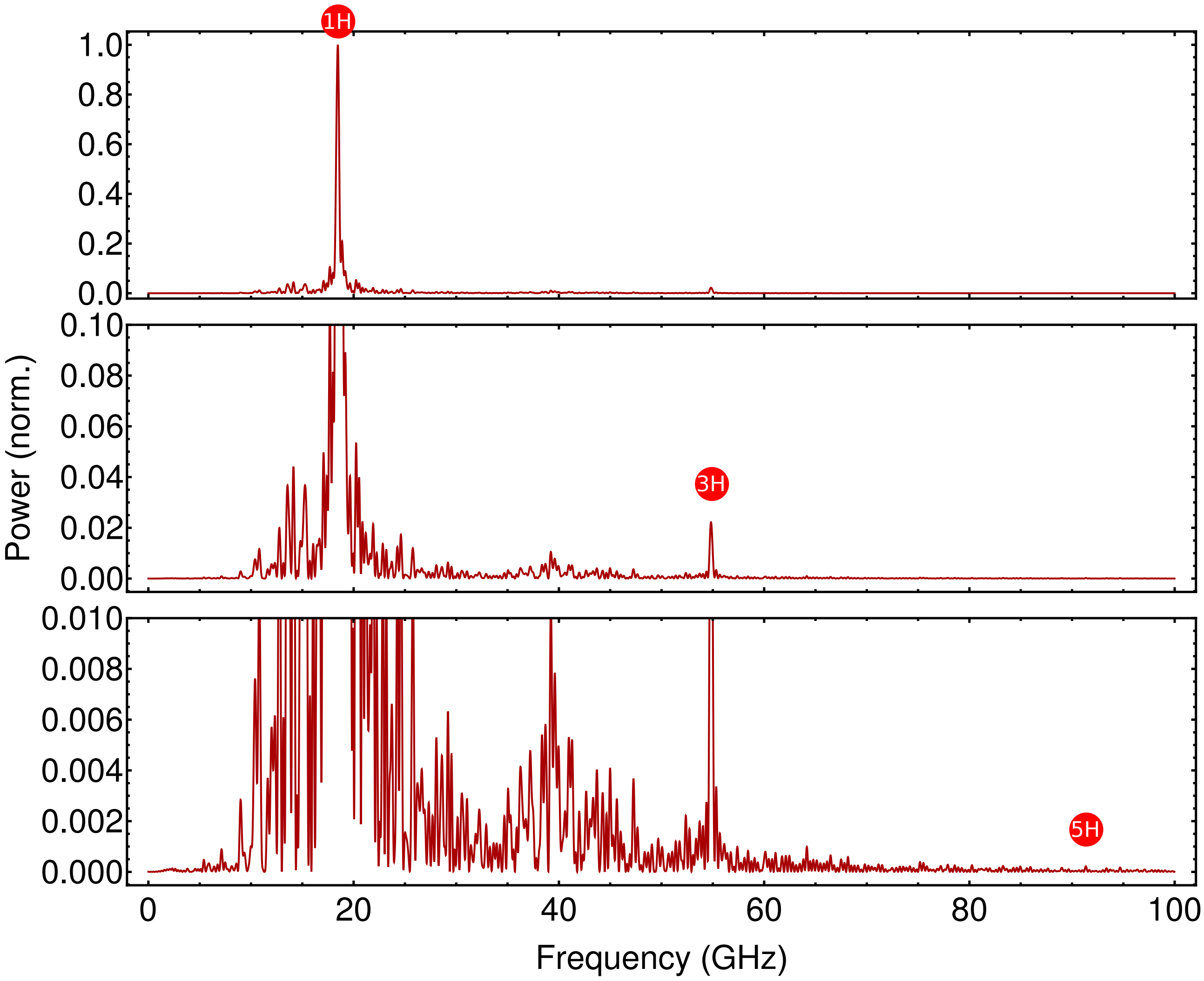

Figure 5.26: Phononic spectrum from the 2.8 μm diameter micropillar resonator when red shifted from the pillar optical cavity mode. Pump and probe power for this measurement were 10.0 mW and 0.7 mW, respectively. Laser pulse duration was fixed at 3.9 ps. Three zoom ins to the same spectrum are presented increasing from top to bottom by a vertical magnification factor of ten on each plot. The first, third and fifth harmonic of the acoustic resonator are found at 18.46 GHz, 54.82 GHz and 91.35 GHz, respectively (and marked by red points with 1H, 3H and 5H accordingly). At the *GaAs* spacer, even harmonics do not contribute to the measured signal since the spatial overlap between electric field and mechanical strain is effectively null. Nevertheless, at the even harmonics, in particular the second one, a series of peaks resulting from modes spanning along the multilayer mirrors appear as seen when measuring planar cavities (see figure 4.18).

and optical cavity dynamics feedback on each other. At the highest power and as seen in the time resolved reflectivity traces, ripples caused by the presence of coherent acoustic phonons are distinguished. The appearance of a reflectivity minimum in the 10 mW time trace suggests that again we are sensing both sides of the optical reflectivity dip.

A zoom into the time resolved reflectivity traces within the first 1500 ps after the pump reflection is presented in figure 5.25. Panel (a) shows the traces measured between 0.3 and 4.0 mW. The rapid shift at zero delay increases with higher powers in this range, as the result of two factors. First, the electronic response of the system, blue shifts the cavity due to the pump excitation. Second, the thermal effects of the pump, red shift the cavity mode prior to its action on the pillar. This accumulation effect caused by the pump arriving at the laser repetition rate (80 MHz) manifest also in the increment of the measured signal at negative delays. Panel (b) shows the reflectivity traces measured between 4.0 and 10.0 mW. The trace can be seen bending while recovering as a result of heating of the sample counteracting the electronic relaxation. At 8.0 and 10.0 mW the peak in reflectivity due to the pump heating the sample starts to appear and increases rapidly with power. At 10.0 mW, the minimum in reflectivity appears. This happened already at lower powers for the case when the laser was tuned at the cavity mode. For the case of the laser red detuned from the cavity mode, less light is coupled into the micropillar, but when increasing power, the cavity and laser align in wavelength and a drastic change in the time trace can be seen. Moreover, phonon induced oscillations can be clearly distinguished during the relaxation process. Another feature seen at higher powers is the trend of the reflectivity at negative delays. It not only increased with pump power, but it changes from a flat signal to a positive and negative slope for 8.0 and 10.0 mW, respectively. This indicates that the 12.5 ns repetition rate of the pump pulses ends up being shorter than the relaxation process duration.

The strongest resonant peak was measured using a pump power of 10.0 mW. Its corresponding spectrum is presented in figure 5.26. The first, third and fifth harmonics of the micropillar resonant frequency can be identified at 18.46 GHz, 54.82 GHz and 91.35 GHz, respectively. In contrast to the measurement with the laser at the cavity mode, the fifth harmonic is barely visible above the background. The resonant peak increases with pump power. We expect this for powers beyond 10 mW, but in order to preserve the integrity of the devices no measurement at higher powers were performed.

The measurement at the red side of the micropillar cavity leads to the high increase in the resonant peak for very high powers. This is the result of an initial thermal red shift inducing proper coupling into the micropillar mode. While at 10 mW the pump power is sufficient such that the laser overpasses the cavity reflectivity dip, more power would be necessary to reach the conditions with maximum detection sensitivity for coherent acoustic phonons.

5.4 Conclusions

In this chapter we have applied the experimental tools developed to detect coherent phonons for the study of micropillar resonators. The sample investigated operates as a Fabry-Perot resonator confining both phonons at 18 GHz and photons around 915 nm in vacuum. The micropillars were fabricated by the groups of Aristide Lemaître and of Isabelle Sagnes at the clean room facilities of the C2N.

Two different approaches to generate and detect coherent acoustic phonons in micropillars were implemented. First, by coupling light in free space into the micropillars using a microscope objective and focusing both pump and probe pulses on top of two micropillars of 2 and 5 μm of diameter, we were able to detect coherent phonons in the micropillars up to around 8 ns after the pump excitation. A model describing the optical cavity dynamics was introduced and relaxation times of both micropillars were estimated. Then, measurements on a third micropillar, also of 5 μm of diameter, were done varying the pump power while the probe power remained fixed. As a result from the power scan we were able to evidence the evolution of the time resolved reflectivity trace as a function of pump power. We showed how the optical cavity dynamics of the micropillar manifests in the time resolved reflectivity trace by introducing a model accounting for the electronic relaxation process after pump excitation. The second approach for the study of micropillar resonator was implemented in collaboration with Quandela SAS. A fiber-integrated micropillar was fabricated by gluing a single-mode fiber to the top of a 2.8 μm diameter micropillar allowing us to couple light into the optical cavity mode through the fiber. A spectral scan around the optical cavity mode was done by tuning the laser wavelength at three different spectral positions: slightly blue shifted from the cavity mode, at the cavity mode and slightly red shifted from it. At each of these three spectral positions pump power scans were done. The experimental results showed an interplay between electronic and thermal dynamics altering the optical cavity mode and manifesting in the time resolved reflectivity trace. While at low power the electronic response of the system is what determines the measured time traces, for high power, the pump heats the sample and increases its relevance affecting the shape of the measured time trace. We showed how the introduced model describing the optical cavity dynamics becomes invalid at high pump powers and we attribute this to the thermal effects not being taken into account by the model. It is possible that the interplay between these two shifts leads to a feedback between them resulting in a complex dynamics that are not captured by the model of a Lorentzian dip shifting in an overdamped exponential fashion. The modeling of such a behavior is, however, beyond the scope of the present work. The interplay between thermal and electronic responses has a direct impact of the phonon detection efficiency as have been demonstrated by the pump power scans done. By predicting the optical cavity dynamic we can expect the possibility to design pump schemes where the phonon detection efficiency can be optimized. Moreover, if we include the idea of engineering multilayer structures we add another degree of freedom control to the dynamic evolution of optical modes. By mixing the engineering of optical cavity modes and pump schemes we could target a full optical control of the cavity dynamics on the picosecond time scale [250, 251].

The experimental realizations of TDBS on fibered-integrated micropillar was evaluated in terms of stability. We found that the setup demonstrates consistent results over the course of more than 42 hours. In contrast with previous experiments on micropillars using state of the art TDBS setups, the presented results with fibered devices are remarkable. In general, we found no previous reports on the stability of such kind of experiments. Outside the field of nanophononics, this kind of technological implementation could open the door to the development of ultrafast acoustic sensors optically probed at a distance through single-mode fibers. Within nanophononics, fiber-integrated micropillars offers a stable platform for experiments capable of being reproduced at any laboratory. The convenience of measuring fibered-integrated micropillars has allowed us to complete an exhaustive study on the different responses of the micropillar at different detunings from the optical cavity mode. From the experience working in both free space and single-mode fiber coupling approaches the time scale of these experiments was significantly reduced by the use of fibered micropillars. These devices offer fast and highly reproducible TDBS results and are suitable for the implementation of a cross polarization scheme in coherent phonon generation an detection experiments. Finally, the fiber-integrated micropillar performing as a plug-and-play device together with the fibered pump-probe technique constitutes a versatile platform for integrated nanoacoustics in the tens gigahertz range featuring stability and removing the need of optical alignment.

Chapter 6

Conclusions and outlook

The control of high frequency mechanical vibrations in solid-state systems opens the door to novel technological developments where not only electrons and photons, but also phonons are controlled for applications purposes. Nanophononics has thus gained interest from different fields of physics [37]. Among these are energy harvesting [255, 256], optoacoustic imaging [120, 121, 198, 257] and quantum technologies [131, 184] for which the control of vibrations at length scales even down to the interatomic distance may offer interesting perspectives. The development of problem-adapted strategies to control, generate and detect phonons at high frequencies are at the basis of these current developments. In this thesis, we investigated the propagation and confinement of longitudinal acoustic phonons in multilayered structures both as planar devices and as micropillars. These types of devices are building blocks in a wide range of optoelectronic applications such as lasers [258, 259], quantum light sources [42, 55] and sensors [58, 260]. Strategies to control phonons based on multilayers are thus highly relevant to existing applications and compatible with established fabrication technologies. In particular, we focused our research on $GaAs/AlAs$-based nanostructures operating as optical cavities and as acoustic resonators. Superlattices are a versatile platform to control the propagation of waves, in particular, to engineer nanophononic devices like mirrors, filters and resonators for longitudinal acoustic phonons [60, 61, 124]. Remarkable realizations have demonstrated coherent phonon amplification [22, 23], co-localization of optical and acoustic modes [69, 70] and hundreds of gigahertz resonators embedded in optical cavities [60, 71, 72]. In this thesis, the presented work followed two research lines. The first research line focused on the engineering of nanophononic resonators based on multilayered structures. The goals include the engineer novel confinement strategies for acoustic phonons that allows the fabrication of resonators with enhanced robustness and the development of nanophononic structures capable of mimicking electronic solid-state physics phenomena. The second research line followed in this thesis focused on the experimental study of acoustic resonators by time-resolved experiments using ultrafast laser action. Three goals were pursued for the experimental research line. First, the development of versatile optical setups that facilitate time-domain Brillouin experiments. Second, the use of the developed optical tools for the study of phonon dynamics in planar nanoacoustic resonators. Third, the study of coherent phonon confinement in hybrid micropillars operating as both acoustic resonators and optical cavities.

Nowadays, state of the art fabrication techniques, such as molecular beam epitaxy, allow the fabrication of multilayered devices that control vibrations in the frequency range between tens and hundreds of gigahertz [50, 72, 125]. The first goal pursued in this thesis was the development of novel strategies to control the propagation of acoustic phonons that allowed the engineering of resonators with enhanced robustness. For this purpose, we introduced an approach to design acoustic local band structures and validated it through numerical simulations. The acoustic local bands are implemented in superlattice-like $GaAs/AlAs$ heterostructures engineered to control longitudinal acoustic phonons in the hundreds of gigahertz range. The results of numerical simulations of $GaAs/AlAs$ heterostructures are presented in Chapter 3 where, starting from the design of superlattice structures, we introduced a method to alter their design parameters in order to implement an acoustic local band structure along multilayered devices. These are termed adiabatic resonators due to their progressive alteration of the superlattice parameters which give rise to a band structure that varies locally along the device. We compared designs for adiabatic resonators confining phonons through band inversion, i.e., through concatenating topologically different superlattices, with a simple potential well design. [125, 150, 151, 154]. Topological confined modes are robust against fluctuations altering the bandwidth of the minigaps of each superlattice [125]. Through simulations we demonstrated the robustness of such a resonator under the presence of noise that leaves the invariants associated with each superlattice unaltered [125]. The results indicate that the adiabatic resonator by band inversion features the same kind of robustness as their previously introduced counterparts using simple distributed Bragg reflectors with inverted bands. Motivated by this result, and in order to apply a more realistic kind of noise, we performed a comparative study where we showed how this adiabatic resonator maintains its performance under the presence of random noise altering its layer thickness. The novel design of an adiabatic resonator by band inversion shows a resonant frequency more robust also to this kind of noise which does change the underlying topological invariants. Nevertheless, we find an enhanced robustness in comparison with other types of resonators such as a Fabry-Perot structure for example. The introduction of an acoustic local band structure and the enhanced robustness demonstrated by an adiabatic resonator mark the first goal of this thesis, for which novel confinement strategies were developed in the context of nanophononics.

Featuring slow propagation speeds and hundreds of micrometers coherent lengths [89] for phonons with wavelengths in the tens of nanometers, nanophononic devices allow the experimental study of phonons in quasi-infinite systems at time scales well below the mechanical oscillation period. This makes nanophononic structures an attractive platform to mimic electronic single particle dynamics. Equipped with the simulation tools developed to model adiabatic resonators, we showed how the acoustic local band structure introduced in chapter 3 allows to engineer phonon propagation along multilayer devices. Exploiting the engineering of local bands, we were able to introduce effective potentials for phonons regardless of their lack of mass and charge. We implemented nanomechanical potentials by altering the group velocity of the propagating acoustic waves and therefore enabled the effective acceleration of phonons. Through simulations, we demonstrate analogous behaviour for the propagation of phonons along effective nanomechanical potentials and electronic dynamics under the influence of different potential landscapes. This method is described at the end of chapter 3 where three different well known examples of potentials are mimicked for acoustic phonons. These are the parabolic, Morse and double well potentials.

Optomechanical systems have been vastly studied over years and have demonstrated several applications on different fields [129]. The perspectives of introduce mechanical system into quantum technologies has shown very attractive with remarkable realizations in recent years [122, 123, 131, 184, 261, 262]. An indispensable requirement for this purpose is to isolate the used mechanical system from the environment decoherence effects. There exists a trade off between how high the operational frequency of mechanical devices is and how low the temperature of its surrounding needs to be in order to access the quantum regime. In this context nanophononic structures operating at tens to hundreds of gigahertz appear as a promising platform capable of operating in a quantum regime at temperatures in the order of Kelvins or higher [70]. Micropillars in particular have been demonstrated as a promising platform capable of reaching optomechanical coupling factors on the order of 10^6 and with quality factor multiplied by operational frequencies on the order of 10^{14} Hz [68, 263]. The experimental study of nanophononic devices typically demands optical setups aligned to couple light into them and to resolve the effects of phonons. Moreover, the experimental challenges faced in nanophononic experiments are accentuated when dealing with three dimensional micrometer scale structures such as micropillars. The second line of research of this thesis focused on the experimental study of acoustic phonons in nanostructures through time resolved experiments. For the first goal in this line of research we developed an optical setup for the study of phononic structures by means of ultra short pulses of light. The results of this work can be found in Chapter 4 where the used time-domain Brillouin scattering (TDBS) technique is described. The second goal in the experimental line of research was accomplished by using the presented optical setup for the study of planar multilayered structures. The experimental results are presented in chapter 4 and correspond to the study of planar nanoacoustic resonators confining phonons with frequencies going from 18 up to almost 400 GHz. The experience gained during the implementation of a TDBS setup in free space, led to the development of two variants of the same setup. Firstly, we addressed mechanical instabilities in our setup rising from the use of an effective 3.6 meters mechanical delay line. In order to deal with the mechanical instabilities we implemented an intermediate spatial mode filtering stage in the optical setup (between the delay line system and the coupling into the acoustic resonator stage) using single-mode fibers. Equipped with the filtering stage, we investigated acoustic resonators operating on the range of hundreds of gigahertz. Secondly, motivated by the obtained high quality results a new strategy was developed for the systematic study of nanoacoustic resonators. In collaboration with Quandela S.A.S. we glued a single-mode fiber on a planar resonator. After gluing a single-mode fiber on the surface of a nanoacoustic resonator we implemented a fibered version of the TDBS technique. By using a single-mode fiber to couple light into the planar resonator the spot size of the pump and probe beams on top of the sample surface were fixed by design. Equipped with the fibered TDBS setup we investigated a hybrid opto-phononic resonator based on phonon confinement through band inversion. We demonstrated the co-localization of topological optical and acoustic modes in the planar structure and showed the effect of the pump-induced optical cavity dynamics on the measured phonon spectrum.

The third goal of the experimental line of research involved the experimental study of hybrid opto-phononic micropillars. For this purpose we used the free space and the fibered TDBS techniques developed for the study of planar samples. Micropillar cavities have been vastly studied in photonics and they are a promising platform for the development of quantum technologies and optomechanics [55, 70, 109, 216, 241–246, 263]. The micropillars investigated in this work operated as an hybrid opto-phononic platform, confining longitudinal acoustic phonons at around 18 GHz and light at wavelengths in free space of around 915 nm. Three micropillars of different sizes (2, 2.8 and 5 μm diameter) were studied by TDBS experiments and the results are presented in Chapter 5. The experimental study is done using two different variants of the TDBS optical setups developed. First, by coupling in free space to the micropillars of 2 and 5 μm diameter, we were able to probe the dynamics of confined coherent longitudinal acoustic phonons and to compare the change on the electronic dynamics affecting the time resolved optical reflectivity measured for different micropillar sizes. The free space setup used to couple into micropillars allowed to change the coupling condition and explore different pillar structures fabricated in the same sample. The capability to couple to different pillars comes at the cost of time demanding alignment requirements due to the small area these pillars have at their top surface. To overcome this demanding alignment, we glued the micropillar to the front facet of a single-mode fiber resulting in a fiber-integrated device. In a similar way as for the investigated planar sample, this kind of device offers fixed coupling conditions but for three dimensional micropillars. By using a TDBS setup featuring a fiber cross polarization scheme as the one developed for planar samples, we were able to measure coherent acoustic phonons in micropillar resonators with unprecedented robustness. We investigated the performance and stability of the obtained phononic spectra through the fibered version of pump and probe experiments and demonstrated high quality signals over the course of more than 40 hours. The fiber-integrated micropillar can be used as a plug-and-play device for nanoacoustic experiments allowing us to perform reproducible TDBS experiments without the need of any alignment. Lifting the need for alignment resulted in less time being required for individual measurements and therefore allowed a systematic study of micropillar structures as a function of pump power (the pulse generating the phonons in a pump and probe detection scheme) and of the detuning from the optical cavity mode. We traced out the evolution of the cavity dynamics and proposed a model to reproduce the measured time resolved reflectivity. The phenomenological model accounts for electronic effects and is consistent with the experimental results obtained at low pump powers, i.e. when thermal effects are absent. The systematic study at different powers allowed us to identify different conditions for optimum phonon detection efficiency at each of the measured spectral detunings.

In this thesis we experimentally studied three different types of multilayered structures operating as nanoacoustic resonators: a Fabry-Perot resonator, an adiabatic resonator and topological resonators based on band inversion. Confined phonons were detected with frequencies going from 18 up to 390 GHz for these structures by using different versions of the TDBS optical setups presented in chapter 4. Most resonator designs featured confinement of not only phonons but photons as well in hybrid structures operating both as optical cavities and as acoustic resonators. In these hybrid structures, the coupling between light and vibrations is enhanced, allowing higher sensing capabilities to detect coherent phonons in pump and probe experiments. Furthermore, for the hybrid resonator by band inversion and the micropillars we were able to evidence the impact of the optical cavity dynamics on the measured phononic spectra as a result of varying the measurement conditions on the nanosecond time scale. A systematic study experimentally showed how the spectral detuning of the laser wavelength around the optical cavity mode and the laser pump power impacted the measured phononic spectrum of hybrid resonators.

One perspective of this work is the study of coherent acoustic-phonon transport [197, 264] in three dimensional structures more complex than micropillars. There are fundamental questions to be answered about the transport of phonons in custom-shaped systems such as sets of connected micropillars, waveguides or even interferometers. The experimental study of the mean free path of phonons, the coupling mechanism between different points in three dimensional structures and the coherence of phonons propagating through them can be investigated by time-resolved Brillouin scattering experiments similar to the ones presented in chapter 4. The capabilities of micropillars to host semiconductor quantum dots [55, 109] motivate the investigation of whether distant quantum systems could be addressed using phononic channels. Experimental demonstrations have shown how phonons can be used for assisting the excitation of quantum dots [42]. Remote optical excitation of quantum dots in optical microcavities has been demonstrated as well [189]. The possibility of addressing remotely the mechanical degrees of freedom of semiconductor quantum dots using ultra-high frequency acoustic phonons could offer novel control parameters for quantum systems. A necessary step towards this long-term objective is the development of a variant of the free space TDBS setup presented in chapter 4, where the coherent phonon generation is decoupled from the detection process. For this purpose, we would need to gain control of both pump and probe focuses on the sample independently from each other. In order to do so, a telescope operating in tandem with the focusing objective as a 4F system can be implemented and has been previously reported for optoacoustic imaging in the gigahertz range using an ASOPS technique [205, 214, 257]. The TDBS optical setup presented in Fig. 5.2 is compatible with such configuration. However, the modifications needed for such implementation were beyond the scope of the present thesis. In this work, we studied micropillars confining both optical and acoustic modes. In coupled micropillars, and in general, in systems fabricated from the same planar wafers, the possibility of coupling not only photons but also phonons through waveguides open new possibilities and challenges for the generation, transport, and detection of coherent acoustic phonons. Questions like where exactly the generation takes place, or how to perform a spatially selective generation in 3D phononic networks remain open.

A second perspective from this work is to use the simulation and experimental tools developed for the study of coherent phonon dynamics in quasi-periodic structures operating in a broad range of scales. In contrast with light, coherent phonons have an approximately linear dispersion relation, covering several orders of magnitude in frequency. Practically, this characteristic implies that the group velocity remains approximately constant over broad bands and length scales, facilitating the investigation of multiscale wave phenomena. By means of TDBS experiments we could access the full acoustic wavefunction of quasi-periodic systems featuring different kinds of phononic states such as: localized, extended and critical [265]. A particular example of such devices are Fibonacci structures [266]. In contrast with Fibonacci structures operating in the optical domain, the short wavelength and the long mean free paths associated to high frequency acoustic phonons allow the fabrication of samples with much more layers than their optical counterparts, enabling higher orders of the Fibonacci array. By time-resolved experiments, the wavefunction of phonons in such systems can be measured making nanophononic Fibonacci structures a promising platform for the investigation of phenomena on scales difficult or impossible to replicate with standard optics or electronics systems. Another example of complex structure where nanoacoustic platforms present a competitive advantage with respect to their optical and electronic counterparts is the Cantor set design [267]. The capabilities of MBE technique allow the fabrication of "Cantor set"-like samples operating from the range of hundreds of megahertz up to a few terahertz, covering layer thicknesses from subnanometer to the tens of micrometers scales. The resulting nanoacoustics devices would extend self-similarity induced wave phenomena to unexplored regimes.

List of publications

- Coherent generation and detection of acoustic phonons in topological nanocavities
  G. Arregui, O. Ortiz, M. Esmann, C.M. Sotomayor-Torres, C. Gomez-Carbonell, O. Mauguin, B. Perrin, A. Lemaître, P.D. García, and N.D. Lanzillotti-Kimura
  APL Photonics **4**, 030805 (2019)

- Phonon engineering with superlattices: Generalized nanomechanical potentials
  O. Ortiz, M. Esmann, and N. D. Lanzillotti-Kimura
  Physical Review B **100**, 085430 (2019)

- Acoustic phonon confinement by band inversion
  M. Esmann, F. R. Lamberti, O. Ortiz, and N. D. Lanzillotti-Kimura
  Materials Today: Proceedings **14**, 126 (2019)

- Mesoporous Thin Films for Acoustic Devices in the Gigahertz Range
  N. Lopez-Abdala, M. Esmann, M. C. Fuertes, P. C. Angelomé, O. Ortiz, A. Bruchhausen, H. Pastoriza, B. Perrin, G. J. A. A. Soler-Illia, and N. D. Lanzillotti-Kimura
  The Journal of Physical Chemistry C **124**, 17165 (2020)

- Subwavelength engineering for Brillouin gain optimization in silicon optomechanical waveguides
  J. Zhang, O. Ortiz, X. Le Roux, E. Cassan, L. Vivien, D. Marris-Morini, N.D. Lanzillotti-Kimura, and C. Alonso-Ramos
  Optics Letters **45**, 3717 (2020)

- Fiber-integrated microcavities for efficient generation of coherent acoustic phonons
  O. Ortiz, F. Pastier, A. Rodriguez, Priya, A. Lemaître, C. Gomez-Carbonell, I. Sagnes, A. Harouri, P. Senellart, V. Giesz, M. Esmann, and N.D. Lanzillotti-Kimura
  Applied Physics Letters **117**, 183102 (2020)

- Fiber-based angular filtering for high-resolution Brillouin spectroscopy in the 20-300 GHz frequency range
  A. Rodriguez, P. Priya, O. Ortiz, P. Senellart, C. Gomez-Carbonell, A. Lemaître, M. Esmann, and N. D. Lanzillotti-Kimura
  Optics Express **29**, 2658 (2021)

- Topological optical and phononic interface mode by simultaneous band inversion
  O. Ortiz, P. Priya, A. Rodriguez, A. Lemaître, M. Esmann, and N. D. Lanzillotti-Kimura
  Optica **8**, in press (2021).

Appendix A

Micropillar spatial mode model for fiber integration

In the same way micropillars operate on two different scales, we can explain the confinement of light in these structures by splitting the problem along the different dimensions micropillars have. Along the etched (growth) direction, we have confinement of optical and acoustic waves caused by the multilayer system (see chapter 3). In the radial direction from the pillar center, the only interface the system has is between the interior and the exterior of the micropillar. In the experimental realization we consider, the structures are studied in a vacuum environment. At the interior of the micropillar however the media varies as the layers of different materials are alternated. For the studied structures these materials were $Ga_{0.9}Al_{0.1}As$ and $Ga_{0.05}Al_{0.95}As$ with refractive index for $n_{Ga_{0.9}Al_{0.1}As}$ and $n_{Ga_{0.05}Al_{0.95}As}$ of roughly 3 and 3.5, respectively. In contrast, the void exterior has a refractive index of 1. As result of this contrast, light is confined within the micropillar regardless of which layer we are considering. In addition to this, typical multilayer designs used have subwavelength features i.e. layer of thicknesses below the scale of the optical wavelength in the material. Then, for the purpose to model the confinement along the radial direction we can assume that light experience an effective medium described by the mixture of $Ga_{0.9}Al_{0.1}As$ and $Ga_{0.05}Al_{0.95}As$ optical properties. As a result, we can study circular micropillars as constituted of two materials, one effective media for the interior and vacuum for the exterior. This allow us to use theory developed for the study of optical waveguides for the modeling of micropillars.

Under the assumptions explained above, we can model circular micropillars confinement of light within the layers plane (see figure 5.1) by modeling the propagation of light as in the case of a circular step-index waveguide. This kind of system has been vastly studied and the calculations to model it have been done following different treatments. Here, we follow the calculation procedure presented by Yariv [252, 253] which have been demonstrated suitable for micropillars used for single photon sources [247]. The model consider a cylinder of radius $r = a$ and refractive index n_{int} and n_{ext} for the interior and exterior of the micropillar, respectively. In the context of a single-mode fiber these are the ones corresponding to the core and cladding materials, respectively. We will not used these terms but differentiated them by interior and exterior refractive index as it accommodates better to the final system to be described, a micropillar.

In order to describe the electromagnetic field along a micropillar, let us consider the following ansatz

$$\begin{aligned}\vec{E}(\vec{r},t) &= \vec{E}(r,\phi)\exp[i(\omega t-\beta z)]\\ \vec{H}(\vec{r},t) &= \vec{H}(r,\phi)\exp[i(\omega t-\beta z)]\end{aligned}\tag{A.1}$$

corresponding to a plane wave along the micropillar axis (z) and general functions in the perpendicular plane (x-y), expressed in polar coordinates r and ϕ. The angular frequency is given by ω and we have defined an effective wave vector β to describe the propagation along the vertical axis. This is a second approximation where we are considering an effective wave propagating along the z axis (the first one correspond to assuming one medium only at the interior of the pillar). This effective wave vector β describe the wave propagating both inside and outside of the pillar therefore it lies between their corresponding wavevectors i.e. $k_{ext} < \beta < k_{int}$, where $k_{ext} = \frac{2\pi}{\lambda/n_{ext}}$ and $k_{int} = \frac{2\pi}{\lambda/n_{int}}$. Then, we can express the wave equation for the electromagnetic field along the vertical axis as

$$\begin{aligned} (\nabla^2 + k^2(r))E_z(r,\phi)e^{i(\omega t-\beta z)} &= 0 && \text{(A.2)} \\ (\nabla^2 + k^2(r))H_z(r,\phi)e^{i(\omega t-\beta z)} &= 0 && \text{(A.3)} \end{aligned}$$

with the wavevector

$$k(r) = \begin{cases} k_{int} & \text{if } r < r_{\mu\text{pillar}} \\ k_{ext} & \text{if } r > r_{\mu\text{pillar}} \end{cases} \tag{A.4}$$

where $r_{\mu\text{pillar}}$ is the micropillar radius. Expressing the Laplacian in cylindrical coordinates we obtain

$$\begin{aligned} \left(\frac{\partial^2}{\partial r^2} + \frac{1}{r}\frac{\partial}{\partial r} + \frac{1}{r^2}\frac{\partial^2}{\partial \phi^2} + (k^2-\beta^2)\right) E_z(r,\phi) &= 0 && \text{(A.5)} \\ \left(\frac{\partial^2}{\partial r^2} + \frac{1}{r}\frac{\partial}{\partial r} + \frac{1}{r^2}\frac{\partial^2}{\partial \phi^2} + (k^2-\beta^2)\right) H_z(r,\phi) &= 0\,. && \text{(A.6)} \end{aligned}$$

The general solution to this type of differential equation allows to separate its variables and express it as

$$\begin{aligned} E_z(r,\phi) &= \Psi_E(r)e^{\pm il\phi} && \text{(A.7)} \\ H_z(r,\phi) &= \Psi_H(r)e^{\pm il\phi} && \text{(A.8)} \end{aligned}$$

where $\Psi_E(r)$ ($\Psi_H(r)$) is the function carrying the radial dependency for the electric (magnetic) field and l a positive integer determining the angular dependency. The exponential function giving this dependency offers two possible solutions solutions per field, $e^{+il\phi}$ and $e^{-il\phi}$ accounting for clockwise and and counter-clockwise fields. We continue considering only $e^{+il\phi}$, but the general solution is given by both contributions or any linear combination of them. Considering solutions A.7 and A.8 we can express equations A.5 and A.6 as

$$\begin{aligned} \frac{\partial^2\Psi_E}{\partial r^2} + \frac{1}{r}\frac{\partial\Psi_E}{\partial r} + \left(k^2-\beta^2-\frac{l^2}{r^2}\right)\Psi_E &= 0 && \text{(A.9)} \\ \frac{\partial^2\Psi_H}{\partial r^2} + \frac{1}{r}\frac{\partial\Psi_H}{\partial r} + \left(k^2-\beta^2-\frac{l^2}{r^2}\right)\Psi_H &= 0\,. && \text{(A.10)} \end{aligned}$$

Solving these equation for the field along the axis of propagation and using Maxwell equations to deduce the electric and magnetic field in the perpendicular plane all components of the field are obtained.

For the interior of the micropillar i.e. $r < r_{\mu\text{pillar}}$ the electromagnetic field is given by

$$\begin{aligned} E_r &= \frac{-i\beta}{h^2}\left(AhJ_l'(hr) + \frac{i\omega\mu l}{\beta r}BJ_l(hr)\right)e^{i(\omega t+l\phi-\beta z)} && \text{(A.11)} \\ E_\phi &= \frac{-i\beta}{h^2}\left(\frac{il}{r}AJ_l(hr) - \frac{\omega\mu}{\beta}BhJ_l'(hr)\right)e^{i(\omega t+l\phi-\beta z)} && \text{(A.12)} \\ E_z &= AJ_l(hr)e^{i(\omega t+l\phi-\beta z)} && \text{(A.13)} \\ H_r &= \frac{-i\beta}{h^2}\left(BhJ_l'(hr) + \frac{i\omega\epsilon_{int}l}{\beta r}AJ_l(hr)\right)e^{i(\omega t+l\phi-\beta z)} && \text{(A.14)} \\ H_\phi &= \frac{-i\beta}{h^2}\left(\frac{il}{r}BJ_l(hr) - \frac{\omega\epsilon_{int}}{\beta}AhJ_l'(hr)\right)e^{i(\omega t+l\phi-\beta z)} && \text{(A.15)} \\ H_z &= BJ_l(hr)e^{i(\omega t+l\phi-\beta z)} && \text{(A.16)} \end{aligned}$$

and for the exterior of the micropillar i.e. $r > r_{\mu\text{pillar}}$ by

$$\begin{aligned} E_r &= \frac{-i\beta}{q^2}\left(ChK_l'(qr) + \frac{i\omega\mu l}{\beta r}DK_l(qr)\right)e^{i(\omega t + l\phi - \beta z)} && \text{(A.17)} \\ E_\phi &= \frac{-i\beta}{q^2}\left(\frac{il}{r}CK_l(qr) - \frac{\omega\mu}{\beta}DqK_l'(qr)\right)e^{i(\omega t + l\phi - \beta z)} && \text{(A.18)} \\ E_z &= CK_l(qr)e^{i(\omega t + l\phi - \beta z)} && \text{(A.19)} \\ H_r &= \frac{-i\beta}{q^2}\left(DhK_l'(qr) + \frac{i\omega\epsilon_{ext} l}{\beta r}CK_l(qr)\right)e^{i(\omega t + l\phi - \beta z)} && \text{(A.20)} \\ H_\phi &= \frac{-i\beta}{q^2}\left(\frac{il}{r}DK_l(qr) - \frac{\omega\epsilon_{ext}}{\beta}CqK_l'(qr)\right)e^{i(\omega t + l\phi - \beta z)} && \text{(A.21)} \\ H_z &= DK_l(qr)e^{i(\omega t + l\phi - \beta z)} && \text{(A.22)} \end{aligned}$$

where $\epsilon_{int} = \epsilon_0 n_{int}^2$ $(\epsilon_e xt = \epsilon_0 n_{ext}^2)$ and $\mu = \mu_0$. The functions J_l and K_l correspond to the first and second kind of Bessel functions of l order. The parameters h and q have β dependent values which are given by equations $h^2 = k_{int}^2 - \beta^2$ and $q^2 = k_{ext}^2 - \beta^2$, respectively. From these set of solutions, there are five parameters to be determined A, B, C, D and β. In order to set these values we need to use the boundaries conditions ensuring the continuity of the tangential field (E_ϕ and E_z) at the boundaries between the interior and exterior of the micropillar. Notice that, besides the boundary condition, no restriction apply to A, B, C and D, therefore these are, in general, complex valued. In contrast, β is the assumed wavevector of the plane wave part of the proposed propagating solution (A.1), then we constrain it to be real. the are complex that need to be determined accordingly to the boundaries conditions. These conditions translate into four equations which reduce the parameters to be determine from 5 to 1, which accounts for a scaling factor. By imposing these conditions, the following equations is obtained

$$\left(\frac{J_l'(hr_p)}{hr_pJ_l(hr_p)} + \frac{K_l'(qr_p)}{qr_pK_l(qr_p)}\right)\left(\frac{n_{int}^2J_l'(hr_p)}{hr_pJ_l(hr_p)} + \frac{n_{ext}^2K_l'(qr_p)}{qr_pK_l(qr_p)}\right) = \\ l^2\left(\left(\frac{1}{hr_p}\right)^2 + \left(\frac{1}{qr_p}\right)^2\right)^2\left(\frac{\beta c}{\omega}\right)^2 \quad \text{(A.23)}$$

$$\frac{C}{A} = \frac{J_l(hr_p)}{K_l(qr_p)} \quad \text{(A.24)}$$

$$\frac{B}{A} = \frac{D}{C} = \frac{i\beta l}{\omega\mu}\left(\left(\frac{1}{hr_p}\right)^2 + \left(\frac{1}{qr_p}\right)^2\right)\left(\frac{J_l'(hr_p)}{hr_pJ_l(hr_p)} + \frac{K_l'(qr_p)}{qr_pK_l(qr_p)}\right)^{-1} \quad \text{(A.25)}$$

where $r_p = r_{\mu\text{pillar}}$. From solving equation A.23 we obtain a locus of discrete values for β. From each of this values, by solving equation A.24 and A.25 we can obtain the full set of complex constant A, B, C and D, excepting the scale factor mentioned above. As a result knowing the optical wavelength to be used, the refractive index at the interior and exterior of the pillar and its radius, these equations allow us to model the electric field profile coming out at the top of the micropillar.

Figure A.1 present the in-plane electric field $\vec{E_\phi} + \vec{E_r}$ of a 2 μm diameter micropillar for its fundamental mode (i.e. $l = 1$ and β is chosen such as it the closest to the wavevector k_{int}). The in-plane components plotted (E_ϕ and E_r) show how the propagating solution found correspond to right circular polarized light. Considering the fact that for $l = -1$, there is also a propagating solution that is left circular polarized, therefore that the fundamental propagating mode is degenerated in polarization.

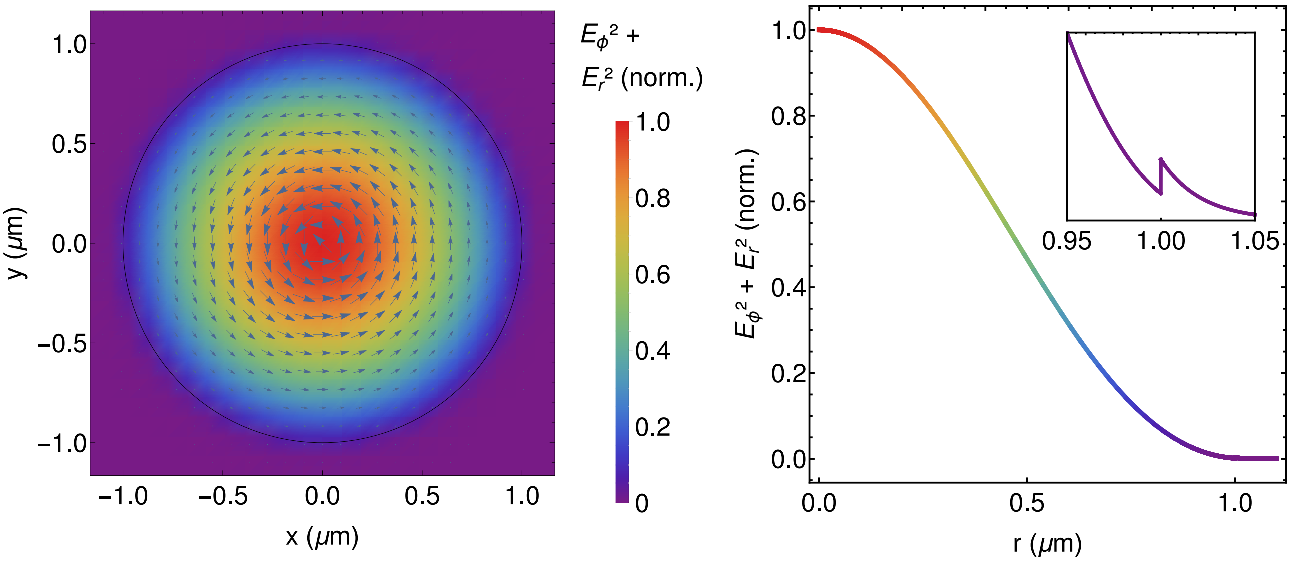

Figure A.1: Left: In-plane electric field $\vec{E_\phi} + \vec{E_r}$ of a modeled 2 μm diameter micropillar fundamental mode. Behind the vector field, information about the intensity is represented color encoded. Right: Intensity profile as a function of radial position in the micropillar. As expected most of the intensity is localized inside the micropillar. At the boundary with the exterior, the tangential field continuity leads to a intensity discontinuity as depicted in the inset around the pillar boundary.

Bibliography

[1] L. Zhmud, “Pythagoras as a mathematician,” *Historia Mathematica*, vol. 16, no. 3, pp. 249 – 268, 1989.

[2] E. Maor, *Music by the Numbers.* Princeton University Press, 2020/06/05/ 2018.

[3] M. Maldovan, “Sound and heat revolutions in phononics,” *Nature*, vol. 503, no. 7475, pp. 209–217, 2013.

[4] J. Johnson and L. Watson, “Monitoring volcanic craters with infrasound “music”,” *Eos*, vol. 100, 2019.

[5] L. M. Watson, J. B. Johnson, M. Sciotto, and A. Cannata, “Changes in crater geometry revealed by inversion of harmonic infrasound observations: 24 december 2018 eruption of mount etna, italy,” *Geophysical Research Letters*, vol. 47, no. 19, p. e2020GL088077, 2020.

[6] W. D. Tompkins, “Afro-peruvian traditions,” *The Garland Handbook of Latin American Music*, pp. 475–487, 2007.

[7] C. E. Llimpe Quintanilla and J. N. Moreno Ruiz, “Estudio preliminar teorico-experimental de las caracteristicas acusticas del cajon peruano,” *31a TECNIACUSTICA, Madrid 2000.*

[8] J. Curie and P. Curie, “Développement par compression de l’électricité polaire dans les cristaux hémièdres à faces inclinées.,” *Bulletin de minéralogie*, vol. 3, no. 4, pp. 90 – 93, 1880.

[9] C. Chilowsky and L. Paul, “Production of submarine signals and the location of submarine objects,” U.S. Patent 1 471 547, Oct. 1923.

[10] A. Elfes, “Sonar-based real-world mapping and navigation,” *IEEE Journal on Robotics and Automation*, vol. 3, no. 3, pp. 249–265, 1987.

[11] J. D. Tardós, J. Neira, P. M. Newman, and J. J. Leonard, “Robust mapping and localization in indoor environments using sonar data,” *The International Journal of Robotics Research*, vol. 21, no. 4, pp. 311–330, 2002.

[12] P. G. Newman and G. S. Rozycki, “The history of ultrasound,” *Surgical clinics of north America*, vol. 78, no. 2, pp. 179–195, 1998.

[13] P. N. Wells, “Ultrasound imaging,” *Physics in Medicine & Biology*, vol. 51, no. 13, p. R83, 2006.

[14] J. W. Judy, “Microelectromechanical systems (MEMS): fabrication, design and applications,” *Smart materials and Structures*, vol. 10, no. 6, p. 1115, 2001.

[15] N. Maluf and K. Williams, *Introduction to microelectromechanical systems engineering.* Artech House, 2004.

[16] M. Tanaka, "An industrial and applied review of new MEMS devices features," *Microelectronic engineering*, vol. 84, no. 5-8, pp. 1341–1344, 2007.

[17] T. Nan, Y. Hui, M. Rinaldi, and N. X. Sun, "Self-biased 215 MHz magnetoelectric NEMS resonator for ultra-sensitive DC magnetic field detection," *Scientific reports*, vol. 3, no. 1, pp. 1–6, 2013.

[18] K. Ekinci and M. Roukes, "Nanoelectromechanical systems," *Review of scientific instruments*, vol. 76, no. 6, p. 061101, 2005.

[19] P. Delsing, A. N. Cleland, M. J. Schuetz, J. Knörzer, G. Giedke, J. I. Cirac, K. Srinivasan, M. Wu, K. C. Balram, C. Bäuerle, *et al.*, "The 2019 surface acoustic waves roadmap," *Journal of Physics D: Applied Physics*, vol. 52, no. 35, p. 353001, 2019.

[20] M. Eichenfield, J. Chan, R. M. Camacho, K. J. Vahala, and O. Painter, "Optomechanical crystals," *Nature*, vol. 462, no. 7269, pp. 78–82, 2009.

[21] M. Esmann, F. R. Lamberti, A. Harouri, L. Lanco, I. Sagnes, I. Favero, G. Aubin, C. Gomez-Carbonell, A. Lemaître, O. Krebs, P. Senellart, and N. D. Lanzillotti-Kimura, "Brillouin scattering in hybrid optophononic Bragg micropillar resonators at 300 GHz," *Optica*, vol. 6, pp. 854–859, Jul 2019.

[22] A. Kent, R. Kini, N. Stanton, M. Henini, B. Glavin, V. Kochelap, and T. Linnik, "Acoustic phonon emission from a weakly coupled superlattice under vertical electron transport: observation of phonon resonance," *Physical review letters*, vol. 96, no. 21, p. 215504, 2006.

[23] R. Beardsley, A. Akimov, M. Henini, and A. Kent, "Coherent terahertz sound amplification and spectral line narrowing in a stark ladder superlattice," *Physical review letters*, vol. 104, no. 8, p. 085501, 2010.

[24] E. Pop, "Energy dissipation and transport in nanoscale devices," *Nano Research*, vol. 3, no. 3, pp. 147–169, 2010.

[25] N. Li, J. Ren, L. Wang, G. Zhang, P. Hänggi, and B. Li, "Colloquium: Phononics: Manipulating heat flow with electronic analogs and beyond," *Reviews of Modern Physics*, vol. 84, no. 3, p. 1045, 2012.

[26] T. Han, X. Bai, D. Gao, J. T. Thong, B. Li, and C.-W. Qiu, "Experimental demonstration of a bilayer thermal cloak," *Physical Review Letters*, vol. 112, no. 5, p. 054302, 2014.

[27] M. Caldarola, P. Albella, E. Cortés, M. Rahmani, T. Roschuk, G. Grinblat, R. F. Oulton, A. V. Bragas, and S. A. Maier, "Non-plasmonic nanoantennas for surface enhanced spectroscopies with ultra-low heat conversion," *Nature communications*, vol. 6, no. 1, pp. 1–8, 2015.

[28] H. S. Choe, R. Prabhakar, G. Wehmeyer, F. I. Allen, W. Lee, L. Jin, Y. Li, P. Yang, C.-W. Qiu, C. Dames, *et al.*, "Ion write microthermotics: Programing thermal metamaterials at the microscale," *Nano letters*, vol. 19, no. 6, pp. 3830–3837, 2019.

[29] R. Hu and X. Luo, "Two-dimensional phonon engineering triggers microscale thermal functionalities," *National Science Review*, vol. 6, no. 6, pp. 1071–1073, 2019.

[30] J. Chan, A. H. Safavi-Naeini, J. T. Hill, S. Meenehan, and O. Painter, "Optimized optomechanical crystal cavity with acoustic radiation shield," *Applied Physics Letters*, vol. 101, no. 8, p. 081115, 2012.

[31] H. Ren, M. H. Matheny, G. S. MacCabe, J. Luo, H. Pfeifer, M. Mirhosseini, and O. Painter, "Two-dimensional optomechanical crystal cavity with high quantum cooperativity," *Nature communications*, vol. 11, no. 1, pp. 1–10, 2020.

[32] F. Novelli, B. Guchhait, and M. Havenith, "Towards intense THz spectroscopy on water: Characterization of optical rectification by GaP, OH1, and DSTMS at OPA wavelengths," *Materials*, vol. 13, no. 6, p. 1311, 2020.

[33] D. Navarro-Urrios, A. Tredicucci, and C. M. Sotomayor-Torres, "Coherent phonon generation in optomechanical crystals," *SPIE Newsroom, doi*, vol. 10, no. 2.1201507, p. 006036, 2015.

[34] M. Heyden, J. Sun, S. Funkner, G. Mathias, H. Forbert, M. Havenith, and D. Marx, "Dissecting the THz spectrum of liquid water from first principles via correlations in time and space," *Proceedings of the National Academy of Sciences*, vol. 107, no. 27, pp. 12068–12073, 2010.

[35] R. Merlin, A. Pinczuk, and W. Weber, "Overview of phonon Raman scattering in solids," in *Raman scattering in materials science*, pp. 1–29, Springer, 2000.

[36] A. A. Balandin, "Nanophononics: phonon engineering in nanostructures and nanodevices," *Journal of nanoscience and nanotechnology*, vol. 5, no. 7, pp. 1015–1022, 2005.

[37] S. Volz, J. Ordonez-Miranda, A. Shchepetov, M. Prunnila, J. Ahopelto, T. Pezeril, G. Vaudel, V. Gusev, P. Ruello, E. M. Weig, M. Schubert, M. Hettich, M. Grossman, T. Dekorsy, F. Alzina, B. Graczykowski, E. Chavez-Angel, J. Sebastian Reparaz, M. R. Wagner, C. M. Sotomayor-Torres, S. Xiong, S. Neogi, and D. Donadio, "Nanophononics: state of the art and perspectives," *The European Physical Journal B*, vol. 89, p. 15, Jan 2016.

[38] A. Fainstein, B. Jusserand, and V. Thierry-Mieg, "Raman scattering enhancement by optical confinement in a semiconductor planar microcavity," *Physical review letters*, vol. 75, no. 20, p. 3764, 1995.

[39] A. Fainstein, M. Trigo, D. Oliva, B. Jusserand, T. Freixanet, and V. Thierry-Mieg, "Standing optical phonons in finite semiconductor superlattices studied by resonant Raman scattering in a double microcavity," *Physical Review Letters*, vol. 86, no. 15, p. 3411, 2001.

[40] C. Perez, "Technological revolutions and techno-economic paradigms," *Cambridge Journal of Economics*, vol. 34, pp. 185–202, 09 2009.

[41] G. Kurizki, P. Bertet, Y. Kubo, K. Mølmer, D. Petrosyan, P. Rabl, and J. Schmiedmayer, "Quantum technologies with hybrid systems," *Proceedings of the National Academy of Sciences*, vol. 112, no. 13, pp. 3866–3873, 2015.

[42] S. Thomas, M. Billard, N. Coste, S. Wein, Priya, H. Ollivier, O. Krebs, L. Tazaïrt, A. Harouri, A. Lemaitre, I. Sagnes, *et al.*, "Efficient source of indistinguishable single-photons based on phonon-assisted excitation," *arXiv preprint arXiv:2007.04330*, 2020.

[43] B. Krummheuer, V. M. Axt, and T. Kuhn, "Theory of pure dephasing and the resulting absorption line shape in semiconductor quantum dots," *Physical Review B*, vol. 65, no. 19, p. 195313, 2002.

[44] A. Vagov, V. M. Axt, and T. Kuhn, "Impact of pure dephasing on the nonlinear optical response of single quantum dots and dot ensembles," *Physical Review B*, vol. 67, no. 11, p. 115338, 2003.

[45] M. V. Gustafsson, T. Aref, A. F. Kockum, M. K. Ekström, G. Johansson, and P. Delsing, “Propagating phonons coupled to an artificial atom,” *Science*, vol. 346, no. 6206, pp. 207–211, 2014.

[46] A. Bienfait, K. J. Satzinger, Y. Zhong, H.-S. Chang, M.-H. Chou, C. R. Conner, É. Dumur, J. Grebel, G. A. Peairs, R. G. Povey, *et al.*, “Phonon-mediated quantum state transfer and remote qubit entanglement,” *Science*, vol. 364, no. 6438, pp. 368–371, 2019.

[47] M. Ekström, T. Aref, A. Ask, G. Andersson, B. Suri, H. Sanada, G. Johansson, and P. Delsing, “Towards phonon routing: Controlling propagating acoustic waves in the quantum regime,” *New Journal of Physics*, vol. 21, no. 12, p. 123013, 2019.

[48] A. Grodecka and P. Machnikowski, “Partly noiseless encoding of quantum information in quantum dot arrays against phonon-induced pure dephasing,” *Physical Review B*, vol. 73, no. 12, p. 125306, 2006.

[49] T. Grange, N. Somaschi, C. Antón, L. De Santis, G. Coppola, V. Giesz, A. Lemaître, I. Sagnes, A. Auffèves, and P. Senellart, “Reducing phonon-induced decoherence in solid-state single-photon sources with cavity quantum electrodynamics,” *Physical review letters*, vol. 118, no. 25, p. 253602, 2017.

[50] N. Lanzillotti-Kimura, A. Fainstein, B. Perrin, B. Jusserand, O. Mauguin, L. Largeau, and A. Lemaître, “Bloch oscillations of THz acoustic phonons in coupled nanocavity structures,” *Physical Review Letters*, vol. 104, no. 19, p. 197402, 2010.

[51] M. Esmann, F. Lamberti, A. Lemaître, and N. Lanzillotti-Kimura, “Topological acoustics in coupled nanocavity arrays,” *Physical Review B*, vol. 98, no. 16, p. 161109, 2018.

[52] O. Ortíz, M. Esmann, and N. Lanzillotti-Kimura, “Phonon engineering with superlattices: Generalized nanomechanical potentials,” *Physical Review B*, vol. 100, no. 8, p. 085430, 2019.

[53] S. Laurent, S. Varoutsis, L. Le Gratiet, A. Lemaître, I. Sagnes, F. Raineri, A. Levenson, I. Robert-Philip, and I. Abram, “Indistinguishable single photons from a single-quantum dot in a two-dimensional photonic crystal cavity,” *Applied Physics Letters*, vol. 87, no. 16, p. 163107, 2005.

[54] S. Richard, K. Bencheikh, B. Boulanger, and J. A. Levenson, “Semiclassical model of triple photons generation in optical fibers,” *Optics letters*, vol. 36, no. 15, pp. 3000–3002, 2011.

[55] N. Somaschi, V. Giesz, L. De Santis, J. Loredo, M. P. Almeida, G. Hornecker, S. L. Portalupi, T. Grange, C. Antón, J. Demory, *et al.*, “Near-optimal single-photon sources in the solid state,” *Nature Photonics*, vol. 10, no. 5, pp. 340–345, 2016.

[56] M. Marconi, J. Javaloyes, P. Hamel, F. Raineri, A. Levenson, and A. M. Yacomotti, “Far-from-equilibrium route to superthermal light in bimodal nanolasers,” *Physical Review X*, vol. 8, no. 1, p. 011013, 2018.

[57] Q. Qiao, J. Xia, C. Lee, and G. Zhou, “Applications of photonic crystal nanobeam cavities for sensing,” *Micromachines*, vol. 9, no. 11, p. 541, 2018.

[58] Y. Luo, J. Shao, S. Chen, X. Chen, H. Tian, X. Li, L. Wang, D. Wang, and B. Lu, “Flexible capacitive pressure sensor enhanced by tilted micropillar arrays,” *ACS applied materials & interfaces*, vol. 11, no. 19, pp. 17796–17803, 2019.

[59] B.-S. Song, T. Asano, S. Jeon, H. Kim, C. Chen, D. D. Kang, and S. Noda, "Ultrahigh-Q photonic crystal nanocavities based on 4H silicon carbide," *Optica*, vol. 6, no. 8, pp. 991–995, 2019.

[60] M. Trigo, A. Bruchhausen, A. Fainstein, B. Jusserand, and V. Thierry-Mieg, "Confinement of acoustical vibrations in a semiconductor planar phonon cavity," *Physical review letters*, vol. 89, no. 22, p. 227402, 2002.

[61] N. Lanzillotti-Kimura, B. Perrin, A. Fainstein, B. Jusserand, and A. Lemaître, "Nanophononic thin-film filters and mirrors studied by picosecond ultrasonics," *Applied Physics Letters*, vol. 96, no. 5, p. 053101, 2010.

[62] B. Jusserand and M. Cardona, "Raman spectroscopy of vibrations in superlattices," *Light Scattering in Solids V*, pp. 49–152, 1989.

[63] B. Jusserand, D. Paquet, and A. Regreny, "" folded" optical phonons in gaas ga 1- x al x as superlattices," *Physical Review B*, vol. 30, no. 10, p. 6245, 1984.

[64] O. Koblinger, J. Mebert, E. Dittrich, S. Döttinger, W. Eisenmenger, P. Santos, and L. Ley, "Phonon stop bands in amorphous superlattices," *Physical Review B*, vol. 35, no. 17, p. 9372, 1987.

[65] P. Santos, A. Sood, M. Cardona, K. Ploog, Y. Ohmori, and H. Okamoto, "Raman scattering from gasb/alsb superlattices: Acoustic, optical, and interface vibrational modes," *Physical Review B*, vol. 37, no. 11, p. 6381, 1988.

[66] A. Fainstein, B. Jusserand, and V. Thierry-Mieg, "Raman efficiency in a planar microcavity," *Physical Review B*, vol. 53, no. 20, p. R13287, 1996.

[67] A. Fainstein and B. Jusserand, "Performance of semiconductor planar microcavities for Raman-scattering enhancement," *Physical Review B*, vol. 57, no. 4, p. 2402, 1998.

[68] F.-R. Lamberti, *Opto-phononic confinement in GaAs/AlAs-based resonators*. PhD thesis, 2018.

[69] A. Fainstein, N. D. Lanzillotti-Kimura, B. Jusserand, and B. Perrin, "Strong optical-mechanical coupling in a vertical GaAs/AlAs microcavity for subterahertz phonons and near-infrared light," *Phys. Rev. Lett.*, vol. 110, p. 037403, Jan 2013.

[70] S. Anguiano, A. E. Bruchhausen, B. Jusserand, I. Favero, F. R. Lamberti, L. Lanco, I. Sagnes, A. Lemaître, N. D. Lanzillotti-Kimura, P. Senellart, and A. Fainstein, "Micropillar resonators for optomechanics in the extremely high 19–95-GHz frequency range," *Phys. Rev. Lett.*, vol. 118, p. 263901, Jun 2017.

[71] N. D. Lanzillotti-Kimura, A. Fainstein, A. Huynh, B. Perrin, B. Jusserand, A. Miard, and A. Lemaître, "Coherent generation of acoustic phonons in an optical microcavity," *Phys. Rev. Lett.*, vol. 99, p. 217405, Nov 2007.

[72] F. R. Lamberti, M. Esmann, A. Lemaître, C. Gomez Carbonell, O. Krebs, I. Favero, B. Jusserand, P. Senellart, L. Lanco, and N. D. Lanzillotti-Kimura, "Nanomechanical resonators based on adiabatic periodicity-breaking in a superlattice," *Applied Physics Letters*, vol. 111, no. 17, p. 173107, 2017.

[73] P. Ruello and V. E. Gusev, "Physical mechanisms of coherent acoustic phonons generation by ultrafast laser action," *Ultrasonics*, vol. 56, pp. 21–35, 2015.

[74] C. Thomsen, J. Strait, Z. Vardeny, H. J. Maris, J. Tauc, and J. J. Hauser, "Coherent phonon generation and detection by picosecond light pulses," *Phys. Rev. Lett.*, vol. 53, pp. 989–992, Sep 1984.

[75] C. Thomsen, H. T. Grahn, H. J. Maris, and J. Tauc, "Surface generation and detection of phonons by picosecond light pulses," *Phys. Rev. B*, vol. 34, pp. 4129–4138, Sep 1986.

[76] H. T. Grahn, H. J. Maris, and J. Tauc, "Picosecond ultrasonics," *IEEE Journal of Quantum Electronics*, vol. 25, no. 12, pp. 2562–2569, 1989.

[77] V. E. Gusev and P. Ruello, "Advances in applications of time-domain Brillouin scattering for nanoscale imaging," *Applied Physics Reviews*, vol. 5, no. 3, p. 031101, 2018.

[78] Y. Peter and M. Cardona, *Fundamentals of semiconductors: physics and materials properties.* Springer Science & Business Media, 2010.

[79] P. Giannozzi, S. De Gironcoli, P. Pavone, and S. Baroni, "Ab initio calculation of phonon dispersions in semiconductors," *Physical Review B*, vol. 43, no. 9, p. 7231, 1991.

[80] B. t. Brockhouse and P. Iyengar, "Normal modes of germanium by neutron spectrometry," *Physical Review*, vol. 111, no. 3, p. 747, 1958.

[81] D. Strauch and B. Dorner, "Phonon dispersion in GaAs," *Journal of Physics: Condensed Matter*, vol. 2, no. 6, p. 1457, 1990.

[82] M. d'Astuto, P. Giura, M. Krisch, M. Lorenzen, A. Mermet, G. Monaco, H. Requardt, F. Sette, A. Shukla, and R. Verbeni, "Phonon dispersion studies of crystalline materials using high-energy resolution inelastic X-ray scattering (IXS)," *Physica B: Condensed Matter*, vol. 316, pp. 150–153, 2002.

[83] Y. Yao and D. König, "Comparison of bulk material candidates for hot carrier absorber," *Solar Energy Materials and Solar Cells*, vol. 140, pp. 422–427, 2015.

[84] S. Baroni, P. Giannozzi, and A. Testa, "Green's-function approach to linear response in solids," *Physical Review Letters*, vol. 58, no. 18, p. 1861, 1987.

[85] X. Gonze, "Perturbation expansion of variational principles at arbitrary order," *Physical Review A*, vol. 52, no. 2, p. 1086, 1995.

[86] N. D. Lanzillotti Kimura, *Dinámica de fonones acústicos en multicapas nanométricas.* PhD thesis, Universidad Nacional de Cuyo, 2009.

[87] M. A. Afromowitz, "Refractive index of Ga1-xAlxAs," *Solid State Communications*, vol. 15, no. 1, pp. 59–63, 1974.

[88] A. W, N. Ashcroft, N. Mermin, N. Mermin, and B. P. Company, *Solid State Physics.* HRW international editions, Holt, Rinehart and Winston, 1976.

[89] A. Huynh, N. D. Lanzillotti-Kimura, B. Jusserand, B. Perrin, A. Fainstein, M. F. Pascual-Winter, E. Peronne, and A. Lemaître, "Subterahertz phonon dynamics in acoustic nanocavities," *Phys. Rev. Lett.*, vol. 97, p. 115502, Sep 2006.

[90] A. Yariv and P. Yeh, *Optical waves in crystals*, vol. 5. Wiley New York, 1984.

[91] J. He, B. Djafari-Rouhani, and J. Sapriel, "Theory of light scattering by longitudinal-acoustic phonons in superlattices," *Physical Review B*, vol. 37, no. 8, p. 4086, 1988.

[92] J. Pendry, "Photonic band structures," *Journal of Modern Optics*, vol. 41, no. 2, pp. 209–229, 1994.

[93] P. Bell, J. Pendry, L. M. Moreno, and A. Ward, “A program for calculating photonic band structures and transmission coefficients of complex structures,” *Computer physics communications*, vol. 85, no. 2, pp. 306–322, 1995.

[94] B. Jusserand and M. Cardona, “Light scattering in solids v,” *Topics in Applied Physics*, vol. 66, p. 49, 1989.

[95] C. Colvard, R. Merlin, M. Klein, and A. Gossard, “Observation of folded acoustic phonons in a semiconductor superlattice,” *Physical Review Letters*, vol. 45, no. 4, p. 298, 1980.

[96] M. Cardona and R. Merlin, “Light scattering in solids ix,” in *Light Scattering in Solid IX*, pp. 1–14, Springer, 2006.

[97] F. Della Picca, R. Berte, M. Rahmani, P. Albella, J. M. Bujjamer, M. Poblet, E. Cortés, S. A. Maier, and A. V. Bragas, “Tailored hypersound generation in single plasmonic nanoantennas,” *Nano letters*, vol. 16, no. 2, pp. 1428–1434, 2016.

[98] C. V. Raman and K. S. Krishnan, “A new type of secondary radiation,” *Nature*, vol. 121, pp. 501–502, Mar 1928.

[99] A. Smekal, “Zur quantentheorie der dispersion,” *Naturwissenschaften*, vol. 11, pp. 873–875, Oct 1923.

[100] N. Lanzillotti-Kimura, A. Fainstein, B. Jusserand, and A. Lemaître, “Resonant raman scattering of nanocavity-confined acoustic phonons,” *Physical Review B*, vol. 79, no. 3, p. 035404, 2009.

[101] C. Thomsen, H. Grahn, H. Maris, and J. Tauc, “Picosecond interferometric technique for study of phonons in the brillouin frequency range,” *Optics Communications*, vol. 60, no. 1, pp. 55 – 58, 1986.

[102] V. Gusev and A. A. Karabutov, *Laser optoacoustics.* Amer Inst of Physics, 1993.

[103] V. E. Gusev, “Contra-intuitive features of time-domain Brillouin scattering in collinear paraxial sound and light beams,” *arXiv preprint arXiv:2006.02221*, 2020.

[104] R. Merlin, “Generating coherent THz phonons with light pulses,” *Solid State Communications*, vol. 102, no. 2-3, pp. 207–220, 1997.

[105] S. A. Akhmanov and V. É. Gusev, “Laser excitation of ultrashort acoustic pulses: New possibilities in solid-state spectroscopy, diagnostics of fast processes, and nonlinear acoustics,” *Soviet Physics Uspekhi*, vol. 35, no. 3, p. 153, 1992.

[106] O. Matsuda and O. B. Wright, “Reflection and transmission of light in multilayers perturbed by picosecond strain pulse propagation,” *J. Opt. Soc. Am. B*, vol. 19, pp. 3028–3041, Dec 2002.

[107] R. Raj, J. Levenson, J. Oudar, and M. Bensoussan, “Vertical microcavity optical amplifying switch,” *Electronics Letters*, vol. 2, no. 29, pp. 167–169, 1993.

[108] C. Simonneau, J. Debray, J. Harmand, P. Vidaković, D. Lovering, and J. Levenson, “Second-harmonic generation in a doubly resonant semiconductor microcavity,” *Optics letters*, vol. 22, no. 23, pp. 1775–1777, 1997.

[109] H. Ollivier, I. Maillette de Buy Wenniger, S. Thomas, S. C. Wein, A. Harouri, G. Coppola, P. Hilaire, C. Millet, A. Lemaître, I. Sagnes, *et al.*, “Reproducibility of high-performance quantum dot single-photon sources,” *ACS Photonics*, vol. 7, no. 4, pp. 1050–1059, 2020.

[110] A. Dousse, J. Suffczyński, A. Beveratos, O. Krebs, A. Lemaître, I. Sagnes, J. Bloch, P. Voisin, and P. Senellart, “Ultrabright source of entangled photon pairs,” *Nature*, vol. 466, no. 7303, pp. 217–220, 2010.

[111] D. Bajoni, P. Senellart, E. Wertz, I. Sagnes, A. Miard, A. Lemaître, and J. Bloch, “Polariton laser using single micropillar gaas- gaalas semiconductor cavities,” *Physical review letters*, vol. 100, no. 4, p. 047401, 2008.

[112] J.-C. Harmand, G. Patriarche, F. Glas, F. Panciera, I. Florea, J.-L. Maurice, L. Travers, and Y. Ollivier, “Atomic step flow on a nanofacet,” *Physical review letters*, vol. 121, no. 16, p. 166101, 2018.

[113] N. Lanzillotti-Kimura, A. Fainstein, B. Perrin, B. Jusserand, L. Largeau, O. Mauguin, and A. Lemaitre, “Enhanced optical generation and detection of acoustic nanowaves in microcavities,” *Physical Review B*, vol. 83, no. 20, p. 201103, 2011.

[114] P. S. Anton, R. Silberglitt, and J. Schneider, *The global technology revolution: bio/nano/materials trends and their synergies with information technology by 2015*. Rand Corporation, 2001.

[115] S. Nakamura, “Background story of the invention of efficient blue InGaN light emitting diodes (Nobel lecture),” *Annalen der Physik*, vol. 527, no. 5-6, pp. 335–349, 2015.

[116] Y. F. Dufrêne, T. Ando, R. Garcia, D. Alsteens, D. Martinez-Martin, A. Engel, C. Gerber, and D. J. Müller, “Imaging modes of atomic force microscopy for application in molecular and cell biology,” *Nature Nanotechnology*, vol. 12, pp. 295–307, Apr 2017.

[117] F. Yang and C. Dames, “Mean free path spectra as a tool to understand thermal conductivity in bulk and nanostructures,” *Physical Review B*, vol. 87, no. 3, p. 035437, 2013.

[118] G. Chen, “Particularities of heat conduction in nanostructures,” *Journal of Nanoparticle Research*, vol. 2, no. 2, pp. 199–204, 2000.

[119] R. S. Prasher, X. Hu, Y. Chalopin, N. Mingo, K. Lofgreen, S. Volz, F. Cleri, and P. Keblinski, “Turning carbon nanotubes from exceptional heat conductors into insulators,” *Physical Review Letters*, vol. 102, no. 10, p. 105901, 2009.

[120] Y. Wang, D. H. Hurley, Z. Hua, T. Pezeril, S. Raetz, V. E. Gusev, V. Tournat, and M. Khafizov, “Imaging grain microstructure in a model ceramic energy material with optically generated coherent acoustic phonons,” *Nature Communications*, vol. 11, no. 1, pp. 1–8, 2020.

[121] M. Kuriakose, S. Raetz, N. Chigarev, S. M. Nikitin, A. Bulou, D. Gasteau, V. Tournat, B. Castagnede, A. Zerr, and V. E. Gusev, “Picosecond laser ultrasonics for imaging of transparent polycrystalline materials compressed to megabar pressures,” *Ultrasonics*, vol. 69, pp. 259–267, 2016.

[122] Y. Chu, P. Kharel, W. H. Renninger, L. D. Burkhart, L. Frunzio, P. T. Rakich, and R. J. Schoelkopf, “Quantum acoustics with superconducting qubits,” *Science*, vol. 358, no. 6360, pp. 199–202, 2017.

[123] M. Forsch, R. Stockill, A. Wallucks, I. Marinković, C. Gärtner, R. A. Norte, F. van Otten, A. Fiore, K. Srinivasan, and S. Gröblacher, “Microwave-to-optics conversion using a mechanical oscillator in its quantum ground state,” *Nature Physics*, vol. 16, no. 1, pp. 69–74, 2020.

[124] N. D. Lanzillotti-Kimura, A. Fainstein, and B. Jusserand, "Towards GHz–THz cavity optomechanics in DBR-based semiconductor resonators," *Ultrasonics*, vol. 56, pp. 80–89, 2015.

[125] M. Esmann, F. R. Lamberti, P. Senellart, I. Favero, O. Krebs, L. Lanco, C. Gomez Carbonell, A. Lemaître, and N. D. Lanzillotti-Kimura, "Topological nanophononic states by band inversion," *Phys. Rev. B*, vol. 97, p. 155422, Apr 2018.

[126] L. Donetti, F. Gámiz, J. B. Roldán, and A. Godoy, "Acoustic phonon confinement in silicon nanolayers: Effect on electron mobility," *Journal of Applied Physics*, vol. 100, no. 1, p. 013701, 2006.

[127] E. B. Ramayya, D. Vasileska, S. M. Goodnick, and I. Knezevic, "Electron transport in silicon nanowires: The role of acoustic phonon confinement and surface roughness scattering," *Journal of Applied Physics*, vol. 104, no. 6, p. 063711, 2008.

[128] F. Kargar, B. Debnath, J.-P. Kakko, A. Säynätjoki, H. Lipsanen, D. L. Nika, R. K. Lake, and A. A. Balandin, "Direct observation of confined acoustic phonon polarization branches in free-standing semiconductor nanowires," *Nature Communications*, vol. 7, p. 13400, Nov 2016.

[129] M. Aspelmeyer, T. J. Kippenberg, and F. Marquardt, "Cavity optomechanics," *Rev. Mod. Phys.*, vol. 86, pp. 1391–1452, Dec 2014.

[130] R. Van Laer, B. Kuyken, D. Van Thourhout, and R. Baets, "Interaction between light and highly confined hypersound in a silicon photonic nanowire," *Nature Photonics*, vol. 9, pp. 199–203, Mar 2015.

[131] R. Riedinger, A. Wallucks, I. Marinković, C. Löschnauer, M. Aspelmeyer, S. Hong, and S. Gröblacher, "Remote quantum entanglement between two micromechanical oscillators," *Nature*, vol. 556, pp. 473–477, Apr 2018.

[132] T. Grange, N. Somaschi, C. Antón, L. De Santis, G. Coppola, V. Giesz, A. Lemaître, I. Sagnes, A. Auffèves, and P. Senellart, "Reducing phonon-induced decoherence in solid-state single-photon sources with cavity quantum electrodynamics," *Phys. Rev. Lett.*, vol. 118, p. 253602, Jun 2017.

[133] A. Artioli, S. Kotal, N. Gregersen, P. Verlot, J.-M. Gérard, and J. Claudon, "Design of quantum dot-nanowire single-photon sources that are immune to thermomechanical decoherence," *Phys. Rev. Lett.*, vol. 123, p. 247403, Dec 2019.

[134] B.-S. Song, S. Noda, T. Asano, and Y. Akahane, "Ultra-high-Q photonic double-heterostructure nanocavity," *Nature Materials*, vol. 4, pp. 207–210, Mar 2005.

[135] P. Velha, E. Picard, T. Charvolin, E. Hadji, J. C. Rodier, P. Lalanne, and D. Peyrade, "Ultra-high q/v fabry-perot microcavity on soi substrate," *Opt. Express*, vol. 15, pp. 16090–16096, Nov 2007.

[136] M. Lermer, N. Gregersen, F. Dunzer, S. Reitzenstein, S. Höfling, J. Mørk, L. Worschech, M. Kamp, and A. Forchel, "Bloch-wave engineering of quantum dot micropillars for cavity quantum electrodynamics experiments," *Phys. Rev. Lett.*, vol. 108, p. 057402, Jan 2012.

[137] P. Lalanne and J. P. Hugonin, "Bloch-wave engineering for high-Q, small-V microcavities," *IEEE Journal of Quantum Electronics*, vol. 39, no. 11, pp. 1430–1438, 2003.

[138] P. Lalanne, S. Mias, and J.-P. Hugonin, "Two physical mechanisms for boosting the quality factor to cavity volume ratio of photonic crystal microcavities," *Optics Express*, vol. 12, no. 3, pp. 458–467, 2004.

[139] T.-Y. Seong, J. Han, H. Amano, and H. Morkoç, eds., *III-Nitride Based Light Emitting Diodes and Applications.* Springer Singapore, 2017.

[140] S. Nakamura, S. Pearton, and G. Fasol, eds., *The Blue Laser Diode.* Springer-Verlag Berlin Heidelberg, 2000.

[141] J. Faist, *Quantum cascade lasers.* OUP Oxford, 2013.

[142] A. Majumdar, K. K. Choi, J. L. Reno, L. P. Rokhinson, and D. C. Tsui, "Two-color quantum-well infrared photodetector with voltage tunable peaks," *Applied Physics Letters*, vol. 80, no. 5, pp. 707–709, 2002.

[143] D. Hofstetter, S.-S. Schad, H. Wu, W. J. Schaff, and L. F. Eastman, "GaN/AlN-based quantum-well infrared photodetector for 1.55 μm," *Applied Physics Letters*, vol. 83, no. 3, pp. 572–574, 2003.

[144] W. Wu, A. Bonakdar, and H. Mohseni, "Plasmonic enhanced quantum well infrared photodetector with high detectivity," *Applied physics letters*, vol. 96, no. 16, p. 161107, 2010.

[145] M. Fox and R. Ispasoiu, "Quantum wells, superlattices, and band-gap engineering," in *Springer Handbook of Electronic and Photonic Materials*, pp. 1–1, Springer, 2017.

[146] A. Fainstein and B. Jusserand, "Raman scattering in resonant cavities," *Light scattering in solid IX*, pp. 17–110, 2006.

[147] S. L. Portalupi, G. Hornecker, V. Giesz, T. Grange, A. Lemaître, J. Demory, I. Sagnes, N. D. Lanzillotti-Kimura, L. Lanco, A. Auffèves, *et al.*, "Phonon-tuned bright single-photon source," *arXiv preprint arXiv:1412.6146*, 2014.

[148] V. Giesz, *Cavity-enhanced Photon-Photon Interactions With Bright Quantum Dot Sources.* PhD thesis, Université Paris-Saclay (ComUE), 2015.

[149] M. Palamaru and P. Lalanne, "Photonic crystal waveguides: Out-of-plane losses and adiabatic modal conversion," *Applied Physics Letters*, vol. 78, no. 11, pp. 1466–1468, 2001.

[150] M. Xiao, Z. Q. Zhang, and C. T. Chan, "Surface impedance and bulk band geometric phases in one-dimensional systems," *Phys. Rev. X*, vol. 4, p. 021017, Apr 2014.

[151] M. Xiao, G. Ma, Z. Yang, P. Sheng, Z. Zhang, and C. T. Chan, "Geometric phase and band inversion in periodic acoustic systems," *Nature Physics*, vol. 11, no. 3, pp. 240–244, 2015.

[152] G. Ma, M. Xiao, and C. T. Chan, "Topological phases in acoustic and mechanical systems," *Nature Reviews Physics*, vol. 1, no. 4, pp. 281–294, 2019.

[153] J. Lu, C. Qiu, L. Ye, X. Fan, M. Ke, F. Zhang, and Z. Liu, "Observation of topological valley transport of sound in sonic crystals," *Nature Physics*, vol. 13, no. 4, pp. 369–374, 2017.

[154] G. Arregui, O. Ortíz, M. Esmann, C. M. Sotomayor-Torres, C. Gomez-Carbonell, O. Mauguin, B. Perrin, A. Lemaître, P. D. García, and N. D. Lanzillotti-Kimura, "Coherent generation and detection of acoustic phonons in topological nanocavities," *APL Photonics*, vol. 4, no. 3, p. 030805, 2019.

[155] N. Lanzillotti-Kimura, A. Fainstein, C. Balseiro, and B. Jusserand, "Phonon engineering with acoustic nanocavities: Theoretical considerations on phonon molecules, band structures, and acoustic Bloch oscillations," *Physical Review B*, vol. 75, no. 2, p. 024301, 2007.

[156] H. Sanchis-Alepuz, Y. A. Kosevich, and J. Sánchez-Dehesa, "Acoustic analogue of electronic Bloch oscillations and resonant zener tunneling in ultrasonic superlattices," *Physical review letters*, vol. 98, no. 13, p. 134301, 2007.

[157] A. Yariv, Y. Xu, R. K. Lee, and A. Scherer, "Coupled-resonator optical waveguide:? a proposal and analysis," *Optics letters*, vol. 24, no. 11, pp. 711–713, 1999.

[158] S. Combrié, G. Lehoucq, G. Moille, A. Martin, and A. De Rossi, "Comb of high-Q resonances in a compact photonic cavity," *Laser & Photonics Reviews*, vol. 11, no. 6, p. 1700099, 2017.

[159] C.-K. Lin, H.-C. Chang, and S. Lin, "Symmetric double-well potential model and its application to vibronic spectra: Studies of inversion modes of ammonia and nitrogen-vacancy defect centers in diamond," *The Journal of Physical Chemistry A*, vol. 111, no. 38, pp. 9347–9354, 2007.

[160] G. Milburn, J. Corney, E. M. Wright, and D. Walls, "Quantum dynamics of an atomic bose-einstein condensate in a double-well potential," *Physical Review A*, vol. 55, no. 6, p. 4318, 1997.

[161] G. Rozas, M. P. Winter, B. Jusserand, A. Fainstein, B. Perrin, E. Semenova, and A. Lemaître, "Lifetime of THz acoustic nanocavity modes," *Physical review letters*, vol. 102, no. 1, p. 015502, 2009.

[162] J. Chan, T. M. Alegre, A. H. Safavi-Naeini, J. T. Hill, A. Krause, S. Gröblacher, M. Aspelmeyer, and O. Painter, "Laser cooling of a nanomechanical oscillator into its quantum ground state," *Nature*, vol. 478, no. 7367, pp. 89–92, 2011.

[163] R. Ohta, Y. Ota, M. Nomura, N. Kumagai, S. Ishida, S. Iwamoto, and Y. Arakawa, "Strong coupling between a photonic crystal nanobeam cavity and a single quantum dot," *Applied Physics Letters*, vol. 98, no. 17, p. 173104, 2011.

[164] Y. Zhang and M. Lončar, "Submicrometer diameter micropillar cavities with high quality factor and ultrasmall mode volume," *Optics letters*, vol. 34, no. 7, pp. 902–904, 2009.

[165] M. A. Nielsen and I. Chuang, "Quantum computation and quantum information," 2002.

[166] J. Majer, J. Chow, J. Gambetta, J. Koch, B. Johnson, J. Schreier, L. Frunzio, D. Schuster, A. A. Houck, A. Wallraff, *et al.*, "Coupling superconducting qubits via a cavity bus," *Nature*, vol. 449, no. 7161, pp. 443–447, 2007.

[167] H. J. Kimble, "The quantum internet," *Nature*, vol. 453, no. 7198, pp. 1023–1030, 2008.

[168] Y. Li, T. Shi, B. Chen, Z. Song, and C.-P. Sun, "Quantum-state transmission via a spin ladder as a robust data bus," *Physical Review A*, vol. 71, no. 2, p. 022301, 2005.

[169] J. Simon, H. Tanji, S. Ghosh, and V. Vuletić, "Single-photon bus connecting spin-wave quantum memories," *Nature Physics*, vol. 3, no. 11, pp. 765–769, 2007.

[170] F. Arute, K. Arya, R. Babbush, D. Bacon, J. C. Bardin, R. Barends, R. Biswas, S. Boixo, F. G. Brandao, D. A. Buell, *et al.*, "Quantum supremacy using a programmable superconducting processor," *Nature*, vol. 574, no. 7779, pp. 505–510, 2019.

[171] Y. Wang, M. Um, J. Zhang, S. An, M. Lyu, J.-N. Zhang, L.-M. Duan, D. Yum, and K. Kim, “Single-qubit quantum memory exceeding ten-minute coherence time,” *Nature Photonics*, vol. 11, no. 10, pp. 646–650, 2017.

[172] J. Preskill, “Quantum computing in the NISQ era and beyond,” *Quantum*, vol. 2, p. 79, 2018.

[173] D. Kielpinski, C. Monroe, and D. J. Wineland, “Architecture for a large-scale ion-trap quantum computer,” *Nature*, vol. 417, no. 6890, pp. 709–711, 2002.

[174] F. Motzoi, J. M. Gambetta, P. Rebentrost, and F. K. Wilhelm, “Simple pulses for elimination of leakage in weakly nonlinear qubits,” *Physical review letters*, vol. 103, no. 11, p. 110501, 2009.

[175] J. J. Burnett, A. Bengtsson, M. Scigliuzzo, D. Niepce, M. Kudra, P. Delsing, and J. Bylander, “Decoherence benchmarking of superconducting qubits,” *npj Quantum Information*, vol. 5, no. 1, pp. 1–8, 2019.

[176] M. Kjaergaard, M. E. Schwartz, J. Braumüller, P. Krantz, J. I.-J. Wang, S. Gustavsson, and W. D. Oliver, “Superconducting qubits: Current state of play,” *Annual Review of Condensed Matter Physics*, vol. 11, 2019.

[177] O. Mukhanov, A. Kirichenko, C. Howington, J. Walter, M. Hutchings, I. Vernik, D. Yohannes, K. Dodge, A. Ballard, B. Plourde, *et al.*, “Scalable quantum computing infrastructure based on superconducting electronics,” in *2019 IEEE International Electron Devices Meeting (IEDM)*, pp. 31–2, IEEE, 2019.

[178] N. C. Jones, R. Van Meter, A. G. Fowler, P. L. McMahon, J. Kim, T. D. Ladd, and Y. Yamamoto, “Layered architecture for quantum computing,” *Physical Review X*, vol. 2, no. 3, p. 031007, 2012.

[179] T. D. Ladd, F. Jelezko, R. Laflamme, Y. Nakamura, C. Monroe, and J. L. O’Brien, “Quantum computers,” *Nature*, vol. 464, no. 7285, pp. 45–53, 2010.

[180] L. Chirolli and G. Burkard, “Decoherence in solid-state qubits,” *Advances in Physics*, vol. 57, no. 3, pp. 225–285, 2008.

[181] U. Patel, I. V. Pechenezhskiy, B. Plourde, M. Vavilov, and R. McDermott, “Phonon-mediated quasiparticle poisoning of superconducting microwave resonators,” *Physical Review B*, vol. 96, no. 22, p. 220501, 2017.

[182] D. Hucul, I. V. Inlek, G. Vittorini, C. Crocker, S. Debnath, S. M. Clark, and C. Monroe, “Modular entanglement of atomic qubits using photons and phonons,” *Nature Physics*, vol. 11, no. 1, p. 37, 2015.

[183] H. Shin, J. A. Cox, R. Jarecki, A. Starbuck, Z. Wang, and P. T. Rakich, “Control of coherent information via on-chip photonic–phononic emitter–receivers,” *Nature communications*, vol. 6, p. 6427, 2015.

[184] A. Wallucks, I. Marinković, B. Hensen, R. Stockill, and S. Gröblacher, “A quantum memory at telecom wavelengths,” *Nature Physics*, pp. 1–6, 2020.

[185] C. Santori and R. G. Beausoleil, “Quantum memory: Phonons in diamond crystals,” *Nature Photonics*, vol. 6, no. 1, p. 10, 2012.

[186] S. J. Whiteley, G. Wolfowicz, C. P. Anderson, A. Bourassa, H. Ma, M. Ye, G. Koolstra, K. J. Satzinger, M. V. Holt, F. J. Heremans, *et al.*, “Spin–phonon interactions in silicon carbide addressed by Gaussian acoustics,” *Nature Physics*, vol. 15, no. 5, pp. 490–495, 2019.

[187] Y.-C. Wen, C.-L. Hsieh, K.-H. Lin, H.-P. Chen, S.-C. Chin, C.-L. Hsiao, Y.-T. Lin, C.-S. Chang, Y.-C. Chang, L.-W. Tu, *et al.*, “Specular scattering probability of acoustic phonons in atomically flat interfaces,” *Physical review letters*, vol. 103, no. 26, p. 264301, 2009.

[188] J.-C. Harmand, G. Patriarche, F. Glas, F. Panciera, I. Florea, J.-L. Maurice, L. Travers, and Y. Ollivier, “Atomic step flow on a nanofacet,” *Physical review letters*, vol. 121, no. 16, p. 166101, 2018.

[189] T. Huber, M. Davanco, M. Müller, Y. Shuai, O. Gazzano, and G. S. Solomon, “Filter-free single-photon quantum dot resonance fluorescence in an integrated cavity-waveguide device,” *Optica*, vol. 7, no. 5, pp. 380–385, 2020.

[190] A. D. Osterkryger, J. Claudon, J.-M. Gérard, and N. Gregersen, “Photonic “hourglass” design for efficient quantum light emission,” *Optics Letters*, vol. 44, no. 11, pp. 2617–2620, 2019.

[191] S. De Silvestri, J. Fujimoto, E. Ippen, E. B. Gamble Jr, L. R. Williams, and K. A. Nelson, “Femtosecond time-resolved measurements of optic phonon dephasing by impulsive stimulated Raman scattering in α-perylene crystal from 20 to 300 K,” *Chemical physics letters*, vol. 116, no. 2-3, pp. 146–152, 1985.

[192] F. Hudert, A. Bruchhausen, D. Issenmann, O. Schecker, R. Waitz, A. Erbe, E. Scheer, T. Dekorsy, A. Mlayah, and J.-R. Huntzinger, “Confined longitudinal acoustic phonon modes in free-standing si membranes coherently excited by femtosecond laser pulses,” *Phys. Rev. B*, vol. 79, p. 201307, May 2009.

[193] C. Rossignol, N. Chigarev, M. Ducousso, B. Audoin, G. Forget, F. Guillemot, and M. Durrieu, “In vitro picosecond ultrasonics in a single cell,” *Applied Physics Letters*, vol. 93, no. 12, p. 123901, 2008.

[194] A. Gadalla, T. Dehoux, and B. Audoin, “Transverse mechanical properties of cell walls of single living plant cells probed by laser-generated acoustic waves,” *Planta*, vol. 239, no. 5, pp. 1129–1137, 2014.

[195] F. Perez-Cota, R. J. Smith, E. Moradi, L. Marques, K. F. Webb, and M. Clark, “Thin-film optoacoustic transducers for subcellular Brillouin oscillation imaging of individual biological cells,” *Applied optics*, vol. 54, no. 28, pp. 8388–8398, 2015.

[196] E. M. Van Goethem, C. W. Pinion, E. E. Cating, J. F. Cahoon, and J. M. Papanikolas, “Observation of phonon propagation in germanium nanowires using femtosecond pump–probe microscopy,” *ACS Photonics*, vol. 6, no. 9, pp. 2213–2222, 2019.

[197] P.-A. Mante, L. Belliard, and B. Perrin, “Acoustic phonons in nanowires probed by ultrafast pump-probe spectroscopy,” *Nanophotonics*, vol. 7, no. 11, pp. 1759–1780, 2018.

[198] V. Gusev, A. Lomonosov, P. Ruello, A. Ayouch, and G. Vaudel, “Depth-profiling of elastic and optical inhomogeneities in transparent materials by picosecond ultrasonic interferometry: Theory,” *Journal of Applied Physics*, vol. 110, no. 12, p. 124908, 2011.

[199] M. Ortolani, A. Mancini, A. Budweg, D. Garoli, D. Brida, and F. de Angelis, “Pump-probe spectroscopy study of ultrafast temperature dynamics in nanoporous gold,” *Physical Review B*, vol. 99, no. 3, p. 035435, 2019.

[200] M. Li, S. Menon, J. P. Nibarger, and G. N. Gibson, “Ultrafast electron dynamics in femtosecond optical breakdown of dielectrics,” *Physical review letters*, vol. 82, no. 11, p. 2394, 1999.

[201] A. Mouskeftaras, S. Guizard, N. Fedorov, and S. Klimentov, “Mechanisms of femtosecond laser ablation of dielectrics revealed by double pump–probe experiment,” *Applied Physics A*, vol. 110, no. 3, pp. 709–715, 2013.

[202] M. Lindberg and S. W. Koch, “Theory of coherent transients in semiconductor pump–probe spectroscopy,” *JOSA B*, vol. 5, no. 1, pp. 139–146, 1988.

[203] J. Shah, *Ultrafast spectroscopy of semiconductors and semiconductor nanostructures*, vol. 115. Springer Science & Business Media, 2013.

[204] O. Matsuda, M. C. Larciprete, R. L. Voti, and O. B. Wright, “Fundamentals of picosecond laser ultrasonics,” *Ultrasonics*, vol. 56, pp. 3–20, 2015.

[205] C. Janke, M. Först, M. Nagel, H. Kurz, and A. Bartels, “Asynchronous optical sampling for high-speed characterization of integrated resonant terahertz sensors,” *Optics letters*, vol. 30, no. 11, pp. 1405–1407, 2005.

[206] V. Gusev, “On the duration of acoustic pulses excited by subpicosecond laser action on metals,” *Optics communications*, vol. 94, no. 1-3, pp. 76–78, 1992.

[207] D. Nardi, M. Travagliati, M. E. Siemens, Q. Li, M. M. Murnane, H. C. Kapteyn, G. Ferrini, F. Parmigiani, and F. Banfi, “Probing thermomechanics at the nanoscale: impulsively excited pseudosurface acoustic waves in hypersonic phononic crystals,” *Nano letters*, vol. 11, no. 10, pp. 4126–4133, 2011.

[208] O. Wright and V. Gusev, “Acoustic generation in crystalline silicon with femtosecond optical pulses,” *Applied physics letters*, vol. 66, no. 10, pp. 1190–1192, 1995.

[209] P. Babilotte, E. Morozov, P. Ruello, D. Mounier, M. Edely, J. Breteau, A. Bulou, and V. Gusev, “Physical mechanism of coherent acoustic phonons generation and detection in GaAs semiconductor,” in *Journal of Physics: Conference Series*, vol. 92, p. 012019, 2007.

[210] K.-H. Lin, C.-T. Yu, Y.-C. Wen, and C.-K. Sun, “Generation of picosecond acoustic pulses using ap-n junction with piezoelectric effects,” *Applied Physics Letters*, vol. 86, no. 9, p. 093110, 2005.

[211] P. Babilotte, P. Ruello, G. Vaudel, T. Pezeril, D. Mounier, J.-M. Breteau, and V. Gusev, “Picosecond acoustics in p-doped piezoelectric semiconductors,” *Applied physics letters*, vol. 97, no. 17, p. 174103, 2010.

[212] Y.-X. Yan, E. B. Gamble Jr, and K. A. Nelson, “Impulsive stimulated scattering: General importance in femtosecond laser pulse interactions with matter, and spectroscopic applications,” *The Journal of chemical physics*, vol. 83, no. 11, pp. 5391–5399, 1985.

[213] H. Tanaka, T. Sonehara, and S. Takagi, “A new phase-coherent light scattering method: first observation of complex Brillouin spectra,” *Physical review letters*, vol. 79, no. 5, p. 881, 1997.

[214] A. Bartels, R. Cerna, C. Kistner, A. Thoma, F. Hudert, C. Janke, and T. Dekorsy, “Ultrafast time-domain spectroscopy based on high-speed asynchronous optical sampling,” *Review of Scientific Instruments*, vol. 78, no. 3, p. 035107, 2007.

[215] P. Sesin, P. Soubelet, V. Villafañe, A. Bruchhausen, B. Jusserand, A. Lemaître, N. Lanzillotti-Kimura, and A. Fainstein, “Dynamical optical tuning of the coherent phonon detection sensitivity in DBR-based GaAs optomechanical resonators,” *Physical Review B*, vol. 92, no. 7, p. 075307, 2015.

[216] S. Anguiano, A. Bruchhausen, I. Favero, I. Sagnes, A. Lemaître, N. Lanzillotti-Kimura, and A. Fainstein, “Optical cavity mode dynamics and coherent phonon generation in high-Q micropillar resonators,” *Physical Review A*, vol. 98, no. 1, p. 013816, 2018.

[217] A. Bartels, T. Dekorsy, H. Kurz, and K. Köhler, “Coherent zone-folded longitudinal acoustic phonons in semiconductor superlattices: Excitation and detection,” *Phys. Rev. Lett.*, vol. 82, pp. 1044–1047, Feb 1999.

[218] M. Broer, “Multiple retroreflector optical delay line,” *Applied optics*, vol. 24, no. 16, pp. 2489–2490, 1985.

[219] H.-A. Bachor, T. C. Ralph, S. Lucia, and T. C. Ralph, *A guide to experiments in quantum optics*, vol. 1. Wiley Online Library, 2004.

[220] E. Suhir, Y.-C. Lee, and C. Wong, *Micro-and opto-electronic materials and structures: physics, mechanics, design, reliability, packaging: Volume I Materials physics-materials mechanics. Volume II Physical design-reliability and packaging*, vol. 1. Springer Science & Business Media, 2007.

[221] O. Ortiz, F. Pastier, A. Rodriguez, Priya, A. Lemaitre, C. Gomez-Carbonell, I. Sagnes, A. Harouri, P. Senellart, V. Giesz, *et al.*, “Fiber-integrated microcavities for efficient generation of coherent acoustic phonons,” *Applied Physics Letters*, vol. 117, no. 18, p. 183102, 2020.

[222] R. Ulrich, S. Rashleigh, and W. Eickhoff, “Bending-induced birefringence in single-mode fibers,” *Optics letters*, vol. 5, no. 6, pp. 273–275, 1980.

[223] A. J. Heeger, S. Kivelson, J. Schrieffer, and W.-P. Su, “Solitons in conducting polymers,” *Reviews of Modern Physics*, vol. 60, no. 3, p. 781, 1988.

[224] W. Su, J. Schrieffer, and A. J. Heeger, “Solitons in polyacetylene,” *Physical review letters*, vol. 42, no. 25, p. 1698, 1979.

[225] W.-P. Su, J. Schrieffer, and A. Heeger, “Soliton excitations in polyacetylene,” *Physical Review B*, vol. 22, no. 4, p. 2099, 1980.

[226] J. Zak, “Berry’s phase for energy bands in solids,” *Physical review letters*, vol. 62, no. 23, p. 2747, 1989.

[227] T. Ozawa, H. M. Price, A. Amo, N. Goldman, M. Hafezi, L. Lu, M. C. Rechtsman, D. Schuster, J. Simon, O. Zilberberg, *et al.*, “Topological photonics,” *Reviews of Modern Physics*, vol. 91, no. 1, p. 015006, 2019.

[228] M. Hafezi, S. Mittal, J. Fan, A. Migdall, and J. Taylor, “Imaging topological edge states in silicon photonics,” *Nature Photonics*, vol. 7, no. 12, pp. 1001–1005, 2013.

[229] M. Hafezi, E. A. Demler, M. D. Lukin, and J. M. Taylor, “Robust optical delay lines with topological protection,” *Nature Physics*, vol. 7, no. 11, pp. 907–912, 2011.

[230] L. Lu, J. D. Joannopoulos, and M. Soljačić, “Topological photonics,” *Nature photonics*, vol. 8, no. 11, pp. 821–829, 2014.

[231] J. Henriques, T. Rappoport, Y. V. Bludov, M. Vasilevskiy, and N. Peres, “Topological photonic tamm states and the su-schrieffer-heeger model,” *Physical Review A*, vol. 101, no. 4, p. 043811, 2020.

[232] L. M. Nash, D. Kleckner, A. Read, V. Vitelli, A. M. Turner, and W. T. Irvine, “Topological mechanics of gyroscopic metamaterials,” *Proceedings of the National Academy of Sciences*, vol. 112, no. 47, pp. 14495–14500, 2015.

[233] S. Klembt, T. Harder, O. Egorov, K. Winkler, R. Ge, M. Bandres, M. Emmerling, L. Worschech, T. Liew, M. Segev, *et al.*, "Exciton-polariton topological insulator," *Nature*, vol. 562, no. 7728, pp. 552–556, 2018.

[234] Y. Meng, X. Wu, R.-Y. Zhang, X. Li, P. Hu, L. Ge, Y. Huang, H. Xiang, D. Han, S. Wang, *et al.*, "Designing topological interface states in phononic crystals based on the full phase diagrams," *New Journal of Physics*, vol. 20, no. 7, p. 073032, 2018.

[235] J. D. Scargle, "Studies in astronomical time series analysis. ii-statistical aspects of spectral analysis of unevenly spaced data," *The Astrophysical Journal*, vol. 263, pp. 835–853, 1982.

[236] W. H. Press, S. A. Teukolsky, W. T. Vetterling, and B. P. Flannery, *Numerical recipes 3rd edition: The art of scientific computing.* Cambridge university press, 2007.

[237] G. Arregui, N. D. Lanzillotti-Kimura, C. M. Sotomayor-Torres, and P. D. García, "Anderson photon-phonon colocalization in certain random superlattices," *Phys. Rev. Lett.*, vol. 122, p. 043903, Feb 2019.

[238] A. Savitzky and M. J. Golay, "Smoothing and differentiation of data by simplified least squares procedures.," *Analytical chemistry*, vol. 36, no. 8, pp. 1627–1639, 1964.

[239] V. Villafañe, P. Soubelet, A. Bruchhausen, N. Lanzillotti-Kimura, B. Jusserand, A. Lemaître, and A. Fainstein, "Slow light and slow acoustic phonons in optophononic resonators," *Physical Review B*, vol. 94, no. 20, p. 205308, 2016.

[240] K.-Y. Jhang, C. J. Lissenden, I. Solodov, Y. Ohara, and V. Gusev, *Measurement of Nonlinear Ultrasonic Characteristics.* Springer, 2020.

[241] J. Loredo, M. Broome, P. Hilaire, O. Gazzano, I. Sagnes, A. Lemaitre, M. Almeida, P. Senellart, and A. White, "Boson sampling with single-photon fock states from a bright solid-state source," *Physical review letters*, vol. 118, no. 13, p. 130503, 2017.

[242] P. Senellart, G. Solomon, and A. White, "High-performance semiconductor quantum-dot single-photon sources," *Nature nanotechnology*, vol. 12, no. 11, p. 1026, 2017.

[243] H. Wang, J. Qin, X. Ding, M.-C. Chen, S. Chen, X. You, Y.-M. He, X. Jiang, L. You, Z. Wang, *et al.*, "Boson sampling with 20 input photons and a 60-mode interferometer in a 1 0 14-dimensional hilbert space," *Physical review letters*, vol. 123, no. 25, p. 250503, 2019.

[244] J. Loredo, C. Antón, B. Reznychenko, P. Hilaire, A. Harouri, C. Millet, H. Ollivier, N. Somaschi, L. De Santis, A. Lemaître, *et al.*, "Generation of non-classical light in a photon-number superposition," *Nature Photonics*, vol. 13, no. 11, pp. 803–808, 2019.

[245] Z.-C. Duan, J.-P. Li, J. Qin, Y. Yu, Y.-H. Huo, S. Höfling, C.-Y. Lu, N.-L. Liu, K. Chen, and J.-W. Pan, "Proof-of-principle demonstration of compiled shor's algorithm using a quantum dot single-photon source," *Optics Express*, vol. 28, no. 13, pp. 18917–18930, 2020.

[246] S. Anguiano, P. Sesin, A. Bruchhausen, F. Lamberti, I. Favero, M. Esmann, I. Sagnes, A. Lemaître, N. Lanzillotti-Kimura, P. Senellart, *et al.*, "Scaling rules in optomechanical semiconductor micropillars," *Physical Review A*, vol. 98, no. 6, p. 063810, 2018.

[247] B. Gayral, "Controlling spontaneous emission dynamics in semiconductor microcavities: an experimental approach," *Ann. Phys. Fr*, vol. 26, no. 2, 2001.

[248] M. P. Winter, G. Rozas, A. Fainstein, B. Jusserand, B. Perrin, A. Huynh, P. Vaccaro, and S. Saravanan, “Selective optical generation of coherent acoustic nanocavity modes,” *Physical review letters*, vol. 98, no. 26, p. 265501, 2007.

[249] M. Hamoumi, P. E. Allain, W. Hease, E. Gil-Santos, L. Morgenroth, B. Gérard, A. Lemaître, G. Leo, and I. Favero, “Microscopic nanomechanical dissipation in gallium arsenide resonators,” *Physical review letters*, vol. 120, no. 22, p. 223601, 2018.

[250] M. Taghinejad and W. Cai, “All-optical control of light in micro-and nanophotonics,” *ACS Photonics*, vol. 6, no. 5, pp. 1082–1093, 2019.

[251] F. Pagliano, Y. Cho, T. Xia, F. Van Otten, R. Johne, and A. Fiore, “Dynamically controlling the emission of single excitons in photonic crystal cavities,” *Nature communications*, vol. 5, no. 1, pp. 1–6, 2014.

[252] A. Yariv *et al.*, *Optical electronics in modern communications*, vol. 1. Oxford University Press, USA, 1997.

[253] A. Yariv and P. Yeh, *Photonics: optical electronics in modern communications (the oxford series in electrical and computer engineering).* Oxford University Press, Inc., 2006.

[254] N. Lanzillotti-Kimura, A. Fainstein, B. Perrin, and B. Jusserand, “Theory of coherent generation and detection of thz acoustic phonons using optical microcavities,” *Physical Review B*, vol. 84, no. 6, p. 064307, 2011.

[255] G. J. Snyder and E. S. Toberer, “Complex thermoelectric materials,” in *Materials for sustainable energy: a collection of peer-reviewed research and review articles from Nature Publishing Group*, pp. 101–110, World Scientific, 2011.

[256] K. Biswas, J. He, I. D. Blum, C.-I. Wu, T. P. Hogan, D. N. Seidman, V. P. Dravid, and M. G. Kanatzidis, “High-performance bulk thermoelectrics with all-scale hierarchical architectures,” *Nature*, vol. 489, no. 7416, pp. 414–418, 2012.

[257] A. Abbas, Y. Guillet, J.-M. Rampnoux, P. Rigail, E. Mottay, B. Audoin, and S. Dilhaire, “Picosecond time resolved opto-acoustic imaging with 48 MHz frequency resolution,” *Opt. Express*, vol. 22, pp. 7831–7843, Apr 2014.

[258] M. Guina, A. Rantamäki, and A. Härkönen, “Optically pumped vecsels: review of technology and progress,” *Journal of Physics D: Applied Physics*, vol. 50, no. 38, p. 383001, 2017.

[259] N. C. Zambon, P. St-Jean, M. Milićević, A. Lemaître, A. Harouri, L. Le Gratiet, O. Bleu, D. Solnyshkov, G. Malpuech, I. Sagnes, *et al.*, “Optically controlling the emission chirality of microlasers,” *Nature Photonics*, vol. 13, no. 4, pp. 283–288, 2019.

[260] C. Charlton, M. Giovannini, J. Faist, and B. Mizaikoff, “Fabrication and characterization of molecular beam epitaxy grown thin-film gaas waveguides for mid-infrared evanescent field chemical sensing,” *Analytical chemistry*, vol. 78, no. 12, pp. 4224–4227, 2006.

[261] I. Marinković, A. Wallucks, R. Riedinger, S. Hong, M. Aspelmeyer, and S. Gröblacher, “Optomechanical bell test,” *Physical review letters*, vol. 121, no. 22, p. 220404, 2018.

[262] S. Hong, R. Riedinger, I. Marinković, A. Wallucks, S. G. Hofer, R. A. Norte, M. Aspelmeyer, and S. Gröblacher, “Hanbury brown and twiss interferometry of single phonons from an optomechanical resonator,” *Science*, vol. 358, no. 6360, pp. 203–206, 2017.

[263] F. Lamberti, Q. Yao, L. Lanco, D. Nguyen, M. Esmann, A. Fainstein, P. Sesin, S. Anguiano, V. Villafañe, A. Bruchhausen, *et al.*, "Optomechanical properties of gaas/alas micropillar resonators operating in the 18 ghz range," *Optics express*, vol. 25, no. 20, pp. 24437–24447, 2017.

[264] Y. Sugawara, O. Wright, O. Matsuda, M. Takigahira, Y. Tanaka, S. Tamura, and V. Gusev, "Watching ripples on crystals," *Physical review letters*, vol. 88, no. 18, p. 185504, 2002.

[265] V. Goblot, A. Štrkalj, N. Pernet, J. Lado, C. Dorow, A. Lemaître, L. Le Gratiet, A. Harouri, I. Sagnes, S. Ravets, *et al.*, "Emergence of criticality through a cascade of delocalization transitions in quasiperiodic chains," *Nature Physics*, vol. 16, no. 8, pp. 832–836, 2020.

[266] D. Tanese, E. Gurevich, F. Baboux, T. Jacqmin, A. Lemaître, E. Galopin, I. Sagnes, A. Amo, J. Bloch, and E. Akkermans, "Fractal energy spectrum of a polariton gas in a fibonacci quasiperiodic potential," *Physical review letters*, vol. 112, no. 14, p. 146404, 2014.

[267] S. Burkov, B. Koltenbah, and L. Bruch, "Phonon localization in one-dimensional quasiperiodic chains," *Physical Review B*, vol. 53, no. 21, p. 14179, 1996.

université
PARIS-SACLAY

ÉCOLE DOCTORALE
Ondes et Matière
(EDOM)

Titre: Dynamique de phonons acoustiques cohérents dans des hétérostructures GaAs/AlAs

Mots clés: Nanophononique, diffusion Brillouin dans le domaine temporel, spectroscopie pompe-sonde, phonons acoustiques, optomécanique, cavité adiabatique, résonateurs acoustiques, micropiliers

Résumé: Les phonons sont des quasi-particules relativement peu exploitées à des fins d'application, en comparaison avec les électrons ou les photons. Les hétérostructures faites de GaAs/AlAs comme les super-réseaux ont été établies comme une plateforme qui permet l'ingénierie de la propagation et du confinement des phonons acoustiques dans les nanostructures. Dans ce travail, nous introduisons de nouveaux systèmes qui contrôlent la propagation des ondes acoustiques et qui, de plus, nous permettent d'étudier et d'imiter des phénomènes de physique des solides de nature différente. Les super-réseaux offrent également la possibilité d'améliorer la transduction des phonons acoustiques en signaux optiques. De nos jours, il existe une demande pour de nouvelles techniques qui facilitent l'étude expérimentale des dispositifs nanophononiques. Au cours de cette thèse, nous avons étudié expérimentalement des hétérostructures faites de GaAs/AlAs qui contrôlent la propagation de phonons acoustiques cohérents de la dizaine aux centaines de gigahertz. Nous développons de nouvelles techniques expérimentales basées sur l'utilisation de fibres monomodes et la spectroscopie pompe-sonde qui nous permettent d'identifier la présence de phonons cohérents avec une robustesse et une reproductibilité sans précédent.

Title: Coherent acoustic-phonon dynamics in GaAs/AlAs heterostructures

Keywords: Nanophononics, time-domain Brillouin scattering, pump-probe spectroscopy, acoustic phonons, Optomechanics, adiabatic cavities, acoustic resonators, micropillars

Abstract: Phonons are quasi-particles relatively unexploited for application purposes, in comparison with electrons and photons. GaAs/AlAs heterostructures like superlattices have been established as a platform that allows engineering the propagation and confinement of acoustic phonons in nanostructures. In this work, we introduce novel devices that control the propagation of acoustic waves and, furthermore, allow us to study and mimic solid-state physical phenomena of different nature. Superlattices also offer the possibility to enhance the transduction of acoustic phonons into optical signals. Nowadays, there exists a demand for novel techniques that facilitate the experimental study of nanophononic devices. In the course of this thesis, we have experimentally studied nanoengineered GaAs/AlAs heterostructures that control the propagation of coherent acoustic phonons in the tens to hundreds of gigahertz range. We develop novel experimental techniques based on the use of single-mode fibers and pump-probe spectroscopy that allow us to identify the presence of coherent phonons with unprecedented robustness and reproducibility.

Université Paris-Saclay
Espace Technologique / Immeuble Discovery
Route de l'Orme aux Merisiers RD 128 / 91190 Saint-Aubin, France